HYDRAULIC FRACTURE MODEL SENSITIVITY ANALYSES OF MASSIVELY STACKED LENTICULAR RESERVOIRS IN THE MESAVERDE FORMATION, SOUTHERN PICEANCE BASIN, COLORADO

by

Dr. Christopher A. Green

A thesis submitted to the Faculty and the Board of Trustees of the Colorado School of Mines in partial fulfillment of the requirements for the degree of Master of Science (Petroleum Engineering).

Golden, Colorado

Date______________________

Signed: ______________________________

Dr. Christopher A. Green

Approved: ______________________________

Dr. Jennifer L. Miskimins
Thesis Advisor

Golden, Colorado

Date______________________

____

Dr. Craig W. Van Kirk
Professor and Head,
Department of
Petroleum Engineering

ABSTRACT

The study area straddles the Colorado River and Interstate 70 in Garfield and Mesa counties, northwestern Colorado. The producing interval of the Mesaverde formation is a 1700 to 2000 ft thick laminated sequence of siltstones, shales and tight sandstones with a coaly interval at the base. The main producing interval is a non-marine reservoir, which exhibits a high degree of heterogeneity, both vertically and horizontally. A significant amount of work has previously been undertaken in the Piceance basin, at the multi-well experiment (MWX) site. A geologic characterization of the Mesaverde group established that the production was predominantly from the fluvial point bar sand bodies, with extremely low matrix permeabilities (<0.0001 mD). Subsequent geologic and geophysical work carried out in the nearby Rulison field established that there was an abundant system of micro-scale natural fractures and a less frequent system of macro-scale fractures. In common with most tight gas reservoirs, hydraulic stimulation is required to interconnect the dual-fracture system with the wellbore to maximize well production.

Well costs are typically $1.25 MM and between 40 and 50% of the total cost may be due to the well stimulation treatment. Therefore, there is a need to optimize the process. Limited success has been achieved using ordinary techniques and a pseudo-three-dimensional model (P3D). This study uses a fully three-dimensional (3D) simulator, GOHFER, to develop a model of a hydraulically fractured well. This research uses a simulator to investigate input parameters, and from the results critical inputs are identified for realistic model development. For the study, input data from sixteen wells were analyzed for the type of data available and the quality of the data. A single well was selected for simulation which had available standard logs as well as mini-fracture

analysis of all the reservoir sands identified by the operator. A comparison well was analyzed to help assess and validate the quality of the input data.

The study used log-derived input data to define the rock elastic properties (Young's modulus, Poisson's ratio and Biot's constant), porosity and lithology, using standard log ASCII (.las) files. The derived properties were compared to previous data from the MWX experiments and then used to help create an accurate lithologic representation of the reservoir. However, the physical properties of rocks are affected by in-situ stress and this was determined using small volume hydraulic fracture analysis, which has previously been used in the Mesaverde by Warpinski and Teufel (1989). This study details the results of fifty-six tests analyzed in both the study well and an adjacent well, for comparison with one another as well as with historical data from the MWX site. A number of cases were then run using GOHFER, and the resulting model compared to microseismic measurements, taken during the treatment. The microseismic information indicates where shear slippage is occurring and provides a means of calibrating the simulator outputs to actual fracture geometry to obtain a matched model. The original hydraulic fracture model run using these data was found to have similar containment to the field data, without any changes being necessary to the stresses in bounding layers. This would suggest that the log-derived stress differences of the reservoir sands and the bounding shale layers are captured in the initial analyses.

Sensitivity analysis of critical inputs is detailed in the study, and the results indicate that total stress and Young's modulus are the primary controlling factors of the simulator outputs. The sensitivity analysis results are similar to those from previous research (Miskimins, 2002; Warpinski et al, 1998) whereby stress, or more precisely stress contrasts, and Young's modulus were shown to play a major role in determining hydraulic fracture dimensions. The other inputs analyzed: permeability, Poisson's ratio and pore pressure were found to be secondary factors controlling fracture growth. The largest difference overall occurred for the advanced parameters analysis and showed their importance in the final matching process, even after other critical input data has been analyzed and validated. Most importantly, the sensitivity analysis indicated that the often used process of ‘net surface pressure matching’ to derive a valid simulator model can lead to significant discrepancies, when compared to a constrained, matched model.

TABLE OF CONTENTS

Page

ABSTRACT iii

TABLE OF CONTENTS vi

LIST OF FIGURES x

LIST OF TABLES xiv

DEDICATION xvi

ACKNOWLEDGEMENTS xvii

CHAPTER 1: INTRODUCTION 1

1.1 Research Objectives 3

1.2 Research Contributions 4

CHAPTER 2: LITERATURE REVIEW 6

2.1 Piceance Basin 6

2.1.1 Geology 8

2.1.2 Stratigraphy 11

2.1.3 Natural Fracture Production 16

2.1.4 Piceance Basin Cumulative Production and Reserves 17

2.1.5 Piceance Well Spacing 17

2.1.6 Piceance Basin Field Production 17

2.1.7 Gas Source and Trapping 21

2.1.8 Mesaverde Reservoir Characterization 22

2.2 Hydraulic Fracturing 22

2.3 Rock-Mechanical Properties 24

2.4 Fracture Containment 33

2.5 Fracture Analysis Techniques 36

2.5.1 Class 1 – Direct Far-Field Techniques 36

2.5.2 Class 2 – Direct Near-Wellbore Techniques 37
2.5.3. Class 3 - Indirect Fracture Techniques 40
2.6 Mini-Fracture Analysis 40
2.7 Fracture Geometry Modeling 43
2.7.1 2D Models 43
2.7.2 P3D Models 44
2.7.3 3D models 45
CHAPTER 3: MODEL INPUT DEVELOPMENT 46
3.1 3D Simulation Software History 50
3.2 Study Wells/Model Development 53
3.3 General Case Development 54
3.3.1 Young's Modulus (E) 58
3.3.2 Poisson's Ratio 60
3.3.3 Biot's Constant 60
3.3.4 In-Situ Stress 61
3.3.4.1 Mini-Hydraulic Fracture Tests 62
3.3.4.2 Process Zone Stress 72
3.3.4.3 Total Stress 74
3.3.5 Permeability Correlation 75
CHAPTER 4: HYDRAULIC FRACTURE SIMULATION MODEL RESULTS AND INPUT SENSITIVITY ANALYSES 82
4.1 Matching the Model using Advanced Parameters 82
4.2 Model Match Results 85
4.2.1 Interval T 87
4.2.2 Interval O 96
4.2.2 Interval M 103
4.2.3 Interval A 110
4.2.4 Interval S 118

4.2.6 Interval G 119
4.3 Matched Model Sensitivity Analyses 130
4.4 Interval O Sensitivity Analysis 149
CHAPTER 5: DISCUSSION 165
CHAPTER 6: CONCLUSIONS AND RECOMMENDATIONS 175
6.1 Conclusions 175
6.2 Hydraulic Fracture Model Field Input Analysis Recommendations 177
6.2 Future Work 178
NOMENCLATURE 181
REFERENCES 183
APPENDIX A: MODEL INPUTS 193
Summary of Data 194
A-1 G-Function Analysis 194
A-2 Rock Properties 198
A-3: Permeability Correlations 202
CD-ROM:
Reports A-1 to A-5: Mini-frac Analyses (Comparison Well) Zones C1 to C5
Reports A-6 to A-10: Mini-frac Analyses (Comparison Well) Zones H1 to H5
Reports A-11 to A-14: Mini-frac Analyses (Comparison Well) Zones I1 to I4
Reports A-15 to A-18: Mini-frac Analyses (Comparison Well) Zones R1 to R4
Reports A-19 to A-23: Mini-frac Analyses (Comparison Well) Zones C1 to C5
Reports A-24 to A-28: Mini-frac Analyses (Study Well) Zones A1 to A5
Reports A-29 to A-33: Mini-frac Analyses (Study Well) Zones G1 to G5
Reports A-34 and A-35: Mini-frac Analyses (Study Well) Zones I1 and I2
Reports A-36 to A-41: Mini-frac Analyses (Study Well) Zones M1 to M6
Reports A-42 to A-46: Mini-frac Analyses (Study Well) Zones O1 to O5
Reports A-47 to A-51: Mini-frac Analyses (Study Well) Zones S1 to S5
Reports A-52 to A-56: Mini-frac Analyses (Study Well) Zones T1 to T5

APPENDIX B: SIMULATOR OUTPUTS CASES 1-11 203

Summary of Data 204

CD-ROM:

B1: Matched Case Outputs with no Perf Factor

B2: Case 1 Simulator Outputs YM-10%

B3: Case 2 Simulator Outputs YM-20%

B4: Case 3 Simulator Outputs PR-10%

B5: Case 4 Simulator Outputs Pr-20%

B6: Case 5 Simulator Outputs PP OFFSET

B7: Case 6 Simulator Outputs NO PARAM

B8: Case 7 Simulator Outputs BIOTS

B9: Case 8 Simulator Outputs PERM

B10: Case 9 Simulator Outputs DEFAULT

B11: Case 10 Simulator Outputs STRESS-10%

B12: Case 11 Simulator Outputs STRESS-20%

MISCELLANEOUS .... CD-ROM

Rock Properties from the MWX

Model Permeability and PZS Correlation Development

LIST OF FIGURES

Page

Figure 2-1: Piceance basin location 7

Figure 2-2: Map of the Piceance basin 9

Figure 2-3: Piceance basin-centered gas model 10

Figure 2-4: Stratigraphic column 12

Figure 2-5: Reservoir and matrix permeability's from the MWX experiments 14

Figure 2-6: Hypothetical meander belt sandstone reservoirs 18

Figure 2-7: Piceance basin total production plot (through 2003) 20

Figure 2-8: Structural map of the Mesaverde group 23

Figure 2-9: A 3-D conceptual fracture model 25

Figure 2-10: The induced strain for or an axial loaded cylinder 31

Figure 2-11: Strain induced by compression on a cylinder 32

Figure 2-12: The Mohr-Coulomb failure diagram 35

Figure 2-13: Principle of tiltmeter fracture mapping 38

Figure 2-14: The principles of microseismic fracture mapping.................................... 39

Figure 2-15: Log-log slope interpretation 42

Figure 3-1: The location of the MWX site 47

Figure 3-2: Cross Plot of EUR versus net pay for a Piceance basin Field 48

Figure 3-3: Workflow diagram of the methodology for a HF model ....56 & 81

Figure 3-4: The actual model layers of the subject well, as defined in LOGCALC..... 57

Figure 3-5: Graph showing a plot of Table 3-4 data 66

Figure 3-6: A summary of the G-function leakoff analysis 69

Figure 3-7: Pore pressure vs total minimum horizontal stress in the Rulison Field 70

Figure 3-8: Pore pressure versus total minimum horizontal stress in the study well ... 71

Figure 3-9: Graph showing the actual data points from Table 3-7 77
Figure 3-10: Total minimum horizontal stress and pore pressure changes with depth 80
Figure 4-1: Matched net surface pressure for Interval T 90
Figure 4-2: GOHFER net fracture pressure (psi) output grid for Interval T 91
Figure 4-3: GOHFER fracture width (inches) output grid for Interval T 92
Figure 4-4: GOHFER proppant concentration (lb/ft^2) output grid for Interval T 93
Figure 4-5: GOHFER conductivity (md-ft) output grid for Interval T 94
Figure 4-6: Microseismic results for Interval T 95
Figure 4-7: Matched net surface pressure for Interval O 97
Figure 4-8: GOHFER net fracture pressure (psi) output grid for Interval O 98
Figure 4-9: GOHFER fracture width (inches) output grid for Interval O 99
Figure 4-10: GOHFER proppant concentration (lb/ft^2) output grid for Interval O 100
Figure 4-11: GOHFER conductivity (md-ft) output grid for Interval O 101
Figure 4-12: Microseismic results for Interval O 102
Figure 4-13: Matched net surface pressure for Interval M 104
Figure 4-14: GOHFER net fracture pressure (psi) output grid for Interval M 105
Figure 4-15: GOHFER fracture width (inches) output grid for Interval M 106
Figure 4-16: GOHFER proppant concentration (lb/ft^2) output grid for Interval M 107
Figure 4-17: GOHFER conductivity (md-ft) output grid for Interval M 108
Figure 4-18: Microseismic results for Interval M 109
Figure 4-19: Matched net surface pressure for Interval A 112
Figure 4-20: GOHFER net fracture pressure (psi) output grid for Interval A 113
Figure 4-21: GOHFER fracture width (inches) output grid for Interval A 114
Figure 4-22: GOHFER proppant concentration (lb/ft^2) output grid for Interval A 115
Figure 4-23: GOHFER conductivity (md-ft) output grid for Interval A 116
Figure 4-24: Microseismic results for Interval A 117
Figure 4-25: Matched net surface pressure for Interval S 120
Figure 4-26: GOHFER net fracture pressure (psi) output grid for Interval S 121

Figure 4-27: GOHFER fracture width (in) output grid for Interval S 122
Figure 4-28: GOHFER proppant concentration (lb/ft^2) output grid for Interval S 123
Figure 4-29: GOHFER conductivity (md-ft) output grid for Interval S 124
Figure 4-30: Matched net surface pressure for Interval G 125
Figure 4-31: GOHFER net pressure (psi) output grid for Interval G 126
Figure 4-32: GOHFER fracture width (in) output grid for Interval G.......................... 127
Figure 4-33: GOHFER proppant concentration (lb/ft^2) output grid for Interval G 128
Figure 4-34: GOHFER conductivity (md-ft) output grid for Interval G 129
Figure 4-35: Net surface pressure plots for all Interval T analyses 143
Figure 4-36: Net surface pressure plots for all Interval O analyses............................. 144
Figure 4-37: Net surface pressure plots for all Interval M analyses 145
Figure 4-38: Net surface pressure plots for all Interval A analyses 146
Figure 4-39: Net surface pressure plots for all Interval S analyses 147
Figure 4-40: Net surface pressure plots for all Interval G analyses 148
Figure 4-41: Matched model proppant concentration outputs for Interval O 150
Figure 4-42: Case 1 proppant concentration outputs for Interval O 151
Figure 4-43: Case 2 proppant concentration outputs for Interval O 152
Figure 4-44: Case 3 proppant concentration outputs for Interval O 153
Figure 4-45: Case 4 proppant concentration outputs for Interval O 154
Figure 4-46: Case 5 proppant concentration outputs for Interval O 155
Figure 4-47: Case 6 proppant concentration outputs for Interval O 156
Figure 4-48: Case 7 proppant concentration outputs for Interval O 157
Figure 4-49: Case 8 proppant concentration outputs for Interval O 158
Figure 4-50: Case 9 proppant concentration outputs for Interval O 159
Figure 4-51: Case 10 proppant concentration outputs for Interval O 160
Figure 4-52: Case 11 proppant concentration outputs for Interval O 161
Figure A-1: LOGCALC Young’s modulus/density curves 198
Figure A-2: LOGCALC Poisson’s ratio curves 199

Figure A-3: Morrow and Ward Permeability correlation 202

LIST OF TABLES

Page

Table 2-1: Piceance Basin Field Production Summary to 2003 19

Table 2-2: The Interrelation of Moduli in Linear-Elastic Theory 29

Table 3-1: Various Zones and Their Log-Derived Grid Layer Values......................... 59

Table 3-2: Study Well Results of G-Function Analysis Closure Pressures 63

Table 3-3: Comparison Well Results of G-Function Analysis Closure Pressure 64

Table 3-4: Mini-Fracture Analysis Results 68

Table 3-5: G-Function Leakoff Analysis Results for the Study Well 69

Table 3-6: Process Zone Stress Values Derived from both Logs and Calculated 73

Table 3-7: G-Function ACA and Porosity Derived Values 78

Table 4-1: Advanced Reservoir Parameters Values 84

Table 4-2: List of the Perforation Factor Changes used in the Matched Model 86

Table 4-3: Perforation and Pore Pressure Offset Values in the Matched Model 89

Table 4-4: Matched HF Model Outputs 131

Table 4-5 Simulator Sensitivity Cases and Associated Reasons 132

Table 4-6: GOHFER Output Values for Cases 1 & 2 – Young’s Modulus Changes .. 136

Table 4-7: GOHFER Output Values for Cases 3 & 4 – Poisson’s Ratio Changes 137

Table 4-8: GOHFER Output Values for Case 5 – Constant Pore Pressure Offset 138

Table 4-9: GOHFER Output Values for Case 6 – No Advanced Parameters Used 138

Table 4-10: GOHFER Output Values for Case 7 – Vertical Biot’s Set at 1 139

Table 4-11: GOHFER Output Values for Case 8 – Permeability Correlation 139

Table 4-12: GOHFER Output Values for Case 9 – Default Inputs 140

Table 4-13: GOHFER Output Values for Case 10 – Total Stress minus 10% 140

Table 4-14: GOHFER Output Values for Case 11 – Total Stress minus 20% 141

Table 5-1: Summary Results for all Cases Compared to the Matched Model 173

Table A-1: Rock Properties MWX-1 Site 200
Table A-2: Rock Properties MWX-2 Site 201

DEDICATION

I would like to dedicate this work to my family. To my wife, Sharon, who never stops amazing me with her strength, resilience, optimism and beauty. My daughter, Rhiannah, deserves special mention as she has now been inspired to become an engineer, albeit after a short spell with WWE. Lastly, this is dedicated to my son Tómas who has the heart of a lion, long may you roar.

ACKNOWLEDGEMENTS

I would especially like to thank my advisor Dr. Jennifer Miskimins who has gone beyond the call of duty to ensure that this work was presented. You have shown great optimism throughout and most importantly, never gave up on me. The last year has been difficult beyond belief but you continually helped with both my professional and personal life. I can only write these few words to tell you how special both you and Dr. Ramona Graves helped make my time at Colorado School of Mines a memorable one. I would also like to thank my unofficial co-advisor Dr. Bob Barree, whose help was freely given. Thankfully, he was easy to distract and coerce into providing help with the practical side of this work, no matter what his workload.

I am deeply indebted to the operator for their support of this research, they provided all the data and an office to enable me to complete this work. I would also like to thank Barree and Associates for allowing the charitable sharing of the software needed for this study, as well as another office.

I am also very grateful to two research consortia at Colorado School of Mines, run by Dr. Miskimins (FAST - Fracturing Acidizing Stimulation Technology) and Dr. Tom Davis (RCP - Reservoir Characterization Project) who generously agreed to provide a financial injection at a time when I really needed it. Thanks also go to my other committee member Dr. Erdal Ozkan, for kindly giving up numerous occasions to discuss transient pressure analysis, horizontal wells and families.

A special note of thanks goes to the rest of my family and friends who made everything possible. To my sister (Denise), brother (Stewart) and best friend (Jason) thanks for being there when I needed a moan. Finally, mum and dad, this is the third and last time (at least you didn't have to pay for this one?).

CHAPTER 1
INTRODUCTION

All early oil and gas wells were drilled vertically as engineers had limited technology available, though they knew that the increased well surface area of horizontal wells would be beneficial to well productivity. It wasn't until the 1920's that R.F. Farris of Stanolind Oil and Gas Corporation, devised a methodology to significantly increase vertical well productivity by hydraulically fracturing the rock. This technique, originally called the 'Hydrafrac' process, was first tested in 1947 on a gas well in Kansas (Clark, 1949) before Halliburton bought the rights in 1949 and subsequently developed the technology. Hydraulic fracturing now plays a major role in enhancing production rates and recoverable reserves from oil and gas fields. It has been estimated that 40% of modern wells are stimulated using this technique and that 20-30% of the total US reserves have been made economic by using this technology (Gidley et al, 1989).

Early applications were carried out using simple low volume, low injection rate procedures but these have now evolved into highly engineered, complex processes that can be used in a number of ways to improve well productivity. Modern applications include uses such as overcoming near wellbore damage in newly drilled wells, as well as increasing injectivity in disposal and injection wells. However, most routine applications are for making deeply penetrating, high conductivity fractures in low permeability (tight) reservoirs, such as in the Piceance basin of northwestern Colorado. The main limitation to the technique's widespread application is its relatively high cost, where a typical hydraulic fracture treatment can be more than half the cost of drilling and completing a well. Recently, the technology of fracturing has improved significantly with the development of new fluids and proppant combinations for applications ranging from shallow, low-temperature formations to deep, high-temperature/high-pressure reservoirs.

However, as the technology has improved, so have the material sophistication and the associated cost. The increased economics mean that there is a requirement for rigorous analysis and optimization of the design economics prior to, and during, job execution.

Despite its common use, hydraulic fracturing still remains one of the most complex and least understood practices employed in the oil industry. For a complete evaluation, the engineer now has to fully evaluate the well potential, as well as the effectiveness of the treatment design for creating the desired fracture. There are also problems deducing reservoir data in certain reservoir types, such as tight gas reservoirs, which are complex, produce from multiple layers and often have permeabilities that are enhanced by natural fractures. Simple layer-type reservoir models often prove to be inaccurate as the oversimplified reservoir descriptions frequently result in overestimated well productivity. Much of this can be attributed to the complexity of the reservoirs themselves, which often have both vertical and horizontal heterogeneities, but it is also due to faults and fractures. The most cost effective method for analyzing tight gas reservoirs usually involves a detailed study of a few select wells. Results from these wells are then used to develop a procedure for analyzing other wells. Unfortunately, the low productivity and marginal economics of tight gas reservoirs often prevents the expenditure of time and money to collect the data required for detailed reservoir studies.

To correctly model and predict hydraulic fracture growth in complex reservoirs requires both an in-depth knowledge of fluid mechanics and the reservoir rock mechanics. Complex reservoirs require an inter-disciplinary approach to reservoir analysis, to generate the necessary input data for effective treatment design. Fracture design is often found to depend as much on the practitioners experience and judgment, as engineering itself. Previously, a major problem for hydraulic fracture theory development was the lack of suitable models for application in heterogeneous reservoirs. Early models were two-dimensional and incorrect assumptions were often made. The models also required significant computing time to fully evaluate fracturing scenarios. It is only recently that the hydraulic fracture engineer has had the tools available to effectively model and analyze the hydraulic fracture process. This has been made possible by the advent of fully three-dimensional models, as well as improvements in reservoir analytical techniques. The ready availability of increased computing power has also helped make analysis not only possible, but reasonable.

This thesis addresses the application of hydraulic fracture modeling techniques, particularly with respect to containment in thinly, inter-bedded shale and sand reservoirs. The selected basin has been extensively studied over the past few decades (Schroeder, 1997) and unique well analysis data sets are available for both comparison and correlation. The subject field is in the Piceance basin, northwestern Colorado, which is an example of a basin-centered, micro-Darcy (tight) gas accumulation. The field produces mainly from the massively stacked, fluvial, point-bar sandstones of the Cretaceous Mesaverde Group, similar to other reservoirs in the Rocky Mountain region. In common with other tight gas reservoirs, operators need to use limited-entry hydraulic fracture stimulation technology to generate economic well production.

1.1 Research Objectives

The overall objective of the study is to investigate the 'best practice' methodology currently used to develop what practitioners consider to be accurate three-dimensional (3D) hydraulic fracture simulations of geologically complex reservoirs. Numerous studies have investigated components of hydraulic fracture propagation in layered formations, on both large and small scales (Gidley et al, 1989). However, no research has so far used a true 3D simulator for the analysis of fracturing in tight gas reservoirs. Previous work has been carried out in the Piceance basin (Ely at al, 1994) and other geologically similar tight gas reservoirs (Craig et al, 2000) using pseudo-three dimensional models. However, these researchers made a number of assumptions and their work had limited success. The unique multi-disciplinary data set available for this investigation will allow a complete evaluation of the current 'best practice' methodology, as recommended in the simulator user manual. The techniques used are those presently applied to generate data to build a model to allow practitioners to simulate hydraulic fractures in complex, fluvial, tight gas reservoirs.

The second research objective is to perform sensitivity analysis of the final matched model and assess key inputs that hydraulic fracture practitioners consider are critical for deriving an accurate simulation. Variation in rock properties and in-situ stress are to be investigated and their effects on fracture dimensions and containment evaluated.

Thirdly, the study aims to use direct diagnostic results from fracture mapping to help constrain the model and aid in the simulator output matching process. To the author's knowledge this has not been undertaken before in this type of reservoir, in part because of the lack of available data sets which have been acquired by operators.

Overall, this study aims to help identify the critical data inputs, i.e. the primary controlling factors, necessary for operators to develop relevant hydraulic fracture models. In situations where operators do not have the data available, this research will give hydraulic fracture practitioners an idea of the percentage error that their assumptions may have introduced into the model. Ultimately, this research will help develop processes and techniques to critically assess limited-entry, as well as other hydraulic fracturing techniques commonly used to stimulate tight gas reservoirs.

This type of detailed hydraulic fracture simulation will be beneficial not only to the massively stacked, lenticular study reservoir systems, but also other geologically complex basins throughout the US and around the world.

1.2 Research Contributions

The research contributions of this thesis are noteworthy because they apply to a unique data set that is investigated in a multi-disciplinary manner. The study incorporates aspects of petroleum engineering that use components of geological interpretation, log analysis and mini-fracture analyses. These results are used to evaluate the formation and rock mechanics, as well as studying hydraulic fracturing in a geologically complex reservoir.

Significant results are presented for a common ‘best practice’ methodology used to develop an accurate model of massively stacked, fluvial reservoir systems comprised of inter-bedded shale, sandstone, coal and mudstone deposits. The process outlines a technique to define lithology and correlate rock mechanical property measurements from detailed logs, which can be used to explain height containment in complex fluvial systems. When coupled together, the hydraulic fracture model and fracture diagnostics can be used to improve the forecasting capacity of simulators.

Overall, the contributions will help improve hydraulic fracture modeling of massively stacked, fluvial systems and thereby aid the development of a simple methodology for direct field application. This research undertakes sensitivity analyses of certain parameters in modeling applications, which will serve to guide hydraulic fracture practitioners in acquiring data necessary for deriving reasonable simulations. The techniques can also be extrapolated for use in similar fields producing from the Mesaverde formation and other low permeability, geologically complex reservoirs.

CHAPTER 2
LITERATURE REVIEW

The ancient Greeks and Persians are known to have used gas but the first proper gas production is considered to have occurred in China, around 347AD. In the United States (US) it wasn't until 1816 that gas was first used and then not until 1858 that the first US gas company, the Fredonia Gas Company, was established (Harts E&P Supplement, 2005). Nevertheless, by the turn of the century gas production was widespread across the US, and in the 1920's the US natural gas industry first emerged. Around this time, the Colorado Interstate Gas (CIG) company was also created to transport gas from the Texas Panhandle to the Front Range area of Colorado. It was then several decades before Colorado began to search for its own gas supplies in areas such as the Piceance basin.

2.1 Piceance Basin

The Piceance basin straddles the Colorado River and I-70 in Garfield and Mesa counties, northwestern Colorado, as shown in Figure 2-1. The basin covers some 6,000 square miles to form an elongated NW-SE trending asymmetrical structural basin, with a steeply dipping eastern flank, known as the Grand Hogback Monocline. The basin is bounded on all sides (north by the Axial Basin anticline, east by the White River Uplift, and to the south by the San Juan volcanics and Uncompahgre Uplift). The Uinta Basin, to the west, shares a common geology but is separated from the Piceance basin by the Douglas Creek Arch.

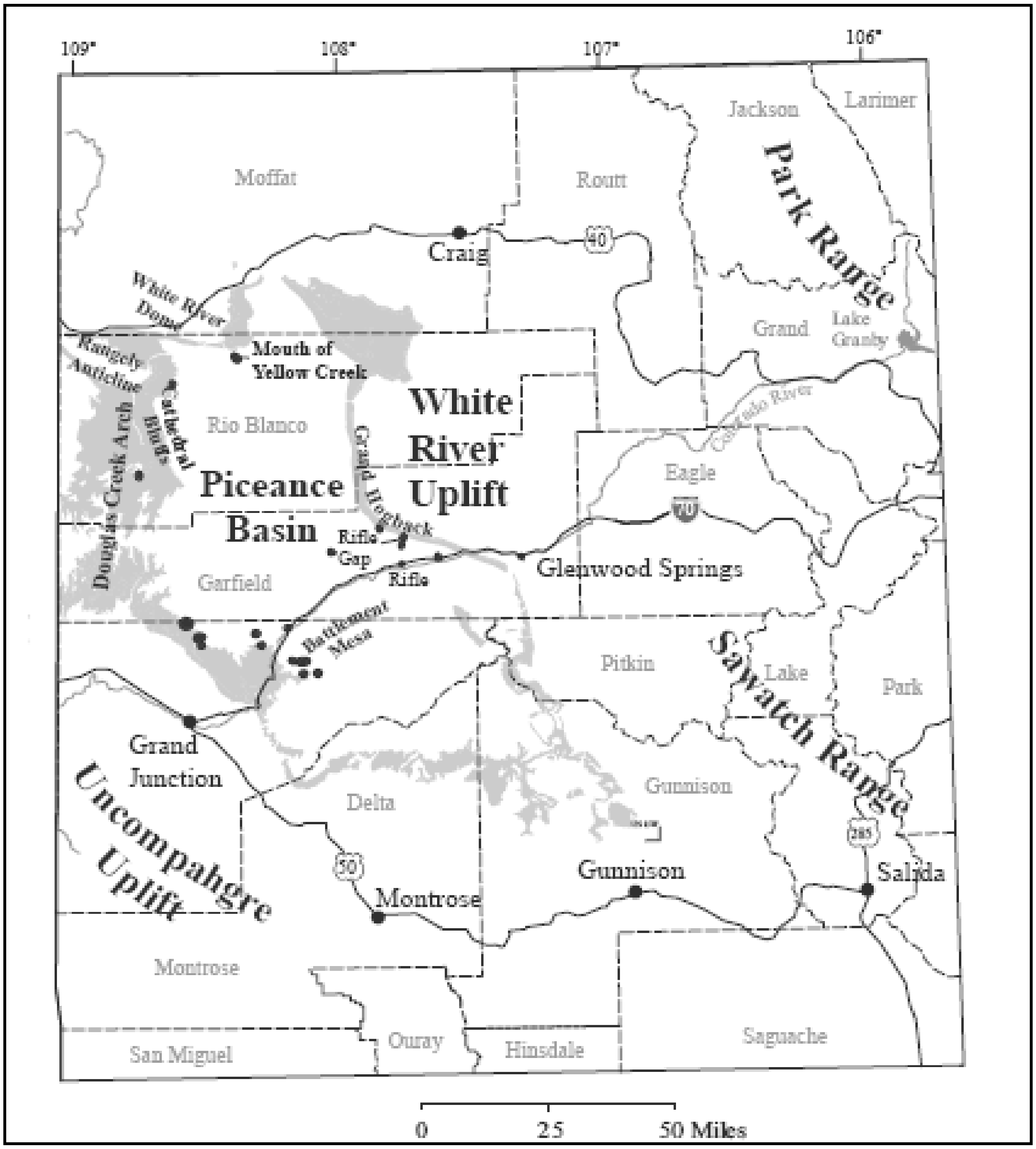

Figure 2-1: Piceance basin location, from Johnson and Flores (2003).

The Piceance basin is considered a basin-centered gas accumulation (BCGA) and is an example of a low porosity, tight gas reservoir (PTTC Symposium, 2000). Typical reservoir porosity is between 3-12 percent and in-situ permeabilities are less than 0.1 millidarcy (mD) to gas.

The south central portion of the basin is gas saturated (Law and Dickinson, 1985) and contains the four main producing fields: Grand Valley, Parachute, Rulison and Mamm Creek fields (GV-P-R-MC) as shown in Figure 2-2.

2.1.1 Geology

The Piceance basin is a structural and sedimentary basin that formed during the Laramide Orogeny. The Laramide Orogeny, in Colorado and Wyoming, changed the general flat mid-continent Cretaceous Foreland Basin into a region of mountain uplifts and deep structural basins (Johnson and Flores, 2003).

Originally, a marine incursion in the area formed the Western Interior Seaway and deposited several thousand feet of Mancos Shale. The shoreline then regressed and transgressed across the basin region resulting in shoreline, delta plain and upper flood plain fluvial sediments. These deposits in the Piceance basin area have created the Mesaverde Group tight gas sand reservoirs. As shown in Figure 2-3, the sediments reached a maximum thickness of 11,000 ft in the deepest part of the basin, creating a thermal blanket that is considered to have created the necessary conditions for the generation of large quantities of gas by Mesaverde group source rocks.

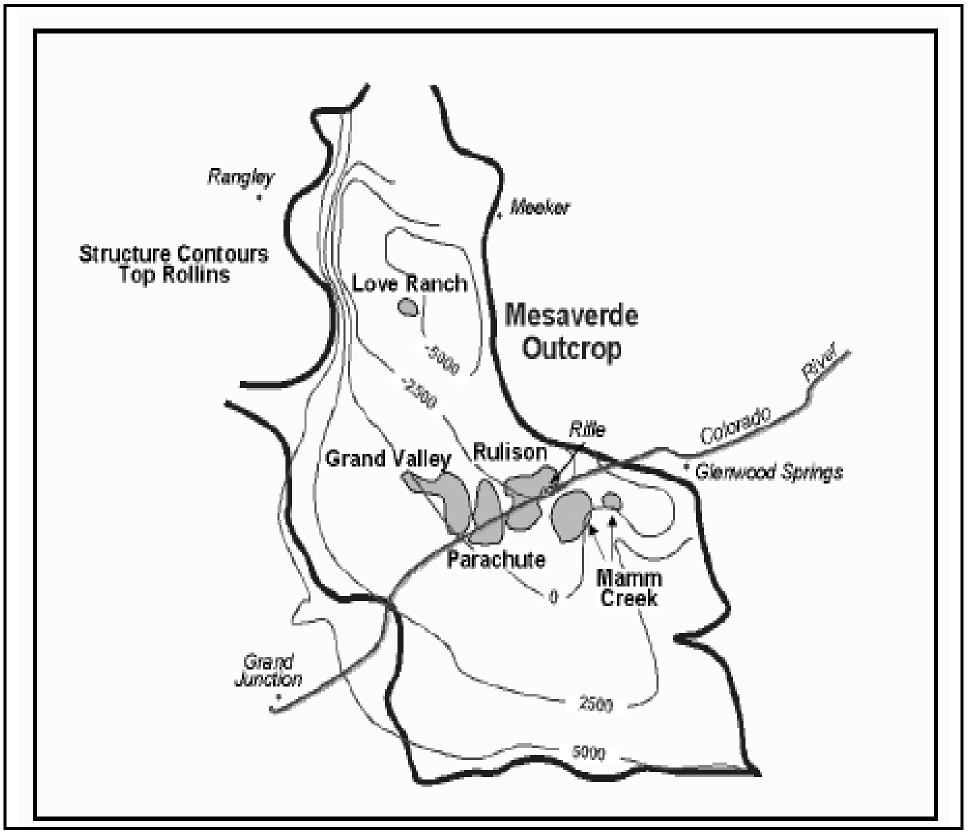

Figure 2-2: Map of the Piceance basin showing the location of the main producing gas fields, from Cumella and Ostby (2003).

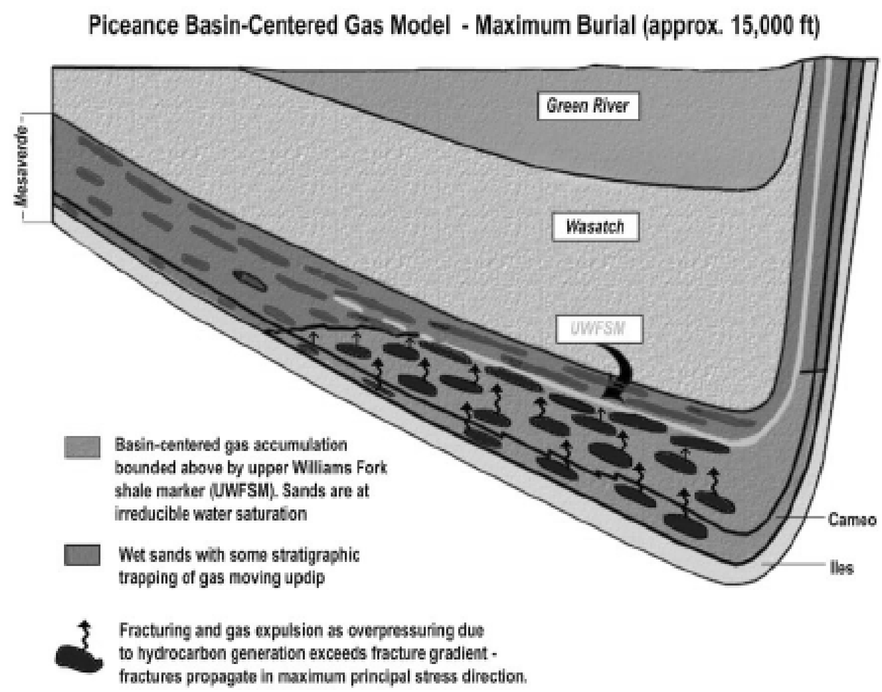

Figure 2-3: Piceance basin-centered gas model – present day cross-section, from Cumella and Ostby (2003).

2.1.2 Stratigraphy

The producing interval of the Mesaverde formation is a 3,000 to 3,500 ft thick sequence of inter-bedded siltstones, shales and tight sandstones with a coaly interval at the base, see Figure 2-4. Area operators normally divide this unit into two main reservoir intervals:

- Lower 550-800 ft - Cameo Coal Interval.

  This zone was deposited in a delta plain setting that included delta front, distributary channel, strand plain, lacustrine and swamp environments.
- Upper 2,450-2,700 ft above the Cameo Coal - Mesaverde Formation.

  The upper Mesaverde is the main producing interval and was deposited in a fluvial setting to create massively stacked, lenticular reservoirs within the interval.

The Mesaverde Formation has been extensively studied by the Department of Energy (DOE) at the Multi-Well Experiment (MWX) site. The MWX research indicated five distinct sandstone intervals, classified according to their depositional environments (Lorenz, 1989) as shown in Figure 2-4. Logs from the MWX site have shown that most reservoirs in the Piceance basin are extensively fractured (Lorenz and Finley, 1991; Lorenz and Hill, 1991; Lorenz et al, 1991). Regional fractures of a unidirectional, sub-parallel character are common in the relatively undeformed rocks of the Mesaverde Formation. Fractures were found to occur principally in the sandstones and siltstones, terminating at the mudstone or shale contacts of a reservoir boundary, as well as at lithologic discontinuities within the reservoirs

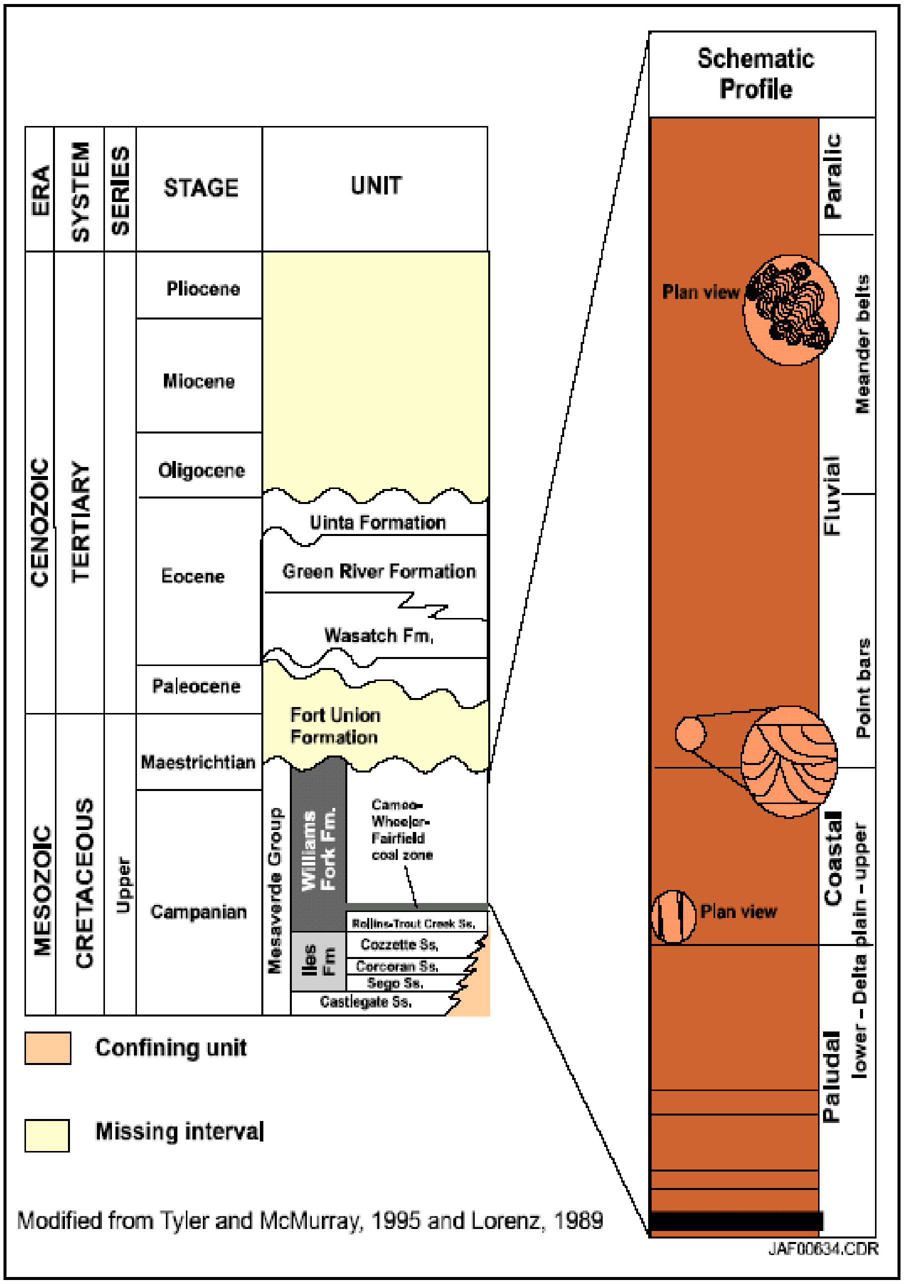

Figure 2-4: Stratigraphic column, depositional environments and reservoir characteristics of the Mesaverde group, from Kuuskraa et al, 1997 (Modified from Lorenz, 1989 and Tyler and McMurray, 1995).

Marine Blanket Sandstone Reservoirs

These are the Corcoran, Cozzette, and Rollins sandstones, which are widespread shoreline-to-marine blanket sandstones interspersed with tongues of Mancos marine shale. These sandstones are the largest and most homogeneous reservoirs within the Mesaverde Formation and have uniform characteristics over many thousands of feet laterally and over several tens of feet vertically. Core and outcrop data suggested two sets of vertical fractures that orient west-northwest and north-northwest.

MWX well tests showed high production rates despite the expected low matrix permeability (see Figure 2-5), indicating the existence of a highly fractured reservoir system.

Lenticular Sandstone Reservoirs (Paludal)

These reservoirs have a more complex composition than the marine deposits, being made up of lenticular distributary channel and splay sandstones inter-bedded with mudstones, siltstones and significant coal deposits. Individual lenticular reservoirs differ in shape and size, but were found to be approximately 200-500ft wide (Lorenz, 1985). The reservoirs contain internal lithologic heterogeneities (clay partings, zones of clay or siderite clasts, layers of carbonaceous debris, etc.) caused by a fluctuating fluvial discharge and lateral channel migrations. The MWX paludal interval was found to be extensively fractured but these commonly terminated at minor lithologic discontinuities within the reservoirs, providing for imperfect communication between reservoir segments.

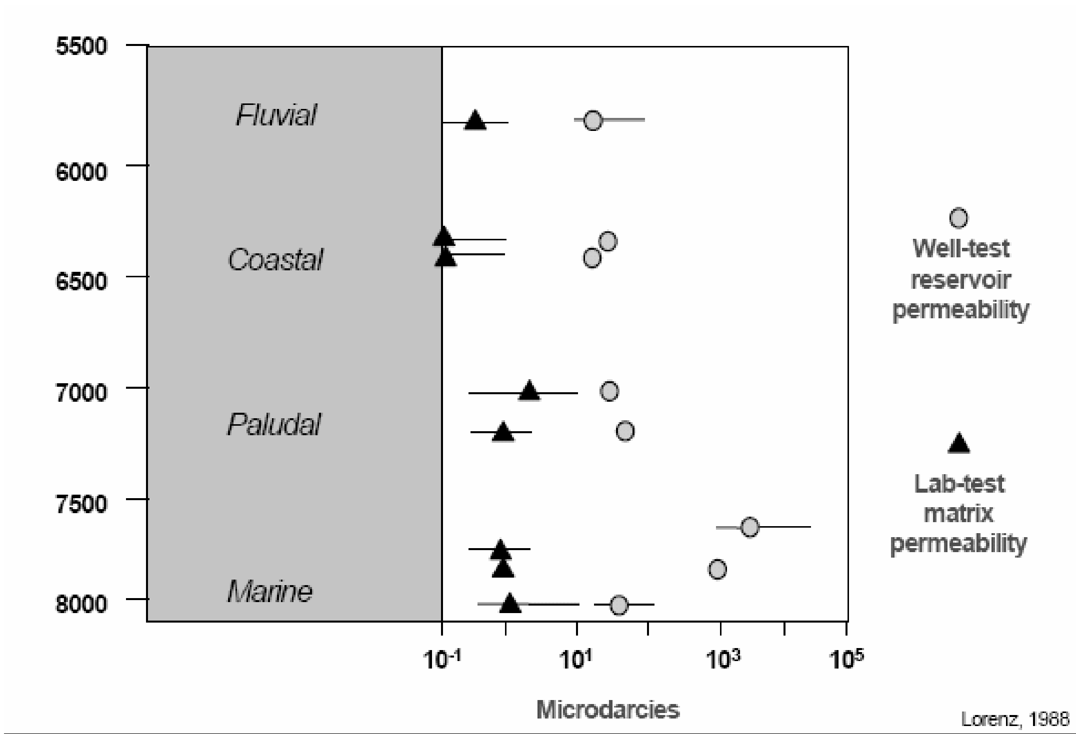

Figure 2-5: Reservoir and matrix permeabilities from the MWX experiments, modified from Lorenz et al (1988).

Lenticular Sandstone Reservoirs (Coastal)

This interval is characterized by distributary channel sandstones, deposited in an upper delta plain environment. These coastal interval reservoirs resemble the underlying paludal interval in size, shape, internal heterogeneity and fracture distribution, except coals are absent. The MWX Coastal interval was found to be fractured but the fractures terminate at the lithologic discontinuities within the reservoir and at the mudstone boundaries for the reservoir.

Fluvial Sandstone Reservoirs

The uppermost interval consists of irregularly shaped, stacked, composite sandstones that were deposited by broad meandering stream systems. These deposits are a combination of many sinuous, point-bar units that have undergone several episodes of erosion and deposition. Sandstones in this interval are elongate and 1000-2500 ft wide with irregular shape, having lobate edges. A regional west-northwest fracture set occurred in most of the MWX fluvial reservoir cores and well tests indicated little or no well communication, with high reservoir permeability anisotropy.

Paralic Sandstone Reservoirs

This is an interval of returned-marine influence with more widespread, uniform sandstones which is considered to be water-saturated over most of the basin and receives little attention from operators in the area.

Overall, the properties in the marine intervals were found to be relatively uniform vertically and could be correlated laterally. However, in the Piceance basin the producing interval is a non-marine reservoir which therefore exhibits a high degree of variability, both vertically and horizontally making it inherently difficult to both study and model.

2.1.3 Natural Fracture Production

The matrix permeabilities of most Rocky Mountain sandstone reservoirs are typically in the microdarcy (μD) to sub-microdarcy range, when measured in the laboratory under restored-state water saturations and confining pressures. Matrix porosities generally range from six to twelve percent. However, the permeabilities of reservoir systems as measured by well tests and production rates are commonly one or two orders of magnitude higher, see Figure 2-5 (Lorenz et al, 1988). The difference can be accounted for by the enhanced conductivity that occurs along natural fractures.

There are two types of natural fracture systems that can occur: fracture sets (commonly multiple) associated with structurally deformed strata. These fractures are caused by local faulting or folding and commonly cut indiscriminately across lithologic boundaries. Secondly, there are single regional fracture sets that are caused by regional stresses of a much lesser magnitude than strata deformation, in conjunction with high pore pressures, and occur in structurally undeformed formations. Outcrop studies showed a unidirectional pattern, aligned parallel to the present maximum horizontal compressive stress.

Fracture systems have been the most promising production targets to date, although they also introduce potential water problems. Conjugate fractures offer a potentially rewarding target but are hard to predict, but nevertheless there has been some success achieved from multidisciplinary studies (Kuuskraa et al, 1996).

2.1.4 Piceance Basin Cumulative Production and Reserves

Kuuskraa et al (1997) estimated gas-in-place (GIP) for the Piceance basin, Williams Fork Formation to be 311 Tcf of gas, including 75 Tcf of gas in the associated coal seams, coal reserves were estimated at between 50 and 150 Tcf of gas-in place. The southern basin (GV-P-R-MC) is estimated to contain some 106 Tcf (34%) of the total. Recently, Cluff and Graff (2003) calculated that in 2003 the Piceance basin had produced nearly 0.75 Tcf of gas and 1.6 MMbo. A large amount of water had also been produced (16 MMbw) with even the fields in the central portion of the basin producing 9 bbls/MMscf of water. Cluff and Graff also calculated that total production from the Mesaverde would be some 1.42 Tcf, without further development over a 50 year period.

2.1.5 Piceance Well Spacing

Originally wells were drilled on 640 acres spacing, which was later reduced to 320 acre spacing (1979), 80 acre spacing (1996), 40 acre (2000) and now 20 acre (2000). 10-acre well spacing tests have also been approved for both the Mamm Creek, Grand Valley, Parachute and Rulison fields by the Colorado Oil and Gas Conservation Commission (COGCC) (Jul 2001), see Figure 2-6.

Kuuskraa et al (1997) estimated the following recovery efficiencies: 160 acre drains 5%, 40 acre drains 26%, 20 acre drains nearly 40% and 10 acre would drain almost 80%.

2.1.6 Piceance Basin Field Production

The Piceance basin is comprised of twenty four producing fields whose production is summarized in Table 2-1 and shown graphically in Figure 2-7. The fields produce mainly from the Mesaverde groups, but some production is also from the Wasatch. Williams Production Company and EnCana Oil and Gas (USA) are the most active producers in

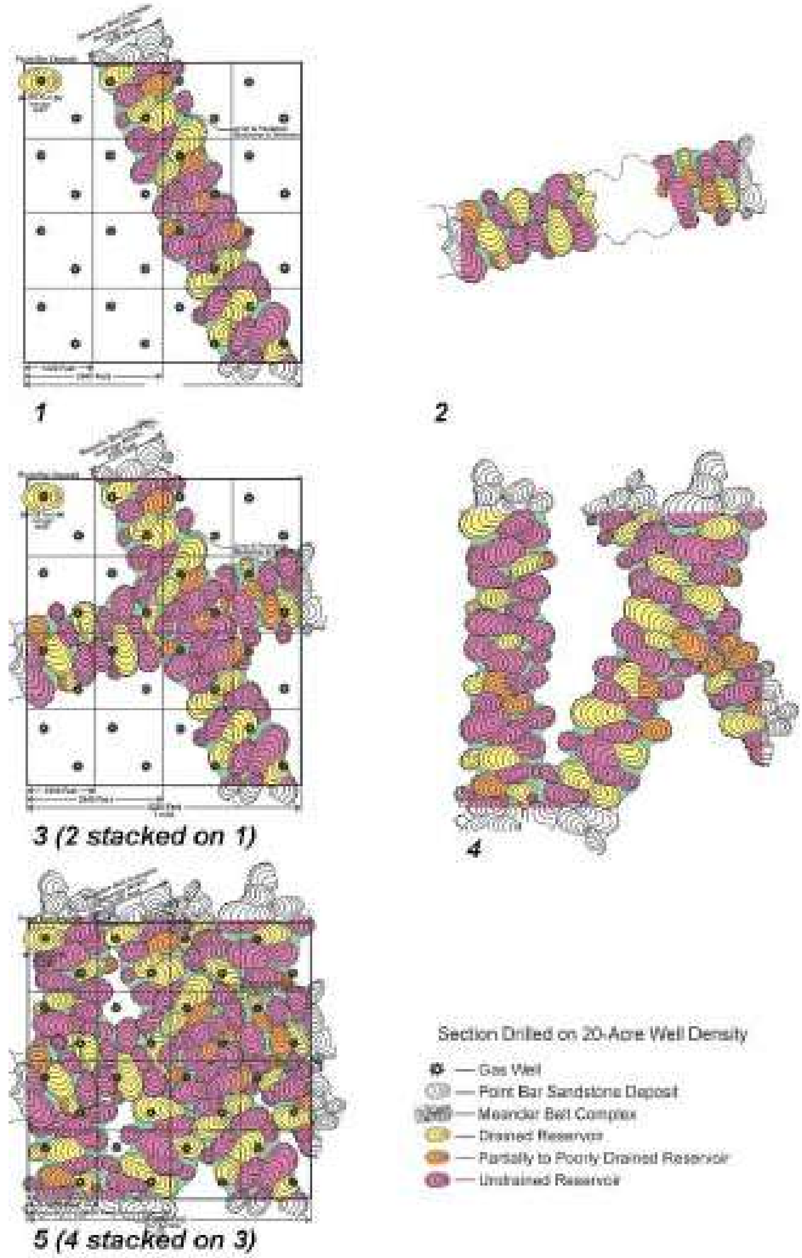

Figure 2-6: Hypothetical meander belt sandstone reservoirs showing that the point bar deposits are often not drained and further drainage would require a 10-acre well density, from Cumella and Ostby (2003, originally done by Terry Barrett).

Table 2-1: Piceance Basin Field Production Summary to 2003, modified from Cluff and Graff (2003):

	Field	Reservoir	Gas	Oil	Water	Well Counts	GOR	WGR
			MMscf	Mbbl	Mbbl	2003	scf/bbl	bbls/MMscf
1	Rulison	Mesaverde	191004	597	2072	253	319765	11
2	Grand Valley	Mesaverde	171177	47	1898	312	3674351	11
3	Mamm Creek	Mesaverde	110741	632	1307	270	175156	12
4	Divide Creek	Mesaverde	64472	2	4986	6	35173141	77
5	Parachute	Mesaverde	57986	10	522	124	5870824	9
6	Plateau	Mesaverde	33706	16	532	22	2173306	16
7	White Dome River	Mesaverde	28011	331	2440	54	84681	87
8	Shire Gulch	Mesaverde	26282	1	91	36	51032610	3
9	Wolf Creek	Mesaverde	12676	0	0	2		0
10	Buzzard Creek	Mesaverde	10609	2	26	1	675092	2
11	Piceance Creek	Mesaverde	5648	28	747	2	198525	132
12	Buzzard	Mesaverde	2799	0	10	4		3
13	Love Ranch	Mesaverde	2321	4	470	5	559423	203
14	Brush Creek	Mesaverde	1889	1	36	13	4097965	19
15	Sulfur Creek	Mesaverde	1562	5	3	5	350289	2
16	Bronco Flats	Mesaverde	1149	0	62	4		54
17	De Beque	Mesaverde	957	0	5	1	8546161	5
18	Gasaway	Mesaverde	309	0	1	2		4
19	Vega	Mesaverde	212	0	2	1	931648	10
20	Pinyon Ridge	Mesaverde	174	3	727	3	53476	4182
21	Scandard Draw	Mesaverde	144	1	5	1	297064	34
22	Skinner Ridge	Mesaverde	110	0	0	2		0
23	Powell Park	Mesaverde	90	5	10	1	17805	106
24	Cathedral	Mesaverde	3	0	0	1		0
		Total	**724027**	**1683**	**15950**	**1125**		
11	Piceance Creek	Wasatch	191454	124.8	572.3	20	1534209	3
5	Parachute	Wasatch	39007.4	3.1	11.2	54	12498371	0
1	Rulison	Wasatch	19859.1	0	2.6	51	620598281	0
7	White Dome River	Wasatch	17117.6	0	3.1	29		0
15	Sulfur Creek	Wasatch	7515.3	2	0.2	1	3803311	0
2	Grand Valley	Wasatch	432.6	0	0.2	1		0
23	Powell Park	Wasatch	319.3	1	0.6	1	314311	2
10	Buzzard Creek	Wasatch	131.9	0	0	1		0
14	Brush Creek	Wasatch	119.9	0	0	1		0
6	Plateau	Wasatch	15.7	0	0.2	1		13
		Total	**275973**	**131**	**590**	**160**		

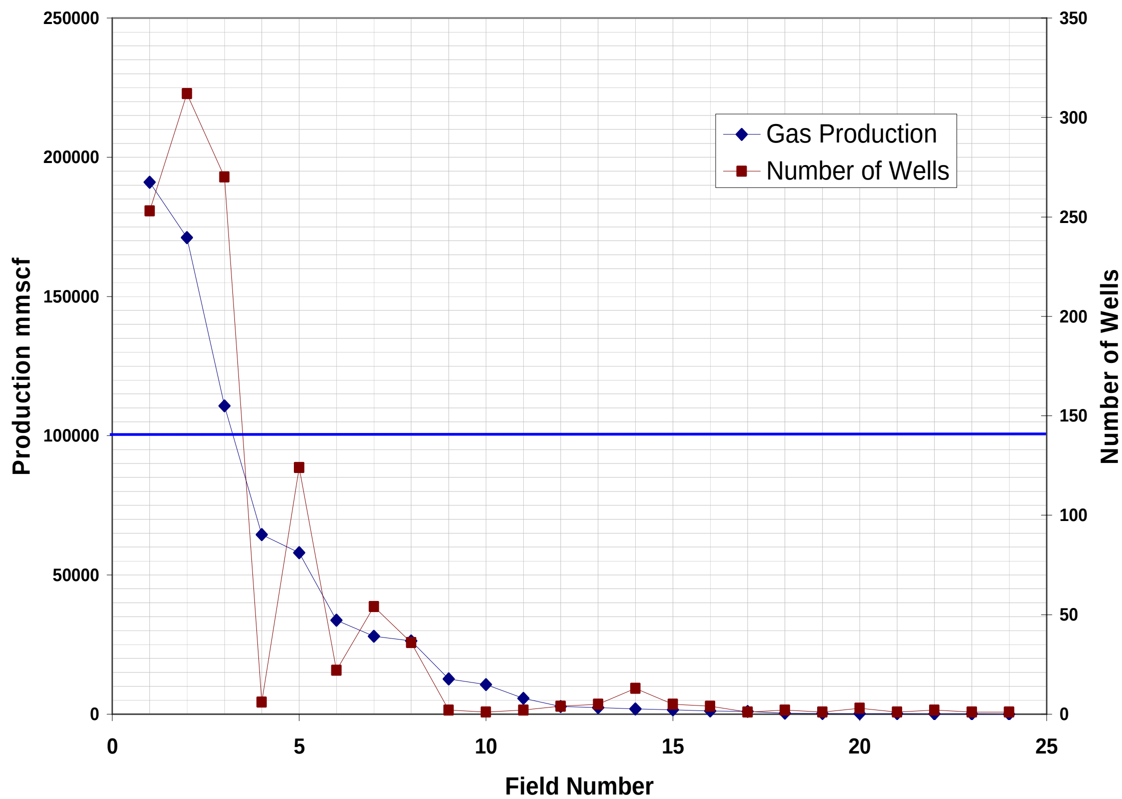

Figure 2-7: Piceance basin total production plot (through 2003) highlighting that the three main fields have each produced over 100,000 MMscf. Field numbers relate to Table 2-1.

the Piceance basin, with most of their production from the Rulison and Mamm Creek fields, respectively.

Rulison was the original Piceance basin field, discovered in 1944 with the first well, Clough #1 (section 22, T6S, R94W). The Clough well was initially abandoned due to uneconomic production from the Wasatch formation, which Rulison then wasn't successfully produced until the 1970's by Carter and Carter with well J.T. Juhan #2 (section 34, , T6S, R94W). Williams Fork production was discovered by the Southern Union Gas Company in 1955 with Juhan Fee #1 (section 26, T6S, R94W). Mamm Creek was then discovered in 1959, by the California Company, with Shaffer #1 well (section 12, T7S, R93W). However, it wasn't until the field discoveries of the 1980's: Grand Valley in 1985 by Barrett Resources Corporation with Crystal #23-1 A2 well, (section 33, T6S, R95W) and Parachute in 1986 with Grand Valley #2 well (section 23, T6S, R97W) that there was significant production coming from the area. Prior to 1989, poor Piceance basin production was the result of targeting production from either the Corcorran or Cozette sandstone members (Iles formation), or the coal seams in the Cameo interval. However, in the 1990's there was significant production growth due to effective stimulations of the massively stacked, lenticular 'tight' sand reservoirs of the Mesaverde group, as a direct consequence of integrated studies in the area (Kuuskraa et al, 1996).

2.1.7 Gas Source and Trapping

Underlying the Mesaverde are shale and coals which are considered to be the thermogenic sources of gas. The shale is also considered to have given rise to oil, which was subsequently thermally broken down. Gas generation is thought to have driven out water, which then accumulated up-dip to hydrodynamically create an over-pressured, basin-centered type gas accumulation (Law and Dickinson, 1985). Researchers also believe that the gas is trapped by a relative permeability barrier, the so-called 'permeability jail' (Shanley et al, 2004). This phenomenon arises because the relative permeability of gas is only 30% at a water saturation of 40%, this difference will trap gas while allowing water to pass through.

The main producing interval of the basin has over-pressured gas down structure from more permeable water filled areas, as shown in Figure 2-8. Most of the study work carried out in the Piceance basin has been undertaken around the central portion of the basin, initially at the MWX site.

2.1.8 Mesaverde Reservoir Characterization

The sandstone reservoirs of the Mesaverde Group have very low permeability due to intense regional diagenisis that has led to partially or completely mineralized pore spaces. In the deepest part of the basin the Mesaverde permeability is only 0.0006-0.055 mD, while core measurements near Rulison gave permeability readings of 0.01-0.1 mD (Rio Blanco Natural Gas Company, 1980). Capillary pressures are relatively high and water saturations are also high, typically between 45-70 percent.

Due to the very low reservoir permeability in the Piceance basin there is an economic need to stimulate wells by hydraulic fracturing. The need to fracture the rock arose from earlier observations of well production in tight gas sand reservoirs which was found to be significantly affected by the presence of natural fractures. The natural fractures have been shown to be the primary transport conduits (Lorenz, 2003), where a well developed fracture network in a tight reservoir has been shown to be a major cause of higher than expected productivity in some wells.

2.2 Hydraulic Fracturing

Hydraulic fracturing is the injection of fluids at sufficient rates and pressures to break the rock matrix, creating two fracture wings on both sides of the well. To keep the

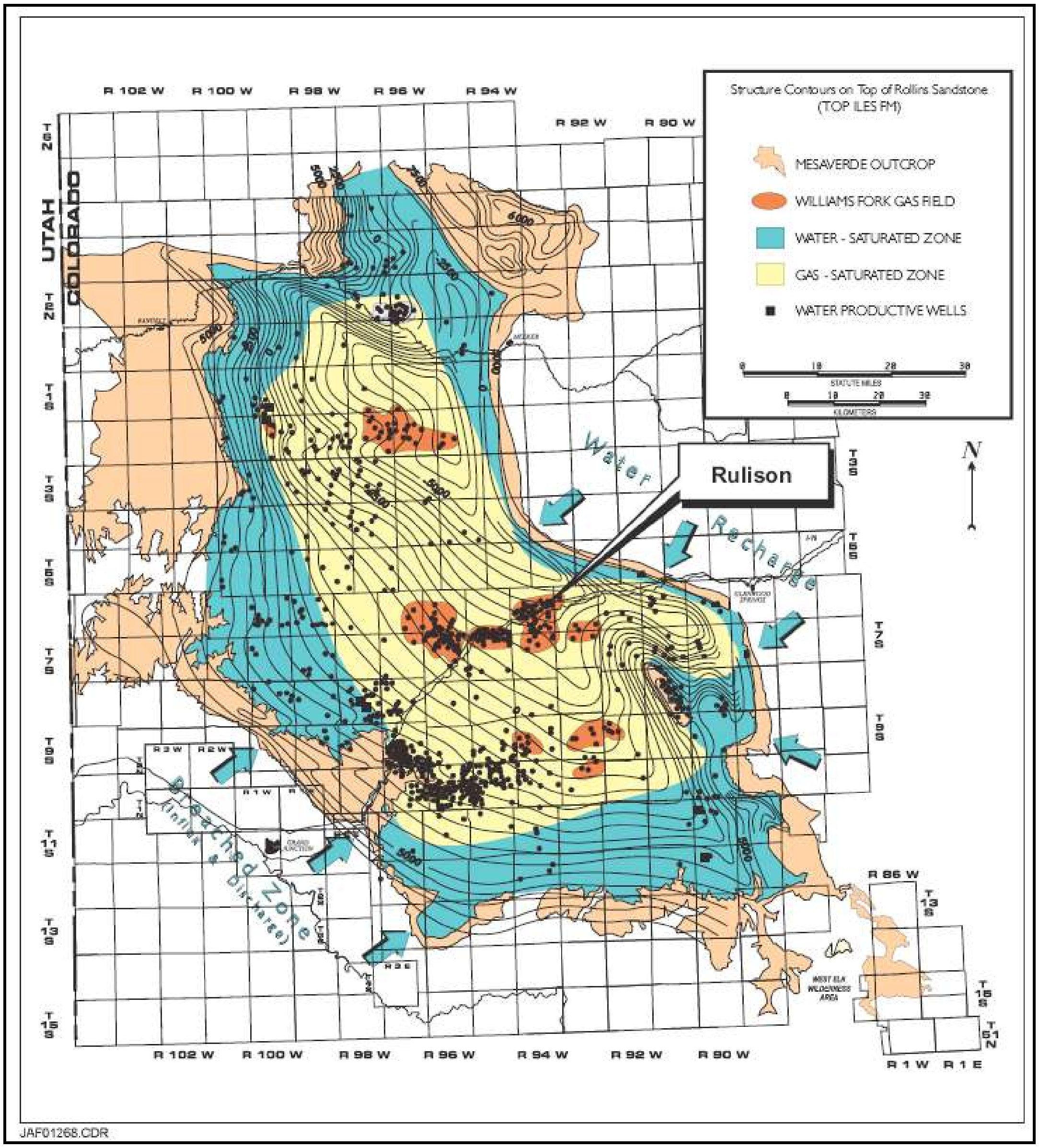

Figure 2-8: Structural map of the Mesaverde group (on top of the Rollins) of the Piceance basin indicating the location of the Rulison field, from Kuuskraa and Campagna (1999).

fracture open after breaking the reservoir rock, either acid etching or a material such as sand (proppant) is injected to hold it open and allow fluids to flow, thereby increasing reservoir conductivity.

It was R.F. Farris of Stanolind Oil and Gas Corporation who devised the concept of hydraulic fracturing, originally called 'hydrafrac'. The technique was first executed in 1947 in the Hugoton gas field, western Kansas, using a poorly performing acidized well, to allow a direct comparison of acidizing and hydraulic fracturing (Clark, 1949) techniques. A napalm-thickened gasoline was injected to create what was considered to be a horizontal fracture. The fracture orientation was deduced from the results of an earlier shallow (15ft) well which, after hydraulically fracturing, was excavated to reveal a horizontal fracture.

It wasn't until the 1950's that Hubbert and Willis (Hubbert and Willis, 1957) clarified the mechanism of fracture propagation. They theorized that a rock should open in the direction of least resistance. At most reservoirs depth overburden will exert the greatest stress, so that the direction of least stress should be horizontal. As a fracture opens perpendicular to the least stress direction, this would form a vertical fracture, as shown in Figure 2-9. At shallow depths, the situation may differ as horizontal stresses can be greatest and horizontal fractures would result, as in the original field experiment.

2.3 Rock-Mechanical Properties

Rock mechanics investigates the response of rocks to the forces applied in their physical environment. For hydraulic fracture design, rock mechanics are important for determining mechanical properties and the in-situ stress state of the reservoir rocks, rock failure and deformation, as well as for determining the final fracture geometry. A number of factors will affect fracture propagation including: variation in the in-situ

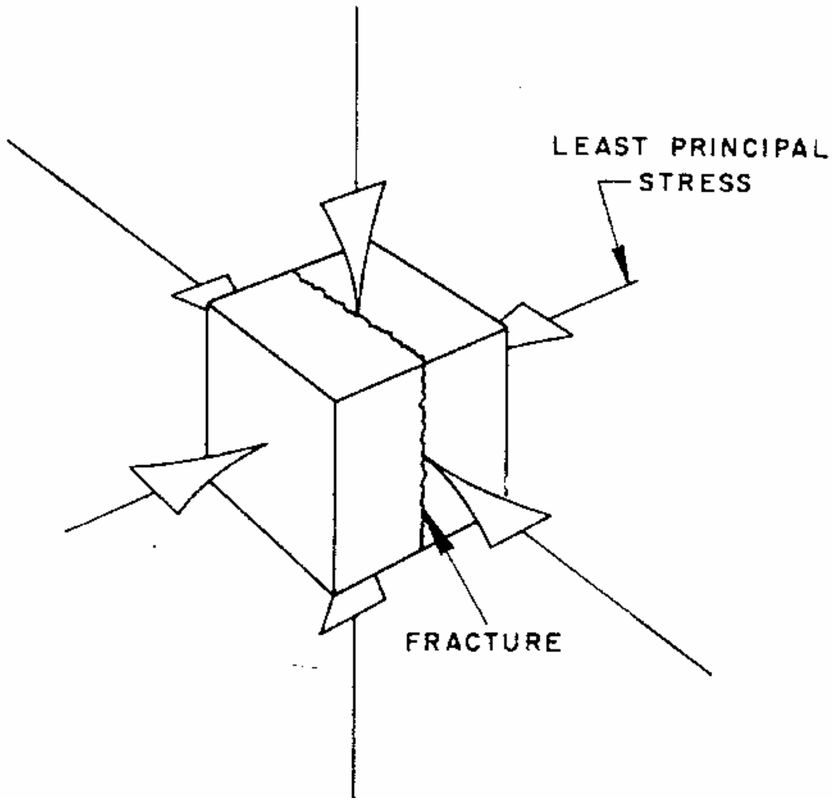

Figure 2-9: A 3-D conceptual model showing a fracture opening perpendicular to the horizontal least principal stress to give a vertical orientation, from Hubbert and Willis (1957).

stresses in different layers, relative bed thickness of other formations in the fracture vicinity, bonding (or lack of) between layers, rock mechanical property variations (elastic moduli, poroelasticity, strength, ductility), fluid pressure gradients in the fracture and variations in pore pressure between layers.

A very important factor for hydraulic fracture design is the in-situ stress field. Knowledge of the in-situ stresses is important in multiple layered formations in order to design the optimum treatment with maximum fracture containment in the productive interval. There are many parameters to be considered when developing the in-situ stress profile for fracture treatment design. Rocks have a local stress state at depth that can be influenced by: weight of over burden stress; pore pressure stress; temperature; rock properties; diagenisis; tectonic movements and creep flow and plasticity.

Hubbert and Willis (1957) developed the first realistic model to relate hydraulic fracturing initiation pressure to the two principal horizontal stresses of the rock. Their work showed that the least horizontal stress is approximately equal to the shut-in pressure. They derived Equation 2-1 which can be modified to use rock mechanical properties to estimate in-situ stresses in the various layers.

$$\sigma_x = \frac{\nu}{(1-\nu)}(\sigma_z - p) + p + \sigma_E \tag{2-1}$$

where,	σ_x	=	Total horizontal stress
	ν	=	Poisson's ratio
	σ_z	=	Total overburden stress
	P	=	Reservoir pressure
	σ_E	=	Any externally generated stress acting on the formation

The third stress term, σ_E , depends upon such factors as tectonic forces and thermal effects. For tectonically relaxed areas, the external stress component is minimal and rock elastic components can be used to estimate fracture gradients. In areas where tectonic forces are considered significant, such as the Piceance basin, it is difficult to accurately estimate horizontal stress gradients and direct field tests must be undertaken to determine their value.

Elastic Properties

When considering hydraulic fracturing mechanics, one of the petroleum engineer's primary concerns is determining the elastic properties of rock, particularly with respect to Young's modulus and Poisson's ratio. Early development of hydraulic fracturing theory assumed that rocks behaved as linear elastic materials, however, most rocks are heterogeneous and have been found to exhibit non-elastic behavior.

Linear elastic theory assumes that the components of stress are linear functions of the components of strain (Jaeger and Cook, 1976):

$$\sigma_x = (\lambda + 2G)\varepsilon_x + \lambda\varepsilon_y + \lambda\varepsilon_z \tag{2-2}$$

$$\sigma_y = (\lambda + 2G)\varepsilon_y + \lambda\varepsilon_x + \lambda\varepsilon_z \tag{2-3}$$

$$\sigma_z = (\lambda + 2G)\varepsilon_z + \lambda\varepsilon_y + \lambda\varepsilon_x \tag{2-4}$$

where,	λ	=	Lamés coefficient
	G	=	Shear modulus
	σ	=	Stress in directions x, y and z
	ε	=	Strain

The shear modulus (G) and Lamé's coefficient (λ) are combined to give ($\lambda + 2G$) which is used to define stress and strain in the same direction, while Lamé's coefficient (λ) defines stress and strain in orthogonal directions. Lamé's constants are seldom used as fracture modeling inputs, instead Young's modulus and Poisson's ratio are used which can be calculated using Lamé's values, as outlined in Table 2-2.

Determining the elastic property values for any given rock is a difficult process and is usually done by conducting static measurements on cores and calibrating using dynamic log measurements. Dynamic moduli of rock can be derived from logging measurements using the following formulas (Warpinski and Smith, 2001):

- Poisson's ratio (ν): the ratio of lateral expansion to longitudinal contraction for a rock under axial stress condition.

$$\nu = \frac{V_p^2 - 2V_s^2}{2(V_p^2 - V_s^2)} \qquad (2\text{-}5)$$

- Shear modulus (G): arises naturally from linear elasticity but is not easily measured and instead is normally computed from E and ν.

$$G = \rho v_s^{\ 2} \qquad (2\text{-}6)$$

- Young's modulus (E): the ratio of stress to strain for a uniaxial load.

$$E = \rho V_s^{\ 2}\left(\frac{3V_p^2 - 4V_s^2}{V_p^2 - V_s^2} \right) \qquad (2\text{-}7)$$

- Bulk moduli (K): the ratio of hydrostatic pressure to the volumetric strain that it produces.

$$K = \rho\left(V_p^{\ 2} - \frac{4}{3}V_s^{\ 2} \right) \qquad (2\text{-}8)$$

Table 2-2: The Interrelation of Moduli in Linear-Elastic Theory

Calculated Property	**Known Property**		
	E, ν	**λ, G**	**K, G**
Shear Modulus, G	$\frac{E}{2(1+\nu)}$		
Lamé's Coefficient, λ	$\frac{\nu E}{(1+\nu)(1-2\nu)}$		$K-\frac{2}{3}G$
Young's Modulus, E		$\frac{G(3\lambda+2G)}{(\lambda+G)}$	$\frac{9GK}{G+3K}$
Poisson's Ratio, ν		$-\frac{\lambda}{2(\lambda+G)}$	$\frac{\frac{3}{2}K-G}{G+3K}$
Bulk Modulus, K	$\frac{E}{3(1-2\nu)}$	$\lambda+\frac{3}{2}G$	

where, ρ = Density (density log)
V_p (compressional) = Acoustic velocities (sonic log)
V_s (shear) = Acoustic velocities (sonic log)

Laboratory measurements have shown that dynamic moduli values are generally higher than static measurements of cores (Warpinski et al, 1998 c). Researchers have attributed the discrepancy to matrix weaknesses (microcracks), in-situ reservoir confining stress and the poroelastic nature of rocks (Economides and Nolte, 1981). Another problem is that accurate dynamic measurements of shear wave velocity are difficult, and small errors can lead to large discrepancies in values. The scale of measurement also affects the final value as the results are strongly dependent on both time (frequency) and size scales (Tiab and Donaldson, 1999). Nevertheless, acceptable measurements are possible, but care must be taken to develop suitable correlations for in-situ moduli based on static measurements of the appropriate scale for the final application (Pantoja, 1998).

Young's modulus is an indication of the hardness or material stiffness, and is a measure of the amount of stress required to generate a given deformation of a sample, as shown in Figure 2-10. High moduli rock require a greater applied stress to yield a given strain. Strain is a dimensionless parameter which can be either positive (compression) or negative (elongation), see Equation 2-9.

$$\text{Strain } (\sigma) = \frac{\text{Change in length}}{\text{Original length}} = \frac{\Delta L}{L} \tag{2-9}$$

A value of Young's modulus measured on an unconfined sample can be very different than that measured on the same sample at reservoir stress conditions. Stress history as well as saturation conditions affect the measured value of Young's modulus (Lama and Vutukuri, 1978). Laboratory core measurements are therefore difficult to use to obtain useful rock elastic properties. Equation 2-10 shows the derivation of Young's modulus (E) values from stress, strain and shear modulus.

$$E = \frac{\sigma}{\varepsilon} = \frac{\frac{F}{A}}{\frac{\Delta L}{L_1}} = \frac{G(3\lambda + 2G)}{\lambda + G} \qquad (2\text{-}10)$$

where,	E	=	Young's modulus
	σ	=	Stress
	F	=	Force acting on area, A
	A	=	Area
	ε	=	Strain
	ΔL	=	Change in length (L_2-L_1)
	L_1	=	Original length
	λ	=	Lamés coefficient
	G	=	Shear modulus

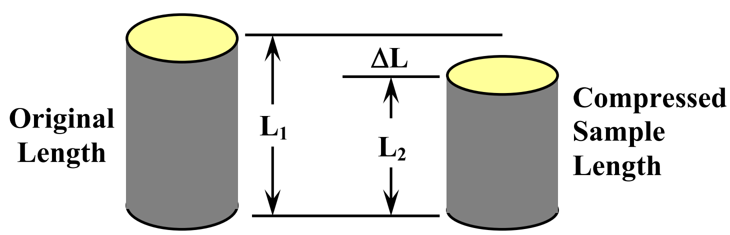

Figure 2-10: Figure showing the induced strain for or an axially loaded cylindrical sample.

Another commonly used rock mechanical property is Poisson's ratio (ν). Poisson's ratio is defined as the ratio of lateral to axial strain under conditions of axial loading (Tiab and Donaldson, 1999). If a load is applied along a given axis a strain results which is proportional to the Young's modulus (E) of the sample, as shown in Figure 2-11.

Strains perpendicular to the axis of the applied load also occur and the magnitude of these lateral strains depends on the Poisson's ratio of the sample.

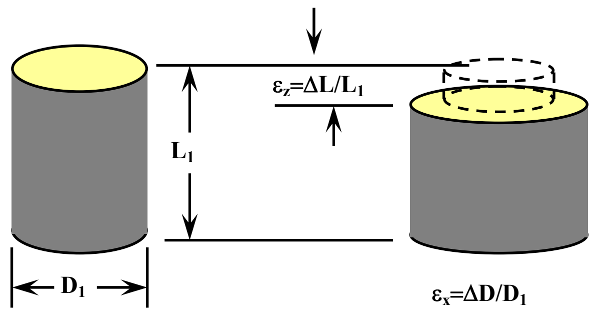

Figure 2-11: Figure showing that if a load is applied along a given axis a strain will occur along the compression axis as well as perpendicular to the axis of the applied load.

The numerical value of Poisson's ratio is calculated using Equation 2-11, values are between 0.0 and 0.5. A value of zero indicates a hard material, where no lateral strain results when the sample is loaded, and a value of 0.5 indicates a soft compressible material.

$$\nu = \frac{\varepsilon_{lat}}{\varepsilon_{ax}} = \frac{\frac{\Delta d}{d_1}}{\frac{\Delta L}{L_1}} = \frac{\lambda}{2(\lambda + G)} \tag{2-11}$$

where,	ν	=	Poisson's ratio
	ε_{lat}	=	Strain in the lateral direction
	ε_{ax}	=	Strain in the axial direction
	Δd	=	Change in diameter
	d_1	=	Original diameter

2.4 Fracture Containment

Hydraulic fracture containment depends on a number of factors that can be assumed or measured in order to model the hydraulic fracture. Initial models of fractures were two-dimensional and required an estimation of constant fracture height, so that width and length could be calculated. As understanding of the complexity of hydraulic fracture processes has increased, the models have also evolved to better represent the containment processes. Pseudo three-dimensional and three-dimensional models calculate fracture variables in all three dimensions by considering several factors that contribute to fracture containment, outlined as follows.

In situ stress contrasts can restrict fracture growth by clamping the fracture tip and reducing fracture width due to high stress. The in situ stress difference is generally considered to be the most important factor controlling fracture height and was suggested early on by Perkins and Kern (1961) and supported by theoretical (Cleary et al, 1981) and field data (Smith et al, 1982). Warpinski and Teufel (1987) showed the dominant effect of stress contrasts, as opposed to rock properties for fracture containment in 'mineback' experiments undertaken in the late 1980's. These experiments were conducted by injecting colored water in horizontal holes in the vicinity of material property interfaces and stress contrasts. The resulting fractures were then excavated to determine the growth characteristics. The researchers then presented work showing that numerous types of geologic discontinuities (faults, bedding planes, joints, and stress contrasts) could have a significant effect on hydraulic fracture growth.

Young's modulus can also restrict fracture growth if the Young's modulus of the boundary layer is greater than that of the pay zone. The width will be smaller in the high Young's modulus material and flow resistance will be higher, making fracturing more difficult. Fracture toughness is a measure of the energy dissipated by fracture growth. This is a controversial issue as some researchers consider it to be a material property, independent of fracture size, while others consider that it is not a material property and increases with fracture size. These differences have a significant effect on energy dissipation with the former considered to be at the fracture tip while the latter occurs in a large irreversible deformation zone, increasing in size as the fracture grows. The effect of fracture toughness is considered to be small, except where stress contrasts are negligible, and it is often ignored.

As a hydraulic fracture grows, the narrow width causes the contained fluid pressure to increase to a point where it pressurizes surrounding pore spaces and is able to invade bed boundary planes, decreasing normal stress. The high fluid pressure acts on the fracture wall, increasing shear stress along the bed boundary plane and reducing the amount of shear stress that can be supported without shear failure (slippage), shown in Figure 2-12 by the Mohr-Coulomb failure envelope. For perfect slippage, no stress is transmitted across the interface, but some stress can be transmitted through friction until the interface opens and frictional coupling is lost. When bed slippage occurs along the bedding plane, displacements below are not transmitted across the boundary. The sliding bed boundary acts as a 'wall', separating the fracture into decoupled zones of displacement (Barree and Winterfield, 1998). Fracture growth across boundaries usually only occurs if the fluid pressure exceeds the stress in the bounding zone, so that it can invade existing cracks or pores of that zone. Zones of decreased stress may exist anywhere along the bedding plane, creating fracture offsets and bifurcations at bed boundaries. Interface slippage can result in immediate termination of fracture growth but under normal circumstances this would only be considered likely at shallow depth, where overburden pressure is small. However, at depths where shear stress is small this could readily occur, such as over-pressurized formations (high pore pressure) and at clay interfaces, where the coefficient of friction is negligible compared to the surrounding rock (Teufel and Clark, 1984).

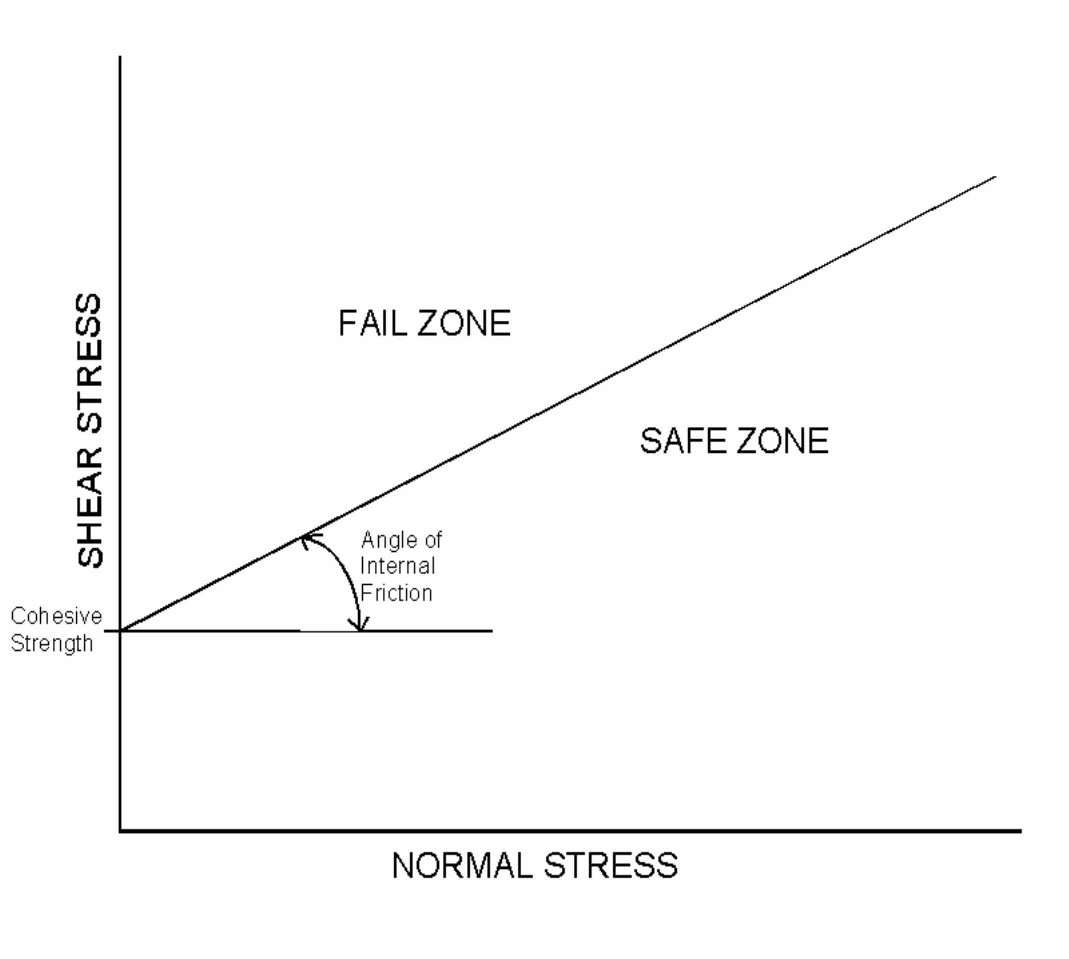

Figure 2-12: The Mohr-Coulomb failure diagram, from Barree and Winterfield (1998).

Daneshy (1977) investigated composite reservoirs and showed a significant relationship between the strength of the interface bond, between two formations, and whether or not a hydraulic fracture would cross that interface. Strongly bonded interfaces were more likely to allow the hydraulic fracture to propagate across the interface.

The inability to physically observe the detailed fracture process together with the complex theory of fracture growth has meant that it is very difficult to accurately model hydraulic fractures. Most of the indirect fracture analysis techniques, such as fracture modeling or net pressure analysis, as well as pressure transient well testing and production data analysis, offer solutions that are often non-unique; and therefore require calibration with direct field observations.

2.5 Fracture Analysis Techniques

During the past decade, diagnostics that measure the actual physical dimensions of fractures as they occur have been developed (GRI, 1998). These advances in analyzing direct as well as indirect hydraulic fracture treatment measurements are helping researchers understand the hydraulic fracturing process to better predict and optimize treatment design. Cipolla and Wright's classification (2000) is used here to describe direct far field (Class 1), direct near wellbore (Class 2) and indirect (Class 3) fracture diagnostic techniques.

2.5.1 Class 1 – Direct Far Field Techniques

These techniques use diagnostics in offset wellbores and/or measurements of the earth's surface and provide information about the far field fracture growth. Though these techniques map the total extent of hydraulic fracture growth, they provide no other information about the fracture properties.

Tiltmeters are tools used to measure the deformation pattern of the earth by recording the tilt either downhole and/or on the surface, see Figure 2-13. The devices used are very precise and measure miniscule deformations on the order of one ten-thousandth of an inch. Surface measurements record the fracture azimuth, dip, depth to the fracture center as well as the total fracture volume; whereas downhole measurements are used to determine height, length and width (Warpinski et al, 1996).

Microseismic hydraulic fracture technology was first developed at the MWX site (Warpinski et al, 1998 b). The technique images shear slippage on bedding planes or natural fractures by measuring microseisms or micro-earthquakes, caused by the hydraulic fracture treatment. The events are detected with downhole receiver arrays of accelerometers or geophones placed across fracture depths in offset wells, see Figure 2-14. Microseismic measurements have been found to provide high-quality time dependent information on the created fracture growth and geometry. However, there are problems in that the technique cannot be used in all formations (some do not generate measurable signals) and there can are also be problems with determining individual fracture planes when multiple fractures occur.

2.5.2 Class 2 – Direct Near-Wellbore Techniques

These techniques are generally run inside the treatment wellbore after the fracture treatment and record a physical property in the near-wellbore region.

Production logging normally surveys with multiple sensors to monitor flow (spinner), temperature, pressure and fluid density, capacitance and gamma ray. These measurements evaluate the amount and type of fluid produced into the well bore from each set of perforations. Cased-hole measurements not only identify open perforations, but also indicate producing intervals and evaluate their contribution to total production.

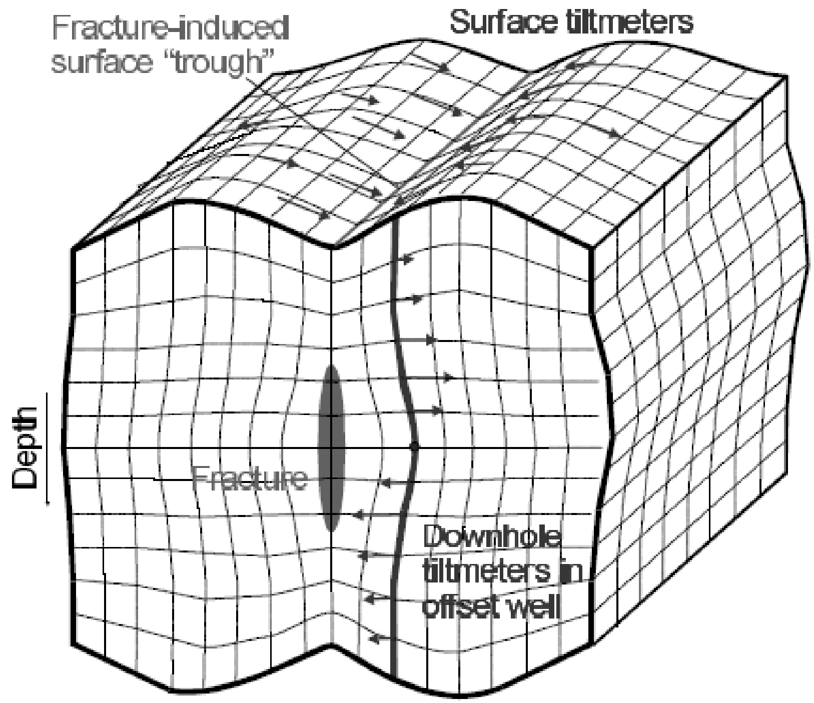

Figure 2-13: Principle of tiltmeter fracture mapping, from Cipolla and Wright (2000).

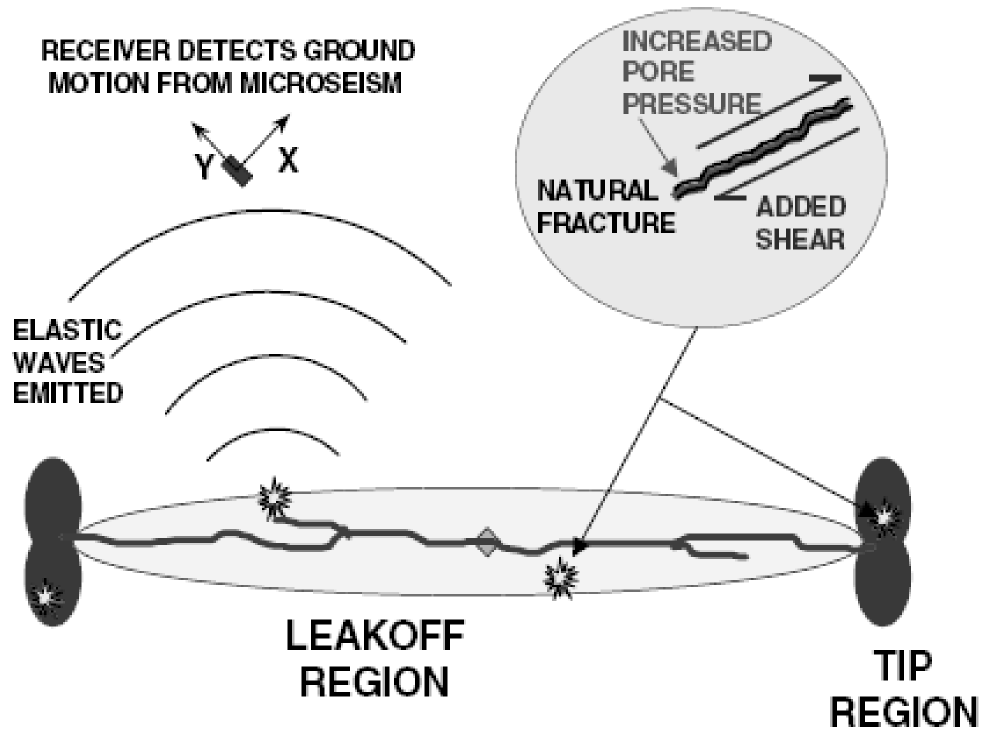

Figure 2-14: Figure showing the origins of microseismic events and the principles of microseismic fracture mapping, from Cipolla and Wright (2000).

Borehole image logs provide oriented images of both the induced and natural fractures along the wellbore circumference. These images can then be interpreted to give the maximum stress direction (fracture azimuth). Caliper logging measurements of wellbore width can be used to indicate formation toughness as well as indicate the orientation the maximum stress, using wellbore breakouts and borehole ellipticity. The main disadvantage is these techniques can only be run in openhole situations.

2.5.3. Class 3 - Indirect Fracture Techniques

Indirect fracture diagnostics include fracture modeling/net pressure analysis, pressure transient testing (well testing), and production data analysis. They are the most commonly used analytical techniques as the data is more readily available. Net pressure or production/pressure responses can be "matched" using reservoir and/or fracture models to provide an estimate of fracture dimensions, fracture conductivity, and effective length. However, the main limitation of these techniques is that solutions are generally non-unique and require calibration with direct field observations.

2.6 Mini-Fracture Analysis

Log and core measurements usually need to be confirmed with in-situ tests in order to derive a well specific evaluation model. The main pre-fracture test carried out is the mini-fracture or injection/leakoff test, which is done by pumping fluid into a zone at a rate sufficient to create a small fracture and then measuring the pressure decline.

Barree (1998) illustrated how pre-fracture tests could be used in formations containing multiple pay intervals to help design large limited-entry stimulations. In the Piceance basin, Warpinski et al (1985) used and refined these techniques at the MWX site before they were applied in the Grand Valley field (Craig and Brown, 1999) and more recently at the Mamm Creek field (Craig et al, 2000) to optimize multiple, limited-entry sand completions. For these field applications researchers performed small-volume fracture injection tests of each productive intervals' target sands and analyzed both G-function and pre-closure pressure fall-off data.

The net pressure (P_{net}) created during the fracturing process is defined as the pressure in the wellbore (P_w) minus the closure pressure (P_c) (Gidley et al, 1989), see Equation 2-12.

$$P_{net} = P_w - P_c \tag{2-12}$$

The net pressure response can be used to determine the type of hydraulic fracture growth and Figure 2-15 shows an idealized net pressure log-log plot. Engineers can use such plots to analyze how the fracture grew in the reservoir as well as indicate direction.

Initially, only net pressure analysis was used to analyze hydraulic fracture stimulations, but Nolte further refined the process by introducing G-function analysis (Gidley et al, 1989). G-function analysis estimates closure pressure using a linear plot of bottom-hole pressure versus the derivative of pressure (*dP/dG*), the so-called G-function (see Appendix A, Section A-1). A "superposition" derivative (*GdP/dG*) was also introduced to minimize diagnostic ambiguities and this is plotted versus the G-function (Barree and Mukherjee, 1996). These short injection/fall-off tests can be used to determine leak-off processes from the characteristic shape of the derivative and superposition derivative curves.

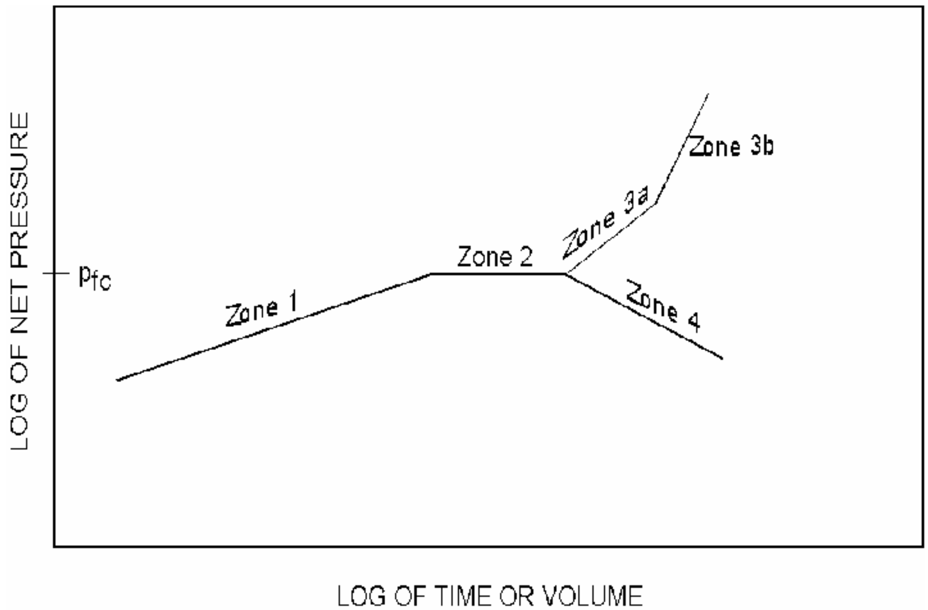

Zone	Approximate Slope	Interpretation
1	1/8-1/4 log-log slope	Restricted height growth and unrestricted extension
2	0 log-log slope	Opening of natural fractures; stable height growth
3a	1-1 log-log slope (unit slope)	Restricted extension growth with two fracture wings
3b	2-1 log-log slope (double slope)	Restricted extension growth with one fracture wing
4	Negative slope	Unstable fracture height growth

Figure 2-15: Log-log slope interpretation for idealized data, from Gidley et al (1989).

The modified Mayerhofer technique is a method for estimating permeabilities from pre-closure pressure falloff data obtained after a short fracture injection test (Mayerhofer et al, 1995). The method assumes a fracture geometry model, either radial (RAD) or confined fracture height (Geertsma-de Klerk-Khristianovic, GDK), to give an upper and lower limit value respectively.

2.7 Fracture Geometry Modeling

The development of effective hydraulic fracture models has been a major breakthrough in trying to solve the hydraulic fracturing puzzle. Physically measuring every hydraulic fracture with diagnostic techniques is cost-prohibitive, but there is a need to predict the fracture dimensions prior to pumping to optimize the treatment process. Improving the computer modeling process is a key component to being able to accurately predict fracture growth and dimensions for a given injection rate, time and fluid leakoff.

Initial attempts to understand hydraulic fracturing used two-dimensional models (2D) that have a fixed fracture height or an equal semicircular dimension. These models then evolved into more complex pseudo three-dimensional (P3D) and three-dimensional (3D) models, which have been made possible with the advent of increased computing power. Nowadays, these models allow the practitioner to undertake lengthy computations in a reasonable time frame for effective investigations of fracture design.

2.7.1 2D Models

Original 2D models were based on three common concepts that gave rise to two types of models, the Perkins-Kern (PK)/Perkins-Kern-Nordgren (PKN) & Geertsma-de Klerk- Khristianovic (GdK) models and the radial (RAD) model. In the PKN and GdK models, fracture height is assumed to be constant along the fracture length and set using lithological boundaries. In the two models fracture extension occurs either by rectangular extension (PKN) or radial/circular extension (GdK). Fracture length and height are calculated from: formation height, Young's modulus, fluid viscosity, leakoff and injection rate and time. These models can be used in reservoirs where there is a high stress contrast between neighboring formations, where the contrast follows lithologic boundaries. However, scenario seldom applies and these models therefore have limited application.

The radial model assumes equal fracture length and height, which are then jointly allowed to vary together with width. This model can be applied in formations of homogeneous stress and mechanical properties, where height is small compared to formation layer thickness.

The application of 2D models in highly heterogeneous reservoirs requires significant manipulation done by estimating fracture heights, usually based on field measurements, and experience. This can be problematic in that under-predicting fracture length will lead to over-predictions of height, neglecting leak-off effects, and the resulting fracture will grow out of zone, creating completion and productivity problems.

2.7.2 P3D Models

P3D models don't require an estimate of fracture height, but do require an input of the minimum horizontal stress in the proposed fracture zone and bounding layers. P3D models use a simplified representation of fluid flow in the fracture in order to reduce calculation time by approximating 2D fluid flow and the pressure-width relation. This is usually done by assuming particular shape, such as an ellipse, but doesn't represent the true pressure distribution in the fracture generated by the fluid flow. Due to the computer power now readily available, P3D models have generally been replaced by 3D capable models.

2.7.3 3D models

3D models require accurate stress contrast data and are the closest approximation to actual fracture growth. The main advantage of this model type is the calculation of fluid flow and pressure along the fracture uses a fully 2D model of fluid flow to calculate the pressure. This calculation is used to give an accurate width at any point.

The main limitation to the use of the new 3D models is the lack of suitably detailed input data to allow for their proper evaluation and further development. Even the most sophisticated fracture propagation model and fracture treatment design require accurate determinations of stress magnitudes, fluid loss profiles and fracture conductivities; which are costly and time consuming for operators to obtain.

It is only by using the newly developed 3D fracture models in fields with unique input data sets that investigators will be able to identify critical data and generate simpler techniques for routine application. With careful post-fracture evaluation the fracture engineer should be able to fine tune the methodology to give the simplest approach for effective field application.

CHAPTER 3
MODEL INPUT DEVELOPMENT

The Department of Energy (DOE)/National Energy Technology Laboratory (NETL) sponsored a number of projects during the 1980's that helped to convert the Piceance basin Mesaverde gas play from a 100 Bcf accumulation into a potentially multi-Tcf gas resource. A significant amount of the research work was undertaken at the Multi-Well Experiment (MWX) site near Rifle, Colorado (Schroeder, 1997), see Figure 3-1.

At the MWX site a geologic characterization of the Mesaverde group established that the production was predominantly from the fluvial point bar sand bodies, with extremely low matrix permeabilities (<0.0001 mD). Subsequent geologic and geophysical work carried out in the nearby Rulison field, established that there was an abundant system of micro-scale natural fractures and a less frequent system of macro scale fractures. In common with most tight gas reservoirs, hydraulic stimulation is required to interconnect the dual-fracture system with the wellbore to maximize well production.

The multi-disciplinary research carried out in the Piceance basin has gone a long way in helping stimulation technology development in tight gas reservoirs. However, further development of stimulation technology requires models that can be used to analyze, target and optimize hydraulic fracture treatments as well as predict well production. The problem in the Piceance basin is that the application of analytical techniques commonly used to correlate well and individual sand productivity, and hence identify pay targets, has proven difficult, see Figure 3-2. Ely et al (1994) attempted to correlate production from over 130 Piceance basin wells using log-derived "net pay" but was unsuccessful. A subsequent study in the Mamm Creek Field (Craig et al, 2000) also found well productivity to be highly unpredictable, but other studies have shown more success within specific stratigraphic intervals (Schubarth et al, 1998). The main problem in trying

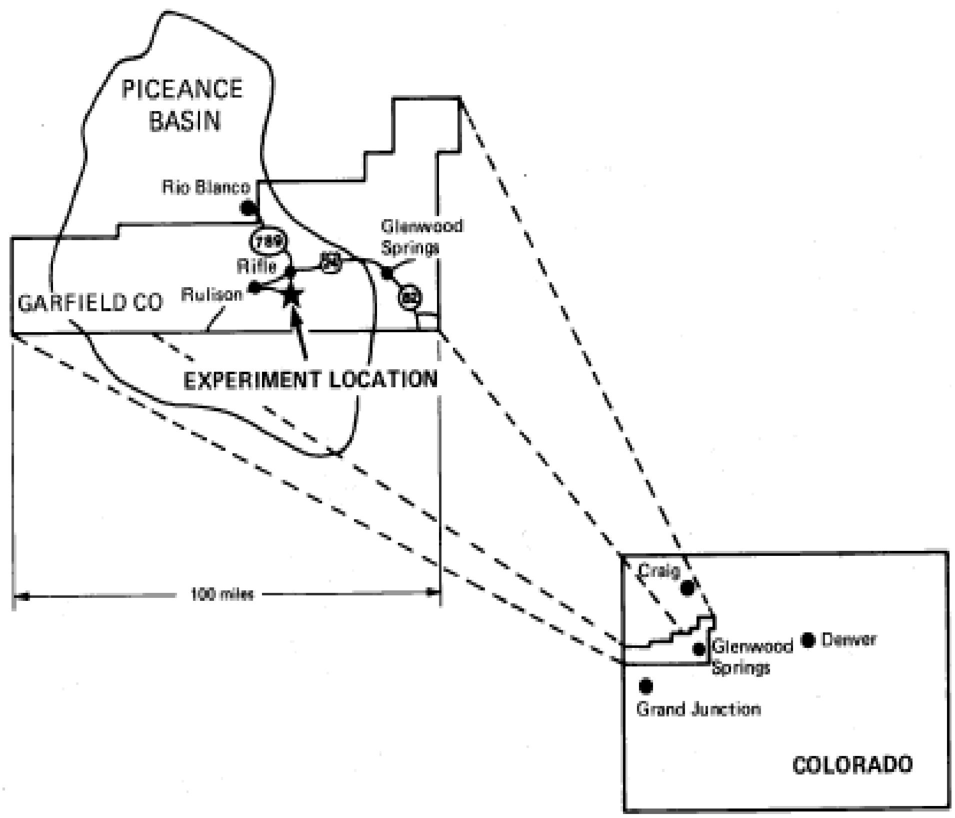

Figure 3-1: Figure showing the location of the MWX site.

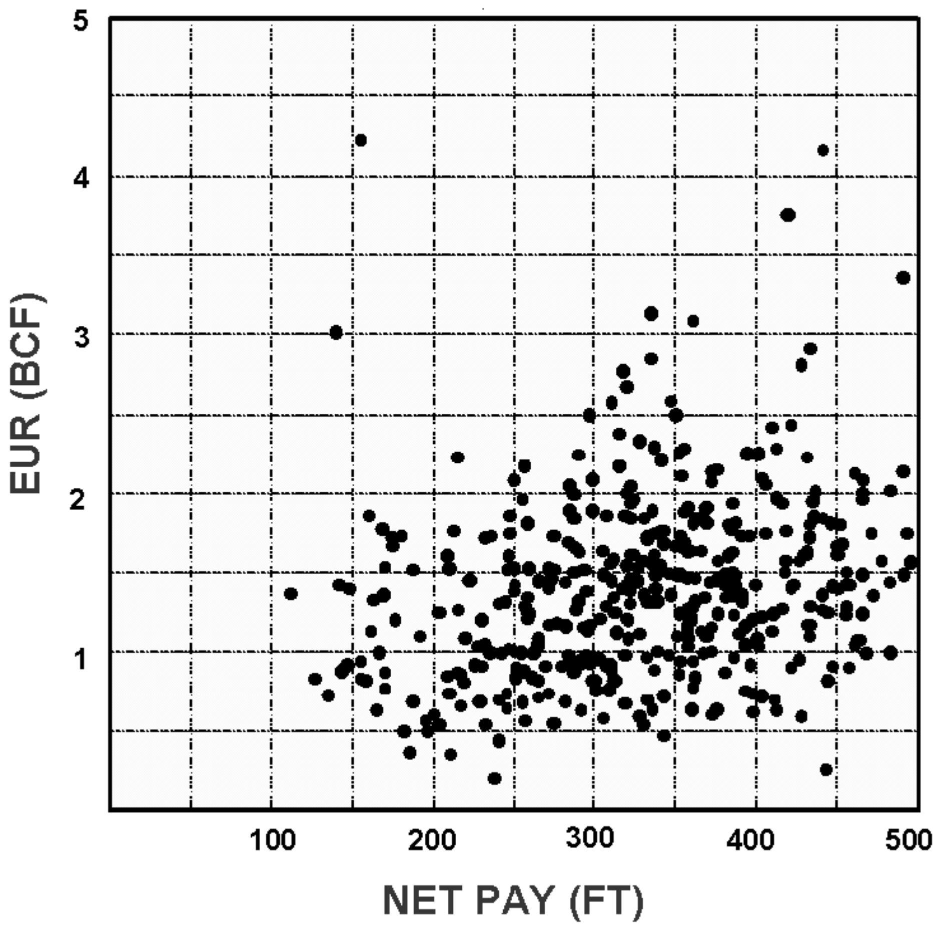

Figure 3-2: Cross Plot of Estimated Ultimate Recovery versus net pay for a Piceance basin Field. (From Cumella and Ostby, 2000)

to develop a Piceance basin model is that well performance deviates from model predictions, which has been attributed to natural fracture clusters (Ely et al, 1994).

Until the early 1990's, operators believed that hydraulic fracturing of the very low permeability lenticular sands would not be very effective. Operators bypassed these sands and completed wells in the Cozzette and Corcoran sands. A variety of stimulation types had been tried from small single zone fracs to multiple massive hydraulic fracture (MHF) designs. After the work by the DOE/GRI (Shroeder et al, 1997), operators began an aggressive program in 1993 to complete/recomplete wells in the massively stacked, lenticular fluvial sand reservoirs. Current completion practices in the Piceance basin are to separate the lenticular sands into a series of intervals containing 400 to 500 ft of gross productive interval. Each interval is then stimulated separately, and most wells have three to five such intervals in a 2,000 ft gas saturated zone.

Early drilling techniques in the Mesaverde tried to minimize damage from the clays in the Wasatch and Williams Fork formation and air drilling was one technique used. Subsequent techniques targeted the Williams Fork wells with KCL mud, which was then completed prior to penetrating the lower Cameo coal seams, where problems often occurred. For these completions; wells were cased, cemented and stimulated (hydraulically fractured) in two or three stages over a 1000 ft interval. Typical treatments used 25,000 to 35,000 gallons of KCL water and 80-100,000 pounds of sand. The stimulated interval increased in thickness during the period 1979-1982, until over 1200 ft was stimulated with less than 150,000 lbs of sands per well. Current practice is to use mud-based drilling with a freshwater (2% KCl) low polymer gel-mud with 1,000 gallons of 7.5% acid to clean-up perforations. On average 300,000 lbs of sand and 100,000 gallons of slickwater are used to stimulate wells prior to production. Nitrogen fracturing has also been tested, but with limited success (DOE report, 1994).

Well costs have been estimated at $750K to $1MM (including four large hydraulic stimulations), with reserves of approximately 2 Bcf per well (Kuuskraa et al, 1997). Kuuskraa et al (1997) also estimated the reserve replacement costs for the area are in the range of 50 cents per Mcf. Typically, the cost of stimulating the well is 40% to 60% of the whole cost of drilling and completing the well. There is a need to optimize the hydraulic stimulation process and early attempts in the Piceance basin, carried out in the Grand Valley. Parachute and Rulison fields, were undertaken using field tests (Ely et al, 1994) and Psuedo-3D (P3D) hydraulic fracture (HF) modeling. The results of the HF modeling showed some success in the fields with failures being attributed to the geological complexity of the reservoir (Ely et al, 1994). The paper contained little detail of the actual models and the published pressure matches lacked detail and show the inability to adequately model complex reservoirs using a P3D HF model with limited layer numbers. Other research in nearby Mamm Creek (Craig et al, 2000) also used the same P3D HF model to develop fracture length inputs for a 22-layer 3D reservoir model. Again little detail of the results from the fracture model is contained in the paper, but these models are normally incapable of incorporating the required detail to fully match job data due to the limited layers and imposed fracture geometries. This study aims to overcome the problems in trying to model a well in the Piceance basin by developing a fully 3D model of a hydraulically fractured well. The research also investigates the effects of various inputs on the fracture model outputs in an effort to identify critical parameters. This work is part of ongoing research to help operators and researchers identify the minimum data necessary to effectively model and optimize hydraulic fracture treatments in geologically complex reservoirs.

3.1 3D Simulation Software History

Early models developed for use in the petroleum industry were simple two-dimensional (2D) simulators, based on the concept of material balance. After considering fluid leakoff and rock moduli, these models consider that the fluid pumped into the formation is directly related to the fracture geometry. These models were seldom found to be representative, due mostly to the unrealistic height restrictions imposed. The restrictions in 2D models led to the development of pseudo three-dimensional (P3D) and three-dimensional (3D) models. The main difference between the 2D/P3D and 3D models is that calculation run times are much greater in 3D models, due to there being no assumptions made on growth patterns. However, the accuracy of 3D models means that a lot of additional reservoir input data is required and this is costly to obtain. Little is known about what constitutes the minimum data required to get a realistic HF model in tight gas reservoirs and so operators tend to apply an 'all-or-nothing' approach to obtaining the input data. Nevertheless, 3D packages have found widespread use and there are a number of 3D software packages available. Settari and Cleary (1986) and Warpinski et al (1993) have reviewed several software packages and also detailed the theories used in each software package. For this research GOHFER (Grid-Oriented Hydraulic Fracture Extension Replicator), currently supplied by Stim-Lab (Duncan, OK) and supported by Barree and associates (Denver, CO), was used to undertake the research (Barree, 1983 and 2000). The reason for choosing the software in this thesis and a discussion about its application, is outlined in the following section.

3D Software - GOHFER

GOHFER is a robust simulator that is used extensively in the petroleum industry to model complex hydraulic fractures, particularly in tight gas reservoirs. It is a 3D geometry, finite difference HF modeling software with a fully coupled fluid/solid transport simulator. One of the advantages of GOHFER is that formulations used in the simulations have been published and made available publicly for peer review. The software was originally written by Barree (1983), developed in-house at Marathon Oil Company and is now offered commercially by Stim-Lab. GOHFER was initially difficult to run on personal computers (PC's) until the development of a windows-based application, that has made it easier to use. The software has developed, along with the development of PC power and memory, to become quicker and more convenient to use on standard PC's and laptops. The software is now routinely used for real-time HF analysis, albeit for more complex fractures.

The program uses a grid structure to describe the entire reservoir, similar to a reservoir simulator. The grid is set up using user-defined nodes which are entered together with both the vertical and horizontal dimensions required. GOHFER then defines a grid of equal sized blocks which defines the computing speed, a smaller node size requiring a greater computational time. The ability to change both the vertical and horizontal node size, means that there is great flexibility in modeling and the simulation of geologically complex reservoirs is possible. The grid is mapped on the surface of the created fracture and is therefore not necessarily planar in space. Variables such as pressure, width, shear rate, fluid age, leakoff rate, proppant concentration, velocity, fluid composition and proppant composition etc. are defined at each grid cell. This allows for both vertical and horizontal variations in properties and all calculations are done on a per-grid-node basis, tracking the exact fracture geometry and proppant placement during the treatment. Vertical variations can be adequately described by information derived from well logs, but lateral variations require additional knowledge of local geology and structure. Modern techniques have been developed that allow the geology and structure to de defined but it is only possible on a scale of tens of feet using 2D/3D seismic, or cross well imaging methods.

A major advantage of GOHFER is that it has the ability to decouple the rock properties in the software. Rocks seldom behave as truly elastic materials, but the equations used to define their stress behavior are often based on the assumption of linearly elastically coupled materials. Shear slippage is a phenomenon that often occurs during hydraulic fractures along interfaces or planes of weakness and it is suspected that this acts as a containment mechanism (Barree and Winterfield, 1998 and Warpinski et al, 1998 b). Warpinski at al (1998 a) described the shear slippage mechanism and how it gives rise to microseismic activity, which can be measured during hydraulic stimulation treatments. GOHFER effectively allows slippage to occur so that net pressures and fracture height growth patterns can be matched, something not possible if only elastically coupled materials are considered. GOHFER also has a mechanism to deal with the non-elastic behavior around the fracture tip, using a 'process zone stress' in the software. The process zone stress helps to account for fluid lag, tensile stresses and non-elastic behaviors in the fracture tip region. Also, GOHFER can be run to replicate either symmetric or asymmetric growth. In asymmetric growth both wings of the fracture are modeled so that the effects of lateral pressure gradients, bed dip or changes in rock properties can be modeled to better represent HF growth.

The major disadvantage of GOHFER is the complexity of the software. A large number of inputs are needed and computational times can be significant when modeling geologically complex reservoirs. In order to try and minimize the required inputs, the software has default values if the data is not available, though this will affect the accuracy of the outputs. For simple reservoirs, where a layer model applies, runs can be easily made in real time taking only several minutes. For more complex reservoirs a large amount of details is required prior to carrying out the simulation, and processing runs can take several hours. However, the detail possible means that GOHFER is ideally suited to model geologically complex reservoirs and is therefore ideal for research purposes. The other drawback with the software is that it models an infinite conductivity reservoir and therefore all changes in net pressure recorded during the treatment have to be modeled using changes that occur in, or very near the wellbore area. For most purposes realistic models are possible but for geologically complex reservoirs there are often problems trying to match actual field data. Within GOHFER there is an ability to change lateral reservoir properties, but input resolution of feet is required which is not yet possible.

3.2 Study Wells/Model Development

In order to fully utilize GOHFER and create as accurate a model as possible as much input data as possible is required, and data should be available to verify the output model geometry. For this study, input data from sixteen wells was analyzed for the type of data available and the quality of the data. A single well was then selected for simulation which had available standard logs as well as mini-fracture analysis of all the reservoir sands identified by the operator. A comparison well was analyzed to help assess and validate the quality of the input data. The mini-fracture analysis in particular is difficult to obtain in tight gas reservoirs as valid data really requires fracture closure, so that after-closure analysis can be undertaken (Nolte, 1997). However, closure in tight gas reservoirs requires tests to be carried out for several weeks and often before-closure analysis is undertaken instead (Craig et al, 2000). For this study all the identified pay intervals in the study and comparison well were tested over several months in order to try and obtain the best data possible. Microseismic data was also recorded and was used to confirm fracture growth to replicate the actual HF treatment. Production logs were also run several months after the treatment to analyze the created fracture production. The well was also chosen because of its proximity to other wells that have similar input data available for future studies by the operator and/or research groups. This research aimed to analyze and optimize the methodology presently used for complex hydraulic fracture modeling, as well as perform sensitivity analysis of the various simulator inputs.

3.3 General Case Development

Hydraulic fracture simulation practitioners tend to develop their own preferred techniques for obtaining the necessary input data and then creating a valid model. The process is normally refined by experience in certain areas and is often limited by the available computing time and the required outputs. Normally, the rock and reservoir data such as: identified pay, zone thickness, rock-mechanical properties, in-situ stresses etc., are derived from openhole logs, other wells in the area or are estimated based on experience in the region. The actual treatment and treatment data (fluid properties, pumping rates, proppant concentrations and quantity, etc.) are provided by the service company and are usually based on treatments that have been optimized practically in the area or found to work in geologically similar areas. The methodology used for this investigation is outlined in Figure 3-3.

The GOHFER model relies heavily upon log derived input data to define rock elastic properties, porosity and lithology, which are input directly from standard log ASCII (LAS) files. GOHFER has a built-in program, LOGCALC, that allows LAS files to be used to generate reservoir and mechanical properties. Once the properties have been derived they can be used to help create an accurate lithologic representation of the well. Ideally the following inputs are required: caliper (Cal), bulk density (RhoB), neutron density (NPhi), gamma ray (GR), transit time-compressional (DTCO), transit time-shear (DTSM) and density porosity (PhiD). However, for this research sonic log data was not available for analysis of the study and reference well and the following minimum curves, required by LOGCALC, were used to generate data: GR, NPhi and RhoB. The data contained in the log tracks was imported on a foot-by-foot basis, though data is averaged in the software over the specified node size. The final lithologic set-up of the well is shown in Figure 3-4 and typifies the laminated nature of the reservoir. It is interesting to note that even within the productive sand zones (shown in red) there are shale laminations. This is one of the reasons that it is difficult to model highly heterogeneous reservoirs using 2D and P3D HF models.

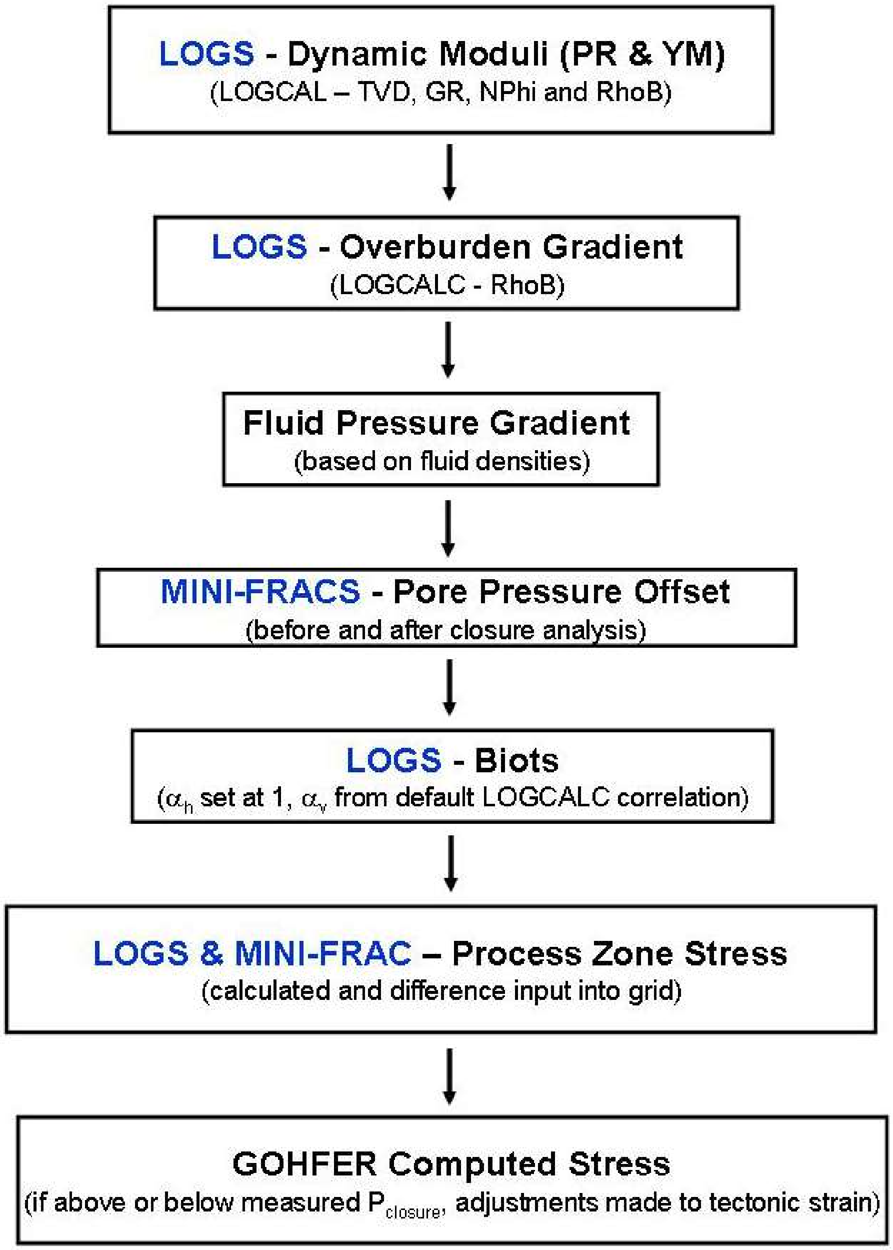

Figure 3-3: Workflow diagram showing the methodology recommended for creating an accurate a hydraulic fracture model.

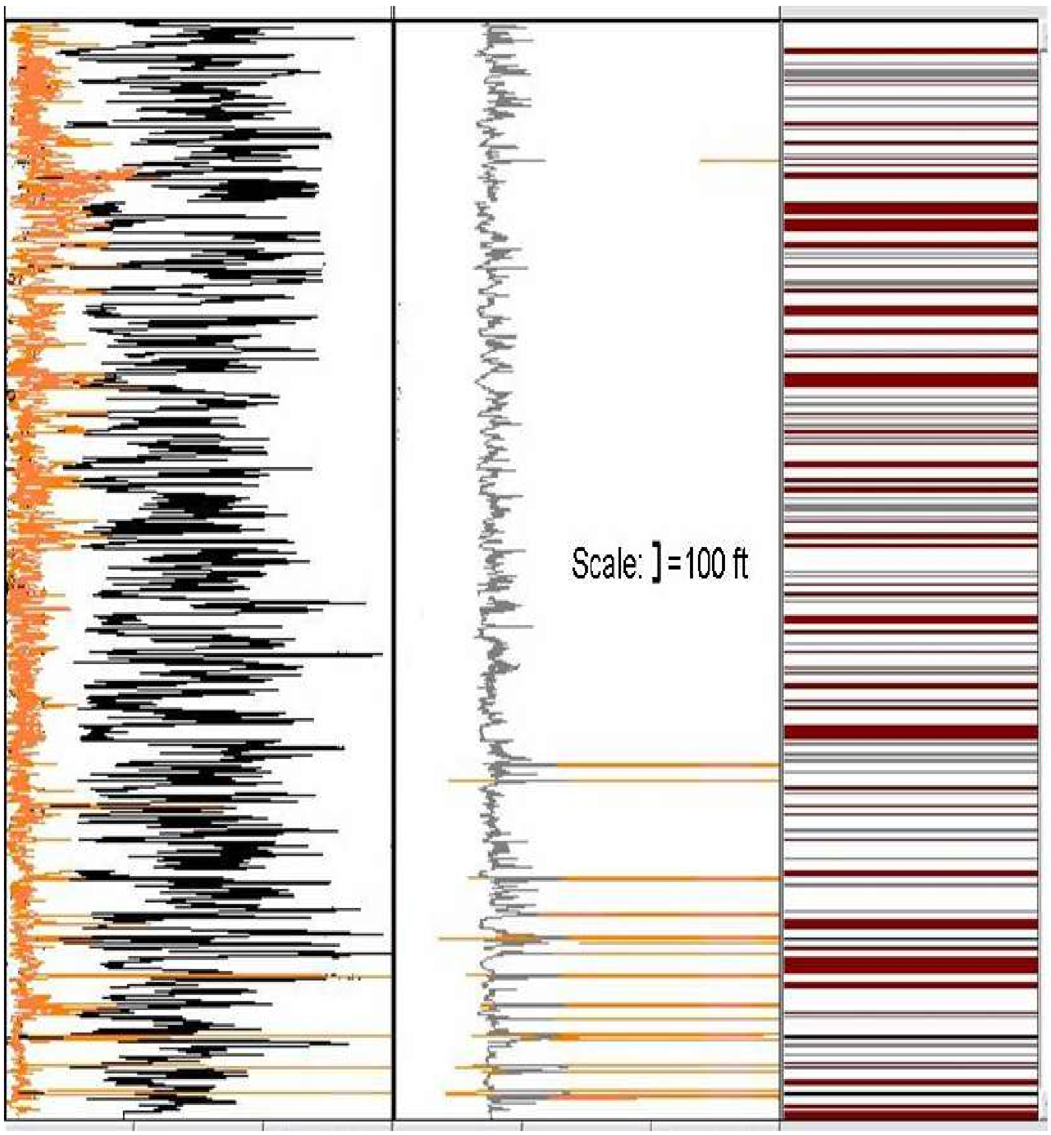

Figure 3-4: Figure showing the actual model layers of the subject well, as defined in LOGCALC. On the right are the gamma ray (GR) and deep resistivity (AHF90) tracks used to define the layers for the representative model on the right.

The values generated were compared to previous data generated from the MWX experiments (Warpinski et al, 1998 c) and found to be reasonable values, see Appendix A Tables A-1 and A-2. The LOGCALC derived values were used in the model without further modification and the grain density tables used to define what constituted a certain lithology. It should be noted that though the lithology was defined (coal, sandstone and coal) and shown in Figure 3-4, the software doesn't use the definition for calculations, but uses the actual log derived values for cell definition.

3.3.1 Young's Modulus (E)

Young's modulus is best estimated from full waveform sonic data in combination with a bulk density log, but it can also be related to the bulk density log using lithology and a corresponding compressional wave times. In the LOGCALC program, the value of E/ρ is determined by determining the lithology and a corresponding compressional wave time in microseconds per foot and the chart value is then multiplied by the rock bulk density g/cm^3, see Figure A-1 (Appendix A). For mixed lithology, the chart value can be interpolated between the pure lithology curves. The derived values were also compared to the values from the MWX site (Warpinski et al, 1998 c), see Tables A-1 and A-2 (Appendix A), found to be comparable and used without modification, see Table 3-1.

Young's modulus is considered to have less effect on fracture containment than Poisson's ratio as it does not affect the in-situ stress calculated from the uniaxial strain model. However, in the case of active tectonic movements, it may influence stresses caused by a uniform regional strain. Previous work at the MWX site (Warpinski and Teufel, 1989) concluded that there is a significant tectonic stress in the Piceance basin, which is discussed in Section 3.5.2.

Table 3-1: Various Intervals and Their Log-Derived Grid Layer Values Calculated Using LOGCALC.

Completion Interval	Gross Height ft	Net Height Ft	Ratio Net/Gross	Porosity %	YM psi	Poisson's Ratio
A	15.2	14	0.9	9.1	6,604,000	0.217
	15.8	11	0.7	7.9	7,113,000	0.223
	18.4	17	0.9	8.3	6,956,000	0.219
	14	10	0.7	8.0	7,051,000	0.223
	21.6	15	0.7	8.8	6,498,000	0.222
S	22.2	10	0.5	6.5	7,716,000	0.221
	29.6	21	0.7	8.5	6,718,000	0.219
	21.9	17	0.8	8.8	6,597,000	0.221
	16.1	13	0.8	8.0	6,587,000	0.225
	40.9	20	0.5	8.4	6,718,000	0.213
G	23.8	19	0.8	9.5	5,875,000	0.215
	20	7	0.4	4.0	9,109,000	0.236
	38.1	30	0.8	6.8	7,597,000	0.218
	36.2	21	0.6	8.3	6,900,000	0.215
	18	10	0.6	6.0	8,015,000	0.224
M	16.5	10	0.6	7.0	7,455,000	0.225
	15.2	12	0.8	7.8	7,147,000	0.222
	15.2	15	1.0	8.7	6,720,000	0.219
	30.5	22	0.7	7.8	6,744,000	0.224
	21.6	22	1.0	9.2	6,370,000	0.22
	14	9	0.6	7.5	7,093,000	0.223
T	21.4	12	0.6	9.5	6,351,000	0.222
	27.1	18	0.7	8.8	6,565,000	0.225
	42.9	20	0.5	9.8	6,106,000	0.222
	20	12	0.6	8.6	6,581,000	0.231
	12.9	12	0.9	9.2	6,539,000	0.219
O	17.2	12	0.7	9.0	5,260,000	0.224
	31.5	21	0.7	11.7	5,530,000	0.225
	36.57	36	1.0	8.7	6,721,000	0.224
	15.7	15	1.0	8.7	6,574,000	0.228
	11.7	7	0.6	7.3	7,291,000	0.223
I	12.85	24	1.9	7.4	7,107,000	0.24
	25.72	34	1.3	4.9	7,163,000	0.234

3.3.2 Poisson's Ratio

Again without a full wave sonic or dipole sonic to derive Poisson's ratio, values are determined in LOGCALC using the lithology and a corresponding compressional wave arrival time (in microseconds/ft). Curves within the program provide an estimate of Poisson's ratio for sandstones, limestone's, dolomites, shale's and coals, see Figure A-2 (Appendix A). The derived values were also compared to the values from the MWX site (Warpinski et al, 1998 c), see Tables A-1 and A-2 (Appendix A), found to be comparable and used without modification. The grid layer values are shown in Table 3-1.

3.3.3 Biot's Constant

The irregularity of pore and grain shapes, together with partial cementation, means that internal fluid pressure is not transmitted perfectly to the rock matrix. Biot's constant is a correction factor (the poroelastic constant) to predict the counteracting stress of the pore pressure against the overburden gradient. LOGCALC estimates the vertical Biot's constant using a linear transform based on the effective porosity trace PhiE, see Equation 3-1 (Detournay and Cheng, 1993):

$$\alpha_v = 0.6 + m \times \phi_E \tag{3-1}$$

where,
- α_v = vertical Biot's constant
- m = slope of linear transform, usually 1.
- ϕ_E = shale-corrected effective porosity from the neutron density crossplot

The values for the vertical Biot's constant were used without modification for the initial grid set-up. A horizontal Biot's constant represents the interaction of the pore fluid pressure and the horizontal stresses. Normally, the pore fluid is considered to be in direct communication with the fracture fluid and the pressure response should be 1:1, where there is no rock deformation or interference. Due to the difficulties in trying to determine the value of Biot's in the horizontal direction for any situation, the value is set at one for all the model runs.

3.3.4 In-Situ Stress

The physical properties of rocks are affected by in-situ stress, and the influence of stress is even more pronounced in naturally fractured reservoirs, where fluid flow is often enhanced by fractures. However, the in-situ stress state at depth is not easily determined and various models have been proposed (Warpinski, 1989) but their application is limited due to the complexity of determining the mechanical property and load conditions of large rock masses at subsurface. The simplest and most common model applied is the elastic uniaxial strain model of Hubbert and Willis (1957). This model depends only on gravitational loading and assumes no lateral displacement during deformation. For this model to apply, the horizontal stresses must be equal and increase with depth, only changing with changes in pore pressure and lithology (Poisson's ratio). The model, though simplistic, does indicate that the horizontal stress is affected by gravitational loading and pore pressure, such that production will change the pore pressure and hence the horizontal stress state. A number of techniques have been developed to measure or infer the principal horizontal stress orientation and magnitude including: hydraulic fracture stress tests (Warpinski et al, 1985), leak-off tests (Kunze and Steiger, 1992), anelastic strain recovery of cores (Warpinski and Teufel, 1989), differential strain curve analysis (Ren and Roegiers, 1983), differential wave velocity analysis (Ren and Hudson, 1985) and wellbore logs to analyze eccentricity and breakouts (Bell and Gough, 1982). For this research, horizontal stress data is determined from closure pressure data using small hydraulic fracture treatments in so-called 'mini-frac' tests.

3.3.4.1 Mini-Hydraulic Fracture Tests

Hydraulic fracture tests are routinely carried out to measure the minimum horizontal stress in cased and perforated completions. Warpinski et al (1985) detailed the procedure. From these tests, it is possible to determine the instantaneous shut-in pressure (ISIP), which is essentially the minimum horizontal stress for small volume tests with low viscosity fluids. The only real problem is that it is often difficult to determine a clear ISIP and because the test is done in a cased hole there is no information on the maximum horizontal stress or the stress orientation. The Mesaverde has been extensively studied using this small volume hydraulic fracture analysis by Warpinski and Teufel (1989). Their work was undertaken in the Rulison Field and estimated the effect of pore pressure on the minimum horizontal stress in the Mesaverde sandstones. For this research thirty-three tests were analyzed in the study well and another twenty-three tests done in an adjacent well, for comparison with the study well and MWX measurements, see Table 3-2 (study well) and Table 3-3 (comparison well). In common with work by Warpinski and Teufel, the tests were characterized by relatively high injection pressures and a large pressure drop at shut-in, however the instantaneous shut-in pressure (ISIP) was difficult to determine accurately in the majority of cases.

Closure stress (or minimum horizontal stress) is known to decrease with reductions in pore pressure in a phenomenon known as the stress-depletion response of the reservoir rock (Addis, 1997). The uniaxial strain relationship (Equation 3-2) has traditionally been used as a simple means of estimating in-situ stress data from log-derived rock properties.

Table 3-2: Study Well Results of the G-Function Analysis Closure Pressure Determination

Completion Interval	BHTP	Av Pump Rate	Pump Time	Volume	Closure
	Psi	bbls/min	mins.	gallon	Psi
G	4173.1	4.78	2.5302	508	3835
	4337.8	4.78	2.5291	508	4015
	4053.0	4.7	2.5168	497	3550
	4082.4	4.71	2.5846	511	3449
	4932.2	4.22	2.8458	505	3931
S	4334.3	4.55	2.684	512	4113
	4345.2	4.47	2.7371	514	4128
	4842.1	4.6	2.6044	503	3984
	5004.5	4.54	2.6645	508	3765
	4956.0	3.53	3.3854	503	4164
A	4883.0	4.7	2.4161	477	4185
	4867.3	4.61	2.6676	517	4630
	4839.4	4.38	2.8053	516	4270
	4853.4	4.49	2.9844	563	4198
	4921.0	4.71	2.5725	509	4323
M	4931.5	4.88	2.4733	507	4453
	4830.2	3.66	3.2559	501	4589
	5233.2	4.71	2.5423	503	5063
	4862.3	4.78	2.5507	512	4259
	4720.1	3.82	3.2833	527	4071
	5678.2	3.7	3.1332	486	5036
O	5705.5	4.36	2.77	508	5071
	5923.5	2.83	4.2737	507	4634
	6388.2	0.35	16.6297	247	5165
	6384.5	4.27	2.7824	499	5743
	6125.3	3.48	3.4851	509	5238
T	6304.8	4.06	2.9657	506	5136
	6148.2	4.16	2.9157	509	5382
	6823.5	3.86	3.1165	506	5926
	7026.5	4.12	2.9141	505	6513
	7315.7	4.08	2.9522	506	5537
I	7142.5	3.99	3.0213	506	5417
	7272.8	4.05	2.9714	505	4287

Table 3-3: Comparison Well Results of the G-Function Analysis Closure Pressure Determination

Completion Interval	BHTP	Av Pump Rate	Pump Time	Volume	Closure
	psi	bbls/min	mins	gallon	Psi
S	4436.58	4.81	2.51	508	3716
	4118.73	4.94	2.41	501	4021
	4413.52	4.35	2.74	501	4256
	4112.63	5.24	2.29	504	4061
	4631.98	4.35	2.52	460	4154
A	4302.32	4.51	2.80	531	4028
	4843.34	4.13	2.87	498	4310
	5092.99	4.52	2.65	503	4354
	4837.52	4.16	2.96	518	4170
M	6156.77	4.25	2.83	506	4729
	4814.77	4.71	2.56	507	4459
	5804.40	4.08	2.97	509	4955
	5944.61	4.21	2.78	492	5002
O	5560.99	4.55	2.67	510	5065
	5920.25	4.17	2.92	510	5142
	5456.03	4.09	2.92	501	4896
	6555.58	2.54	2.76	293	5473
	6320.55	3.27	3.72	510	4859
T	6478.54	2.95	3.71	460	5985
	7239.31	3.27	3.60	494	6403
	6998.57	3.20	3.76	505	6158
	6571.42	2.45	4.92	505	6150
	7114.76	3.32	3.60	503	6100

$$\sigma_{\min} = \frac{\nu}{(1-\nu)}\left[\sigma_z - \alpha_z P_{res}\right] + \alpha_h P_{res} + \sigma_{ext} \tag{3-2}$$

where,			
	σ_{min} ($\sim P_c$)	=	total minimum horizontal stress
	ν	=	Poisson's ratio
	P_{res}	=	reservoir pressure
	α_z	=	vertical Biot's poroelastic constant
	α_h	=	horizontal Biot's poroelastic constant
	σ_z	=	total overburden stress
	σ_{ext}	=	externally generated stress

However, Warpinski, et al (1998 c) showed significant differences between the in-situ stresses estimated from log-derived rock properties and measured stresses. Therefore, the application of the uniaxial strain relationship is normally tested and calibrated for a field to ensure a reasonable relationship between calculated and measured in-situ stresses. For these experiments the closure stress was determined from the mini-fracture tests and this should be approximately equal to the minimum horizontal stress, Equation 3-2 was used to estimate the closure pressure, using the determined pore pressure and Poisson's ratio values for every sand within each interval. This method was used to assess whether Equation 3-2 could be applied to derive the stress profile for the well. As can be seen in Figure 3-5, unlike the MWX data, the uniaxial strain relationship was found to give a fairly good estimate of the closure pressure (using mini-frac pore pressures and the LOGCALC Poisson's ratio). It is also interesting to note that most of the closures follow a closure gradient of 0.75 psi/ft, a gradient that has been found by fracture engineers to often apply in the Rocky Mountains basins.

Using Equation 3-2 and the determined pore pressure, a Poisson's ratio value of 0.21 was found to give good estimates of the closure pressure, and this value of Poisson's ratio was also found applicable in the comparison well, see Table 3-4.

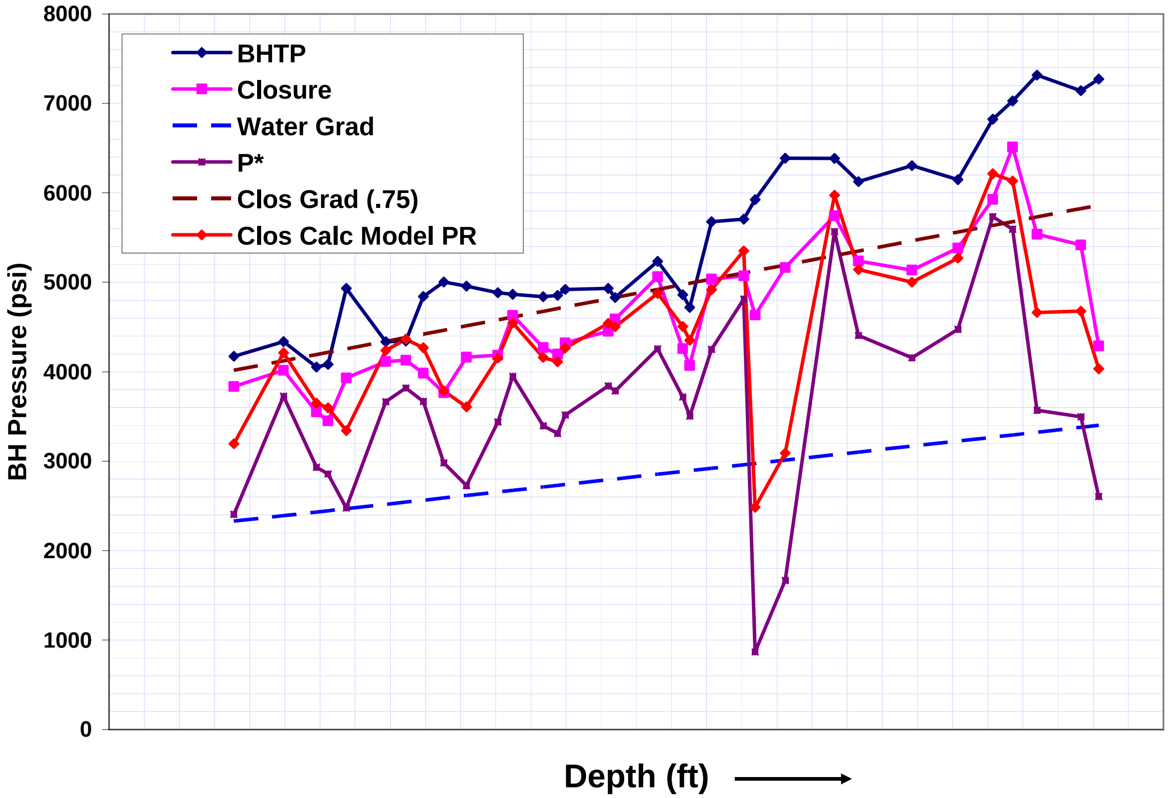

Figure 3-5: Graph showing a plot of the data from Table 3-4. As can be seen the closure calculated using Equation 3-2 can be applied and most of the data follows a 0.75 psi/ft gradient. Note the potentially depleted intervals towards the bottom of the well.

For the cases where the estimated reservoir pressure is different, the averaged Poisson's ratio value for the grid may be wrong, or the closure pressure might not be indicative of the minimum in-situ stress. The data shown in Table 3-4 suggests that on the whole the uniaxial strain relationship will provide reasonable pore-pressure estimates for these Piceance basin Mesaverde sands, and agrees with work by Craig and Brown (1999) in Grand Valley.

From the G-function analyses (see G-function reports in Appendix A) and most tests (57.6%) indicated pressure-dependent leakoff (PDL) due to fissure opening, while almost a fifth exhibited normal leakoff behavior, see Table 3-5 and Figure 3-6. Only twelve percent showed fracture height recession or fracture tip extension. These numbers compare favorably with data obtained in the Mamm Creek field (Craig et al, 2000) where a similar percentage of tests showed PDL, but normal and fracture height recession was only shown in 17 and 11 percent of tests, respectively. Craig et al's results also showed greater fracture tip extension (34.7%) and could be due to more extensive natural fracturing of the reservoir.

Warpinski and Teufel (1989 b) found that in the Rulison Field the total minimum horizontal stress increases with depth, but pore pressure showed significant variation with depth. Figure 3-7 shows their plot of pore pressure versus total minimum horizontal stress, which shows significant scatter.

The two wells were investigated for input development in the present study and a summary of the results from the mini-fracture analyses of the study well are shown in Figure 3-8 (see Appendix A). These results indicate a correlation between the minimum horizontal stress (σ_h) and pore pressure (p_p), similar to the MWX results. The correlation can be represented in the study well as:

$$\sigma_h = 0.43\ p_p \text{ (psi)} \qquad (3.3)$$

Table 3-4: Mini-Fracture Analysis Results for the Pore Pressure and Calculated Closure Pressure as well as Value Constant Values of Closure Pressure (0.75 psi/ft) and Poisson's Ratio (0.21).

Completion Interval	P*	$P_{Closure}$	$P_{Closure}$ Gradient (0.75 psi/ft)	$P_{Closure}$ Calculated Using PR=0.21
	psi	psi	Psi	psi
A	3437	4185	4579.5	4146.5
	3950	4630	4611.0	4534.3
	3397	4270	4676.3	4151.4
	3311	4198	4707.0	4099.2
	3515	4323	4723.5	4254.8
S	3666	4113	4340.3	4229.8
	3818	4128	4383.0	4356.6
	3668	3984	4420.5	4259.7
	2981	3765	4464.0	3770.8
	2728	4164	4512.8	3602.3
G	2407	3835	4016.3	3190.6
	3726	4015	4122.0	4196.5
	2934	3550	4192.5	3640.0
	2858	3449	4217.3	3593.0
	2476	3931	4256.3	3326.4
M	3843	4453	4815.0	4528.0
	3786	4589	4830.0	4491.5
	4255	5063	4920.8	4868.0
	3716	4259	4974.0	4491.1
	3505	4071	4989.0	4341.5
	4251	5036	5035.5	4905.7
T	4156	5136*	5463.0	4987.5
	4473	5382	5561.3	5255.1
	5734	5926*	5635.5	6207.2
	5593	6513	5678.3	6118.8
	3569	5537	5730.0	4651.2
O	4813	5071	5104.5	5342.8
	868	4634*	5128.5	2455.0
	1666	5165*	5193.0	3063.7
	5567	5743	5298.0	5964.9
	4406	5238	5349.0	5130.6
I	3497	5417	5823.8	4631.5
	2605	4287	5862.0	3990.2

* No closure was observed and closure pressure was assumed

Table 3-5: G-Function Leakoff Analysis Results for the Study Well

Leakoff Mechanism	1-Normal	2-PDL	3-Fracture Height Recession	4-Fracture Tip Extension
Totals	6	19	4	4
Percentage	18.2%	57.6%	12.1%	12.1%
Total Tests	33			

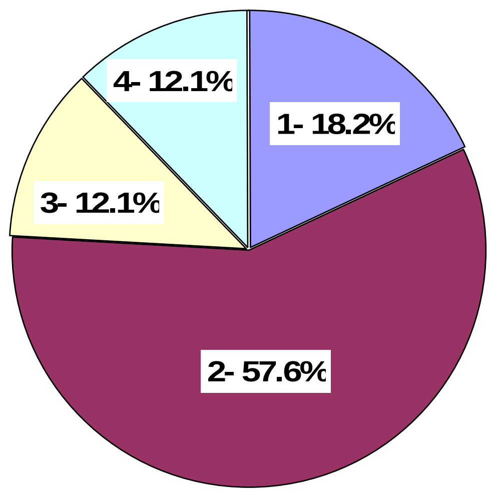

Figure 3-6: Figure showing a summary of the G-function leakoff analysis.

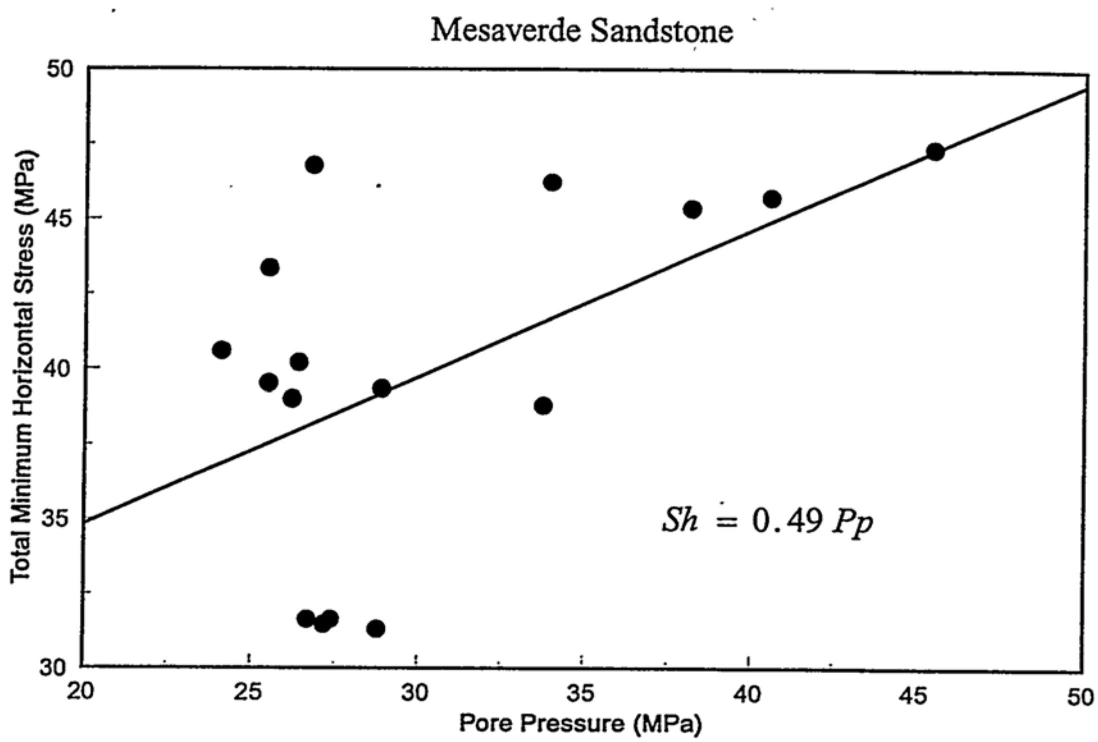

Figure 3-7: Plot of pore pressure versus total minimum horizontal stress for the Mesaverde sandstone in the Rulison Field, Colorado (From Warpinski and Teufel, 1989).

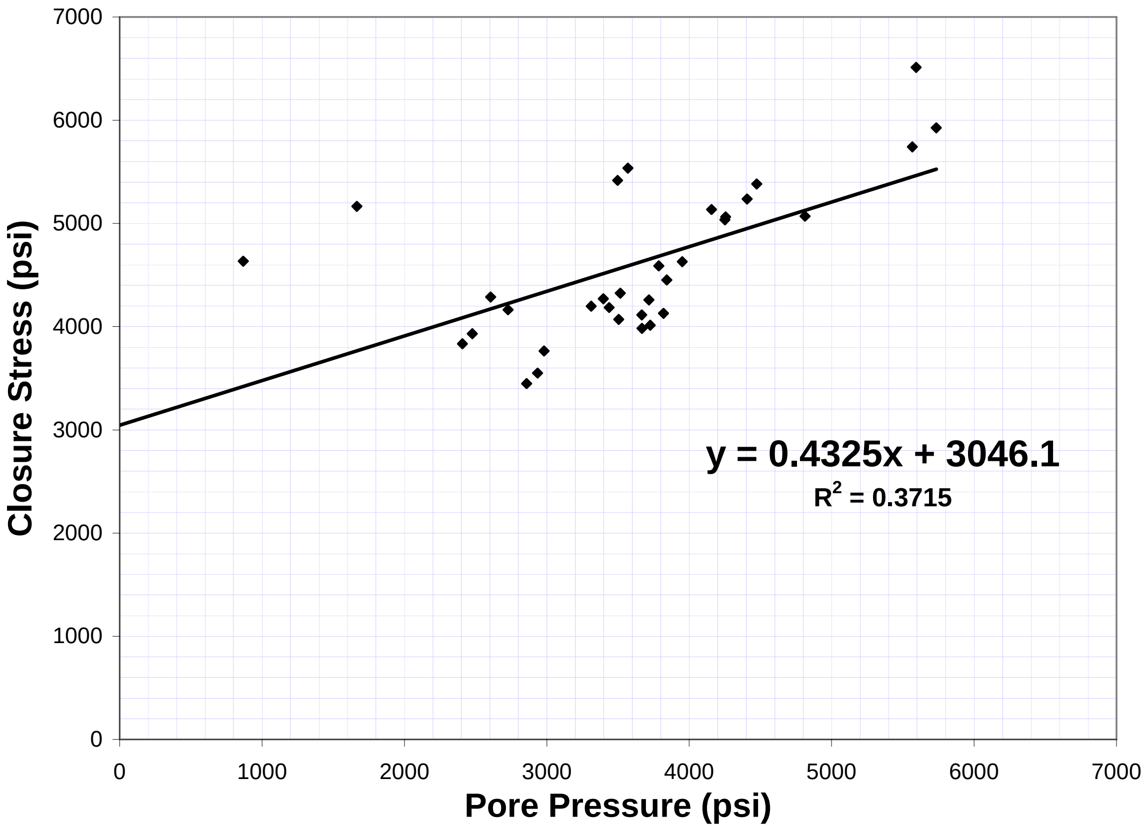

Figure 3-8: Plot of pore pressure versus total minimum horizontal stress for the Mesaverde sandstone in the study well.

3.3.4.2 Process Zone Stress

The process zone stress (PZS) is a directly measured pressure taken from the extension pressure and the closure pressure in a mini-fracture analysis. Because the PZS includes the effect of fluid lag, intact rock strength (tensile strength) and other non-linear stress dissipations around the tip of the fracture, it is not related to just a single property. The combined effects of all these mechanisms that restrict fracture growth can be directly measured, quantified and input into the fracture model as the PZS. For these experiments the PZS is obtained from log data using the bulk density in Equation 3-4 to get a value used initially to set up the grid.

$$PZS_{\rho} = r_1 \times \rho^2 + r_2 \qquad (3\text{-}4)$$

where, Constants r_1 = 200 and r_2 = 100

The log-derived grid values were then changed in order to find constants that fulfilled Equation 3-5 in the tested interval, and also give an approximately 300-1000 psi contrast between the weakest and strongest zones, see Table 3-6:

$$PZS = ISIP - P_{closure} \qquad (3\text{-}5)$$

The values calculated from Equation 3-5 and the values derived from logs were then subtracted and the final value, 600 psi, averaged from both wells, was used in the models as the grid value for all intervals to represent the process zone stress. PZS values are often used derived this way for input into the model, mainly due to the difficulties in trying to calculate an actual PZS for each grid.

Table 3-6: Process Zone Stress Values Derived from both Logs and Calculated to Give an Average Difference to be Input into the Study Well

Calculated			Log Value	PZS Diff. (Log-Calculated)
ISIP	Pc	PZS	PZS (ISIP-$P_{closure}$)	
Psi	psi	psi	Psi	Psi
4173	3835	338	100.3	238
4337	4015	322	260.5	62
4053	3550	503	138.4	365
4082	3449	633	107.0	526
4932	3931	1001	188.6	812
4334	4113	221	199.5	22
4345	4128	217	103.5	114
4842	3984	858	109.9	748
5004	3765	1239	107.1	1132
4956	4164	792	104.1	688
4883	4185	698	103.9	594
4867	4630	237	112.4	125
4839	4270	569	106.0	463
4853	4198	655	118.5	536
4921	4323	598	103.5	494
4931	4453	478	119.4	359
4830	4589	241	1031.3	-790
5233	5063	170	104.2	66
4862	4259	603	107.0	496
4720	4071	649	102.3	547
5678	5036	642	112.3	530
5705	5071	634	107.5	526
5923	4634	1289	100.1	1189
6388	5165	1223	107.1	1116
6384	5743	641	101.4	540
6125	5238	887	117.6	769
6304	5136	1168	105.7	1062
6148	5382	766	106.0	660
6823	5926	897	101.3	796
7026	6513	513	106.5	406
7315	5537	1778	104.7	1673
7142	5417	1725	180.0	1545
7272	4287	2985	126.4	2859
			Average Difference	644
			Comparison well Average Difference	558
			Value used in the Model	**600**

3.3.4.3 Total Stress

The total stress in GOHFER is calculated for each cell using the PR, YM, pore pressure, horizontal Biot's constant, vertical Biot's constant, tectonic strain and tectonic stress. The total fracture closure stress calculation is shown in Equation 3-6:

$$P_c(\sigma_{\min}) = \frac{\nu}{(1-\nu)}\left[D_{tv}\gamma_{ob} - \alpha_v\left(D_{tv}\gamma_p + P_{off}\right)\right] + \alpha_h\left(D_{tv}\gamma_p + P_{off}\right) + \varepsilon_x E + \sigma_t \qquad (3\text{-}6)$$

where,	P_c	=	Closure pressure, psi
	ν	=	Poisson's ratio
	D_{tv}	=	True vertical depth, feet
	γ_{ob}	=	Overburden stress gradient, psi/ft
	γ_p	=	Pore fluid gradient, psi/ft
	α_v	=	Vertical Biot's poroelastic constant
	α_h	=	Horizontal Biot's poroelastic constant
	P_{off}	=	Pore pressure offset, psi
	ε_x	=	Regional horizontal strain, microstrains
	E	=	Young's Modulus, million psi
	σ_t	=	Regional horizontal tectonic stress

The application of Biot's constant is a point of discussion within the industry at this point in time. For this work the general method of stress matching was used. In these experiments G-Function and after-closure analysis are used to investigate pressure-dependent leakoff, as well as to estimate pore pressure and permeability. Many processes affect the fracture closure pressure including: fluid leakoff into the formation, formation heterogeneities, fracture growth geometry, and fracture growth after shut-in. Therefore, where such analysis was not possible, the values were extrapolated to give an initial value for input into the model and then refined based upon simulator results.

3.3.5 Permeability Correlation

A number of methods are available for estimating pore pressure and permeability in both openhole and cased-hole environments. In tight gas reservoirs many methods are ineffective or unpractical where there may be up to fifty individual lenticular reservoir sands to test. Mini-fracs are an alternative test method where a small hydraulic fracture is carried out and the pressure transient fall-off data is monitored and analyzed. Several methods are available for analyzing the data looking at both before- and after-closure data. Craig and Brown (1999) illustrated the use of before closure analysis to evaluate the Grand Valley Field in the Piceance basin. After-closure analysis is preferred, but due to the time required to achieve pseudolinear or pseudoradial flow it is not always possible.

The Gas Research Institute's Tight Gas Sands program (Schroeder, 1997) developed relative permeability relationships for tight gas formations from extensive core analysis of the Mesaverde sands during the Multi-well Experiment. Ward and Morrow (1987) provided a relative permeability relationship for tight gas sandstones, shown graphically in Figure A-3 (Appendix A).

Jones and Owens (1980) published an empirical correlation for Mesaverde core data (Equation 3-7):

$$k_g = ak_{air}{}^{b} \tag{3-7}$$

where k_g = Gas permeability

k_{air} = Core routine air permeability

(for moderate stress $a = {}^{1}/_{7.5}$ and $b = 1.9$)

Craig et al (2000) used their correlation and the data of Ward and Morrow to develop the following correlation for Mesaverde core:

$$(k_w)_{abs} = 19.136(k_\infty)^{1.8589} \tag{3.8}$$

For permeability analysis, Perkins-Kern-Norgren (PKN) fracture geometry is assumed to be created during the diagnostic injection, which is supported by work undertaken at the M-site (Warpinski and Teufel, 1989). Fracture height is estimated based on the gross sand thickness indicated by the openhole log, as detailed in Table 3-1. For this experiment the permeability correlation, based on the empirical correlation of Jones and Owens (1980) and detailed in the GOHFER user manual, was used. The correlation is outlined in Equation 3-9 and the development of K_1 and K_2 values is shown in Table 3-7:

$$k = K_1 \times \phi^{K_2} \tag{3-9}$$

where,	k	=	Permeability, md
	K_1	=	Constant, varying from 50 for tight reservoirs to 300 for moderate reservoirs
	K_2	=	Constant usually 1-3.

The graph of permeability results and the permeability correlation derived from these results and used for the model is shown in Figure 3-9. As can be seen in the graph

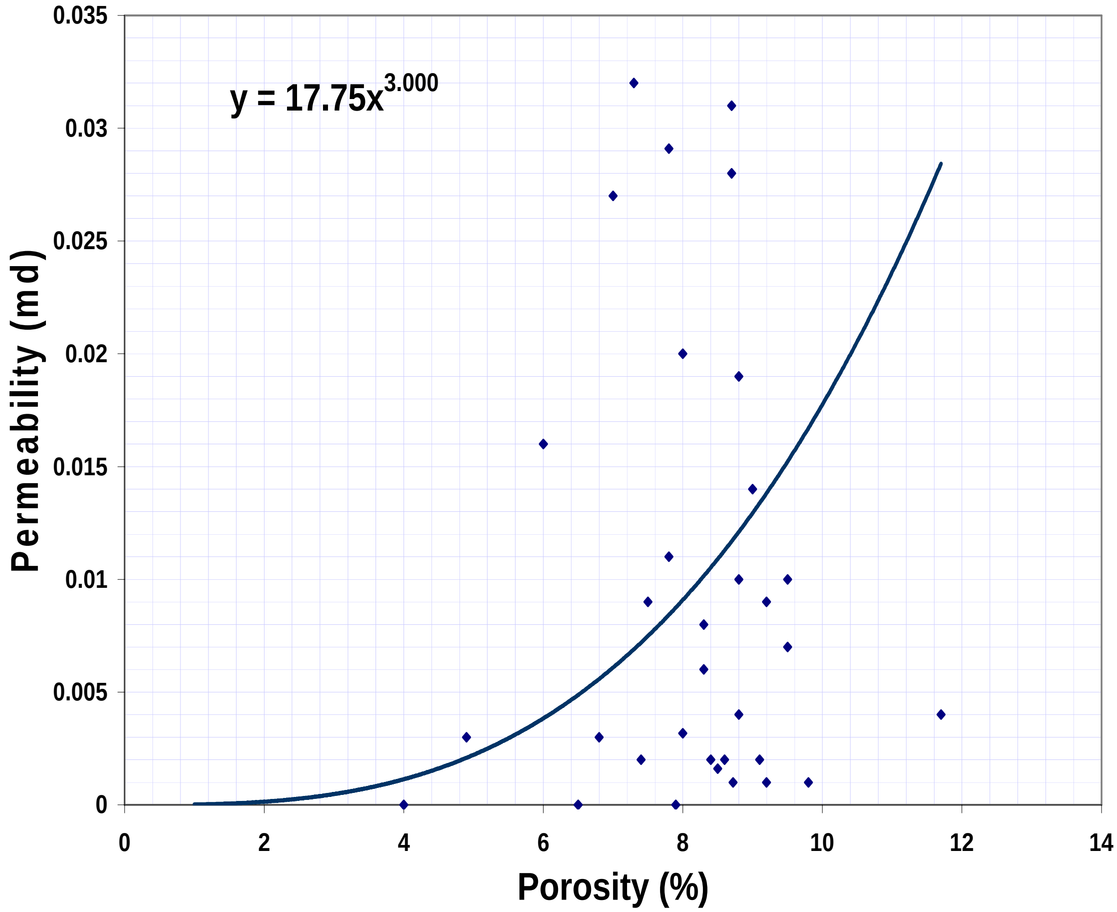

Figure 3-9: Graph showing the actual data points and the final correlation graph used in the HF model. The actual data used for the analysis is shown in Table 3-7.

Table 3-7: G-Function After Closure Analysis Results and the Porosity Derived Values Used to Derive the Permeability Correlation Values for Constants K_1 and K_2

Completion Interval	Porosity	k_g	k_g Calc	k_g Difference
A	9.1	0.002	0.013	0.011
	7.9	0.000	0.009	0.009
	8.3	0.008	0.010	0.002
	8.0	0.020	0.009	-0.011
	8.8	0.004	0.012	0.008
S	6.5	0.000	0.005	0.005
	8.5	0.002	0.011	0.009
	8.8	0.010	0.012	0.002
	8.0	0.003	0.009	0.006
	8.4	0.002	0.011	0.009
G	9.5	0.007	0.015	0.008
	4.0	0.737	0.001	Not used in correlation
	6.8	0.003	0.006	0.003
	8.3	0.006	0.010	0.004
	6.0	0.016	0.004	-0.012
M	7.0	0.027	0.006	-0.021
	7.8	0.029	0.008	-0.021
	8.7	0.031	0.012	-0.019
	7.8	0.011	0.008	-0.003
	9.2	0.009	0.014	0.005
	7.5	0.009	0.007	-0.002
T	9.5	0.010	0.015	0.005
	8.8	0.019	0.012	-0.007
	9.8	0.001	0.017	0.016
	8.6	0.002	0.011	0.009
	9.2	0.001	0.014	0.013
O	9.0	0.014	0.013	-0.001
	11.7	0.004	0.028	0.024
	8.7	0.001	0.012	0.011
	8.7	0.028	0.012	-0.016
	7.3	0.032	0.007	-0.025
I	7.4	0.002	0.007	0.005
	4.9	0.003	0.002	-0.001
			Σ Differences	0.026
			k_1	**17.75**
			k_2	**3**

the correlation, whilst adequate for modeling purposes, clearly needs further work to better represent these heterogeneous reservoirs.

For these experiments the total minimum horizontal stress, and pore pressure as a function of depth for the reservoir, are plotted in Figure 3-10. The total vertical and horizontal stresses and pore pressure were found to increase in a generally linear trend with depth. The total horizontal stress gradient is 0.84 psi/ft and the pore pressure gradient is 0.52 psi/ft. Similar values were also obtained for the comparison well. Of interest is that if an overpressure of 900 psi is applied to the closure gradient trend line (intercept +900 instead of -887) the linear trend is approximately the same that for the pore pressure. This value was used in the model for the virgin reservoir pore pressure offset.

This chapter has outlined a general methodology (as defined in the GOHFER user manual) that is typically employed to generate input data for the model grids. This general methodology is used to define the stress model used by GOHFER. If the computed stress is above or below the measured closure pressure differences are attributed to tectonic strain. The methodology is summarized in Figure 3-3 and uses what practitioners consider are required inputs, necessary to produce an accurate detailed hydraulic fracture model. The model is run with the input grid data and necessary changes made to match available data, prior to performing sensitivity analysis. The input matching and sensitivity analyses are outlined in the following section, Chapter 4.

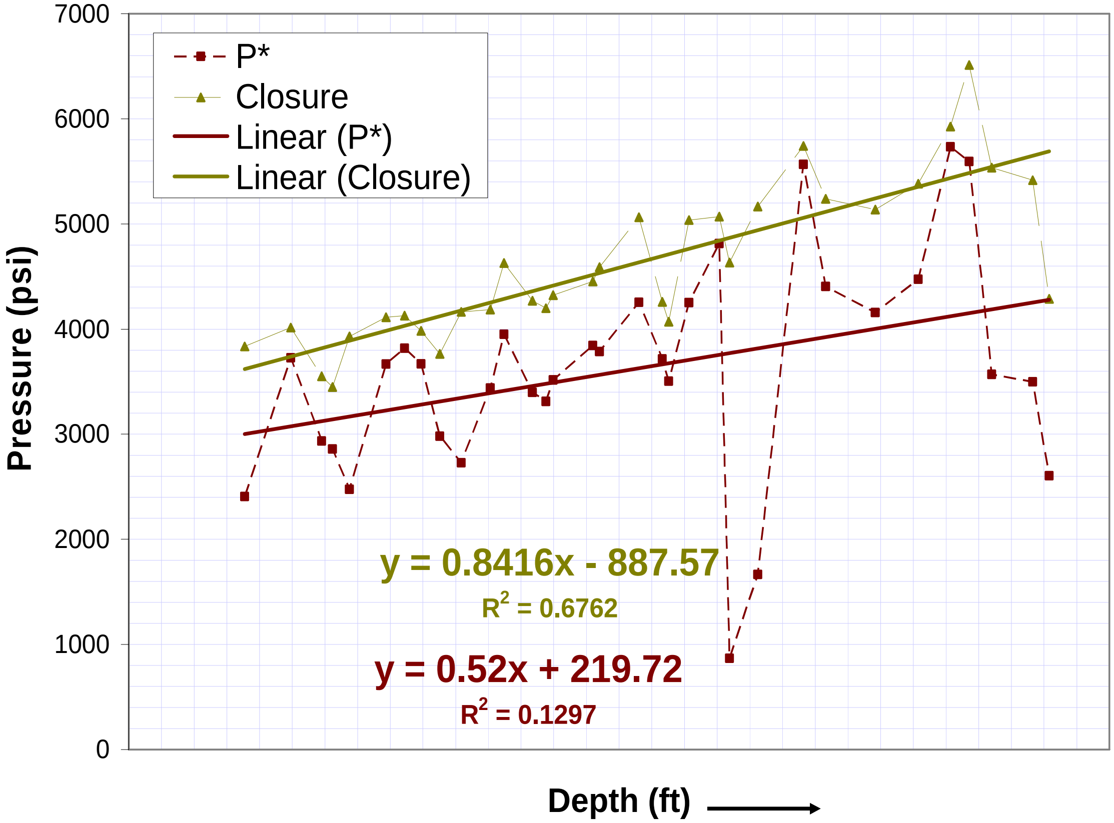

Figure 3-10: Plot of the total minimum horizontal stress and pore pressure changes with increasing depth.

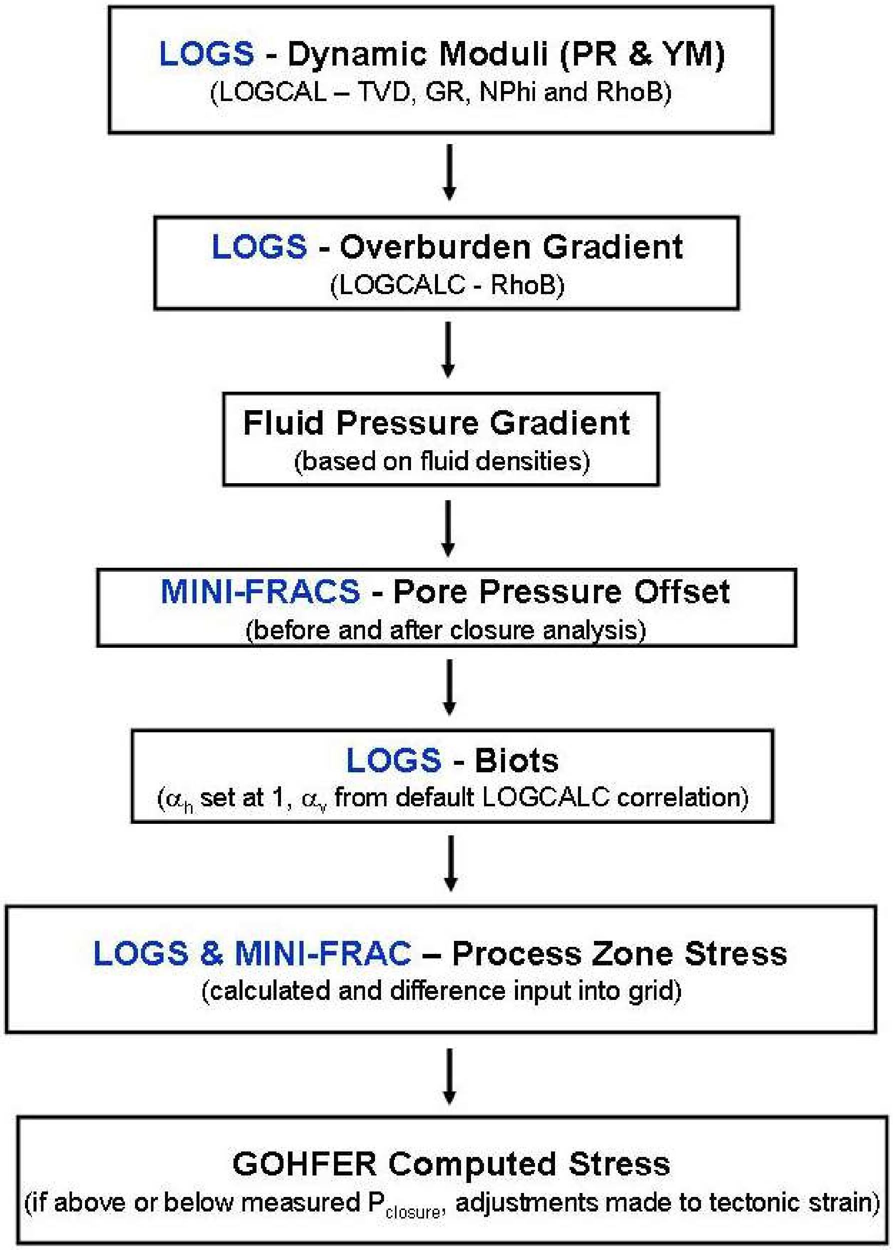

Figure 3-3: Workflow diagram showing the methodology recommended for creating an accurate a hydraulic fracture model.

CHAPTER 4
HYDRAULIC FRACTURE SIMULATION MODEL RESULTS AND INPUT SENSITIVITY ANALYSES

This chapter describes the matching of the individual hydraulic fracture simulations to the actual data recorded during the treatments. This chapter reports the specific details of how the model inputs were matched to microseismic measurements. The process of modifying advanced parameters in the hydraulic fracture simulator to match wellbore events with the measured pressure data is described. Sensitivity analysis of various inputs that reflect what is considered to be critical information, by hydraulic fracture (HF) practitioners, is also presented.

4.1 Matching the Model using Advanced Parameters: Pressure-Dependent Modulus Stiffness Factor, Pressure-Dependent Leak-off Coefficient, Relative Permeability Ratio and Transverse Storage Coefficient

The ability to acquire as much input data as possible for a hydraulic fracture model minimizes the need for assumptions which may be unreasonable. When significant data, specific to that treatment, is available, the simulator output data can be matched to actual results by using advanced parameters within the software. The advanced parameters make it more likely to match phenomena, such as natural fracture clusters or changing lateral reservoir parameters, that cannot be easily detected using present data acquisition techniques. Often input data is not available or unrealistic assumptions are made, due to time and economic constraints, where few analytical tests are available, the input values from single tests are often used for the whole interval.

As described in Chapter 3, the development of grid values allows the stress profile of the well to be calculated, and then basic reservoir parameters (fluid viscosity, bottomhole temperature, total compressibility, produced water/brine gradient, depth below sea level, overburden gradient, and pore pressure gradient) can be entered from field measurements. However, the problem for any hydraulic fracture simulation is trying to match the simulator to actual field data. The matching process usually involves manipulation of the model by entering input values for the advanced reservoir parameters. Advanced parameters include: pressure-dependent modulus stiffness factor (MSF), pressure-dependent leak-off coefficient (PDL), relative permeability ratio and transverse storage coefficient (TSC).

MSF is used to determine the magnitude of the Young's modulus change created when opening natural fractures. The value is used in an exponential equation such that as the pressure exceeds the fissure opening pressure, the modulus will change exponentially. Normally, values for the MSF are between 0 and 0.01, with positive values causing the apparent Young's modulus to increase when opening the fractures. For the matched subject well model, a value of 0.001 is used for all intervals (see Table 4-1).

PDL is used to determine the magnitude of leak-off change created by opening the natural fractures. This value is usually determined from mini-frac analysis of a single reservoir interval. For this study, individual reservoir sands were tested, and the values determined were used to give upper and lower limits for this input in each interval. The values are used in an exponential equation, such that as the pressure exceeds the fissure opening pressure, the leak-off will change exponentially. Typical values are between 0 and 0.01, where a value of zero indicates no PDL and only matrix behavior, and a negative value indicates open natural fractures. For this study, typical values were in the 0.0025 to 0.0040 range (see Table 4-1).

A relative permeability ratio is normally used to account for the change in permeability between the reservoir fluids and the invading fluid (frac fluid). For this model, each of the sands had previously been tested using mini-fracs and a value for permeability of the invading fluid obtained from both before-closure (modified Mayerhofer technique; Craig and Brown, 1999) and after-closure analysis (pressure transient fall-off analysis). The data was re-analyzed as part of the quality control process, but in general the values supplied by the service company experts were used without modification.

TSC is a hard to determine parameter that defines how much fluid is moved from the main planar hydraulic fracture to a presumed system of natural fractures, transverse to the created main fracture. Changing this parameter allows both frac fluid and proppant to be moved into 'storage' and changes are used to significantly reduce fracture half-lengths without affecting the net pressure. This value is changed when trying to match post frac analytical results of fracture half-length, in this case the results of microseismic and tiltmeter analysis. The value of TSC determines the amount of fluid lost during the treatment and is highly dependent upon the net pressure of the system. For the matching process, this value was kept within a reasonable range and typically values of 0.002 to 0.004 were used (see Table 4-1).

Table 4-1: Advanced Reservoir Parameters Values used to Match the Simulator Model to the Real Data.

Completion Interval	**MSF**	**PDL**	**TSC**
	1/psi	**1/psi**	
T	0.001	0.0030	0.002
O	0.001	0.0025	0.004
M	0.001	0.0020	0.003
A	0.001	0.0040	0.004
S	0.001	0.0025	0.003
G	0.001	0.0025	0.003

4.2 Model Match Results

As discussed in Section 2.6, historically hydraulic fracture treatments have been analyzed by matching the net surface pressure recorded during the treatment to the idealized net surface pressure data from the model and then the general growth characteristics are determined. This modeling process offers non-unique solutions and can provide a number of options to match the pressure data. Unfortunately, pressure matching generally cannot answer the important questions in complex reservoirs, i.e. which intervals were treated and what was the final fracture geometry? The process of developing relevant models has been greatly improved by the use of techniques that are able to map fracture growth and provide the physical dimensions (height, half-length and width) of the fracture itself. These techniques are detailed in Section 2.5. For this study, microseismic data was used to constrain the model. Using both pressure and physical dimension data, the model should theoretically result in a more applicable simulation hydraulic fracture model of a Piceance basin well. In common with typical hydraulic fracture treatments, bottomhole data was not available on the subject well and the net pressure is the data recorded at surface and extrapolated to bottomhole in the simulator. The net surface pressure, pumping rate and proppant concentration of the actual hydraulic fracture treatment are all input directly into the simulator and are the driving force for the model.

A major assumption for the simulator data matching is that changes in pressure data need to be modeled as occurring in or near the wellbore. Generally applied scenarios for modeling near wellbore pressure changes are as follows: gradual increases - attributed to lateral lithologic changes; rapid increases - tip screen-out effects; and, gradual decreases (linear trend) with constant injection rate - perforation erosion. In the following Sections 4.2.1 to 4.2.6, the matched simulator models are described together with a summary of the matching process. In general, the models were found to adequately describe the early-time pressure responses without major modifications, but some problems were encountered in matching the late-time data. Typically, late-time pressures dropped in the simulation, following the decreasing pumping rate and proppant concentration injection trends. However, the actual net surface pressure data often 'peaked' with sudden rapid increases and then stayed at a high pressure, despite the reduced pumping rates and proppant concentrations. To account for these effects, the model output net surface pressure was matched by modifying the perforation ratio, i.e. the percentage of perforations that stay open from that time onwards. In the simulator, the number of perforations open at any given time during the treatment is controlled by an input titled the 'perforation factor'. A list of the perforation factors and the times that they were implemented during the interval models are listed in Table 4-2 and discussed further in the following sections. Interestingly, the initial log-derived grid parameters seemed to give adequate height containment in the fractured intervals. Finally, the pore pressure offset and the perforation numbers were used to modify the zones fractured to give a fracture distribution that matched the microseismic analysis.

Table 4-2: A List of the Perforation Factor Changes used in the Matched Model Intervals

Completion Interval	**Perforation Changes**	
	Perforation Factor	**Time Instituted (minutes)**
A	0.75	39.82
S	NA	NA
G	0.125	86.9
M	NA	NA
T	0.17	81.3
	0.16	84.38
O	0.9	44.05
	0.65	45.3
	0.5	52.12

As discussed in the following sections, modeling fracture distributions to correspond to the depletion seen in the microseismic data was the most difficult part of simulator matching to actual field data. Often fractures grew outside the 2000 ft grid, especially in thin zones or 'stringers'. Stringers are considered to commonly occur during real frac treatments and they rapidly grow beyond what are regarded as reasonable lengths for the detection of microseismic events. Stringer growth was ignored during the microseismic matching process in order to limit the use of unreasonable advanced parameter values in the simulator to force a match to these phenomena.

4.2.1 Interval T

The net surface pressure, pumping rate and proppant concentration of the actual treatment and matched data for Interval T, are shown in Figure 4.1. As can be seen in the early-time model output, pressure data matches the actual treatment data. However, after 81 minutes the simulator pressure decreases to follow the injected rate and concentration parameters, while the actual measured data remained high. To account for this discrepancy, the proppant concentration in the wellbore was increased sharply by simulating a proppant pack-off in the wellbore, due to a decreased perforation factor. This is reasonable to do as rapid pressure increases are modeled as screenouts and when this occurs a reduced number of perforations are open to accept proppant fluid. The decrease in the perforation factor increases the modeled net surface pressure to match the real treatment net surface pressure data. Matching the fracture geometry to the microseismic data proved difficult. Initial attempts indicated that fracture growth occurred into the lower zones first and then grew upwards before growing into the upper two zones, T1 and T2 (Figure 4-2). Microseismic data indicated growth occurred in all five zones, but mainly in the upper Zones T1 and T2. In order to simulate the actual growth pattern, the pore pressure offset and perforation numbers were manipulated to get the fracture to match the microseismic distribution (see Figures 4-2 to 4-6). Using this methodology, a final match was obtained using the values shown in Table 4-2. Most of the perforations were 'screened out' towards the end of the treatment (after 81 minutes) and were probably all closed at the end of the treatment. The simulator was not able to perform calculations for a perforation ratio of less than 0.16, for the last section of the treatment (after 84 minutes). Below the threshold of 0.16 the simulator assumes that no significant fracturing will occur (probably due to screen-outs) and calculations are no longer performed. Ideally the perforations would be closed in the lower zones and left open in the upper zones. However, the perforation factor is applied across all the zones which could explain this problem in the simulator. To accommodate the 'shutting-off' of lower perforations during the late-time treatment, the perforation distribution was changed in the simulator. Almost 75 % of the perforations were placed in the upper two zones, T1 and T2, in order to adequately stimulate these two zones and match the microseismic data.

The following simulator outputs are shown in Figures 4-2 to 4-5: net pressure distribution (Figure 4-2), fracture width (Figure 4-3), proppant concentration (Figure 4-4) and fracture conductivity (Figure 4-5). As can be seen in Figures 4-2 and 4-3, the fracture actually grows beyond the 2000 ft grid size in Zones T1 and T2. Figure 4-2 shows that the net pressure was evenly distributed throughout the interval but the fracture width was greatest in Zone T2 (Figure 4-3), where growth had occurred out of interval into the shale layer (width of 0.177 inches).The proppant concentration (see Figure 4-4) shows that the proppant had fallen to the bottom of the fractures in Zones T1 and T5 but had increased upwards in Zone T2. This suggests that the T2 proppant had built-up in the near wellbore area and grown into the upper bounding shale layers. Microseismic analysis shows that significant microseisms (see Figure 4-6) originated in the area of the out-of-zone growth.

Table 4-3: Perforation and Pore Pressure Offset Values from Mini-frac Analysis in the Matched Model

Completion Interval	Zone	Number of Perfs Shot	% of Completion Interval Perforations	GOHFER-Calculated Open Perforations	% of Interval Total Perforations Open	Mini-frac Pore Pressure Offset (psi)	GOHFER Pore Pressure Offset (psi)
A	**A1**	1	11%	12	34%	750	-500
	A2	1	11%	9	26%	1200	-300
	A3	2	22%	0	0%	650	200
	A4	3	33%	10	29%	550	-300
	A5	2	22%	4	11%	750	0
Total		*9*		*35*			
S	**S1**	1	11%	1	7%	1100	1100
	S2	1	11%	1	7%	1200	1000
	S3	2	22%	1	7%	1000	1000
	S4	3	33%	4	27%	400	350
	S5	2	22%	8	53%	100	0
Total		*9*		*15*			
G	**G1**	1	11%	2	14%	100	300
	G2	1	11%	2	14%	1300	300
	G3	2	22%	3	21%	500	100
	G4	2	22%	3	21%	400	100
	G5	3	33%	4	29%	0	0
Total		*9*		*14*			
M	**M1**	2	20%	8	15%	1000	-100
	M2	1	10%	8	15%	1000	-100
	M3	2	20%	6	11%	1300	300
	M4	2	20%	14	26%	800	-100
	M5	2	20%	14	26%	600	-100
	M6	1	10%	3	6%	1300	500
Total		*10*		*53*			
T	**T1**	2	25%	3	32%	1000	200
	T2	2	25%	4	42%	1200	100
	T3	1	13%	1	11%	2500	900
	T4	1	13%	1	11%	2300	900
	T5	2	25%	1	5%	200	300
Total		*8*		*10*			
O	**O1**	1	13%	1	6%	1800	900
	O2	1	13%	3	33%	-2000	500
	O3	2	25%	1	11%	-1300	500
	O4	2	25%	4	44%	2500	0
	O5	2	25%	1	6%	1300	500
Total		*8*		*9*			

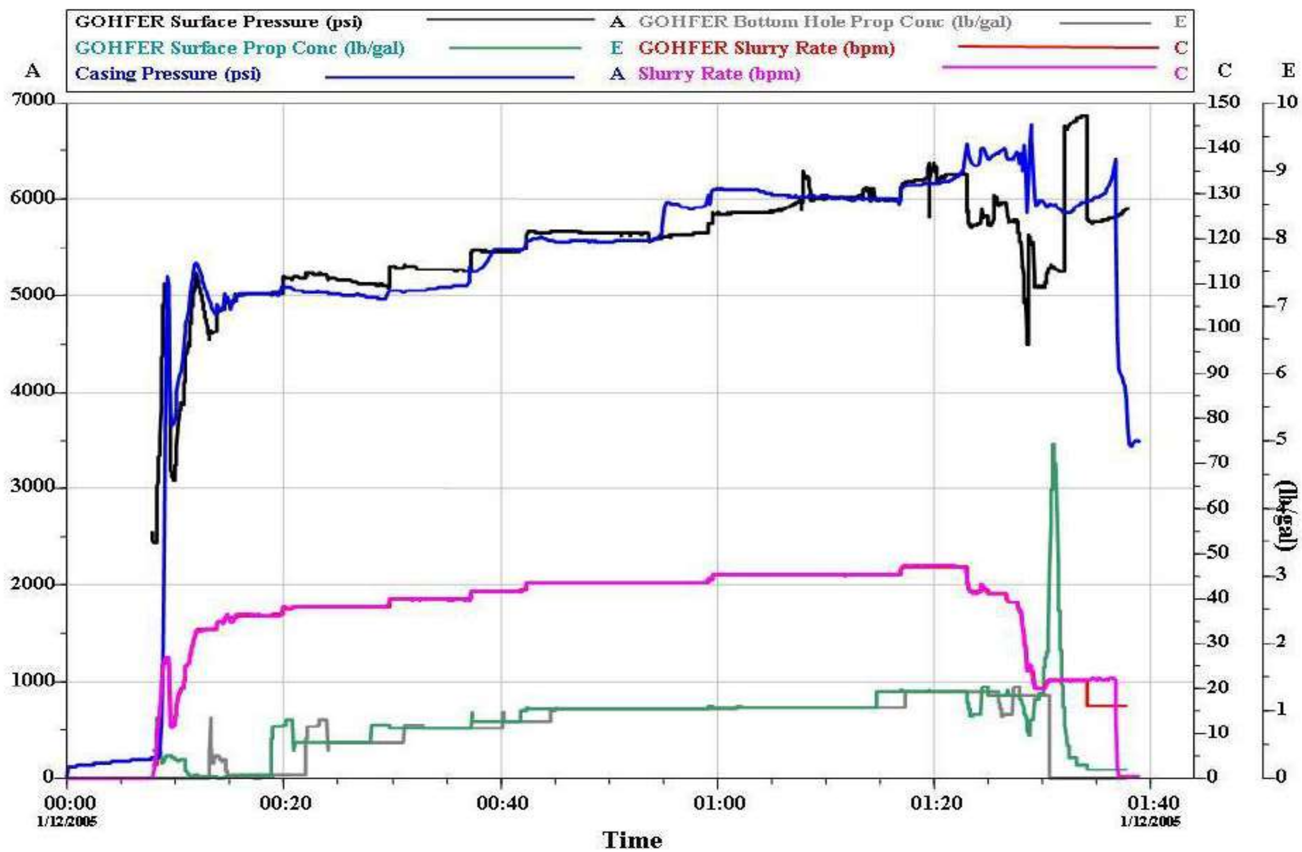

Figure 4-1: Graph showing the matched GOHFER net surface pressure (black) compared to the measured net surface pressure (blue) recorded during the actual treatment of Interval T.

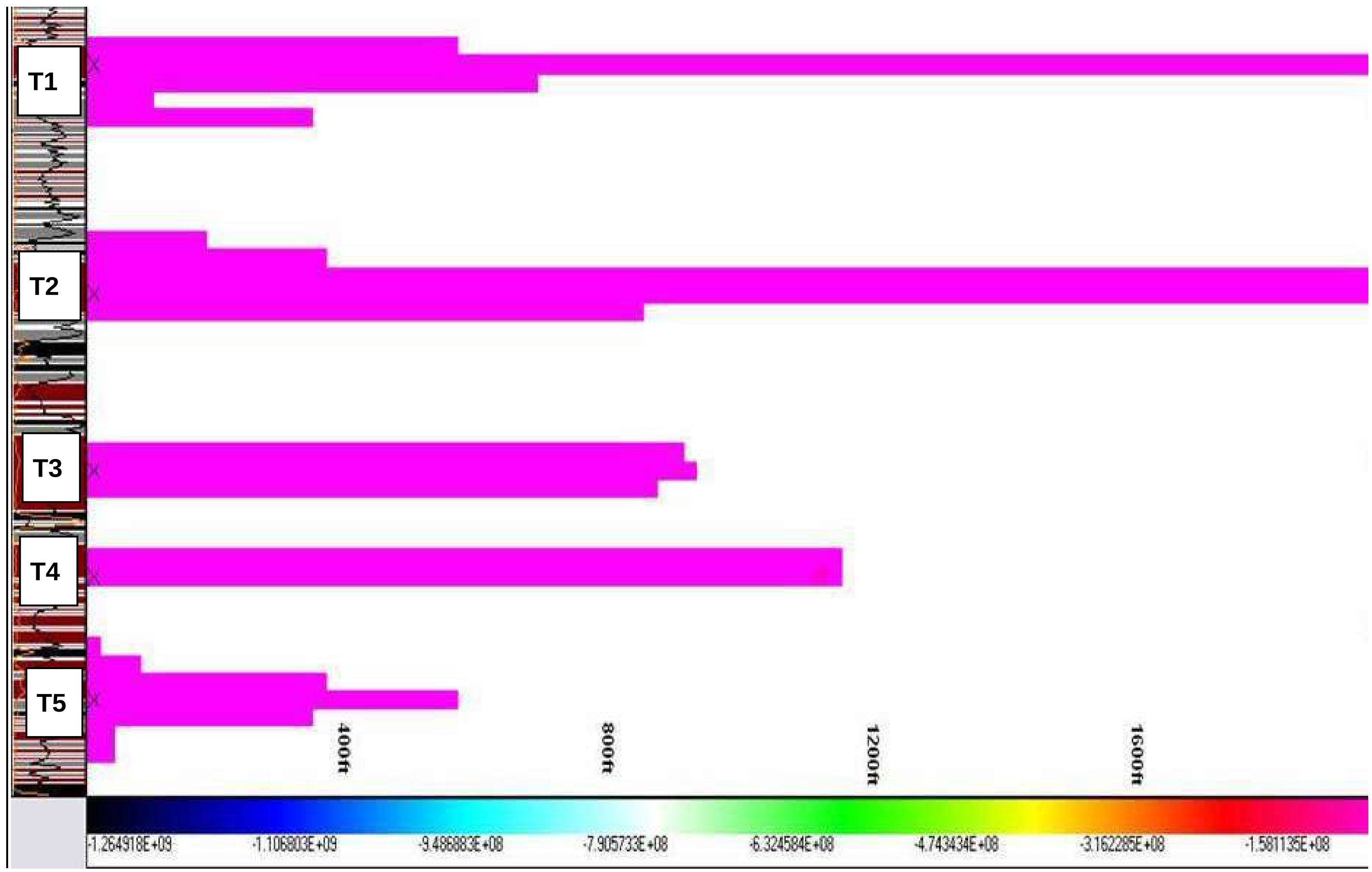

Figure 4-2: GOHFER net pressure (psi) output grid for the Interval T final simulator run.

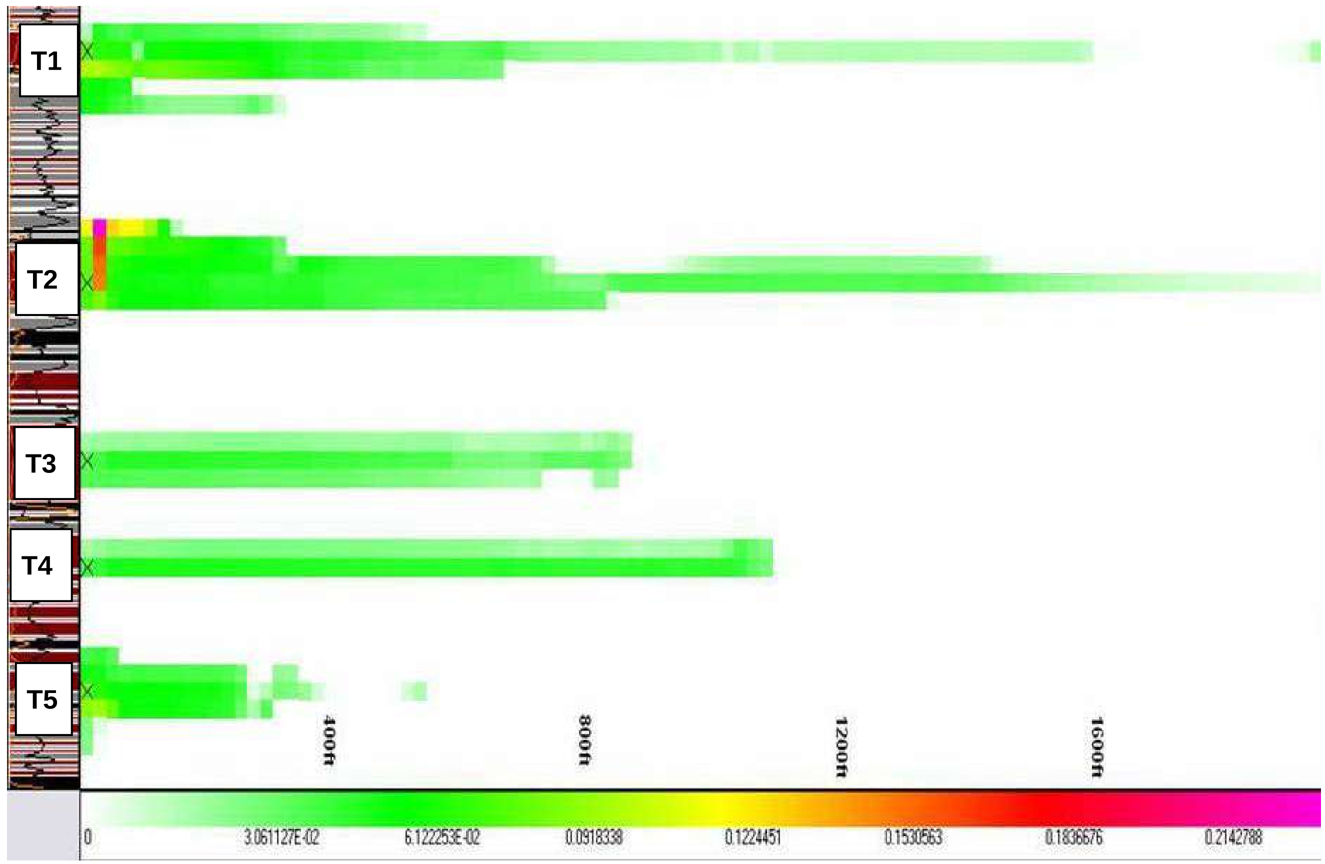

Figure 4-3: GOHFER fracture width (inches) output grid for the Interval T final simulator run.

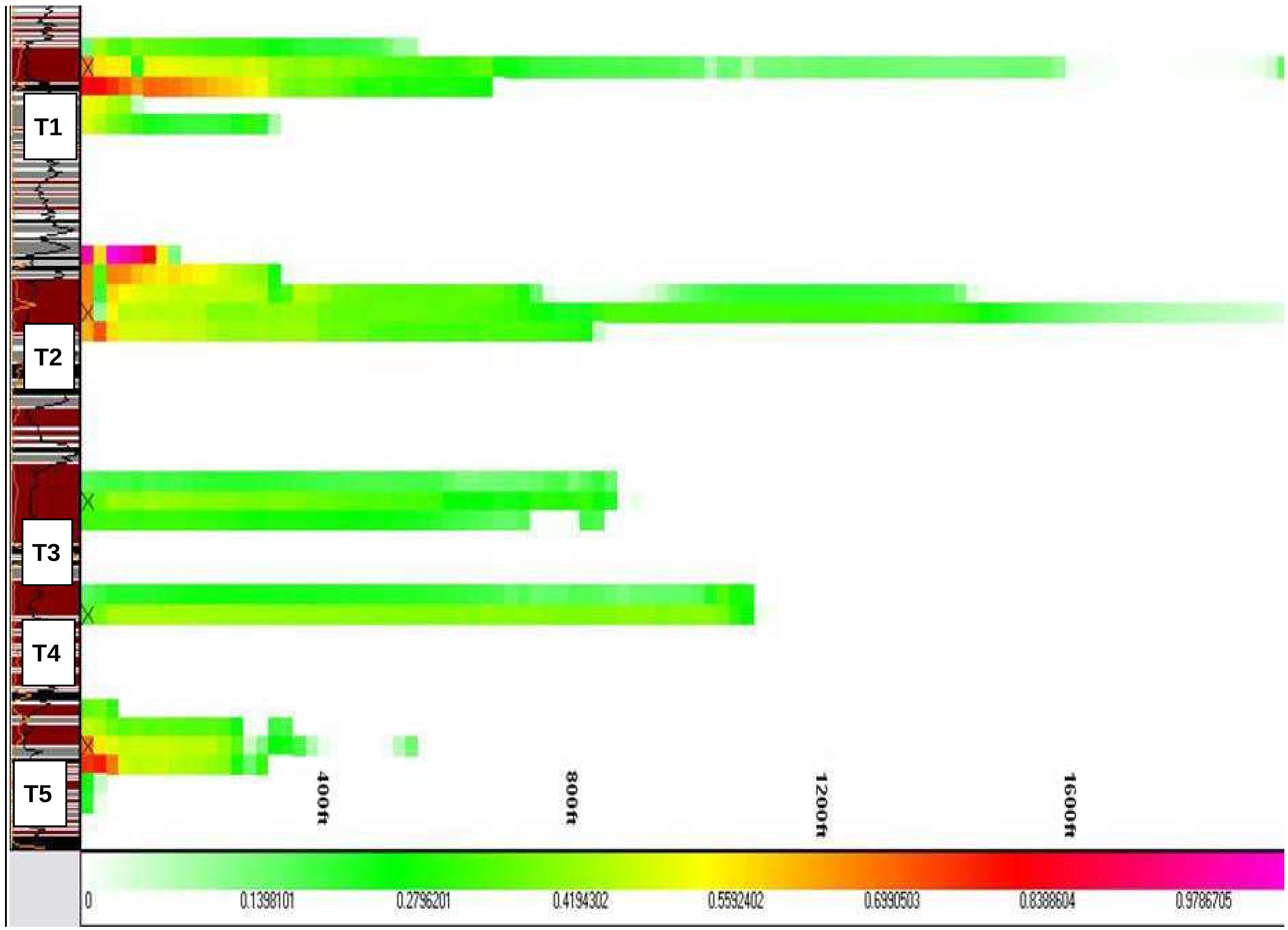

Figure 4-4: GOHFER proppant concentration (lb/ft^2) output grid for the Interval T final simulator run.

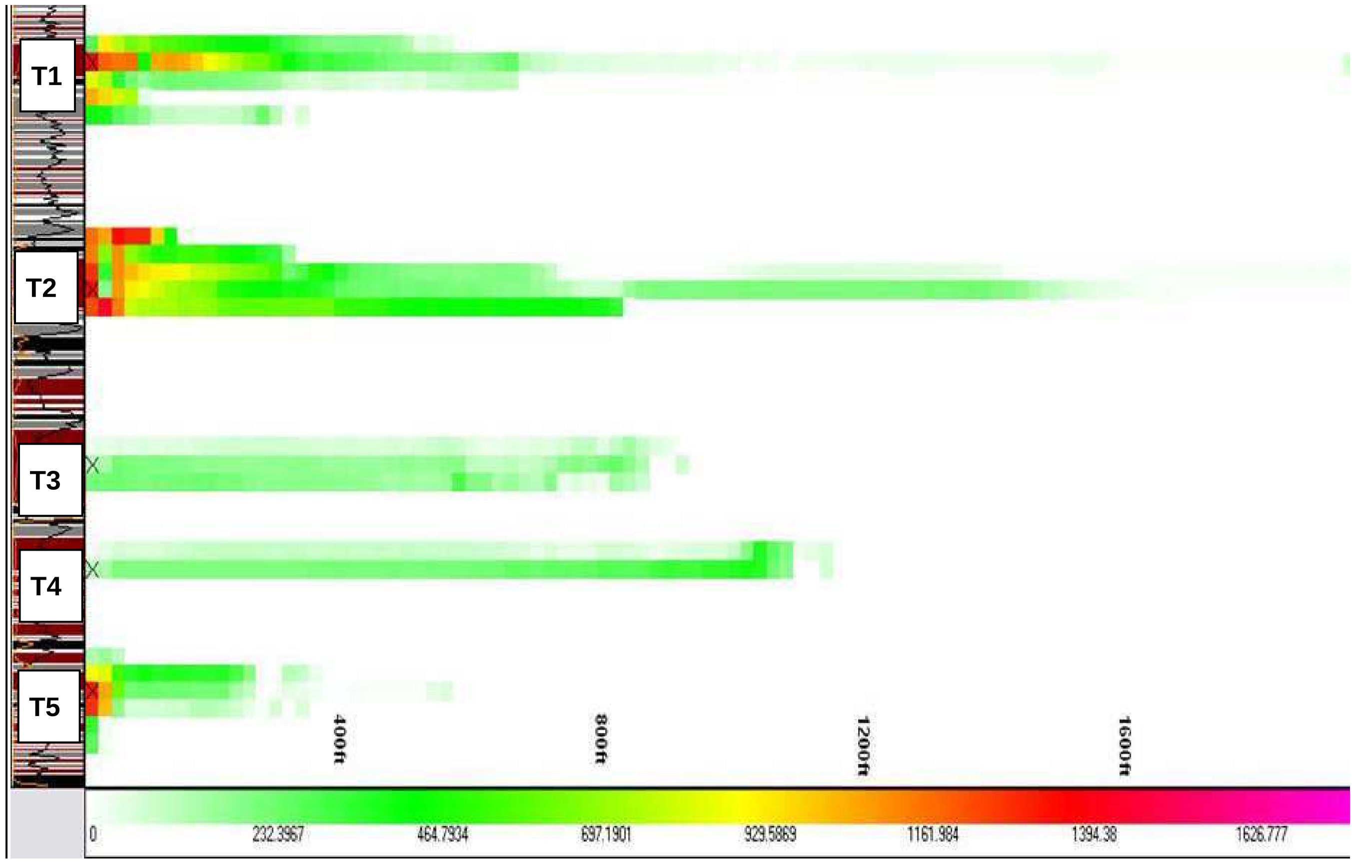

Figure 4-5: GOHFER conductivity (md-ft) output grid for the Interval T final simulator run.

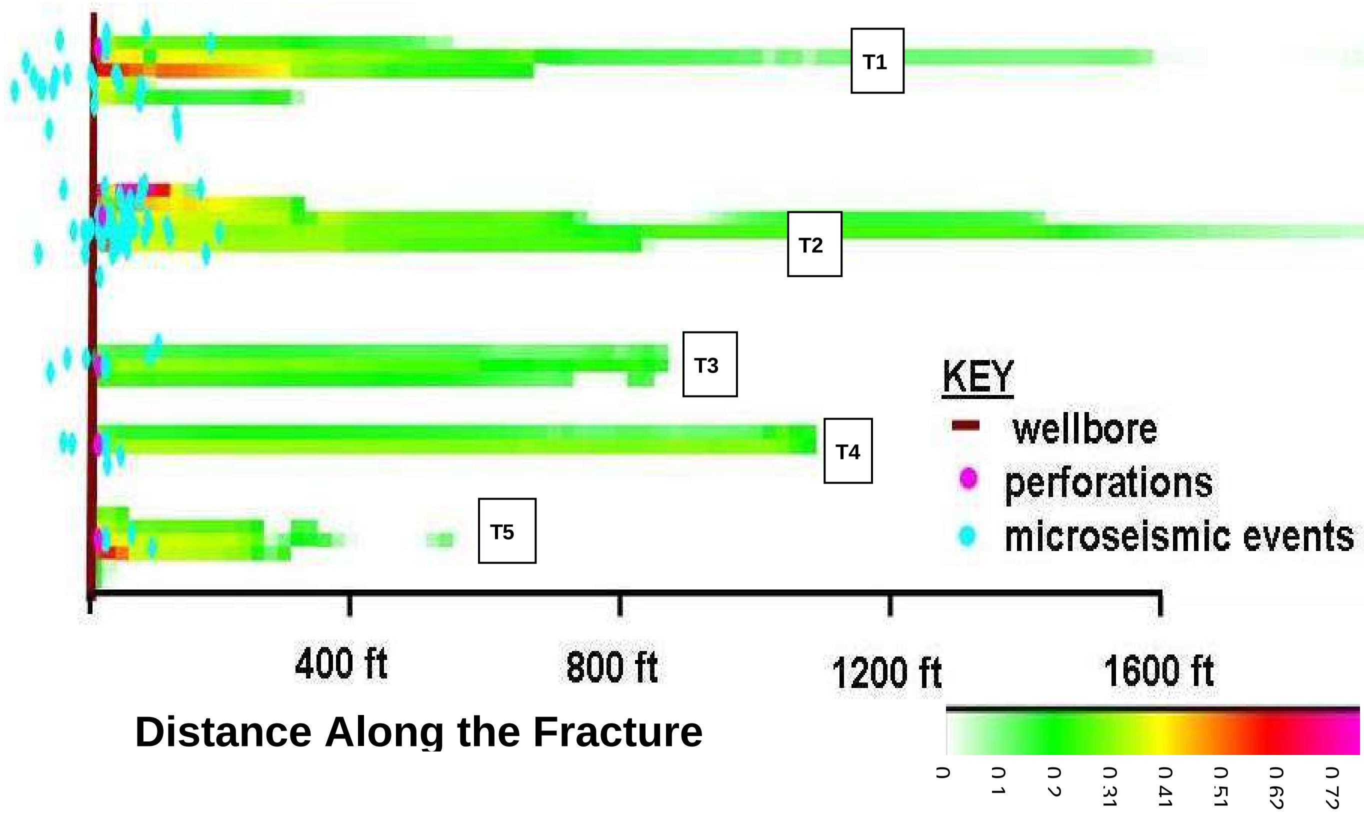

Figure 4-6: The microseismic results are overlain with the proppant concentration (lb/ft^2) output grid of the matched model. During the initial runs, the fracture went mostly into the lower zones. As can be seen from the microseismic, most of the fracture went into the upper two zones, T1 and T2.

4.2.2 Interval 0

The net surface pressure, pumping rate and proppant concentration of the actual treatment and matched data for Interval O are shown in Figure 4.7. The early-time model pressure data could only be matched to the actual treatment data by having no fluid in the wellbore at the start of the treatment. This meant that a full wellbore of fluid had leaked off prior to starting the treatment, either into an open fracture network or into a depleted zone within the interval. The mini-frac analysis indicated the possible existence of open fractures, as there was no closure in two of the zones tested (O2 and O3). In common with the majority of the other intervals treatments at the end of the initial simulator runs, the model output net surface pressure decreased (after 44 minutes), while the actual treatment gave a high net surface pressure reading. In order to match the high pressures towards the middle- and late-time portions of the recorded data, 10% of the perforations were closed after 44 minutes, 35 % after 45 minutes and 50% after 52 minutes. However, the late-time data could not be properly matched, without causing significant screen-out of proppant and unreasonably high increases in the net surface pressure.

From the treatment data, it is clear that there were problems encountered during the actual stimulation, as proppant concentrations peaked after 40 minutes and both the rate and proppant concentration were then reduced five minutes later. Matching the fracture geometry to the microseismic data proved difficult as the original interval perforations numbers resulted in fracture growth mainly in the lower two zones, O4 and O5. The perforation numbers and the pore pressure offset were modified, see Table 4-3, to model the fracture growth into the upper zones (O1 and O2) and the associated containment indicated in the microseismic distribution (see Figures 4-8 to 4-12).

The following simulator outputs are shown in Figures 4-8 to 4-10: net pressure distribution (Figure 4-8), fracture width (Figure 4-9), proppant concentration (Figure 4-10) and fracture conductivity (Figure 4-11). The simulator indicated that the fracture width was evenly distributed throughout the interval, apart from a high value in the coal

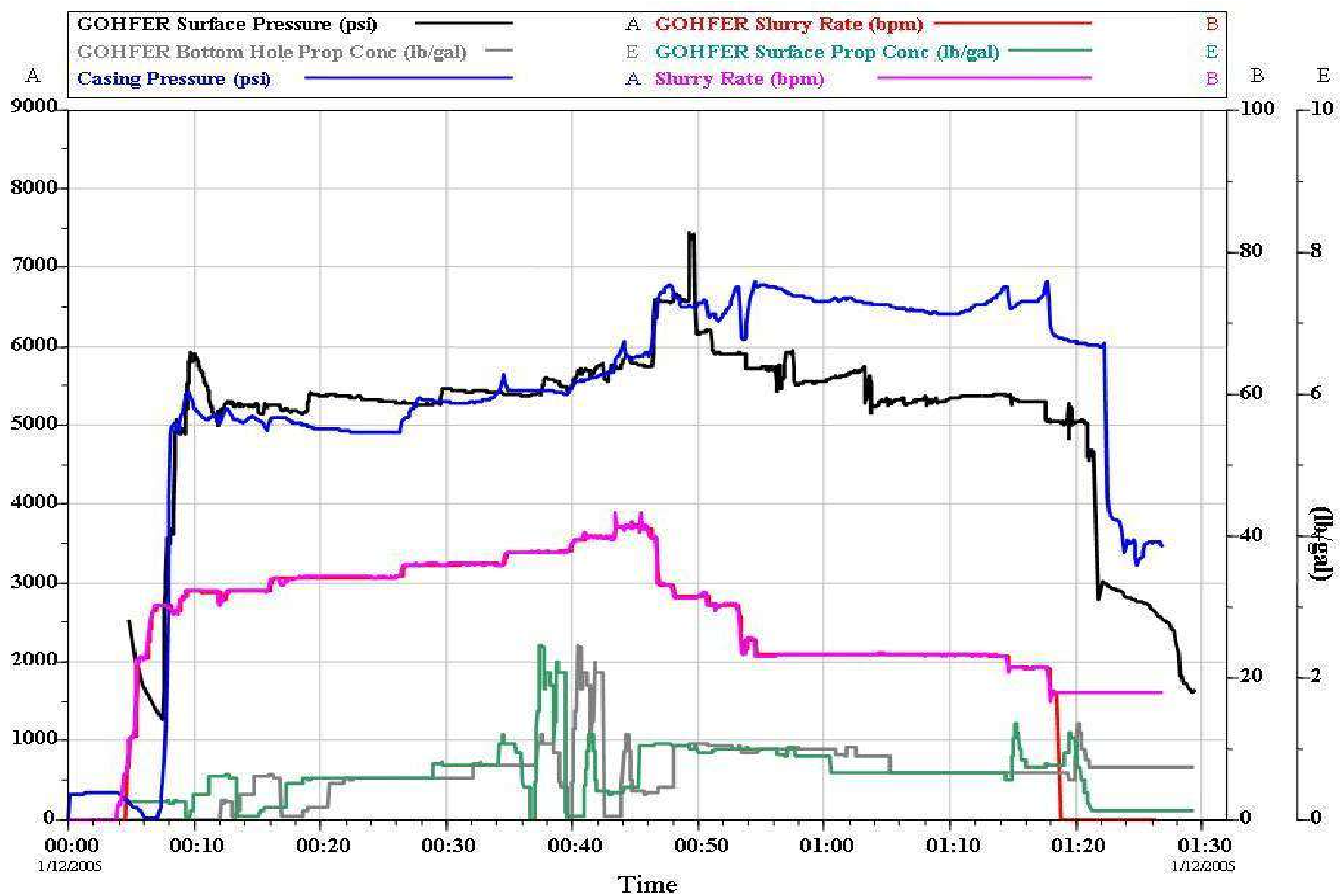

Figure 4-7: Graph showing the matched GOHFER net surface pressure (black) compared to the measured net surface pressure (blue) recorded (psi) during the actual treatment of Interval O.

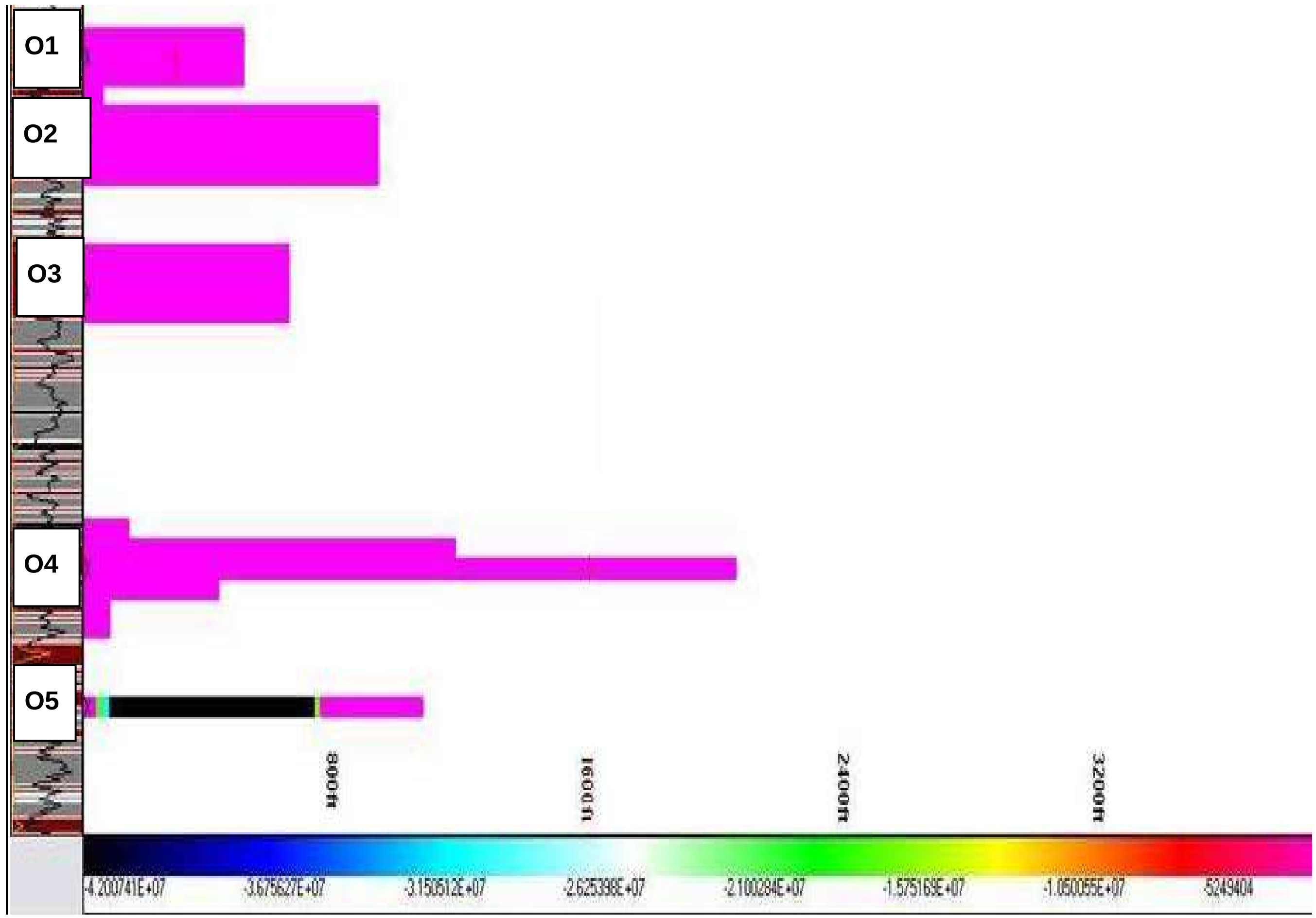

Figure 4-8: GOHFER net pressure (psi) output grid for the Interval O final simulator run.

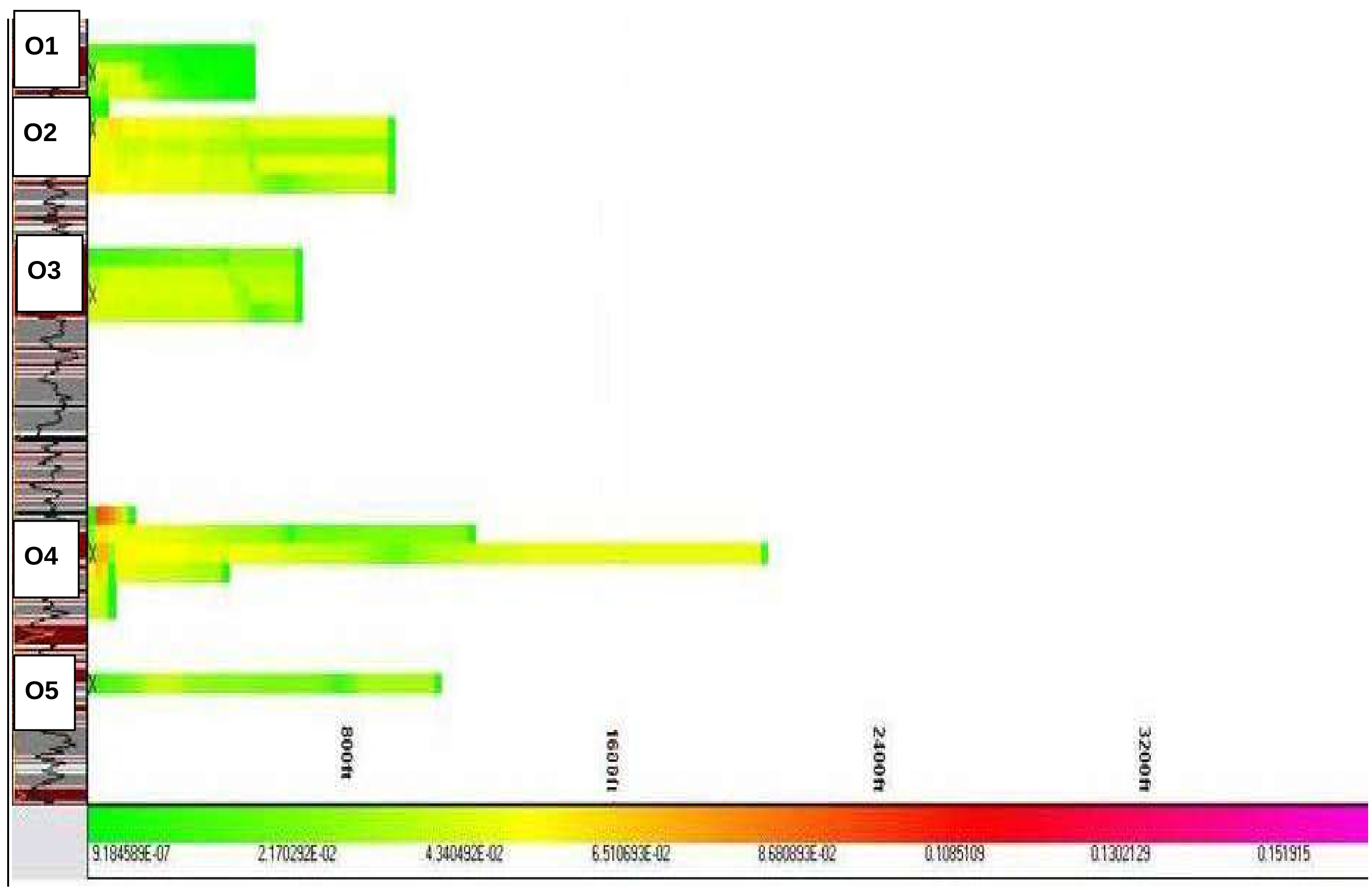

Figure 4-9: GOHFER fracture width (in) output grid for the Interval O final simulator run.

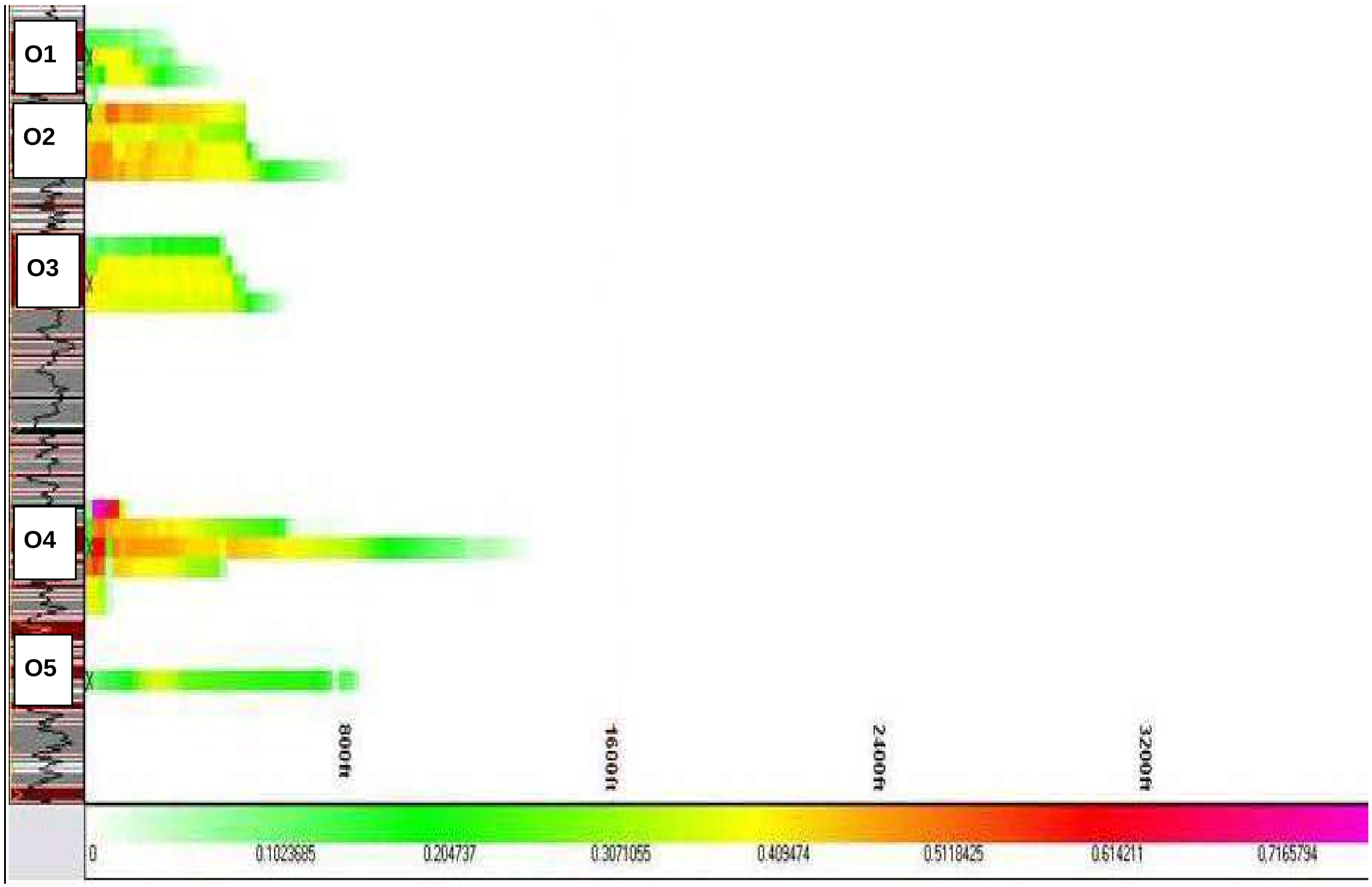

Figure 4-10: GOHFER proppant concentration (lb/ft^2) output grid for the Interval O final simulator run.

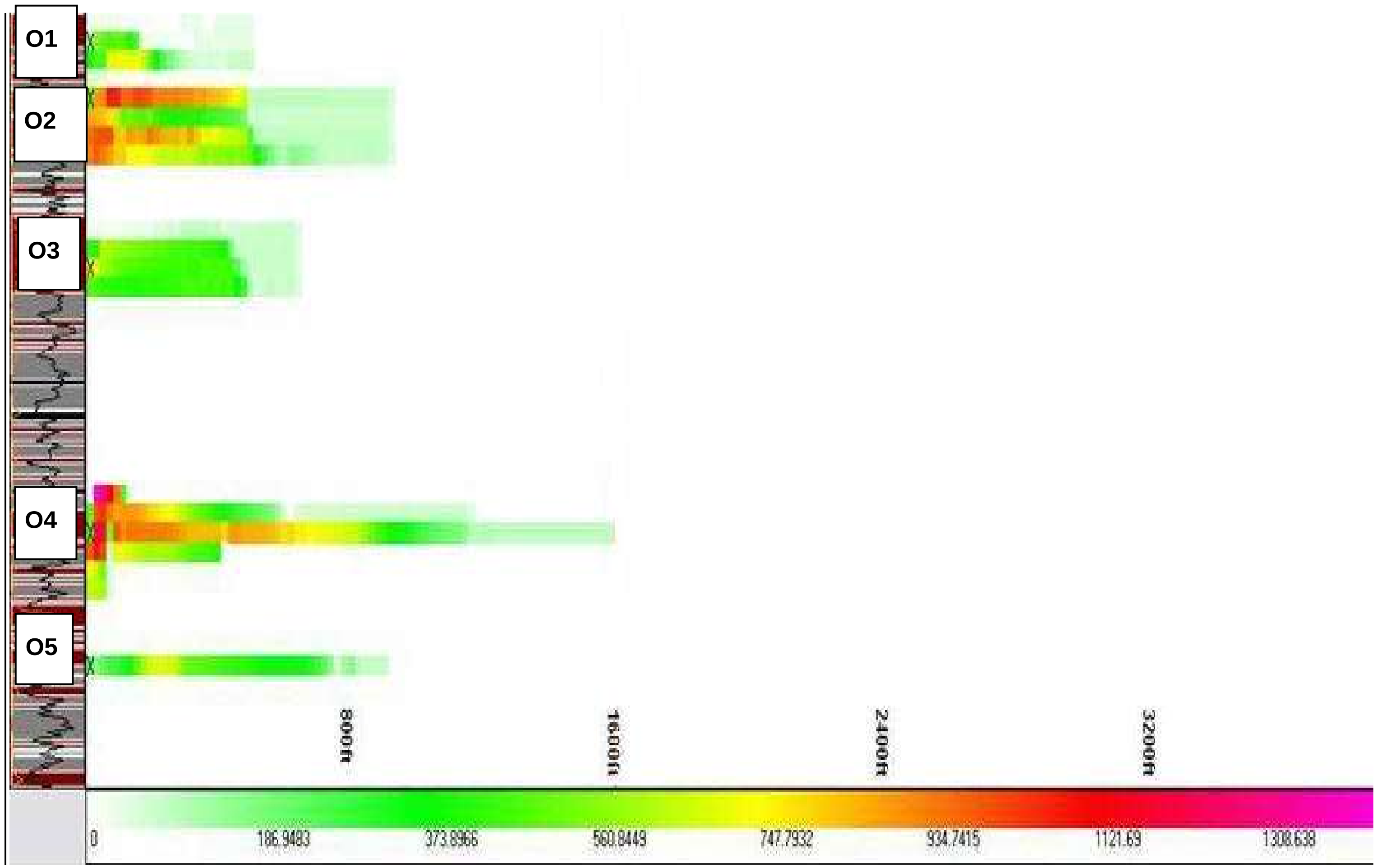

Figure 4-11: GOHFER conductivity (md-ft) output grid for the Interval O final simulator run.

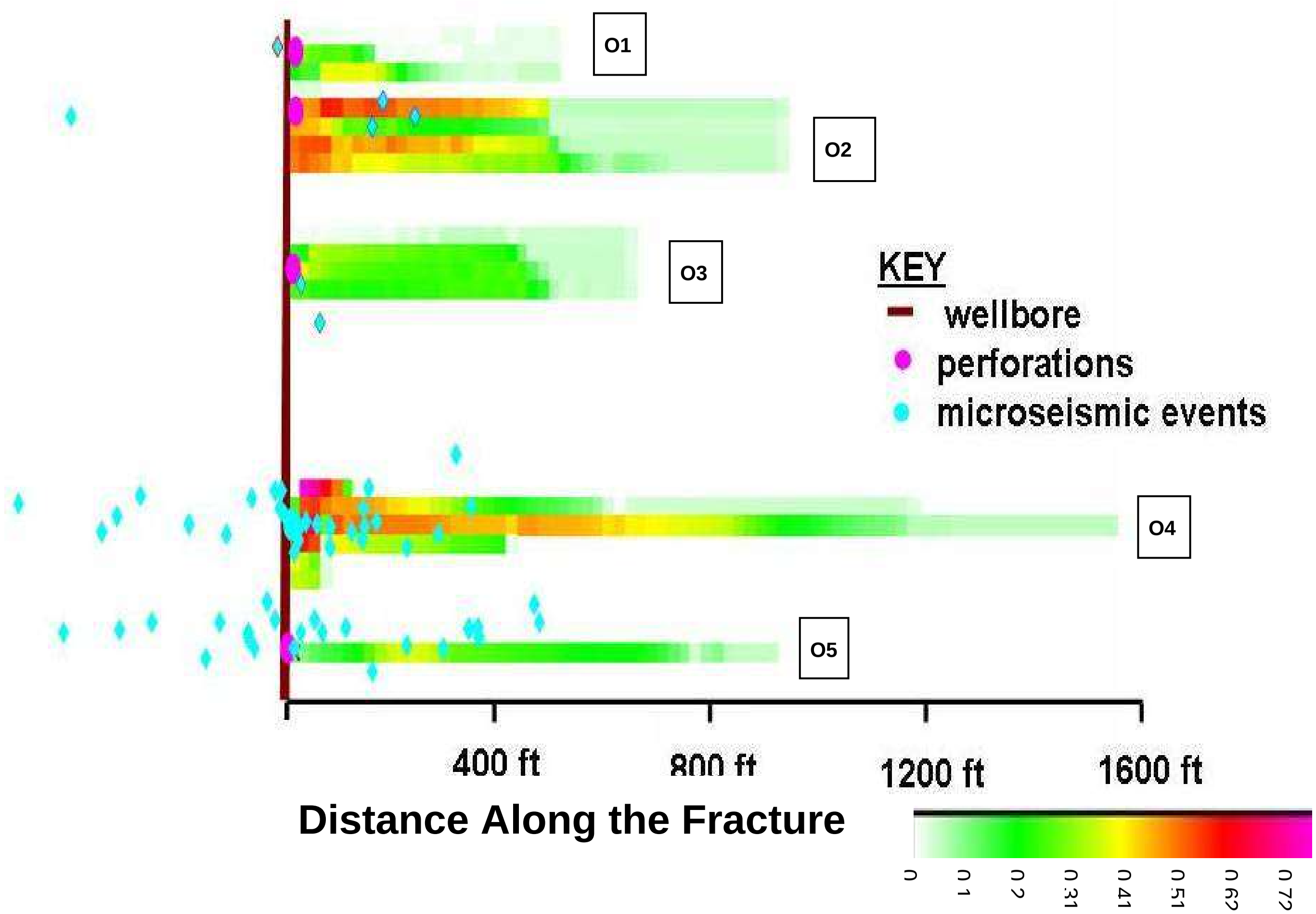

Figure 4-12: The microseismic results are overlain with the proppant concentration output grid (lb/ft^2) of the matched model. During the initial runs the fracture went only into the lower two zones. The microseismic indicates that: most of the fracture goes into Zones O2, O4 and O5; asymmetric growth is seen in Zone O4; and out-of-zone growth occurs in Zones O5 and O3.

just above Zone O4 and at the ends of the fracture in Zone O2 (Figure 4-9). Proppant concentrations (Figure 4-10) were highest at the bottom of Zones O1 and O2, but at the top of Zone O4. In Zone O4, the high concentration is due out-of-zone growth which occurred into the shales and the upper coal layer, where the highest concentration was recorded. Fracture conductivity was greatest in Zones O2 and O4 (see Figure 4-11) and followed the proppant concentration trend. This interval was the only simulator set up with a 3000 ft grid size to allow a comparison of the fracture half-lengths in the sensitivity section analysis (see Section 4.3).

4.2.2 Interval M

The net surface pressure, pumping rate and proppant concentration of the actual treatment and matched data for Interval M are shown in Figure 4-13. The matching of the treatment net surface pressure data was problematic until the microseismic data was used. The pore pressure was modified (see Table 4-3) to allow the model geometric growth to match the real data, and the net surface pressure was then found to match the actual treatment data. It is interesting to note that the large sands in the interval modeled as significantly depleted, and therefore might be connected and drained by neighboring wells. The pressure difference at the end of the treatment could not be adequately modeled without causing screen-outs and the concurrent rapid increase in net surface pressure. In order to match the late-time net surface pressure, the perforation numbers were changed so that 50% of the perforations were distributed between Zones M5 and M6, with only 6 percent in the lower Zone M6 (see Table 4-4).

The following simulator outputs are shown in Figures 4-14 to 4-17: net pressure distribution (Figure 4-14), fracture width (Figure 4-15), proppant concentration (Figure 4-16) and fracture conductivity (Figure 4-17). As can be seen in Figures 4-14 and 4-15, the fracture actually grows beyond the 2000 ft grid size in Zones M3 and M5.

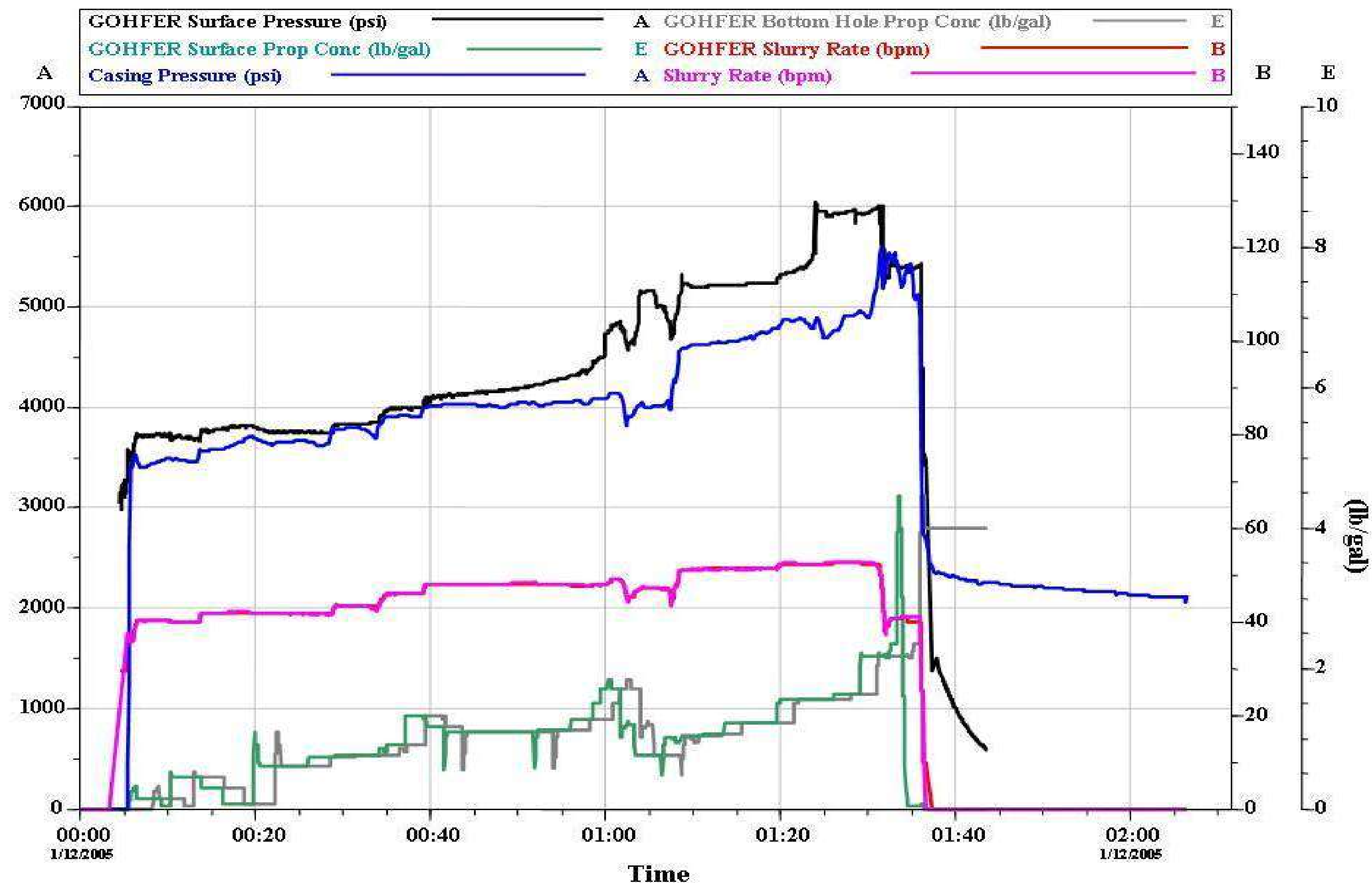

Figure 4-13: Graph showing the matched GOHFER net surface pressure (black) compared to the measured net surface pressure (blue) recorded (psi) during the actual treatment of Interval M.

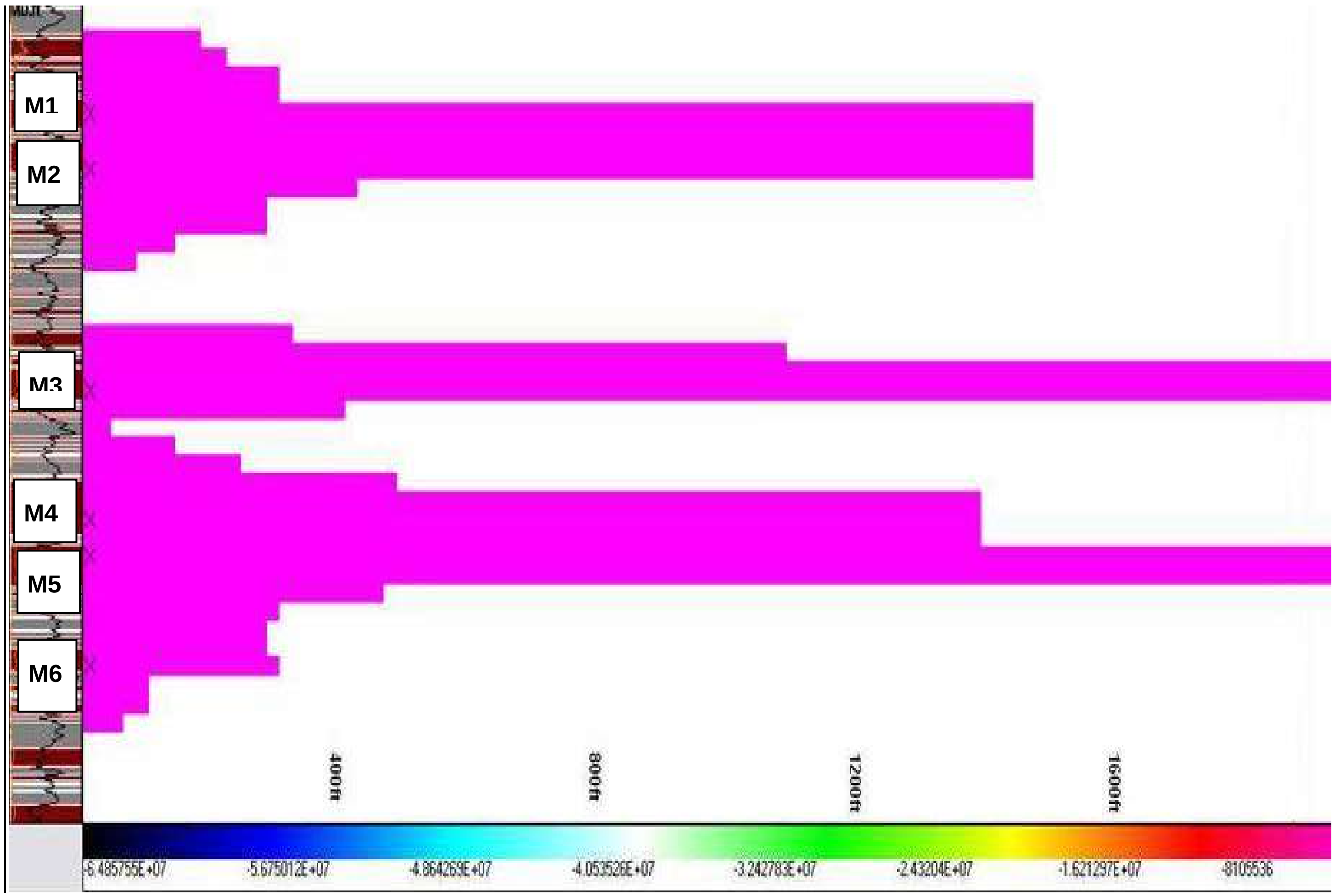

Figure 4-14: GOHFER net pressure (psi) output grid for the Interval M final simulator run.

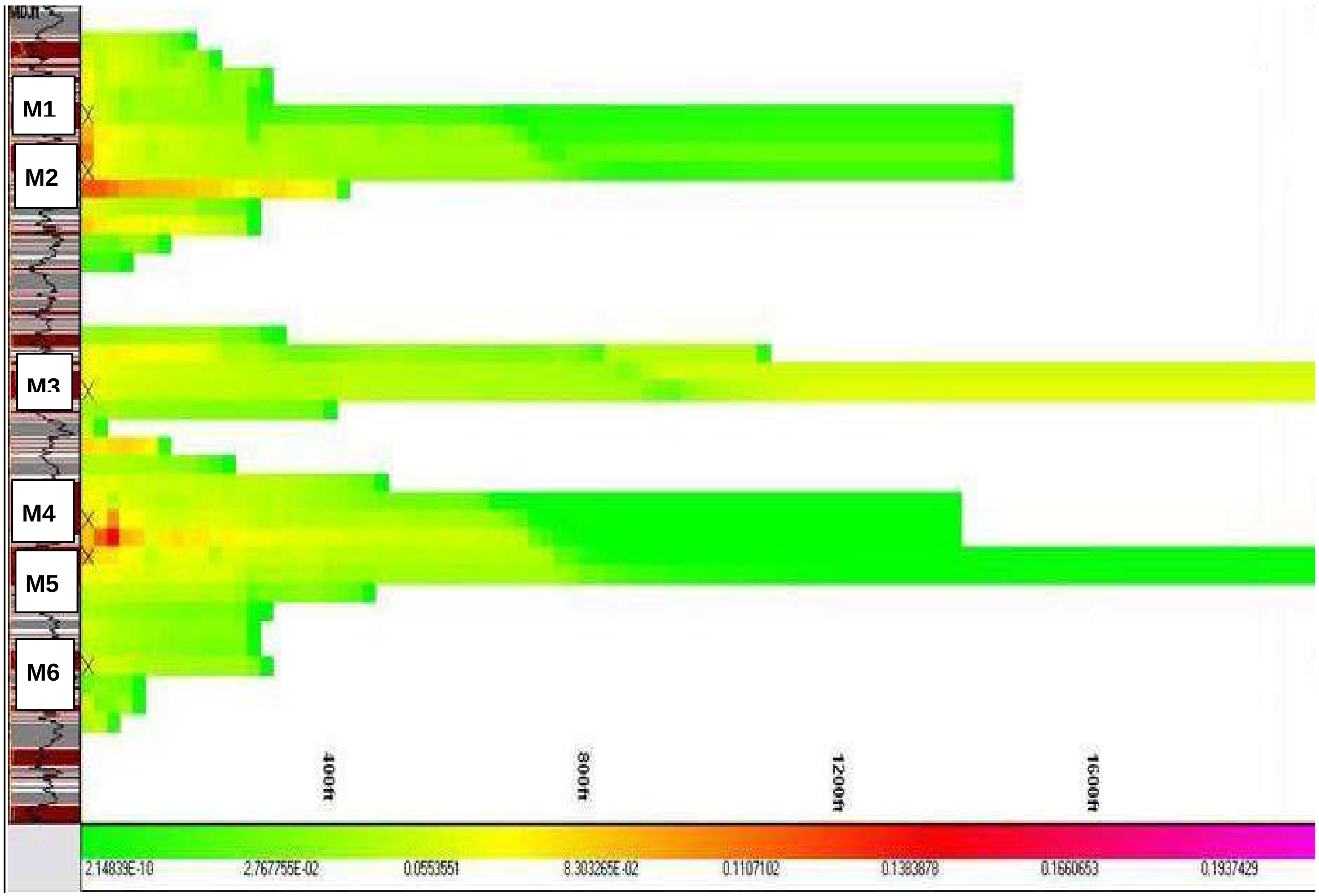

Figure 4-15: GOHFER fracture width (in) output grid for the Interval M final simulator run.

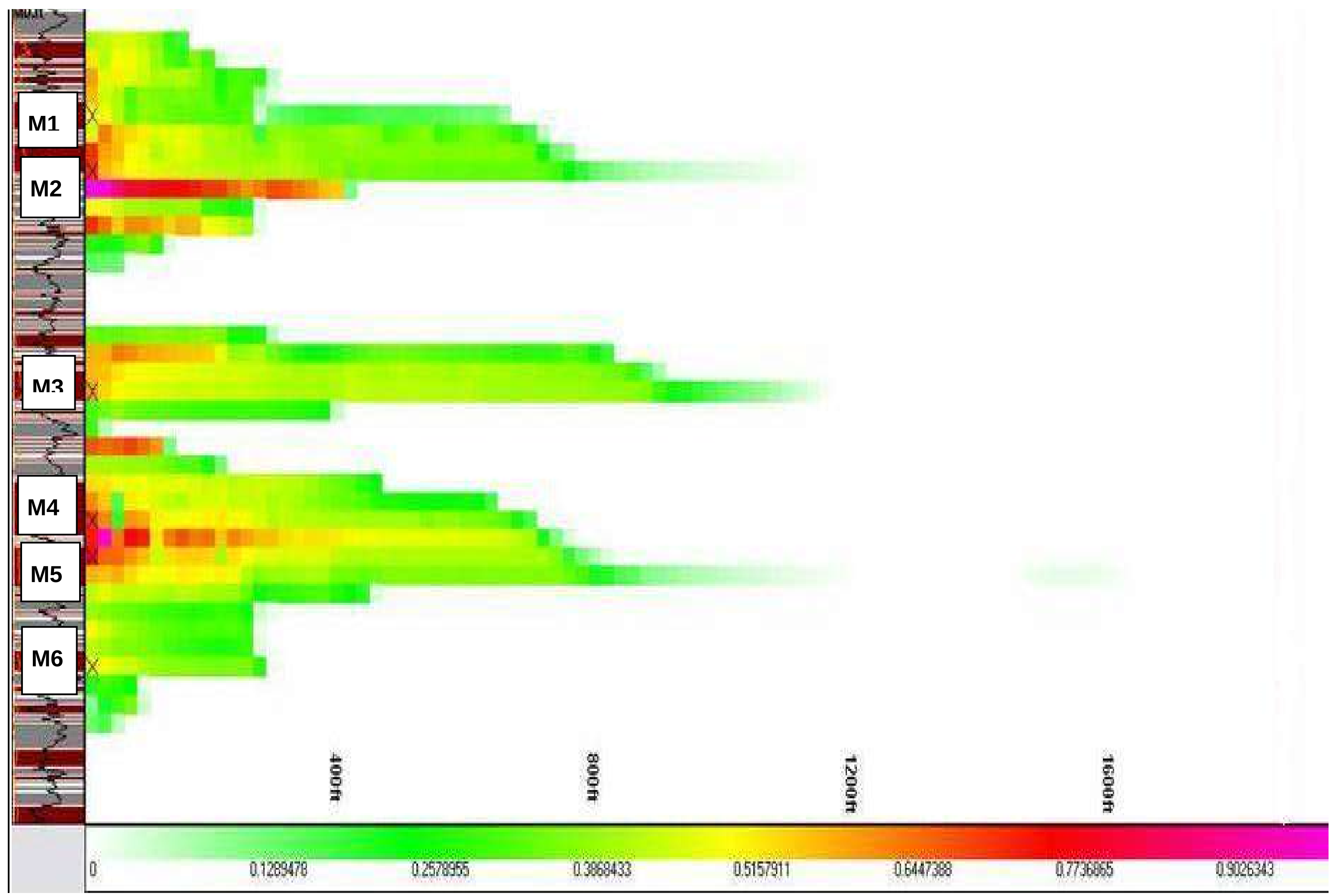

Figure 4-16: GOHFER proppant concentration (lb/ft^2) output grid for the Interval M final simulator run.

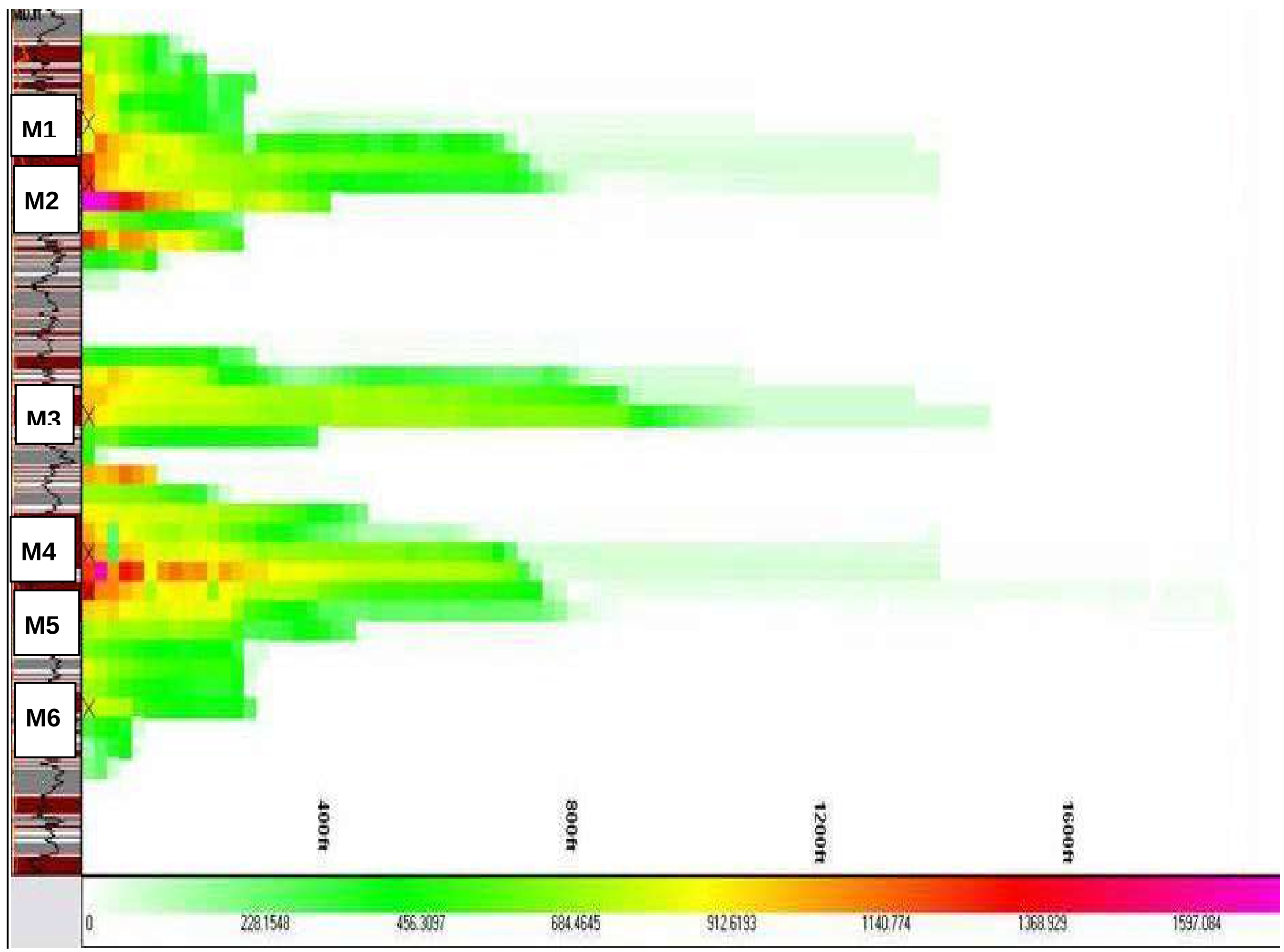

Figure 4-17: GOHFER conductivity (md-ft) output grid for the Interval M final simulator run.

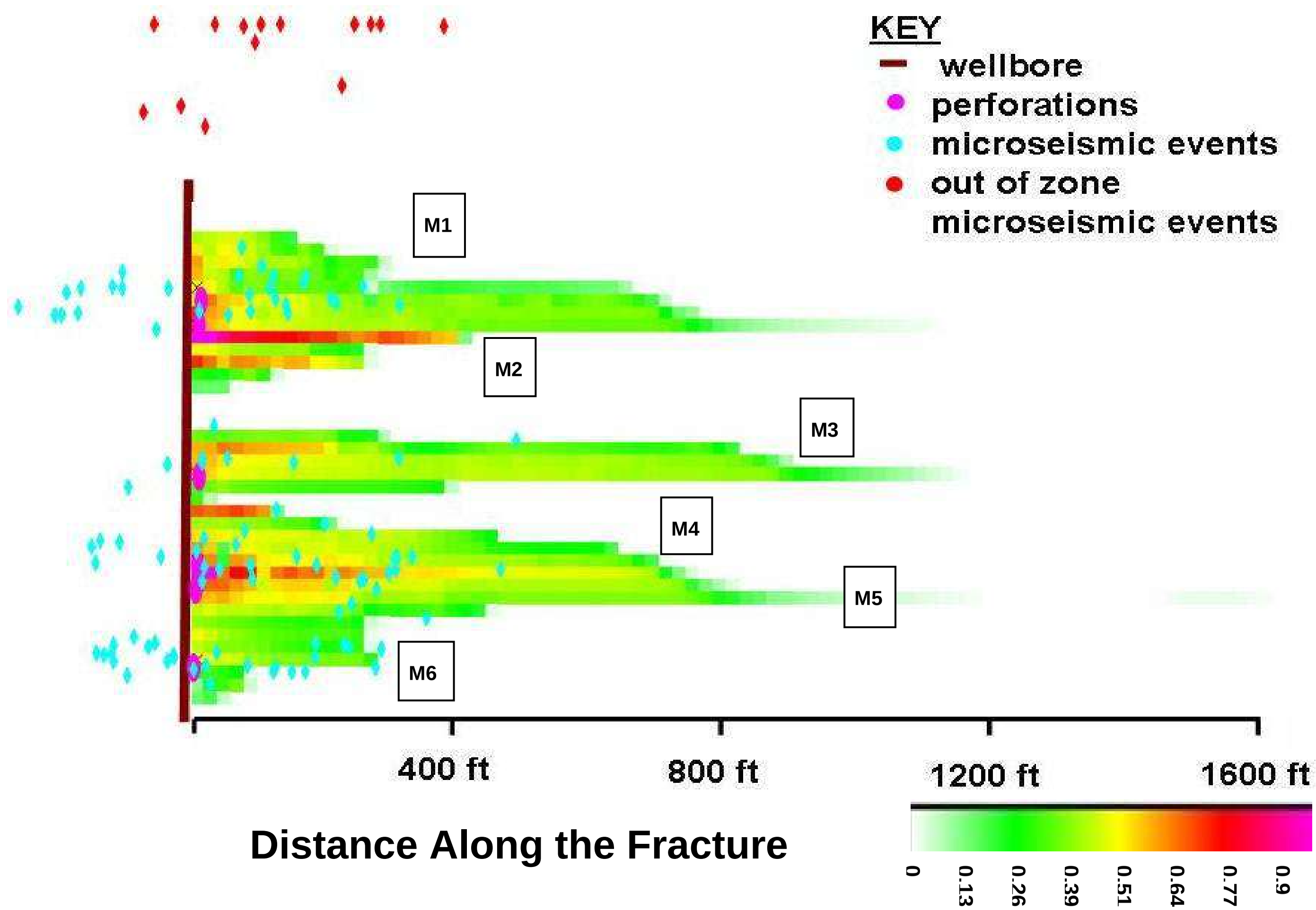

Figure 4-18: The microseismic results are overlain with the proppant concentration output grid (lb/ft^2) of the matched model. During the initial runs, the fracture went only into the lower three zones. As can be seen from the microseismic there is an even distribution of the fracture throughout the interval with significant out-of-zone upward growth in the lower Zones M4, M5 and M6.

In common with Interval A, the microseismic analysis indicated growth into two higher zones of another interval. This out-of-interval microseismic could be due to things such as packer failure or growth up a badly cemented casing. The model half-lengths might therefore be correct for the total treatment fluid and proppant amounts treating this interval only. Similarly, modeling the upper interval, Interval A, is now problematic as the stress state will have been changed by the treatment of the lower two zones within the interval. This fracturing of the lower two zones will alter the real data as the microseismic measurements are actually now monitoring a re-stimulation of the lower zones in the upper interval. The net pressure (Figure 4-14) is evenly distributed throughout the interval but fracture width is greatest at the end of Zone M2, where out-of-zone growth occurs. The proppant concentration (Figure 4-15) and conductivity (Figure 4-16) are greatest in the lower Zones M4, M5 and M6, as well as, below M3 due to fracture growth between the zones. The microseismic data (Figure 4-18) matches the hydraulic fracture growth within the interval and particularly overlies the out-of-zone growth areas.

4.2.3 Interval A

The net surface pressure, pumping rate and proppant concentration of the actual treatment and the matched data for Interval A are shown in Figure 4.19. The early-time pressure data increase could only be matched to the treatment data by having no fluid in the wellbore at the start of the treatment. Similar to Interval O, this meant that a full wellbore of fluid had leaked off prior to starting the treatment, either into an open fracture network, or into a severely depleted zone. In common with other intervals, there were problems trying to match late-time data as the treatment data seems to indicate perforation erosion, while the uncorrected model data indicated a constant pressure. The pore pressure offset and perforation changes necessary to model the real data are detailed in Table 4-3 and Zone A3 had no perforations (termed ‘shut-off’) in order to match the microseismic results.

As can be seen, the pore pressure offset differences were the greatest used for any of the six simulated intervals and were found to be significantly different from the mini-frac data interpretation results. The pore pressure modifications were necessary in order to try and get most of the fracture growth in the upper two zones (A1 and A2), as indicated by the microseismic data (see Figure 4-24). The Zones A1, A2 and A4 were input as significantly depleted, with the lower Zone A5 less depleted and normally pressured. The recorded net surface pressure middle-time data increased, while the initial model had a significant decrease. To model this pressure increase, 25% of the perforations were shut-off after 40 minutes. This decrease of open perforations led to a ‘screen-out’ (rapid pressure increase). After 75 minutes the initial simulation pressures remained constant, while the treatment net surface pressure plot suggested perforation erosion. The perforation erosion is indicated by a gradual pressure decreased (linear trend) with a constant injection rate. The simulation indicated a significant screen-out (seen as a rapidly changing bottomhole concentration – the solid grey line in Figure 4-19) at the end of the treatment and this is likely to be the reason that the injection rate was suddenly decreased from 50 to 40 barrels a minute at this point. The pore pressure offset and perforation number changes necessary to match the real data are shown in Table 4-4.

The following simulator outputs are shown in Figures 4-20 to 4-23: net pressure distribution (Figure 4-20), fracture width (Figure 4-21), proppant concentration (Figure 4-22) and fracture conductivity (Figure 4-23). As can be seen in Figures 4-21 and 4-22, the fracture actually grows beyond the 2000 ft grid size in the upper zone (A1) only. In common with Interval M, the microseismic analysis indicated growth into the two lower zones of a higher interval. This out-of-interval fracturing was probably due to packer failure and the model half-lengths might be correct for the total treatment fluid and proppant amounts treating this interval only. Again, modeling the interval above this one is now problematic, as the stress state is changed by the treatment of the lower two zones within the interval. The microseismic analysis of the above interval will actually be monitoring a re-stimulation treatment of the lower two zones.

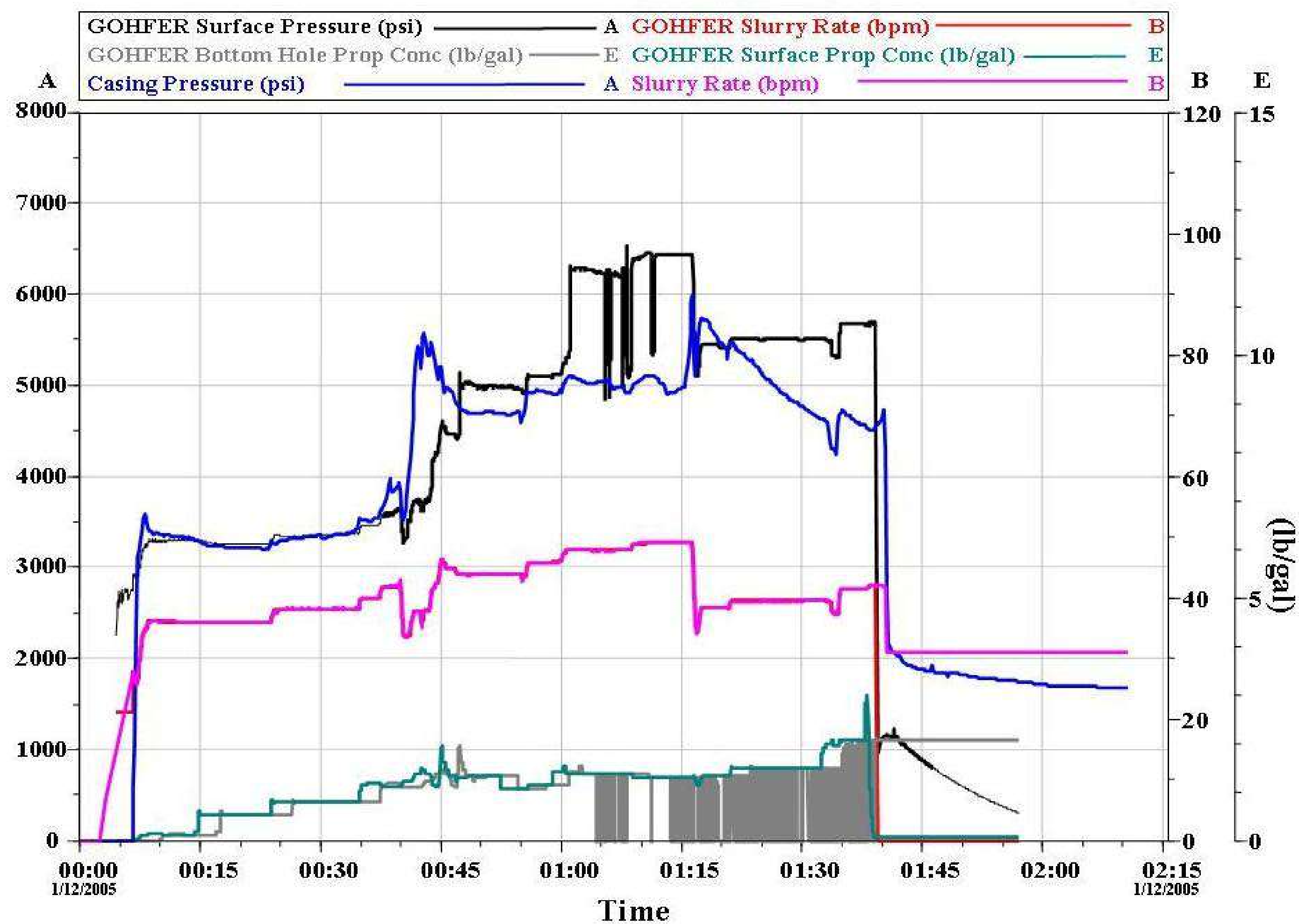

Figure 4-19: Graph showing the matched GOHFER net surface pressure (black) compared to the measured net surface pressure (blue) recorded (psi) during the actual treatment of Interval A.

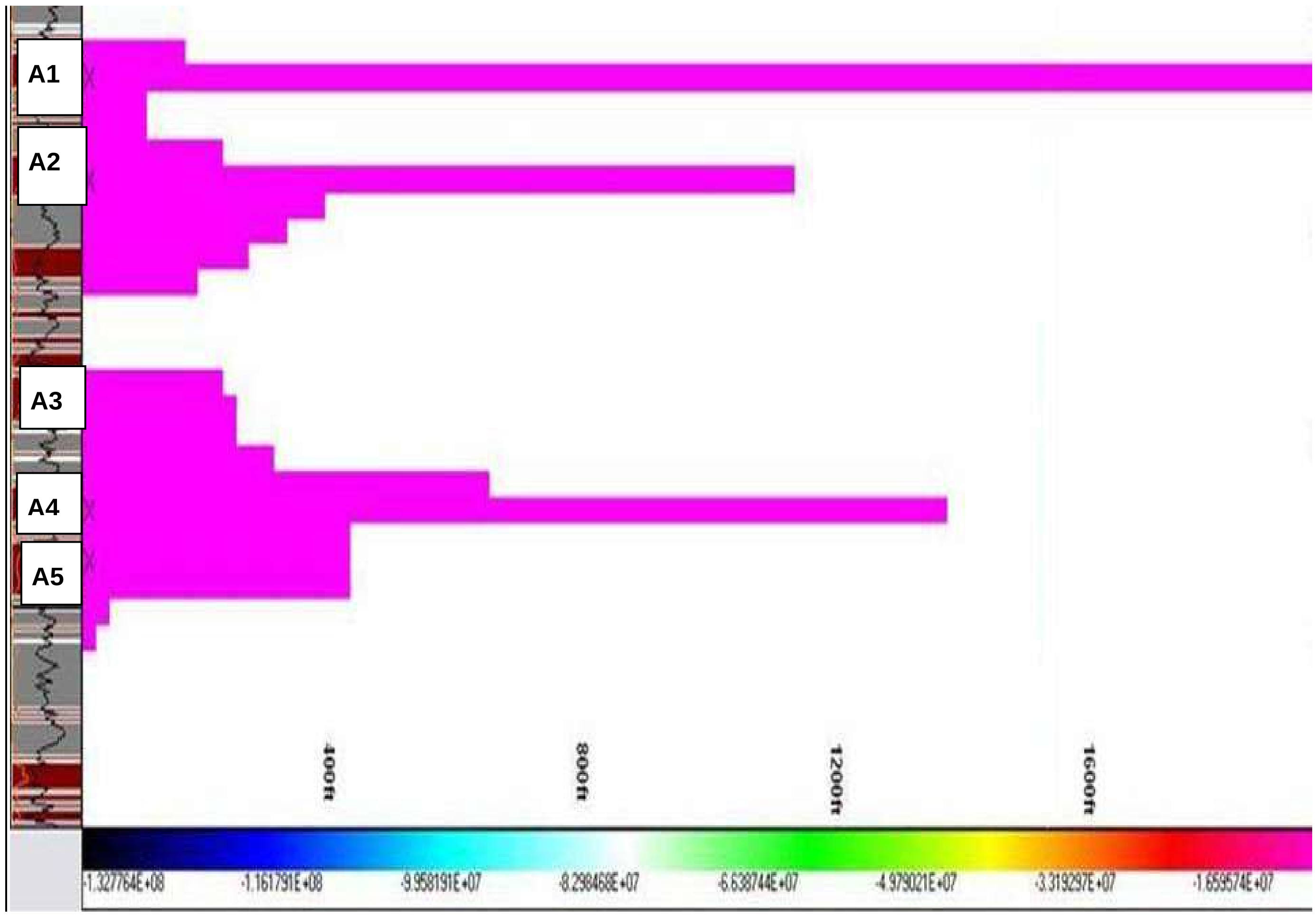

Figure 4-20: GOHFER net pressure (psi) output grid for the Interval A final simulator run.

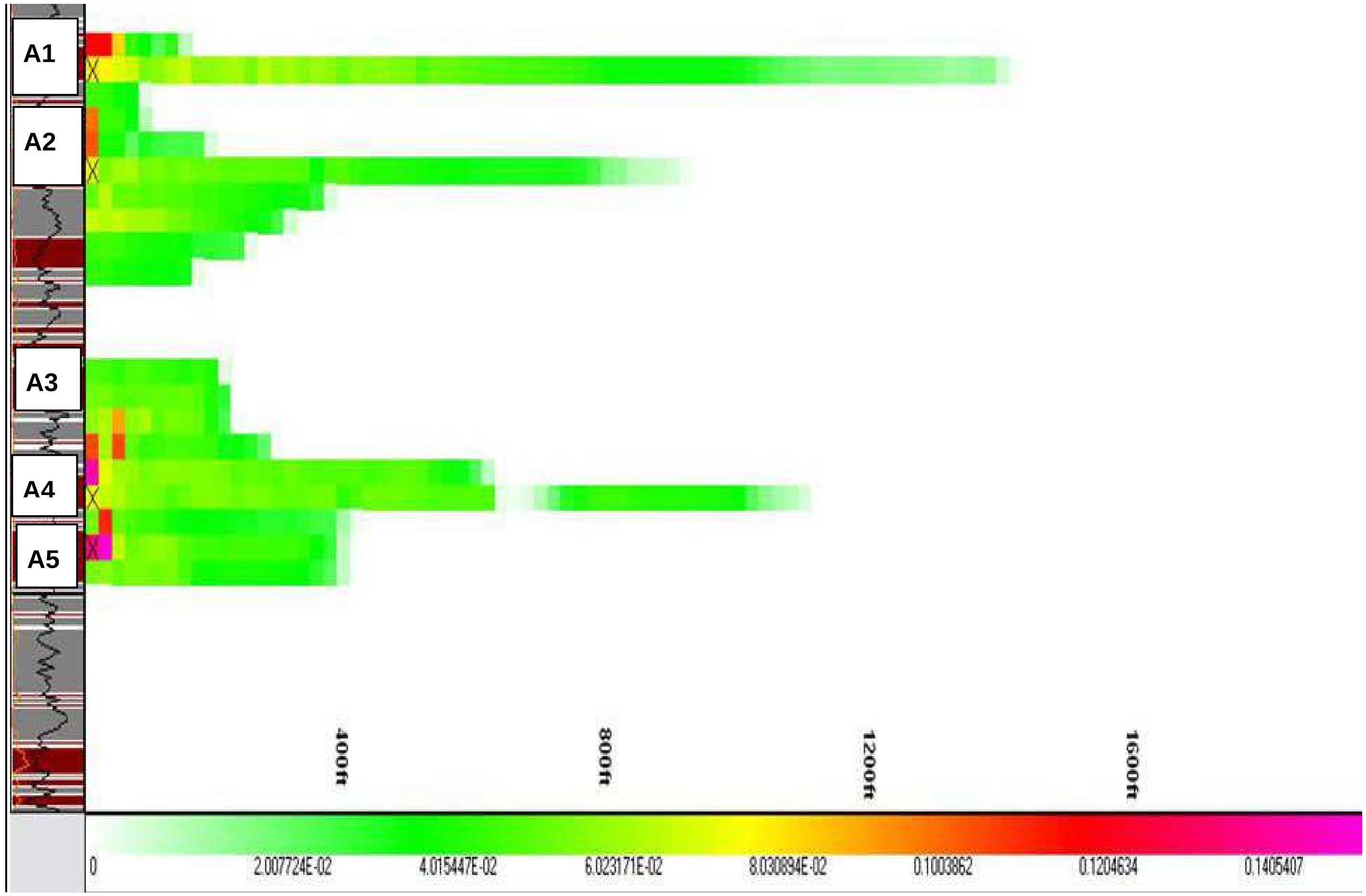

Figure 4-21: GOHFER fracture width (inches) output grid for the Interval A final simulator run.

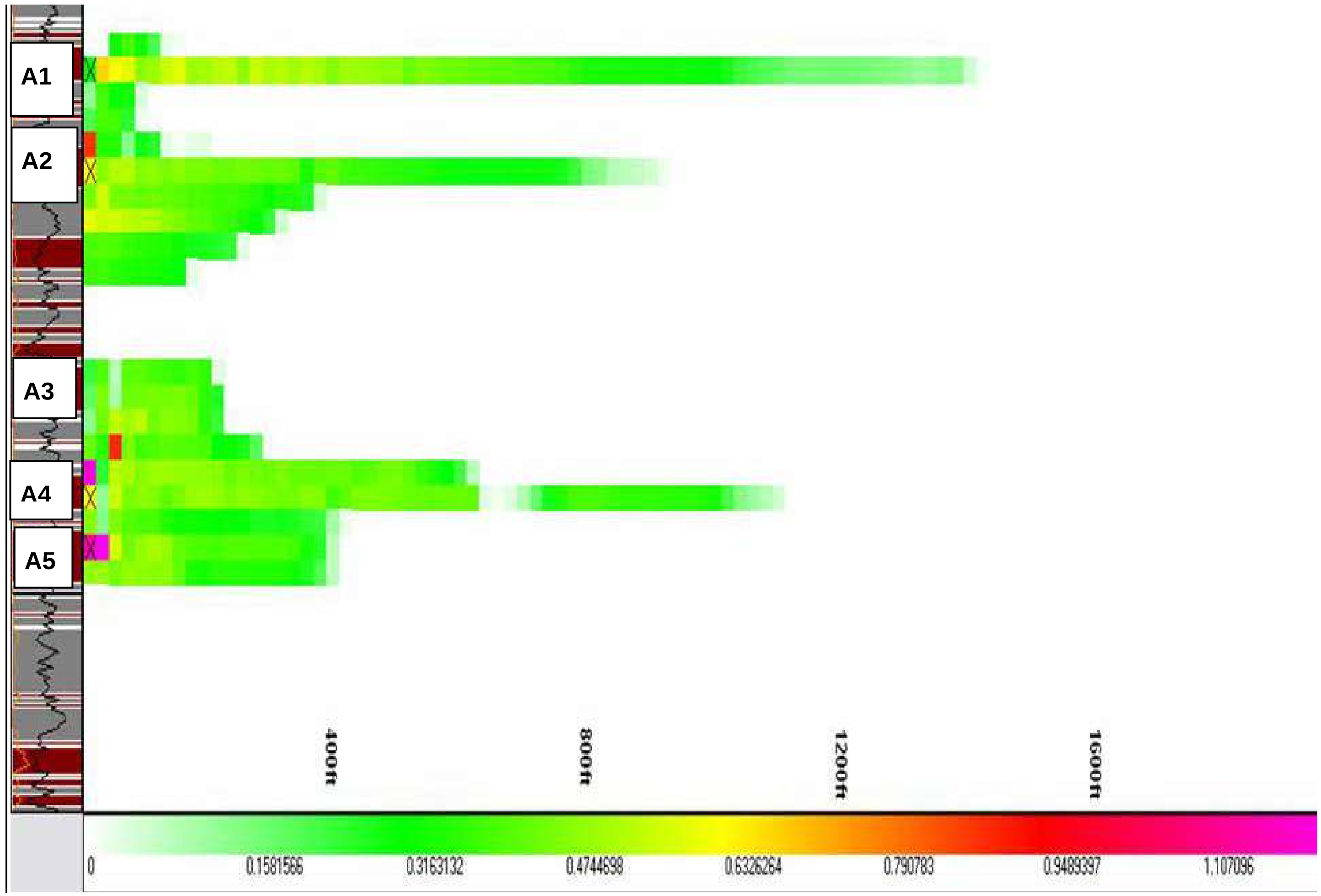

Figure 4-22: GOHFER proppant concentration (lb/ft^2) output grid for the Interval A final simulator run.

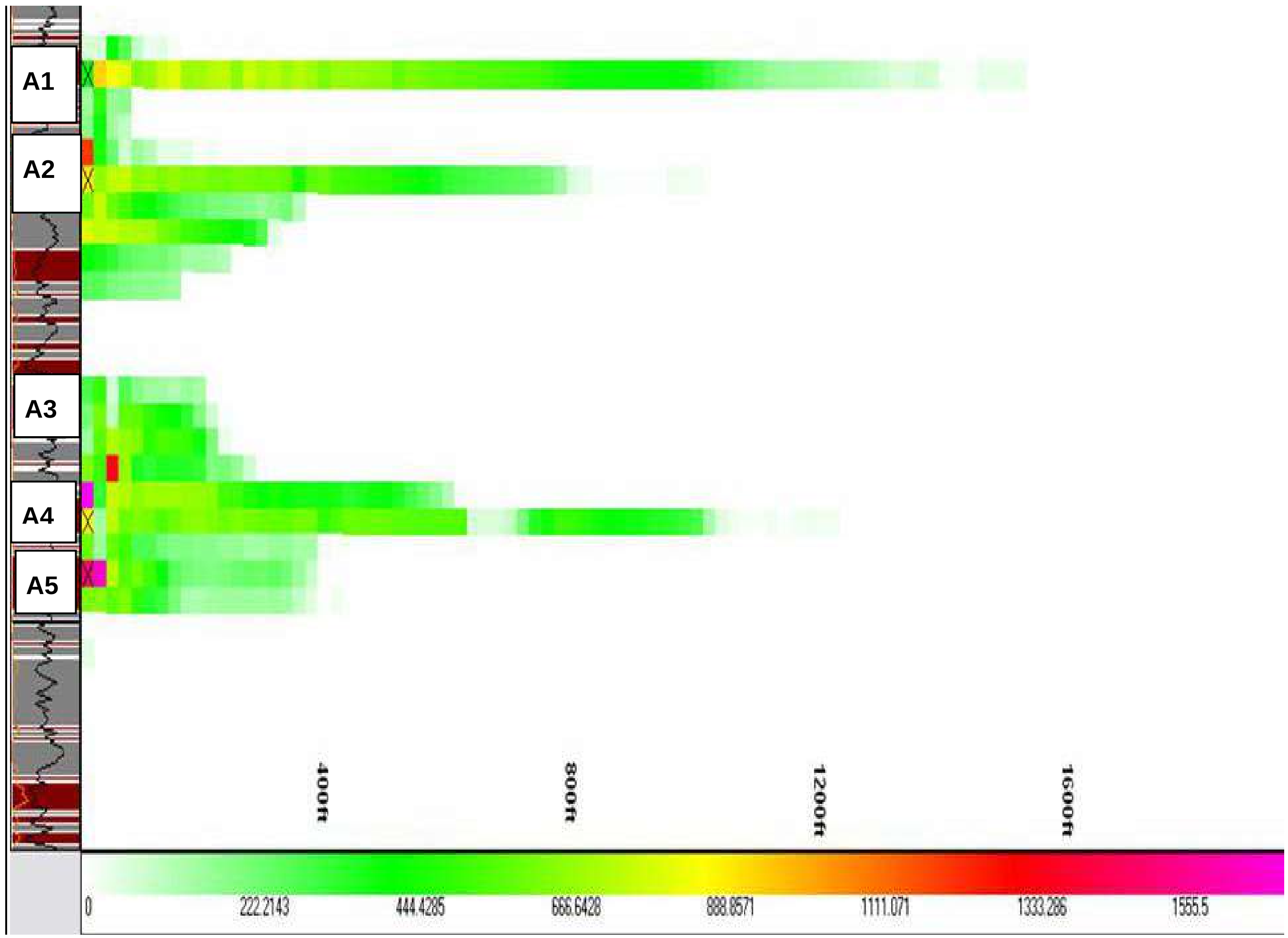

Figure 4-23: GOHFER conductivity (md-ft) output grid for the Interval A final simulator run.

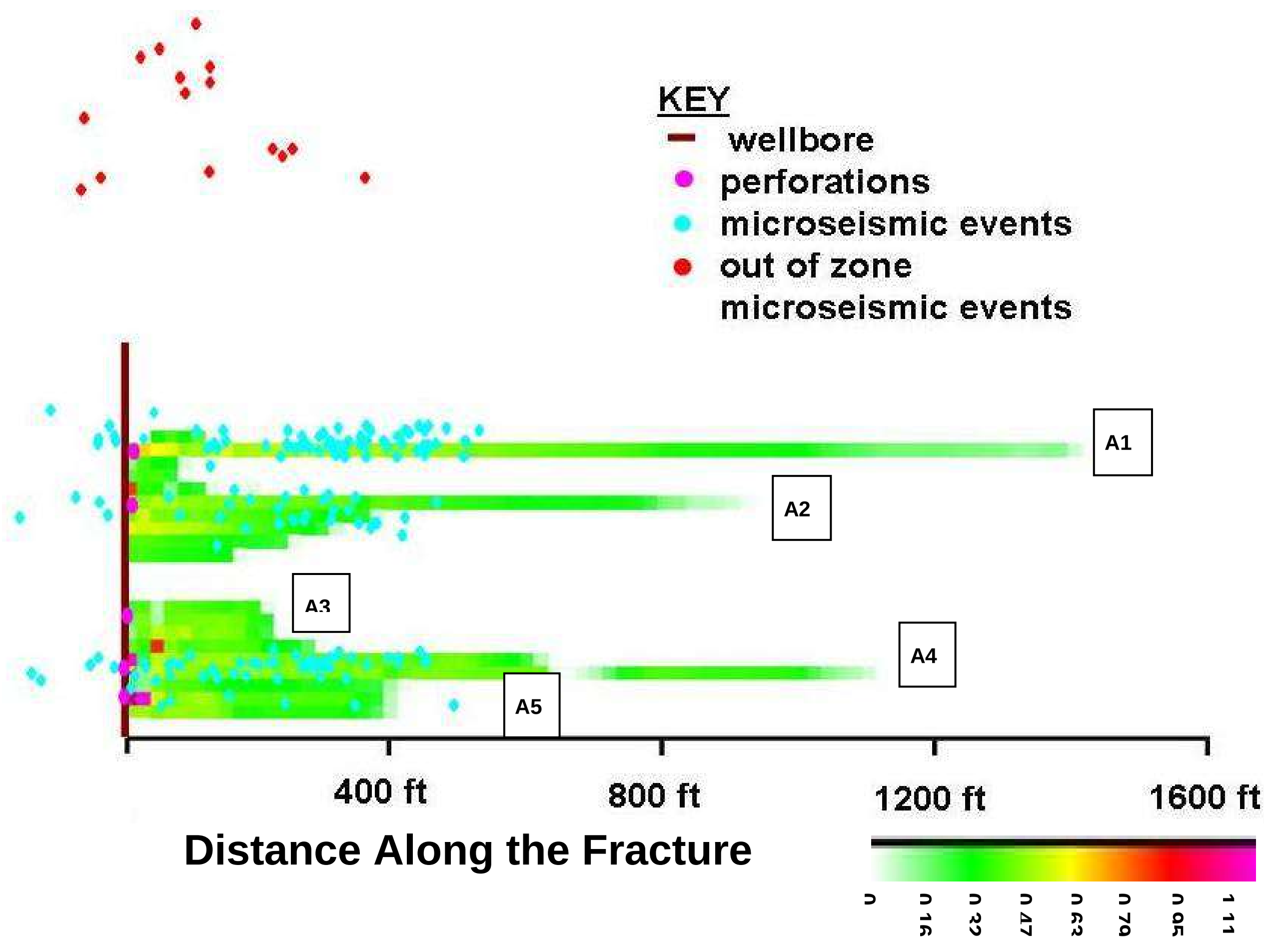

Figure 4-24: The microseismic results are overlain with the proppant concentration output grid (lb/ft^2) of the matched model. During the initial runs the fracture went mainly into the lower three zones. As can be seen from the microseismic, the fracture goes mainly into the upper two zones. Zone A3 shows no microseisms, so it was shut-off for the net surface pressure match.

The net pressure distribution (Figure 4-20) shows an even distribution throughout the interval, but the fracture width (Figure 4-21) is greatest where out-of-zone growth has occurred, above Zones A1 and A4. The proppant concentration (Figure 4-22) and conductivity (Figure 4-23) follow the fracture width trend, apart from the zone above A1 (see Figure 4-22) where no significant increases in proppant concentration occurs. The microseisms (Figure 4-23) overlap some of the out-of-zone growth, but the upper zones of this interval exhibited highly asymmetrical growth. The growth is probably due to the highly asymmetrical reservoirs and the associated lenticular sand geology found in this interval

4.2.4 Interval S

The net surface pressure, pumping rate and proppant concentration of the actual treatment and the matched data for Interval S are shown in Figure 4.25. The data matching for this and Interval G were probably the easiest undertaken. Microseismic analysis was not available and the pore pressure offsets used were similar to the actual data from the mini-frac analysis (see Table 4-3). At the beginning of the treatment, the pressure ‘spike’ was modeled using a 2:1 liquid-to-gas ratio in the wellbore, indicating that some fluid (approximately one-third) has been lost to fractures or a severely depleted zone. The lack of microseismic data meant that this and Interval G served as examples of net surface pressure matching without the constraints on fracture geometry imposed by microseismic data.

The pore pressure offsets and perforation changes are detailed in Table 4-3, and 80% of the perforations were placed in the lower two zones, S4 and S5. The shape of the recorded net surface pressure is similar to other intervals where packing-off in the wellbore and perforation erosion is indicated at the end of the treatment. However, in this case the model was found to adequately simulate the increase in proppant without changes to the perforation factor.

The following simulator outputs are shown in Figures 4-26 to 4-29: net pressure distribution (Figure 4-26), fracture width (Figure 4-27), proppant concentration (Figure 4-28) and fracture conductivity (Figure 4-29). As can be seen in Figures 4-26 and 4-27, the fracture only grows beyond the 2000 ft grid size in the lower zone, S4. The net pressure (see Figure 4-26) is evenly distributed throughout the interval, but the fracture width (Figure 4-27), proppant concentration (Figure 4-28) and conductivity (Figure 4-29) all follow a general trend of larger values in the lower three zones, decreasing to a minimum in Zone S1. The only exception to the general trend is just below the perforation in Zone S2, where out-of-zone growth occurs into the lower shales.

4.2.6 Interval G

The net surface pressure, pumping rate and proppant concentration of the actual treatment and the matched data for Interval G are shown in Figure 4.30. Similar to Interval S, the data matching was relatively straightforward as the pore pressure data used was comparable to the results from the mini-fracture analysis (see Table 4-3). The ratio of perforation numbers used for the Zones G1 through G5 were also the original perforations from the well report. In common with most intervals, the major problem was encountered when trying to match the late-time net surface pressure data to the simulator outputs. To match the treatment data, 87.5% of the perforations where shut-off after 87 minutes. The model indicated that the wellbore packed-off, but the simulator is unable to make calculations when all the perforations were shut-off.

The following simulator outputs are shown in Figures 4-31 to 4-34: net pressure distribution (Figure 4-31), fracture width (Figure 4-32), proppant concentration (Figure 4-33) and fracture conductivity (Figure 4-34). As can be seen in Figures 4-26 and 4-27, the fracture grows beyond the 2000 ft grid size in the lower zones, G4 and G5. The net pressure is evenly distributed over the interval (see Figure 4-31), except for just above Zone G3 where the value decreases as the fracture grows out-of-zone. The fracture width

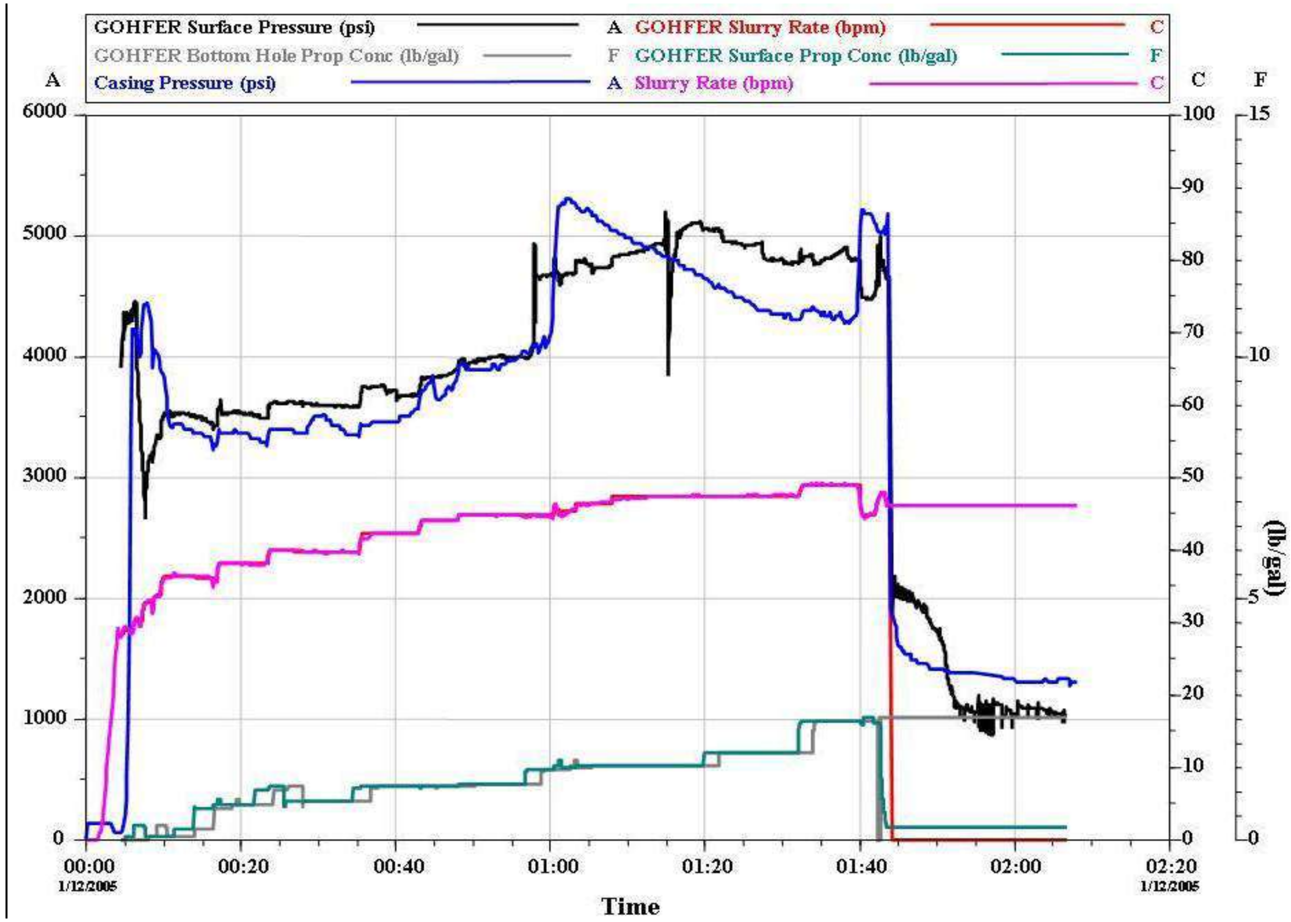

Figure 4-25: Graph showing the matched GOHFER net surface pressure (black) compared to the measured net surface pressure (blue) recorded (psi) during the actual treatment of Interval S.

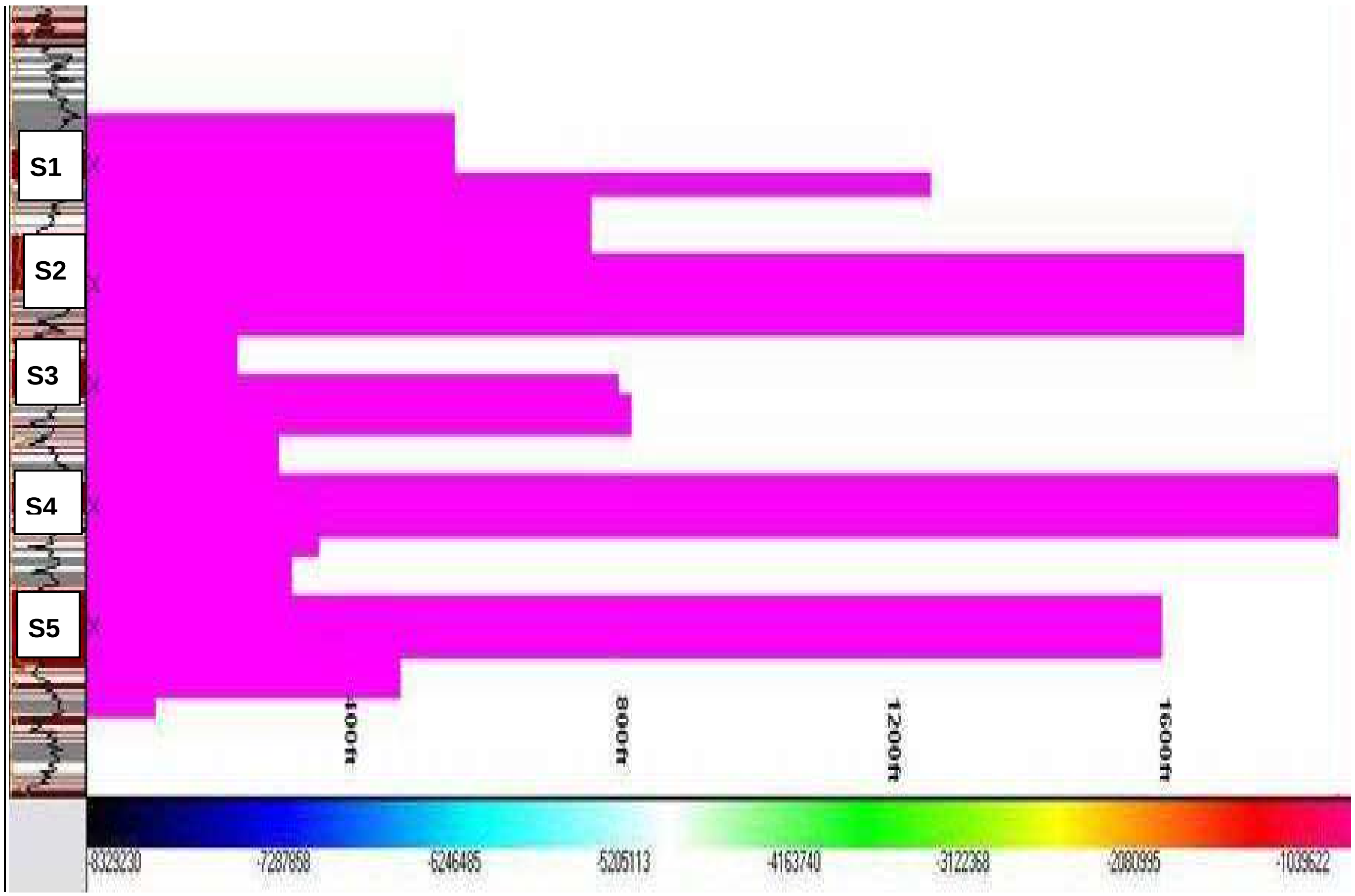

Figure 4-26: GOHFER net pressure (psi) output grid for the Interval S final simulator run.

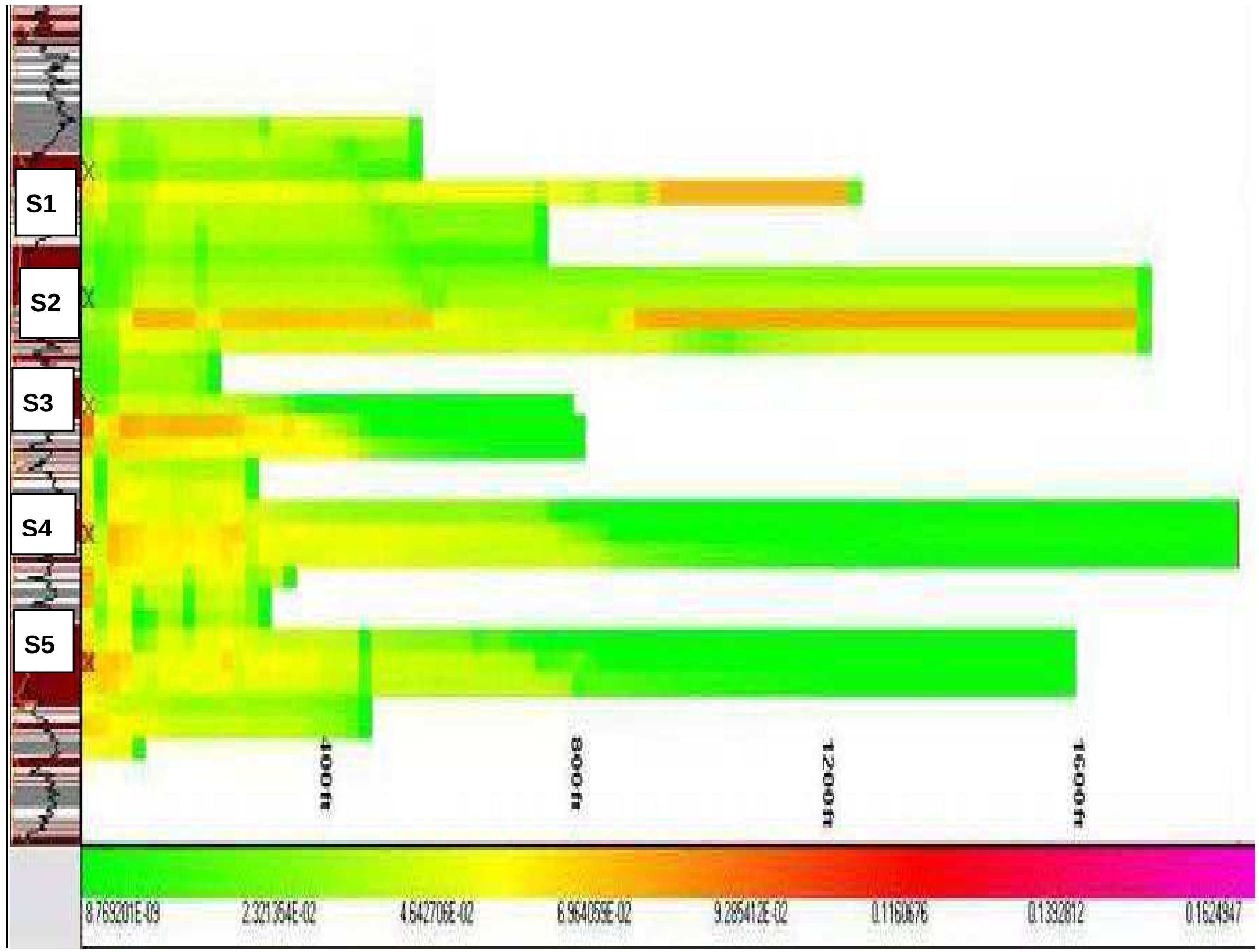

Figure 4-27: GOHFER fracture width (in) output grid for the Interval S final simulator run.

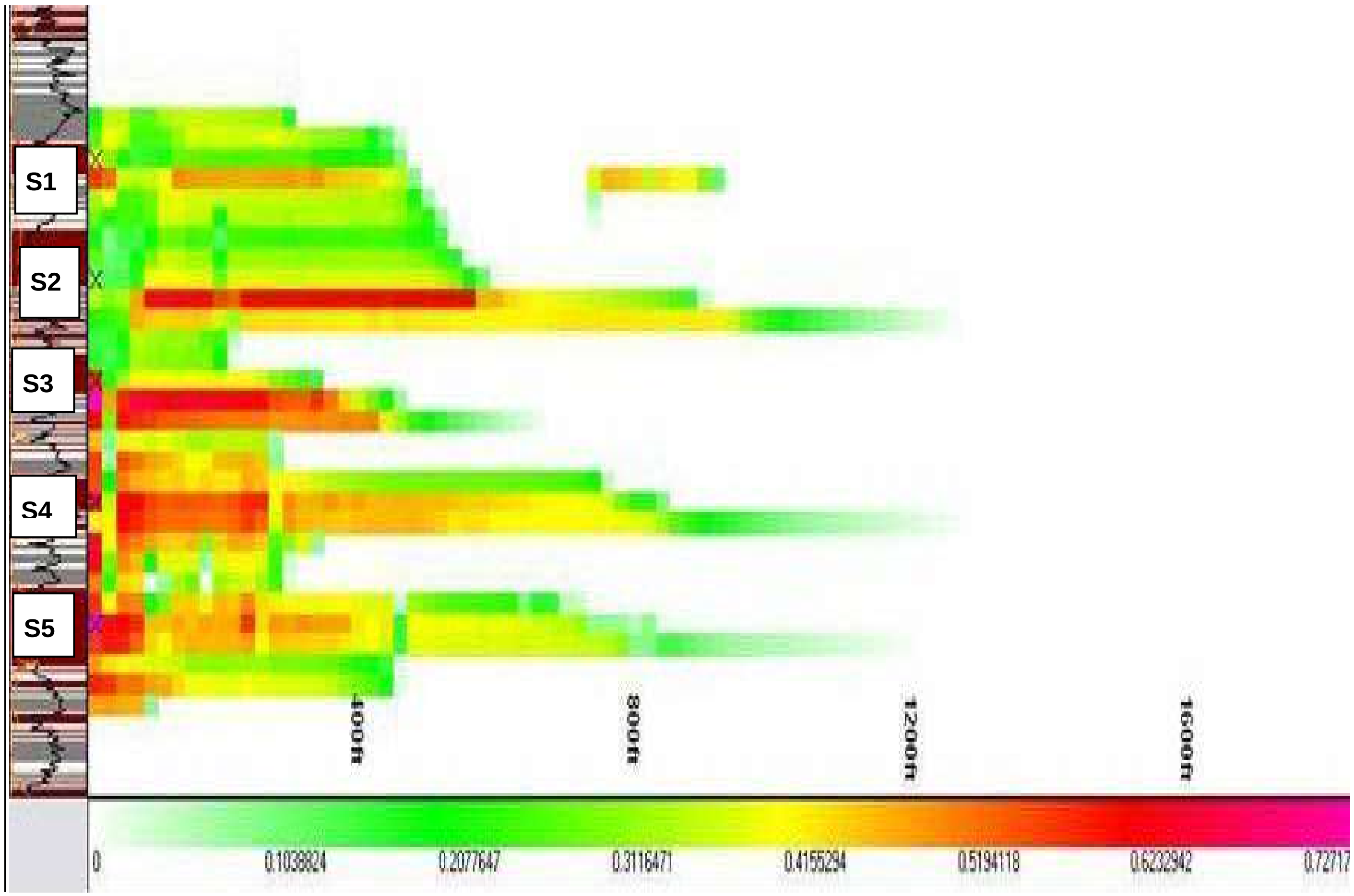

Figure 4-28: GOHFER proppant concentration (lb/ft^2) output grid for the Interval S final simulator run.

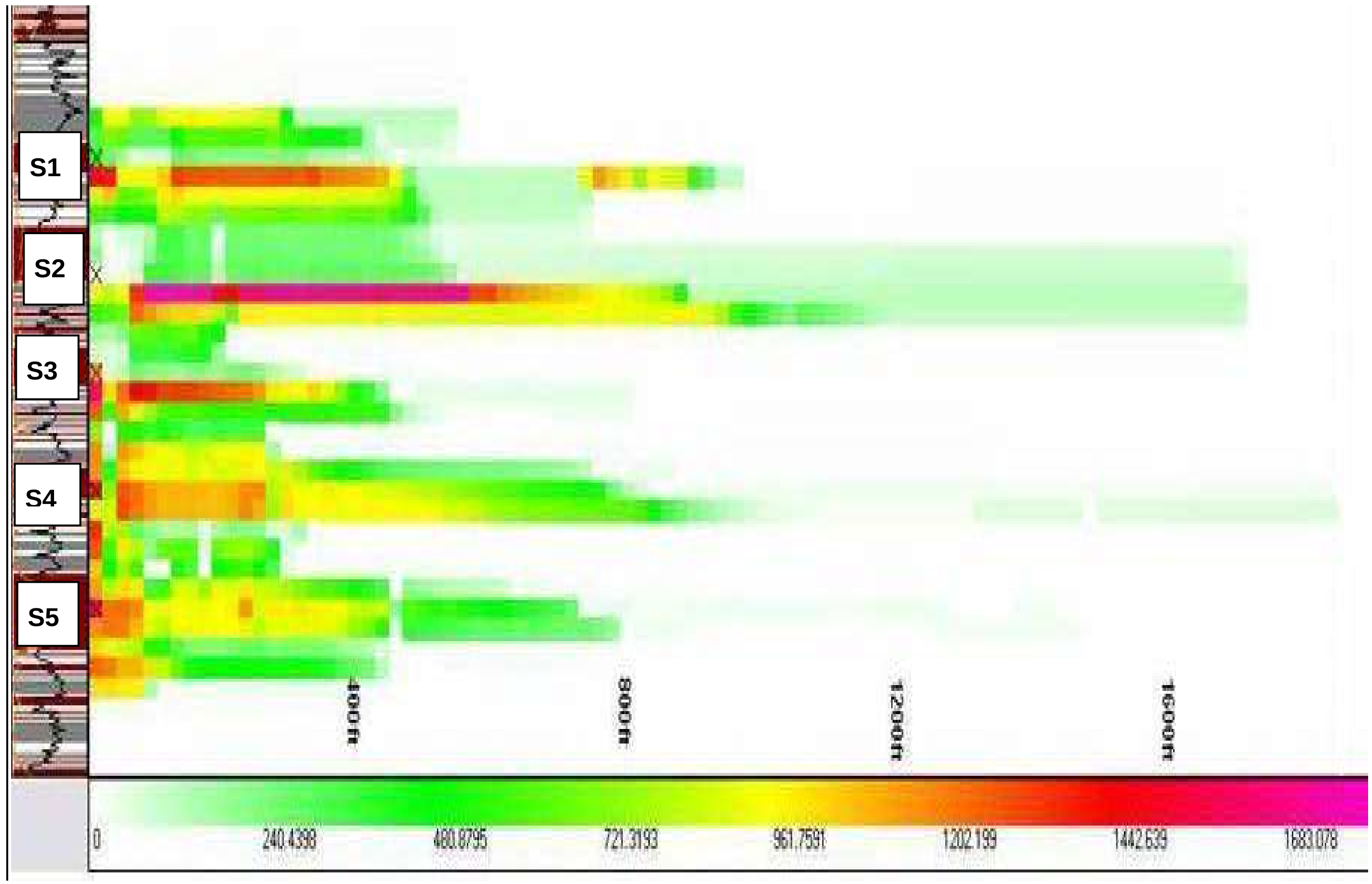

Figure 4-29: GOHFER conductivity (md-ft) output grid for the Interval S final simulator run

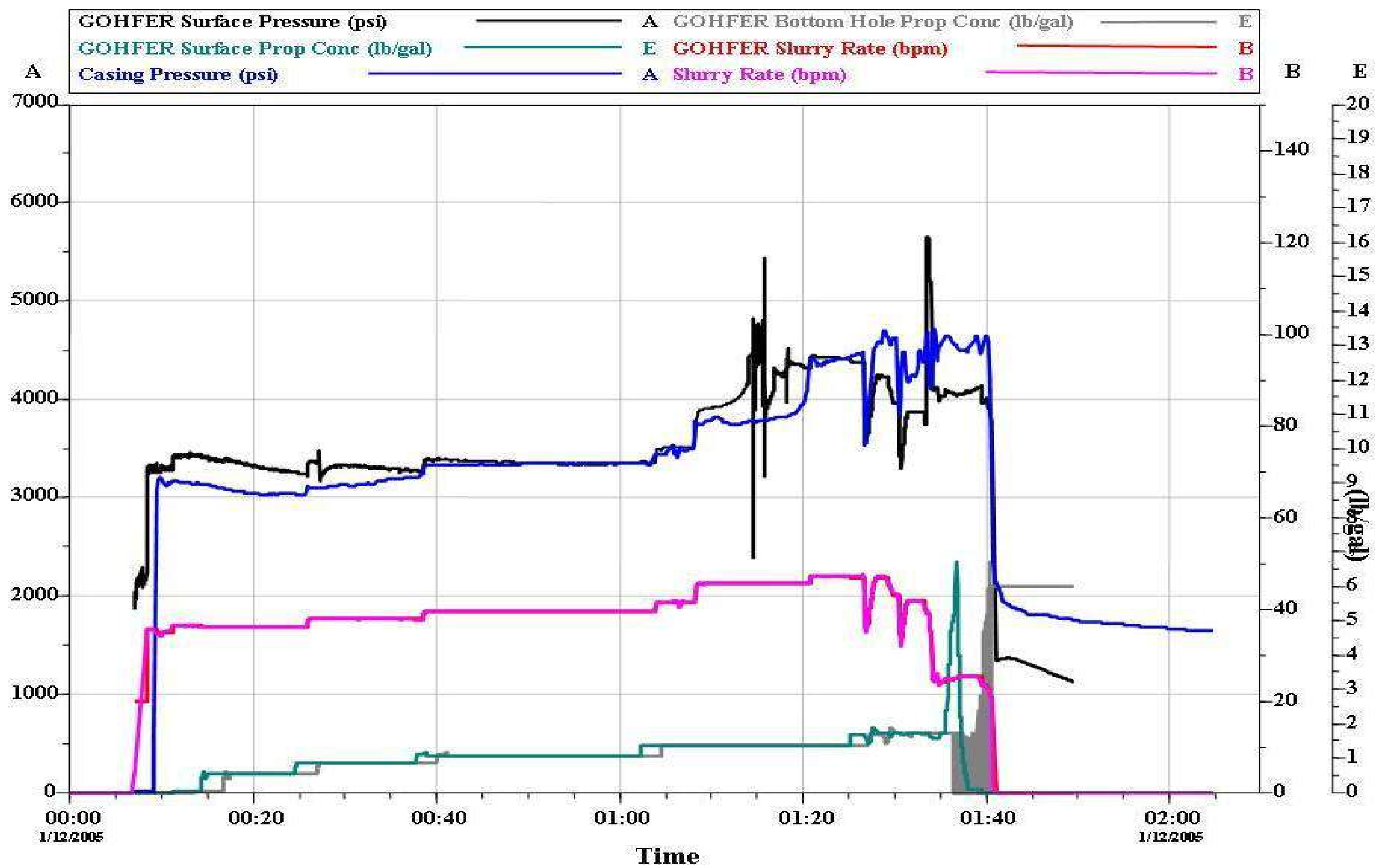

Figure 4-30: Graph showing the matched GOHFER net surface pressure (black) compared to the measured net surface pressure (blue) recorded (psi) during the actual treatment of Interval G.

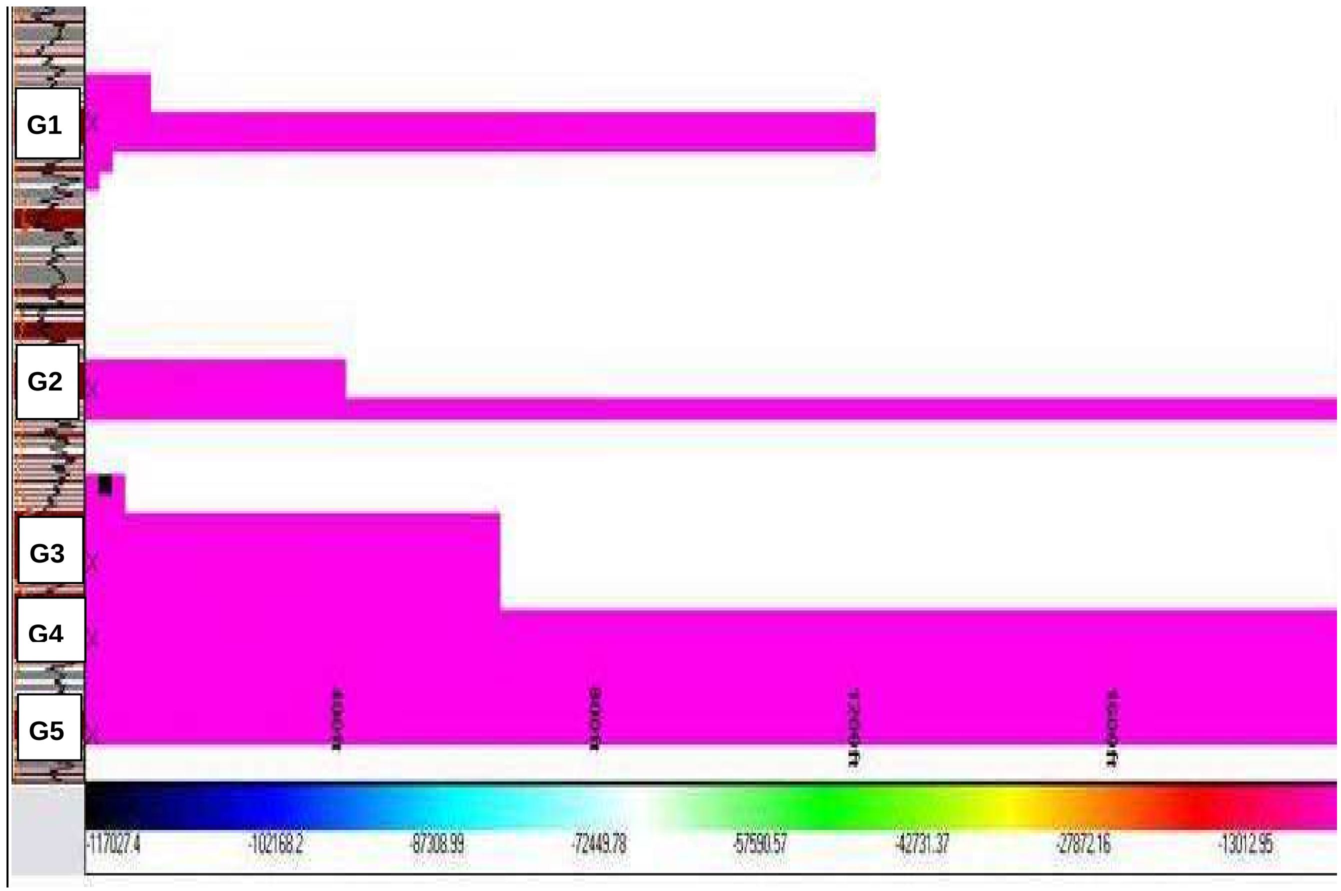

Figure 4-31: GOHFER net pressure (psi) output grid for the Interval G final simulator run.

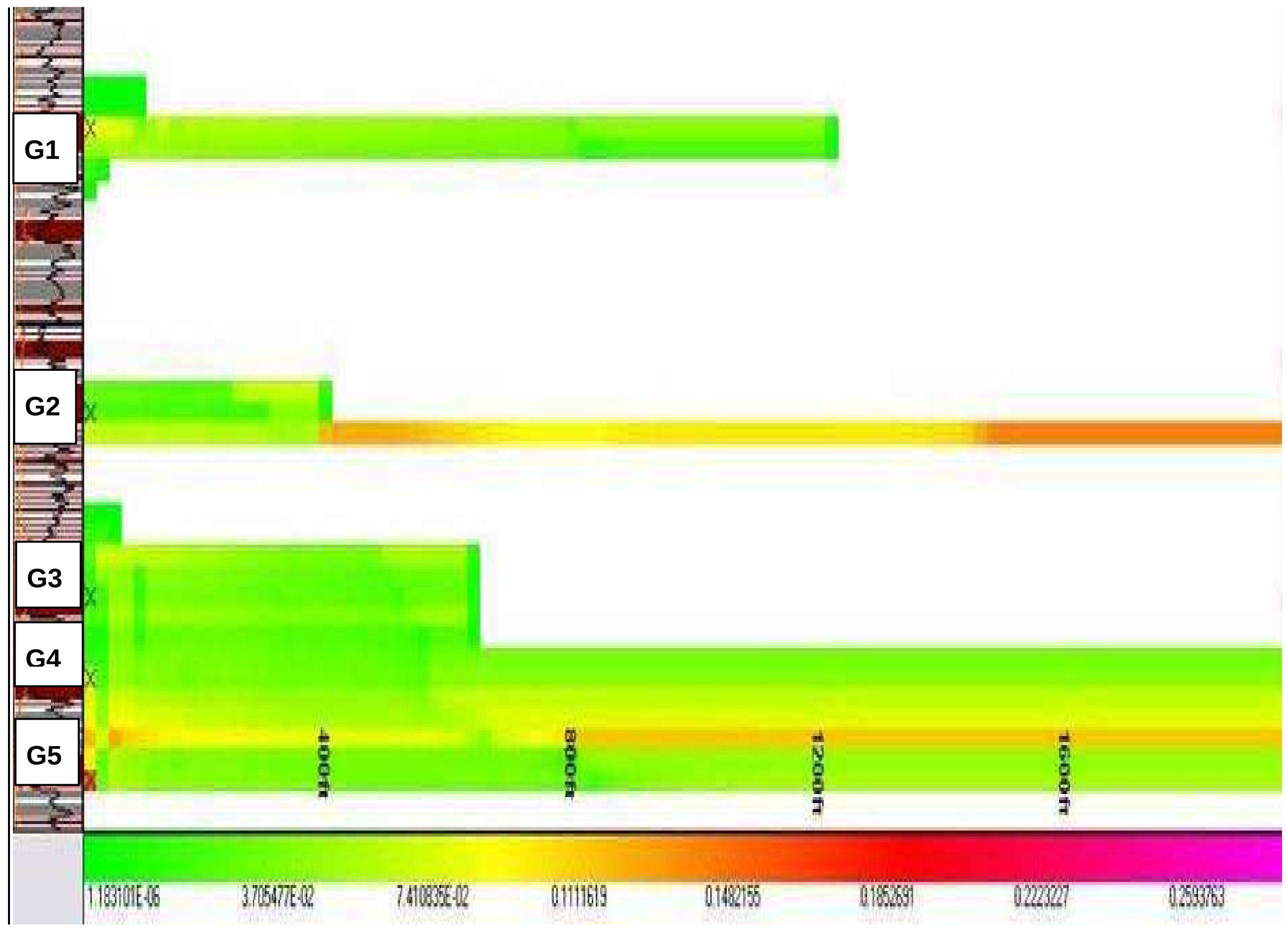

Figure 4-32: GOHFER fracture width (in) output grid for the Interval G final simulator run.

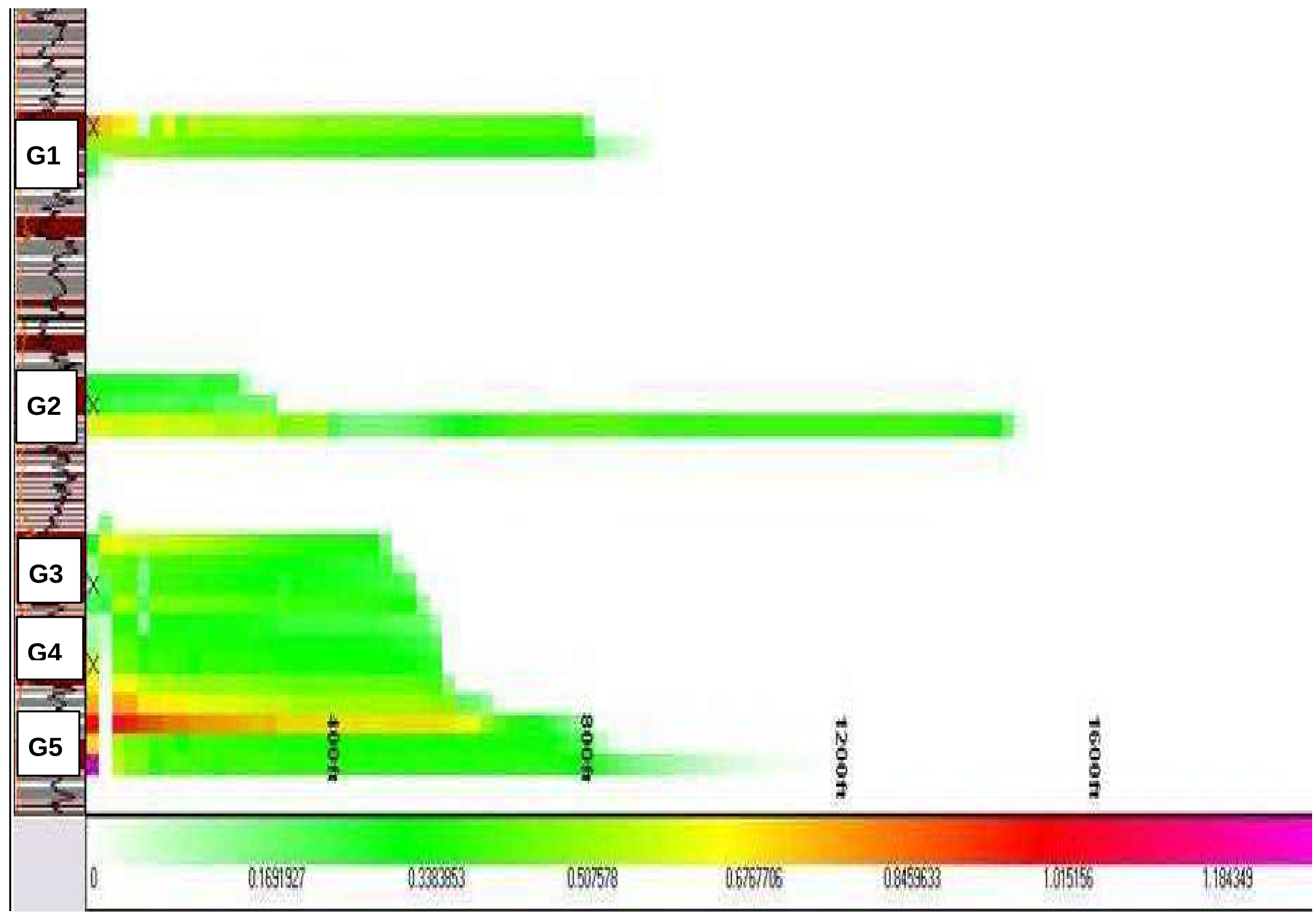

Figure 4-33: GOHFER proppant concentration (lb/ft^2) output grid for the Interval G final simulator run.

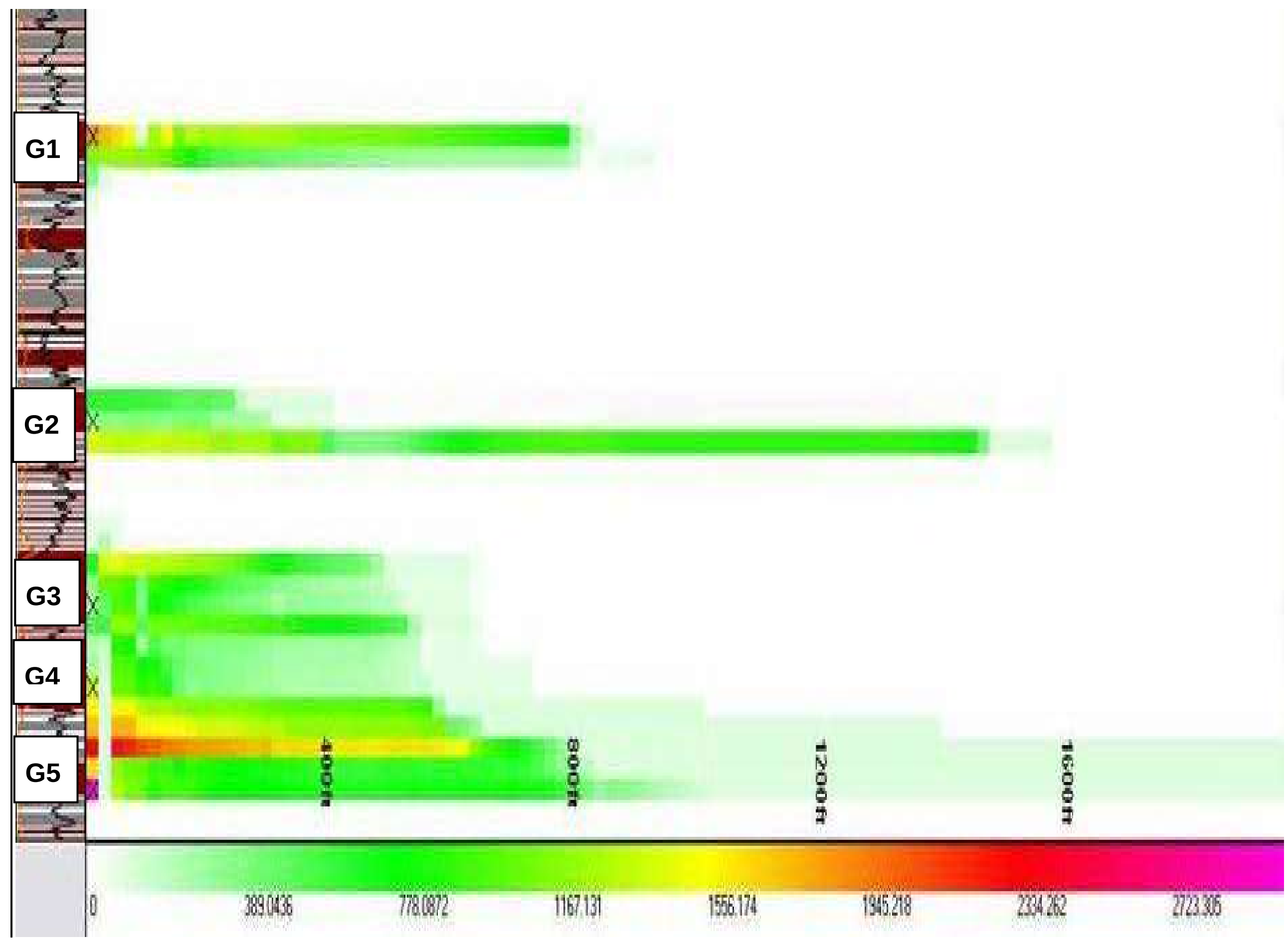

Figure 4-34: GOHFER conductivity (md-ft) output grid for the Interval G final simulator run.

(Figure 4-32), proppant concentration (Figure 4-33) and fracture conductivity (Figure 4-34) all follow a general gradient decreasing upwards in the interval, with the greatest concentration in the lowest Zone G5.

4.3 Matched Model Sensitivity Analyses

The previous section described the workflow, reasoning and decision-making process used to arrive at the final matched models for the six study well intervals. In this section, the matched model results are used to perform sensitivity analyses of various key inputs. The base matched models are those from Sections 4.2.1 – 4.2.6 without any perforation factors (used to match the late-time data) incorporated. The justification for not including perforation factors is that screen-outs are common in all the models unless the perforation factor was removed. Not incorporating perforation factors does not affect the sensitivity analysis but does allow the full range of possible outcomes to occur. The model parameters used for comparison in the sensitivity analyses are net pressure, fracture width, proppant concentration and fracture conductivity. The results of these parameters from the matched models are outlined in Table 4-4.

The interval matched models (Table 4-4) are compared against nine cases (detailed in Table 4-5) used to assess the effects of key inputs on the final matched model outputs. The reasoning behind the nine options is explained in Table 4-5 and is intended to represent data deficiencies that hydraulic modeling practitioners might face. When undertaking simulations, one of the biggest unknowns is what percentage error might a model have if certain inputs are assumed or ignored? This section addresses this question in relation to the final matched models.

Table 4-4: The Matched HF Model Outputs

MATCH Model Outputs from Section 4.2		Intervals					
		A	G	M	O	S	T
Av. prop conc.	**#/ft^2**	0.3167	0.2107	0.2353	0.2126	0.2193	0.3102
Fracture Efficiency	**%**	4.98%	28.53%	9.43%	9.63%	10.47%	4.94%
Fracture Length Created	**ft**	1940	>2000 ft	>2000 ft	1940	1840	>2000 ft
Fracture Height	**ft**	200	240	370	220	310	230
Average Fracture Width	**in**	0.0415	0.0638	0.0358	0.0429	0.0356	0.0339
Maximum Fracture Width	**in**	0.1635	0.1614	0.1103	0.0871	0.0991	0.1769

Table 4-5: Simulator Sensitivity Cases and Associated Reasons

Case Name	Description	Reason
MATCH	Original matched model without the perforation factors	
1-YM-10%	Model with Young's modulus grid x 0.9	If suitable logs are not available and calculated Young's Modulus has a 10% error.
2 –YM-20%	Model with Young's modulus grid x 0.8	As Case 1 but with a 20% error, done for comparison purposes with the 10% error.
3 –PR-10%	Model with Poisson's ratio grid x 0.9	If suitable logs are not available and calculated Poisson's ratio has a 10% error.
4 –PR-20%	Model with Poisson's ratio grid x 0.8	As Case 3 but with a 20% error, done for comparison purposes with the 10% error.
5 -PP OFFSET	Model with the pore pressure offset the same throughout the interval.	If limited mini-frac tests are available and the grid is set at an overpressure of the largest sand reservoir within the interval.
6 -NO PARAM	Matched model with no advanced parameters (i.e. MSF, PDL, etc.)	No advanced parameters used.
7 -BIOTS	Matched model with the vertical Biot's (a_v) grid set to 1	If both the horizontal and vertical Biot's values are set at 1.
8 -PERM	Matched model using the default permeability correlation	If the default values for permeability in tight gas sands are used.
9 -DEFAULT	Matched model with all the default values and no advanced parameters.	If all the default values are used, no advanced parameters and a constant fluid gradient.
10 –STRESS-10%	Model with the total stress grid ($P_{closure}$) grid x 0.9	If the model has a 10% error for the calculated total stress.
11 –STRESS-20%	Model with the total stress grid ($P_{closure}$) grid x 0.8	If the model has a 20% error for the calculated total stress.

Result of Cases 1 & 2 – Young's modulus

The results of the simulations of changes to the Young's modulus grid are shown in Table 4-6. As can be seen, the average proppant concentration, efficiency, fracture half-length created and maximum and average fracture widths all increase in value, with the only decrease being fracture height. While the general trends were the same, the values for individual intervals differed slightly. Interval T had the greatest decrease for Case 1 and Interval A the least, while all intervals except A showed a decrease in fracture height only for Case 2.

Results of Cases 3 & 4 – Poisson's ratio

The results for the simulations where the Poisson's ratio was altered are shown in Table 4-7. In general, average proppant concentration, fracture half-length created and fracture height all decrease. The reduction is not greater for all outputs in Case 4 when compared to Case 3. Differences are probably due to the fact that Case 3 decreases half-length greater than Case 4, but Case 4 decreases height greater than Case 3. The average fracture width and maximum fracture width increase in both cases. While the general trends were the same, the values for individual intervals differed slightly. Interval T had the greatest reductions for Case 3 and Interval A the least reductions, while Interval O had the greatest reductions for Case 4 and Interval G the least.

Result of Cases 5 – Constant pore pressure offset

The results for the constant pore pressure offset simulations are shown in Table 4-8. In general the average proppant concentration, fracture height, average fracture width and maximum fracture width all increase, while efficiency and fracture half-length created decrease. The intervals differed in the values that were increased or decreased with only Intervals G and M having all values increased.

Interval A was unable to be effectively modeled with a constant pore pressure offset, and the simulator gave unreasonable values for efficiency.

Result of Cases 6- No advanced parameters

The results for the simulations using no advanced parameters (defined in Section 4.1) are shown in Table 4-9. The efficiency, created fracture half-length, average fracture width and maximum fracture width all increase while the fracture height generally decreases. However, the changes were not uniform across the intervals with only Intervals G and M having a similar decrease in fracture height. As in other models Interval T and Interval A outputs were different when compared to the other intervals.

Result of Cases 7 – Vertical Biot's constant at 1

The results for simulations of the vertical Biot's constant changes are shown in Table 4-10. The intervals show a general decrease in the average proppant concentration and fracture half-length created, though the differences are only minor, -1% and -4% respectively. Efficiency, fracture height created, average fracture width and maximum fracture width all increase. Similar to other analyses, the output values seem to be interval specific and only Intervals G and S show no decreases in any of the simulator outputs.

Result of Cases 8 – Permeability correlation

The results for simulation of the values for the permeability correlation are shown in Table 4-11. The permeability correlation used for this experiment is described in Section 3.4.5., where K_1 equals 17.75 and K_2 equals 3. For tight gas reservoirs a typical value for K_1 of 50 is recommended in the simulator manual and this was simulated in Case 8 and compared to the study match permeability correlation. The permeability correlation gives a permeability just over double the value used for the matched simulations and is intended to assess the effect of small permeability changes. As can be seen, the values change significantly with average proppant concentration, fracture height and maximum fracture width increasing in value. Efficiency, fracture half-length created and average fracture width all decrease in value. Increasing the permeability decreases the efficiency and fracture half-length across all intervals. However, the fracture width decreases in Intervals O and G but increases in Intervals M, S, T and A. Similarly the fracture height decreases in Intervals M and O but increases in Intervals A, G, S and T.

Result of Cases 9 – Default inputs used

This simulation is a “worst case” scenario where all the default values are used together with the actual perforation numbers from the well file, as shown in Table 4-3. The values for the inputs were as in Cases 5, 6, 7, 8 and 9 where default values were used throughout and the pore pressure offset and Biot’s constant were the same value for the interval. The results for simulations with the default values are shown in Table 4-12. The average proppant concentration, fracture height, average fracture width and maximum fracture width all increase, while efficiency and created fracture half-length decrease.

Results of Cases 10 & 11 – Stress – 10% and 20%

One of the most important and difficult areas for hydraulic fracture modelers is trying to build a representative stress model. Critical to this model is determining closure stress. The simulation of total stress minus 10 % showed little differences when compared to the matched model. The efficiency and average fracture width increase, while the average proppant concentration, fracture height

Table 4-6: GOHFER Output Values for Cases 1 & 2 – Young's Modulus Changes

YM-10% Model Outputs		Interval												Av. Diff.
		A		G		M		O		S		T		
		New Value	% Diff	New Value	% Diff	New Value	% Diff	New Value	% Diff	New Value	% Diff	New Value	% Diff	
Av. prop. conc.	#/ft^2	0.3595	14	0.2148	2	0.272	16	0.2409	13	0.2399	9	0.3133	1	9%
Efficiency	%	5.53	11	32.84	15	11.30	20	12.42	29	11.94	14	4.68	-5	14%
Fracture Length Created	Ft	>2000		>2000		>2000		2140	10	>2000		>2000		10%
Fracture Height	Ft	200	0	220	-8	340	-8	180	-18	330	6	210	-9	-6%
Average Fracture Width	In	0.0459	11	0.0737	16	0.0417	16	0.0614	43	0.0415	17	0.0438	29	22%
Maximum Fracture Width	In	0.1884	15	0.1661	3	0.1212	10	0.0986	13	0.1005	1	0.1343	-24	3%

YM-20% Model Outputs		Interval												Av. Diff.
		A		G		M		O		S		T		
		New Value	% Diff	New Value	% Diff	New Value	% Diff	New Value	% Diff	New Value	% Diff	New Value	% Diff	
Av. prop. conc.	#/ft^2	0.4043	28	0.2342	11	0.281	19	0.2433	14	0.256	17	0.3209	3	15%
Efficiency	%	6.97	40	31.34	10	13.29	41	15.15	57	14.76	41	5.70	15	34%
Fracture Length Created	Ft	>2000		>2000		>2000		2260	16	1920	4	>2000		10%
Fracture Height	Ft	200	0	220	-8	300	-19	160	-27	300	-3	200	-13	-12%
Average Fracture Width	In	0.0512	23	0.0898	41	0.059	65	0.0762	78	0.0528	48	0.0492	45	50%
Maximum Fracture Width	In	0.1429	-13	0.1847	14	0.1292	17	0.1169	34	0.1215	23	0.1659	-6	12%

Table 4-7: GOHFER Output Values for Cases 3 & 4 – Poisson's Ratio Changes

PR-10% Model Outputs		Interval												
		A		G		M		O		S		T		Av. Diff.
		New Value	% Diff	New Value	% Diff	New Value	% Diff	New Value	% Diff	New Value	% Diff	New Value	% Diff	
Av. prop. conc.	#/ft^2	0.3242	2	0.2166	3	0.2145	-9	0.2083	-2	0.1768	-19	0.305	-2	-4%
Efficiency	%	4.28	-14	32.21	13	10.24	9	9.83	2	12.33	18	4.90	-1	4%
Fracture Length Created	ft	>2000		>2000		1940		1660	-14	>2000		>2000		-14%
Fracture Height	ft	220	10	240	0	360	-3	210	-5	310	0	210	-9	-1%
Average Fracture Width	in	0.0421	1	0.0659	3	0.0347	-3	0.0446	4	0.044	24	0.0415	22	9%
Maximum Fracture Width	in	0.1667	2	0.154	-5	0.12	9	0.0962	10	0.1251	26	0.1353	-24	3%

PR-20% Model Outputs		Interval												
		A		G		M		O		S		T		Av. Diff
		New Value	% Diff	New Value	% Diff	New Value	% Diff	New Value	% Diff	New Value	% Diff	New Value	% Diff	
Av. prop. conc.	#/ft^2	0.3207	1	0.224	6	0.2346	0	0.2182	3	0.2137	-3	0.3041	-2	1%
Efficiency	%	7.88	58	33.77	18	10.11	7	9.57	-1	13.63	30	5.05	2	19%
Fracture Length Created	ft	>2000		>2000		>2000		1820	-6	1840		>2000		-6%
Fracture Height	ft	180	-10	250	4	340	-8	190	-14	310	0	230	0	-5%
Average Fracture Width	in	0.0414	0	0.0699	10	0.0419	17	0.044	3	0.043	21	0.0414	22	12%
Maximum Fracture Width	in	0.182	11	0.1577	-2	0.1169	6	0.0937	8	0.1182	19	0.1438	-19	4%

Table 4-8: GOHFER Output Values for Case 5 – Constant Pore Pressure Offset

PP OFFSET Model Outputs		Interval												Av. Diff.
		A		G		M		O		S		T		
		New Value	% Diff	New Value	% Diff	New Value	% Diff	New Value	% Diff	New Value	% Diff	New Value	% Diff	
Av. prop. conc.	#/ft^2	0.2933	-7	0.2179	3	0.2609	11	0.2072	-3	0.2703	23	0.3154	2	5%
Efficiency	%	0.00	-100	29.62	4	10.15	8	10.88	13	12.43	19	4.88	-1	-10%
Fracture Length Created	ft	1740		>2000		>2000		1560	-20	>2000		>2000		-20%
Fracture Height	ft	380	90	340	42	410	11	230	5	370	19	250	9	29%
Average Fracture Width	in	0.0418	1	0.0706	11	0.0433	21	0.052	21	0.0445	25	0.0444	31	18%
Maximum Fracture Width	in	0.2104	29	0.1698	5	0.1183	7	0.1017	17	0.0937	-5	0.1906	8	10%

Table 4-9: GOHFER Output Values for Case 6 – No Advanced Parameters Used

NO ADV PARAMETERS Model Outputs		Interval												Av. Diff.
		A		G		M		O		S		T		
		New Value	% Diff	New Value	% Diff	New Value	% Diff	New Value	% Diff	New Value	% Diff	New Value	% Diff	
Av. prop. conc.	#/ft^2	0.2694	-15	0.2255	7	0.2442	4	0.1704	-20	0.2777	27	0.3151	2	1%
Efficiency	%	12.64	154	29.41	3	20.96	122	16.03	66	15.30	46	7.04	43	72%
Fracture Length Created	ft	>2000		>2000		>2000		3760	94	>2000		>2000		94%
Fracture Height	ft	220	10	180	-25	270	-27	160	-27	310	0	220	-4	-12%
Average Fracture Width	in	0.058	40	0.1087	70	0.0888	148	0.0682	59	0.061	71	0.0549	62	75%
Maximum Fracture Width	in	0.1617	-1	0.2775	72	0.2031	84	0.1112	28	0.1209	22	0.1503	-15	32%

Table 4-10: GOHFER Output Values for Case 7 – Vertical Biot's Set at 1

BIOTS Model Outputs		A		G		M		O		S		T		Av. Diff.
		New Value	% Diff	New Value	% Diff	New Value	% Diff	New Value	% Diff	New Value	% Diff	New Value	% Diff	
Av. prop. conc.	#/ft^2	0.304	-4	0.2449	16	0.234	-1	0.1951	-8	0.2195	0	0.2802	-10	-1%
Efficiency	%	0.00	-100	47.76	67	8.96	-5	11.25	17	23.05	120	4.51	-9	15%
Fracture Length Created	ft	>2000		>2000		>2000		1860	-4	>2000		>2000		-4%
Fracture Height	ft	250	25	270	13	380	3	230	5	340	10	240	4	10%
Average Fracture Width	in	0.0383	-8	0.071	11	0.0393	10	0.0481	12	0.0519	46	0.0393	16	15%
Maximum Fracture Width	in	0.3343	104	0.1759	9	0.1091	-1	0.0966	11	0.1411	42	0.1173	-34	22%

Table 4-11: GOHFER Output Values for Case 8 – Permeability Correlation from the GOHFER User Manual

PERM Model Outputs		A		G		M		O		S		T		Av. Diff.
		New Value	% Diff	New Value	% Diff	New Value	% Diff	New Value	% Diff	New Value	% Diff	New Value	% Diff	
Av. prop. conc.	#/ft^2	0.3165	0	0.2403	14	0.2828	20	0.2482	17	0.2483	13	0.3225	4	11%
Efficiency	%	3.00	-40	19.96	-30	7.44	-21	5.47	-43	9.56	-9	1.28	-74	-36%
Fracture Length Created	ft	1700	-12	>2000		1680		1580	-19	1580	-14	1500		-15%
Fracture Height	ft	230	15	250	4	350	-5	210	-5	310	0	270	17	4%
Average Fracture Width	in	0.0421	1	0.0497	-22	0.0384	7	0.0357	-17	0.0361	1	0.0414	22	-1%
Maximum Fracture Width	in	0.17	4	0.2733	69	0.1673	52	0.0852	-2	0.0907	-8	0.1438	-19	16%

Table 4-12: GOHFER Output Values for Case 9 – Default Inputs used

DEFAULT Model Outputs		Interval												Av. Diff.
		A		G		M		O		S		T		
		New Value	% Diff	New Value	% Diff	New Value	% Diff	New Value	% Diff	New Value	% Diff	New Value	% Diff	
Av. prop. conc.	#/ft^2	0.3274	3	0.2287	9	0.274	16	0.2246	6	0.2628	20	0.3194	3	9%
Efficiency	%	4.74	-5	20.93	-27	9.77	4	7.02	-27	7.47	-29	3.52	-29	-19%
Fracture Length Created	ft	1960		>2000		>2000		1340	-31	>2000		1540		-31%
Fracture Height	ft	370	85	300	25	370	0	210	-5	410	32	380	65	34%
Average Fracture Width	in	0.0394	-5	0.0785	23	0.0505	41	0.0447	4	0.035	-2	0.0506	49	18%
Maximum Fracture Width	in	0.0907	-45	0.2164	34	0.1224	11	0.0838	-4	0.1216	23	0.177	0	3%

Table 4-13: GOHFER Output Values for Case 10 – Total Stress minus 10%

STRESS -10 Model Outputs		Interval												Av. Diff.
		A		G		M		O		S		T		
		New Value	% Diff	New Value	% Diff	New Value	% Diff	New Value	% Diff	New Value	% Diff	New Value	% Diff	
Av. prop. conc.	#/ft^2	0.3285	4	0.188	-11	0.2281	-3	0.2116	0	0.1967	-10	0.2892	-7	-5%
Efficiency	%	5.54	11	31.67	11	11.20	19	11.98	24	13.00	24	5.01	1	15%
Fracture Length Created	ft	>2000		>2000		>2000		1940	0	>2000		>2000		0%
Fracture Height	ft	210	5	250	4	350	-5	180	-18	310	0	220	-4	-3%
Average Fracture Width	in	0.0421	1	0.0622	-3	0.0422	18	0.0544	27	0.0439	23	0.0392	16	14%
Maximum Fracture Width	in	0.3285	4	0.188	-11	0.2281	-3	0.2116	0	0.1967	-10	0.2892	-7	-5%

Table 4-14: GOHFER Output Values for Case 11 – Total Stress minus 20%

STRESS -10 Model Outputs		Interval												Av. Diff.
		A		G		M		O		S		T		
		New Value	% Diff	New Value	% Diff	New Value	% Diff	New Value	% Diff	New Value	% Diff	New Value	% Diff	
Av. prop. conc.	#/ft^2	0.3123	-1	0.1707	-19	0.2152	-9	0.1783	-16	0.2134	-3	0.2602	-16	-11%
Efficiency	%	6.18	24	31.78	11	14.50	54	15.19	58	19.54	87	7.20	46	47%
Fracture Length Created	ft	>2000		>2000		>2000		2420	25	>2000		>2000		25%
Fracture Height	ft	270	35	230	-4	340	-8	180	-18	330	6	210	-9	0%
Average Fracture Width	in	0.04	-4	0.0706	11	0.0499	39	0.0609	42	0.0604	70	0.0416	23	30%
Maximum Fracture Width	in	0.1367	-16	0.155	-4	0.1146	4	0.0929	7	0.1333	10	0.1352	-24	-4%

and maximum fracture width all decrease. However, only Intervals T and M show this trend with Interval A showing increased values for all parameters and Interval O and S only having one lower value for average proppant concentration and fracture height respectively. However, decreasing the total stress a further 10% in Case 11 shows an average reduction in only the average proppant concentration and maximum fracture width. The efficiency, fracture half-length created and average fracture width all increase.

The net surface pressure plots for each interval, overlain with the sensitivity cases simulator outputs, are shown in Figures 4-35 to 4-40. As can be seen from the graphs of Intervals T (Figure 4-35), M (Figure 4-37), S (Figure 4-39) and G (Figure 4-40), most of the cases studied resulted in similarly shaped net surface pressure graphs, when compared to the measured data. Intervals O (Figure 4-36) and A (Figure 4-38) screened out towards the end of the job and the matching process could only be carried out on the early time data, but showed similar trends to the other intervals.

Often operators use a “net surface pressure matching process” to derive models that they then consider reasonable for field application. These results show that the net surface pressure matching process could be easily undertaken using any of the cases, and the resultant model would be significantly different to the “matched” model found in this study.

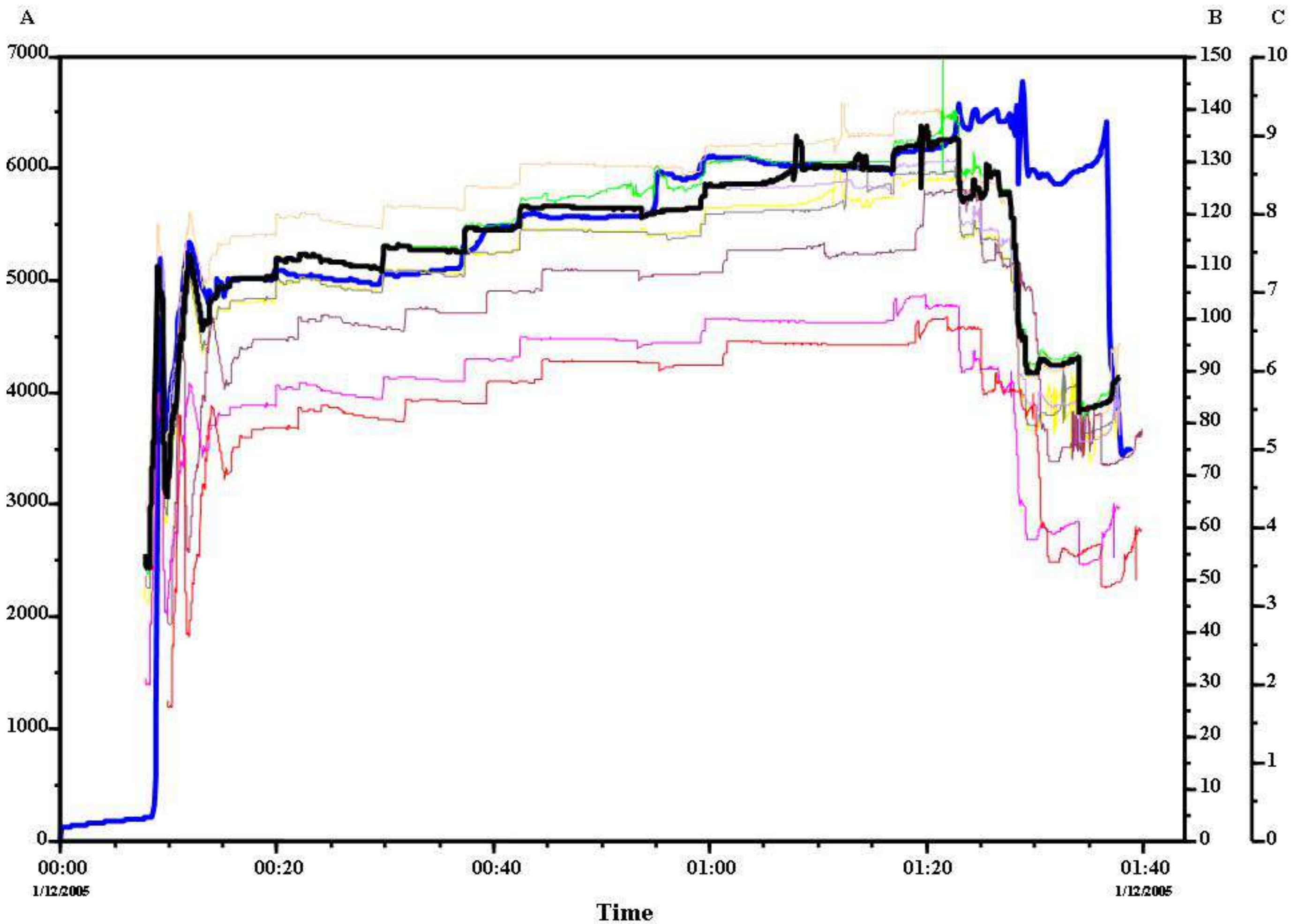

Figure 4-35: Net surface pressure output plots for Interval T sensitivity analyses. The matched graph (black) and original net surface pressure plot (blue) are highlighted.

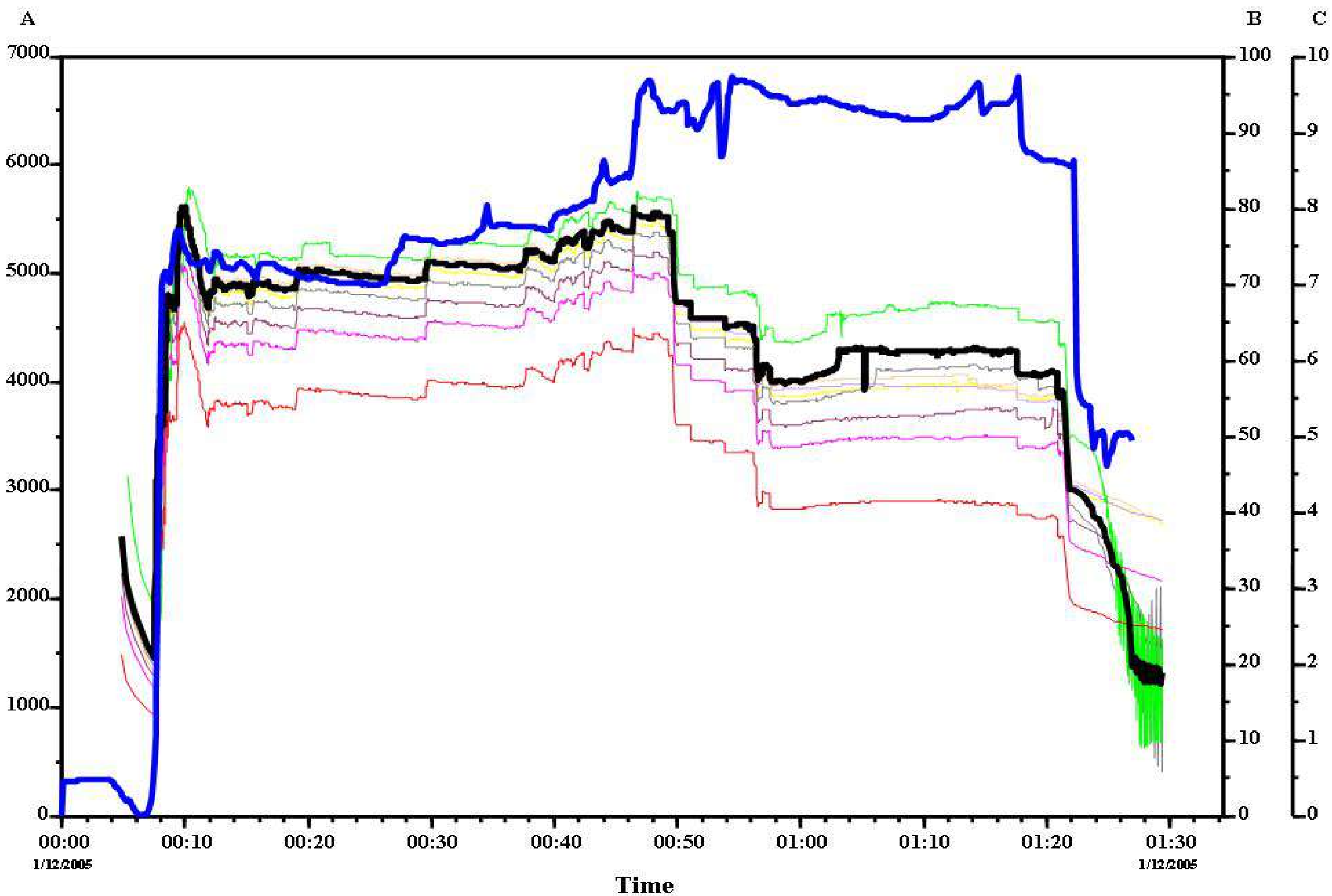

Figure 4-36: Net surface pressure output plots for Interval O sensitivity analyses. The matched graph (black) and original net surface pressure plot (blue) are highlighted.

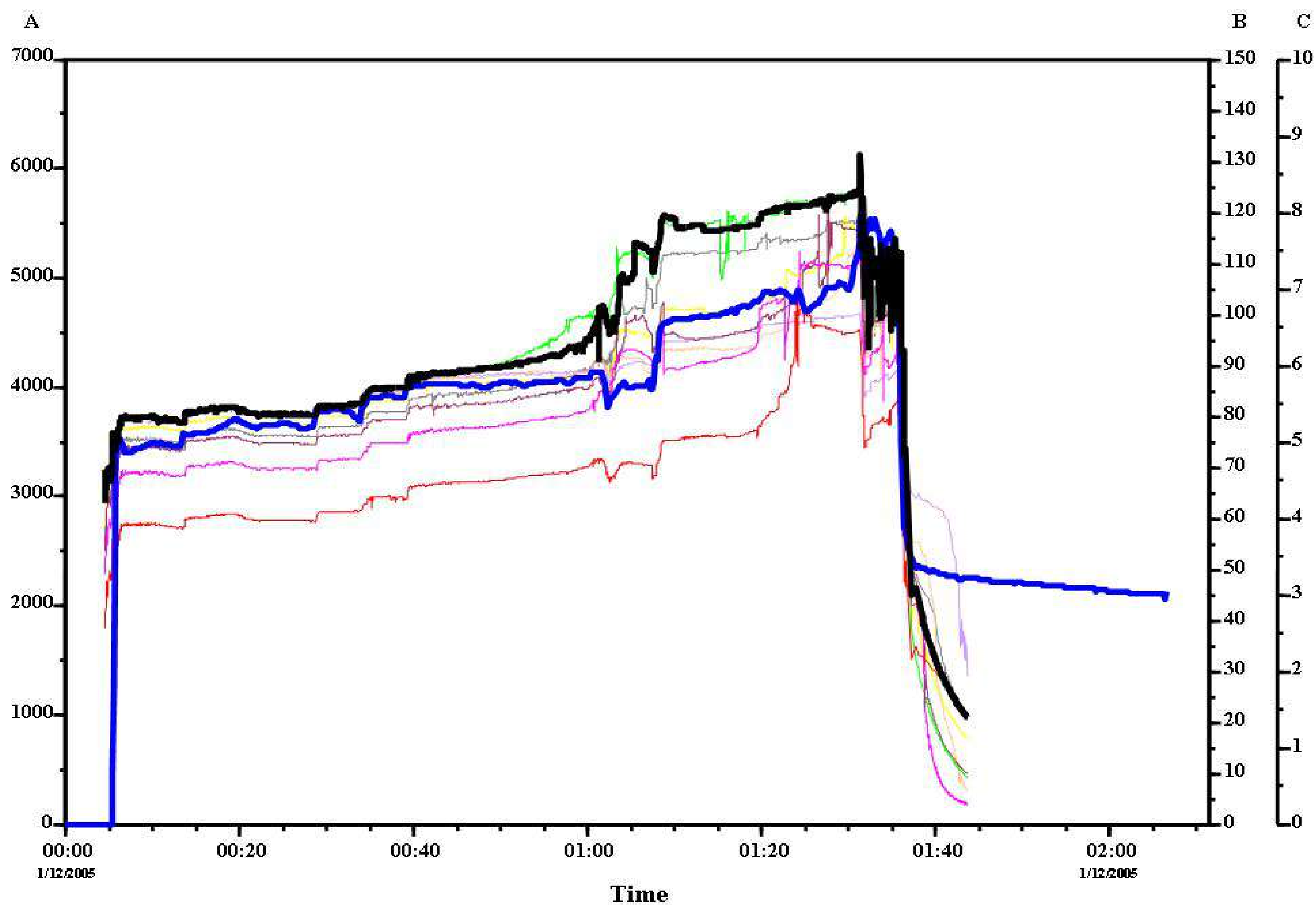

Figure 4-37: Net surface pressure output plots for Interval M sensitivity analyses. The matched graph (black) and original net surface pressure plot (blue) are highlighted.

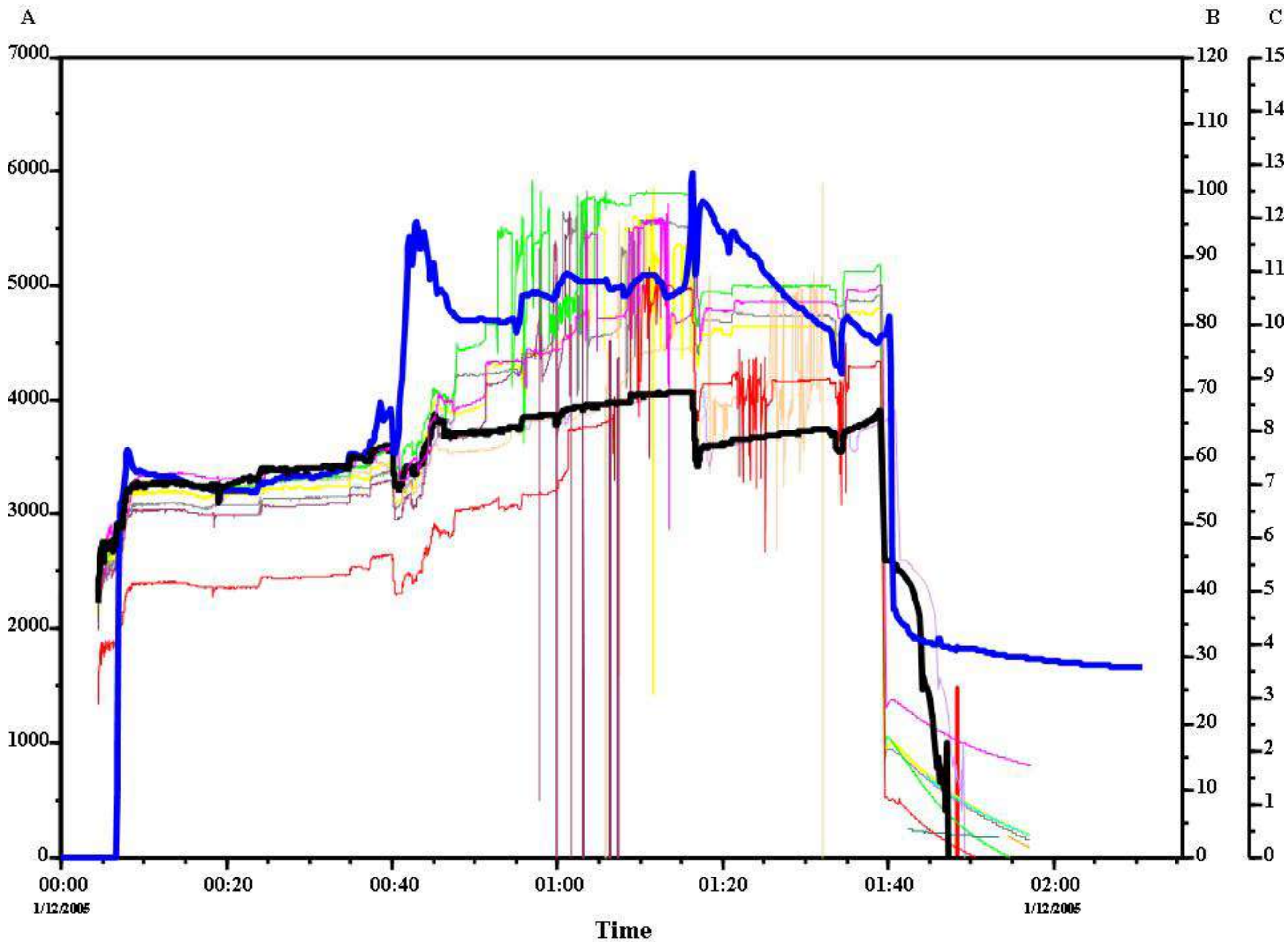

Figure 4-38: Net surface pressure output plots for Interval A sensitivity analyses. The matched graph (black) and original net surface pressure plot (blue) are highlighted.

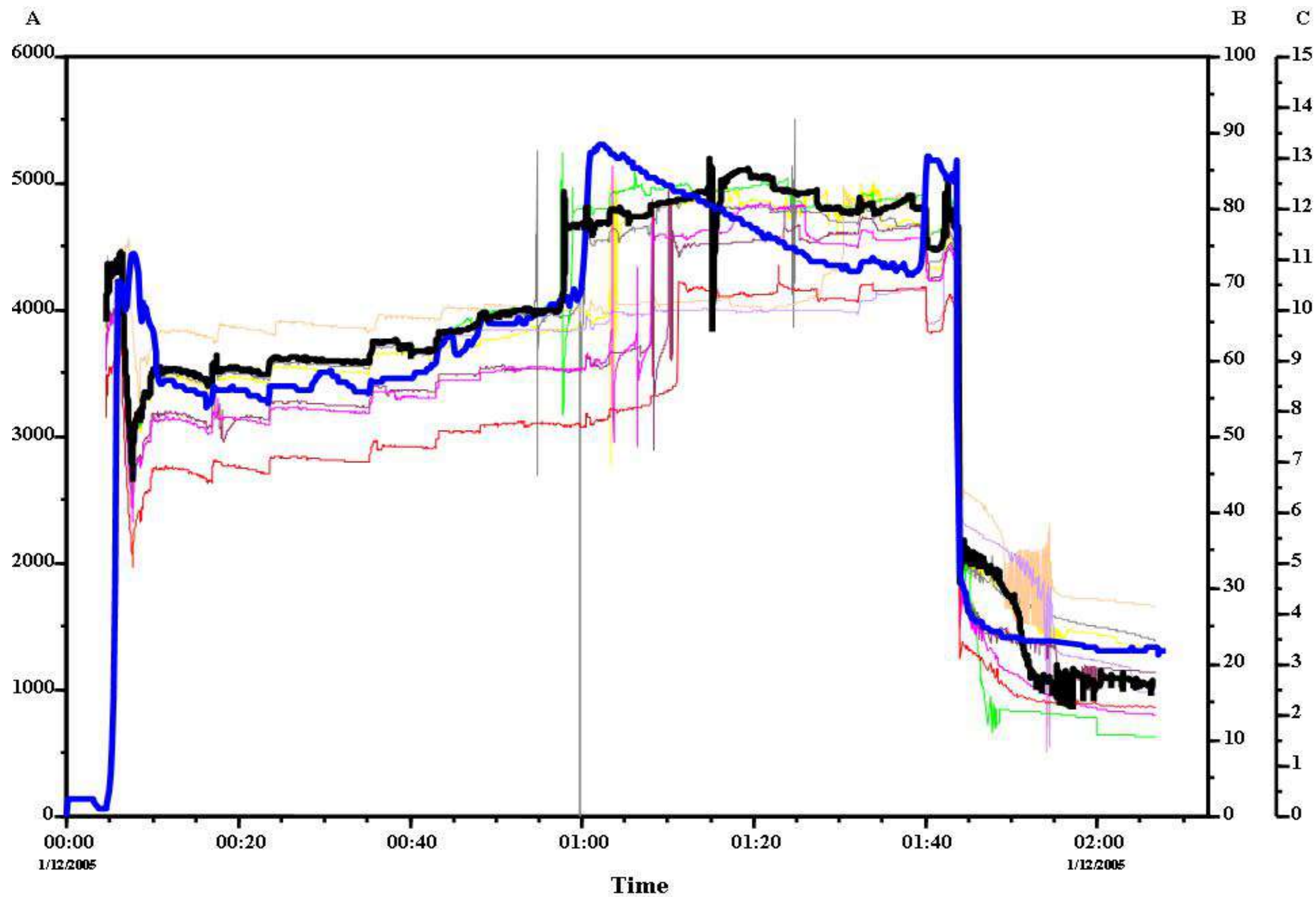

Figure 4-39: Net surface pressure output plots for Interval S sensitivity analyses. The matched graph (black) and original net surface pressure plot (blue) are highlighted.

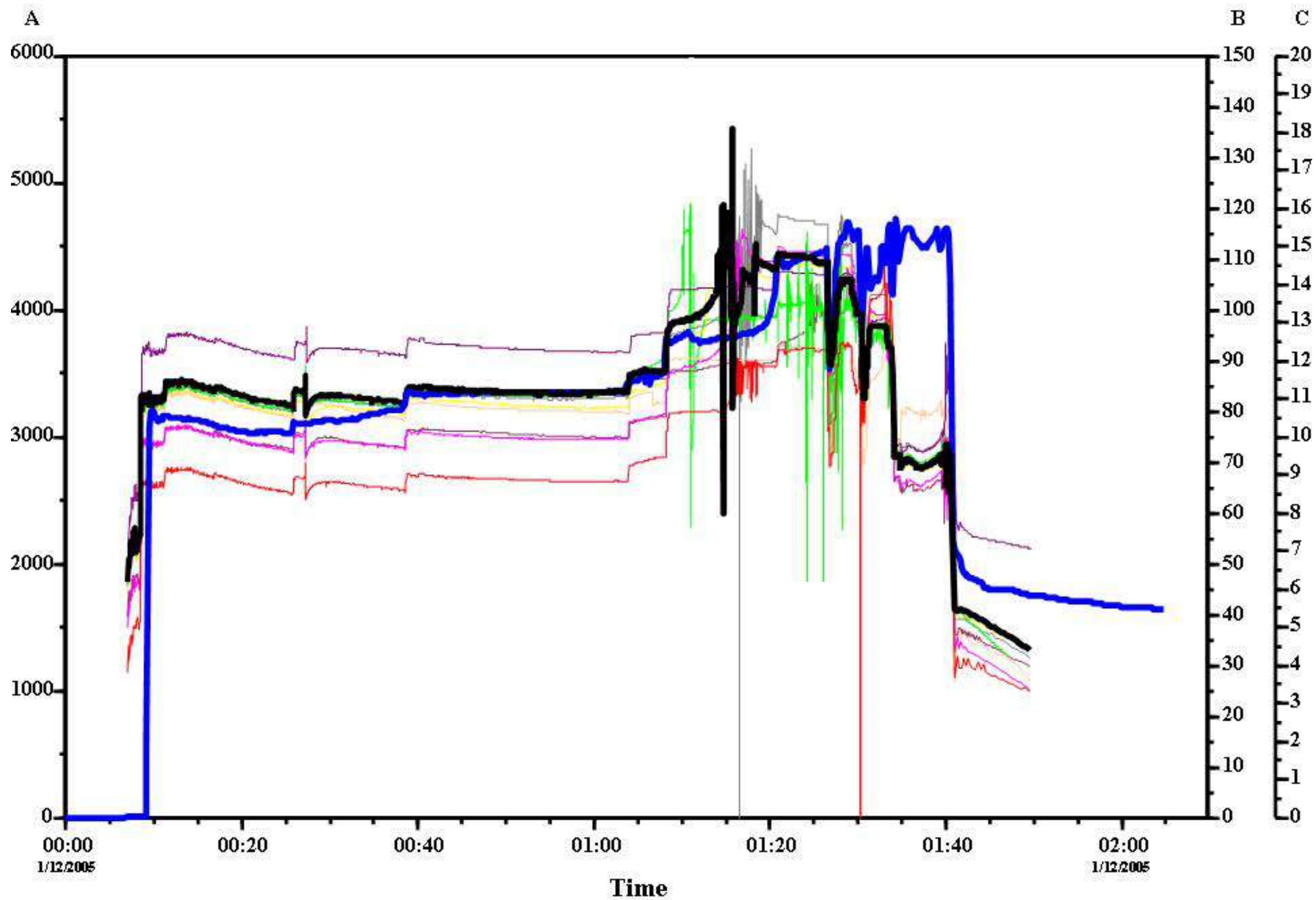

Figure 4-40: Net surface pressure output plots for Interval G sensitivity analyses. The matched graph (black) and original net surface pressure plot (blue) are highlighted.

To get a more detailed insight into the sensitivity analysis of a single interval, Interval O model outputs were investigated in detail. The simulator outputs are described in the following section.

4.3.1 Interval O Sensitivity Analysis

Summary data outputs, like those presented in Tables 4.6 – 4.14, are too general in some instances to give a complete picture of parameter sensitivities. For instance, the created fracture length is the half-length of the longest fracture only within a given zone, and there is little information about changes in proppant distribution across the entire interval. To more fully analyze differences from the various cases (Table 4-5), a single interval, Interval O, was investigated. The proppant concentration outputs for the carious cases are shown in Figures 4-41 to 4-52, and the complete set of outputs are in Appendix B.

Result of Cases 1 & 2 – Young's modulus

The net surface pressure in the match gives a fairly even pressure distribution over the whole interval. In Cases 1 and 2, the net pressure shows a wide variation with a minimum in the lower two zones, O4 and O5. In Case 2, the fracture grows longer in Zones O4 and O5 and this leads to decreased fracture height growth. The fracture width increases in Cases 1 and 2; and, similarly, there is an increasing proppant concentration with the highest concentrations observed in Case 2 (see Figures 4-42 and 4-43). The proppant concentration is highest in Zone O4, but is otherwise fairly well distributed throughout the interval for both Cases 1 and 2, while the matched model highest proppant concentrations are in Zones O2 and O4. The net surface pressure graphs are approximately the same as the matched model plots.

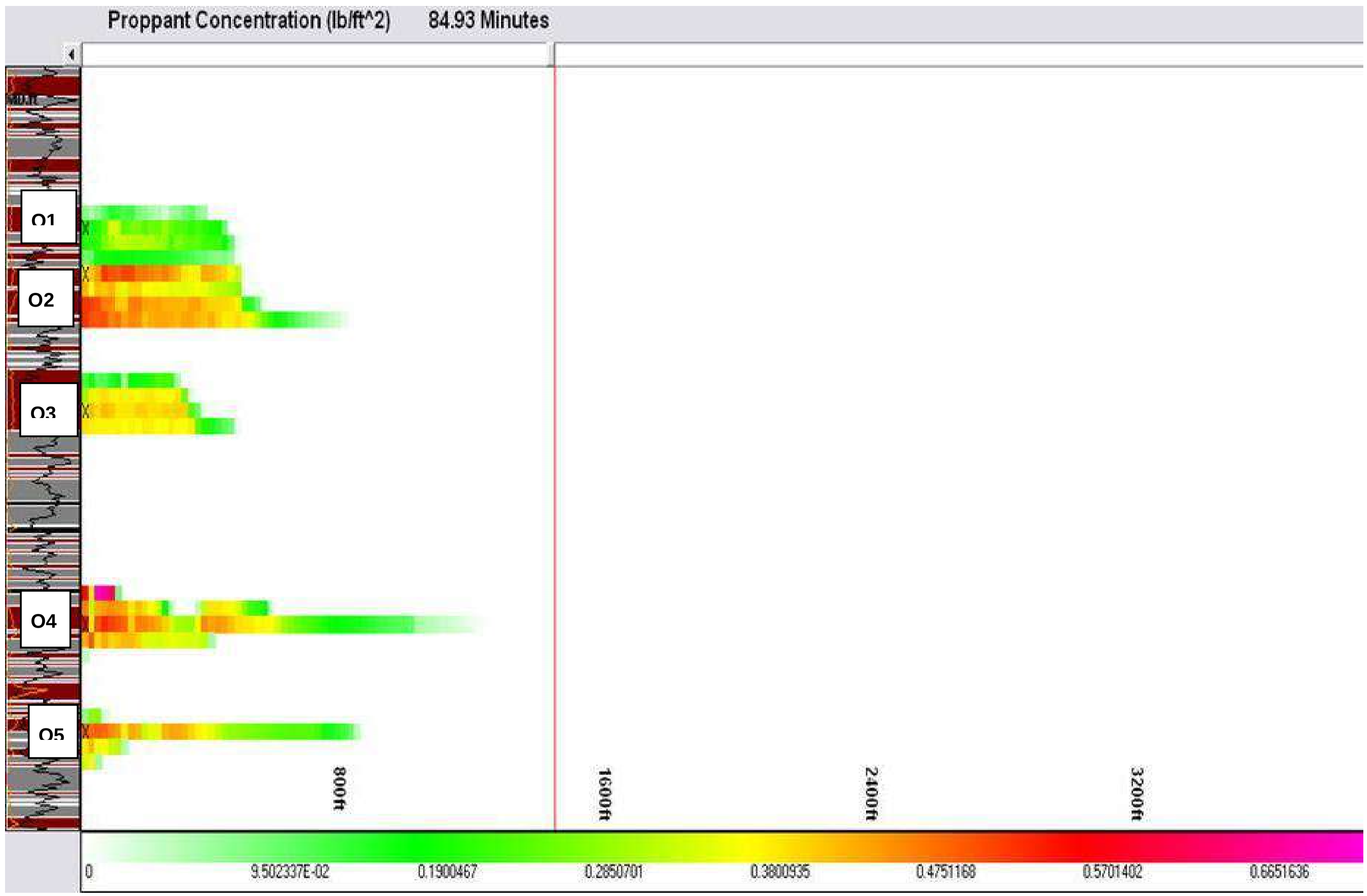

Figure 4-41: Matched model outputs for Interval O showing the proppant concentration grid with the perforated zones highlighted.

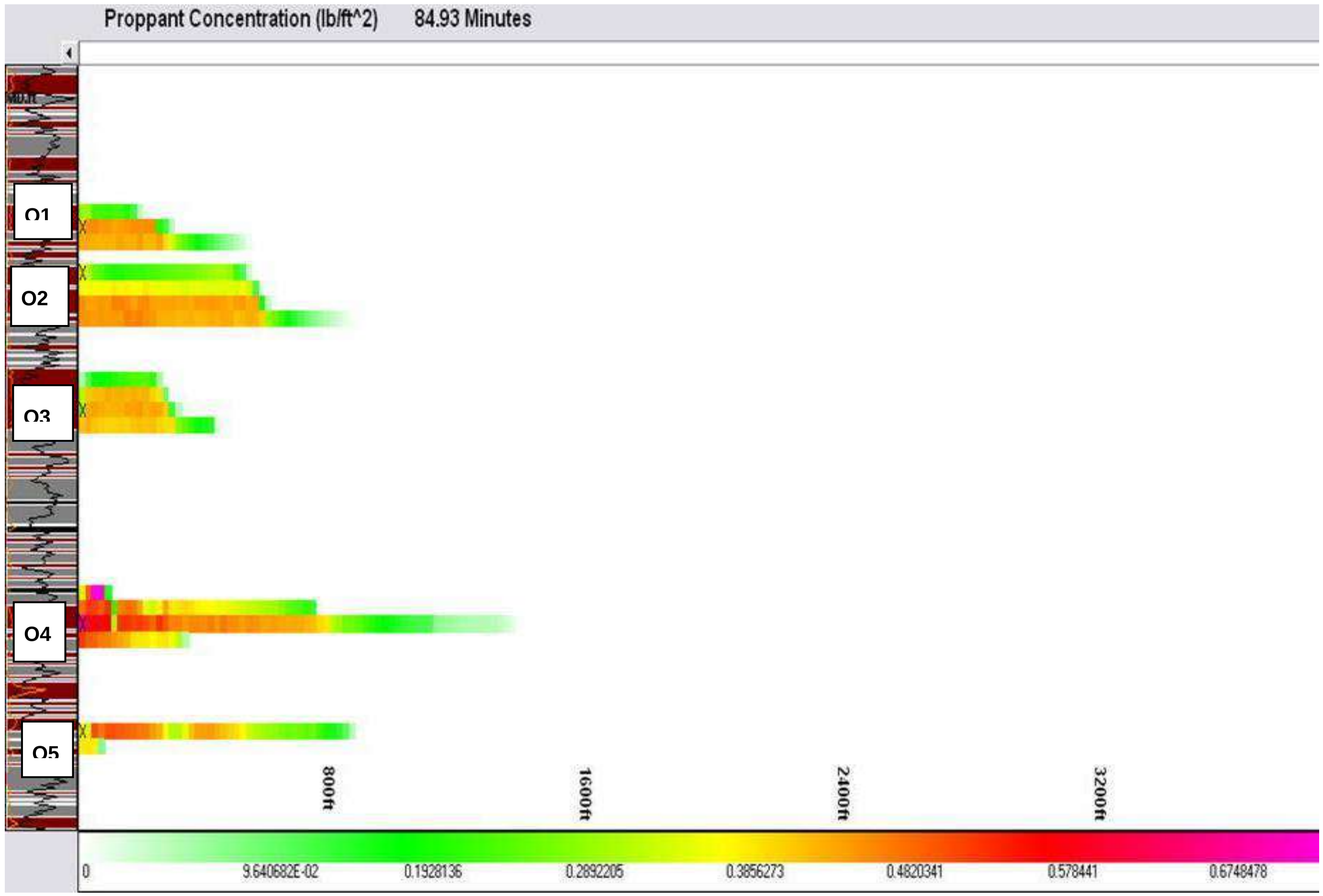

Figure 4-42: YM10 (Young's modulus minus 10%). Case 1 outputs for Interval O showing the proppant concentration grid with the perforated zones highlighted.

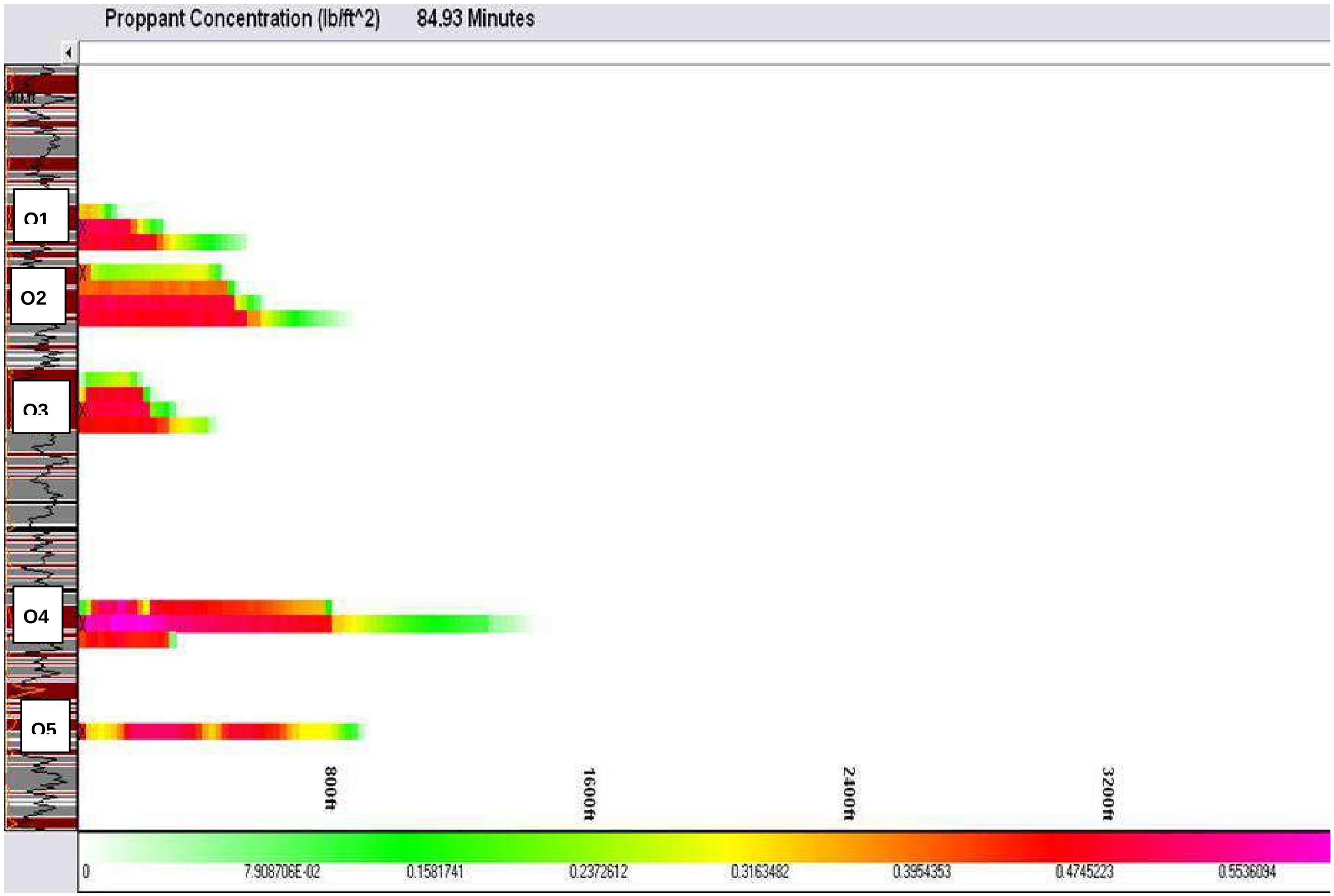

Figure 4-43: YM20 (Young's modulus minus 20%). Case 2 outputs for Interval O showing the proppant concentration grid with the perforated zones highlighted.

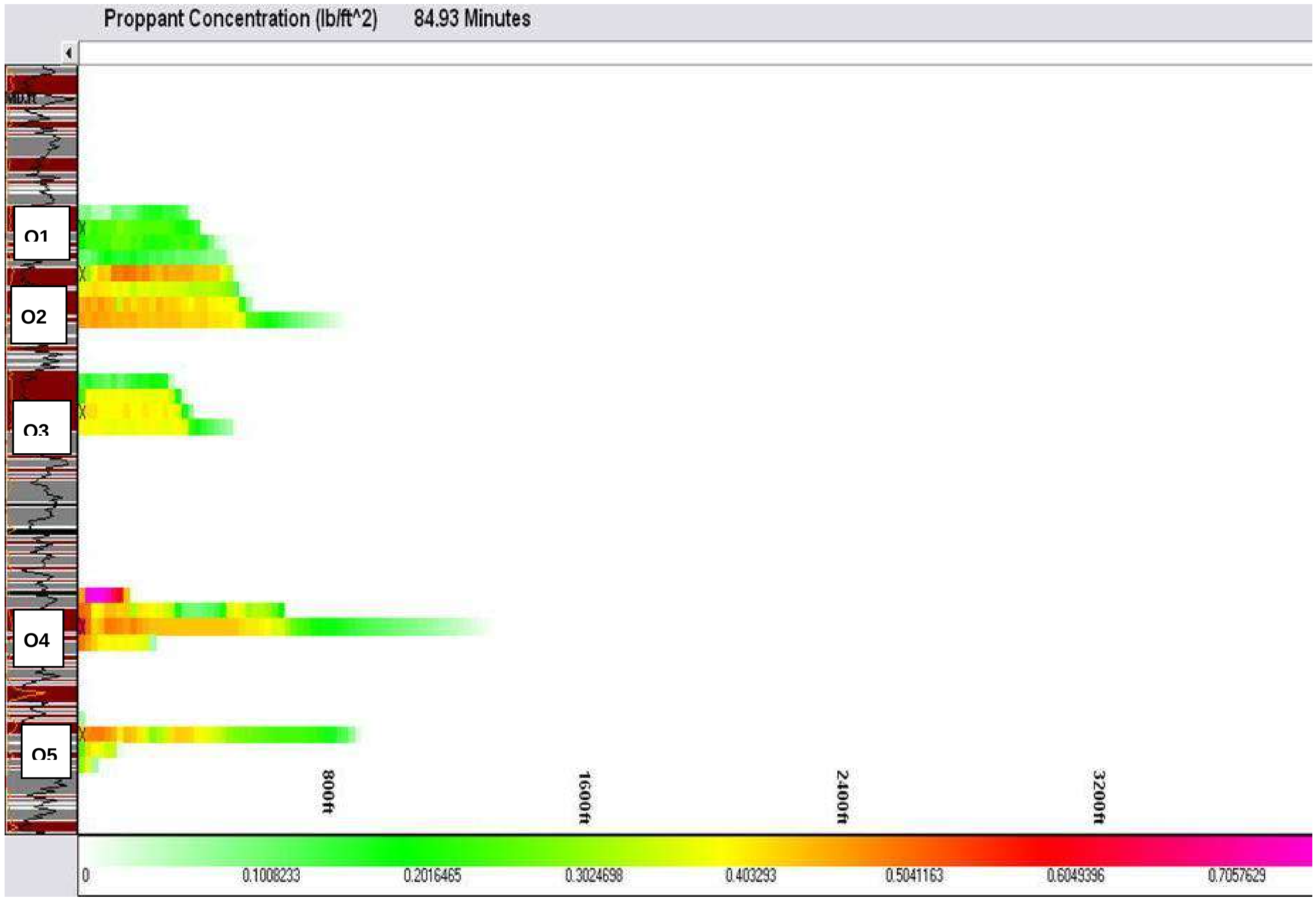

Figure 4-44: PR10 (Poisson’s ratio minus 10%). Case 3 outputs for Interval O showing the proppant concentration grid with the perforated zones highlighted.

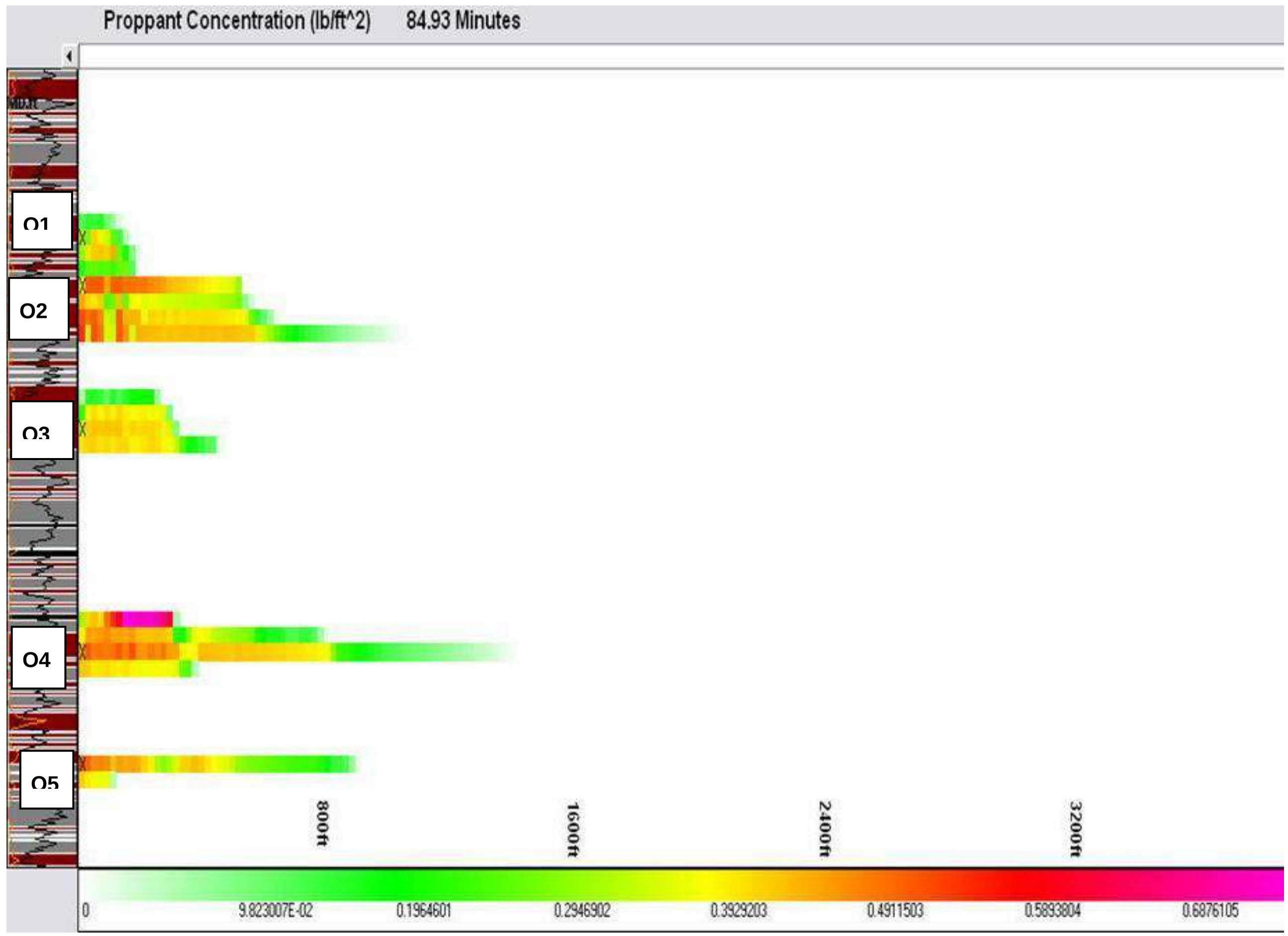

Figure 4-45: PR20 (Poisson's ration minus 20%). Case 4 data run for Interval O showing the proppant concentration grid with the perforated zones highlighted.

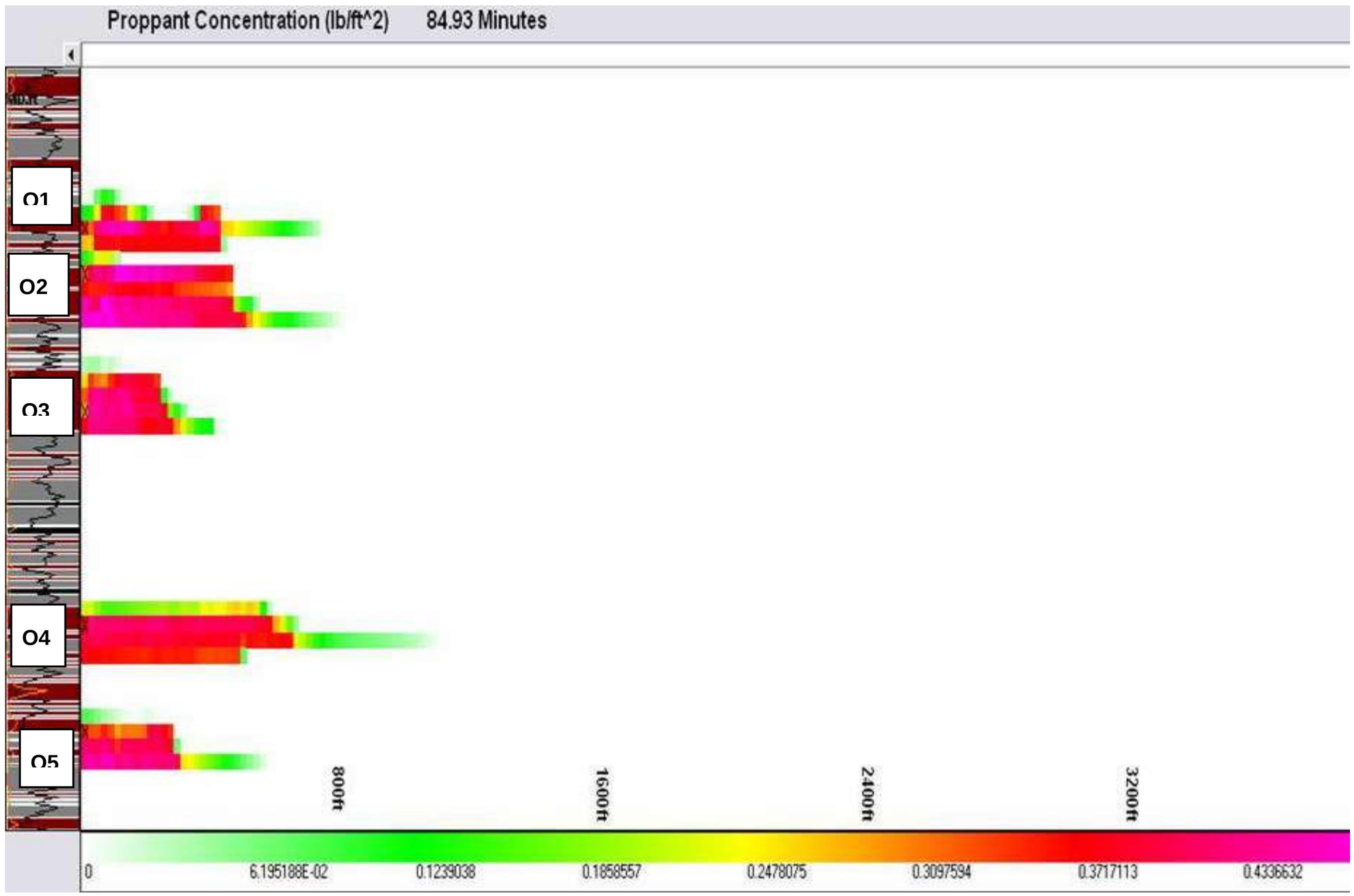

Figure 4-46: PP OFFSET (same 900 psi pore pressure offset gradient). Case 5 output for Interval O showing the proppant concentration grid with the perforated zones highlighted.

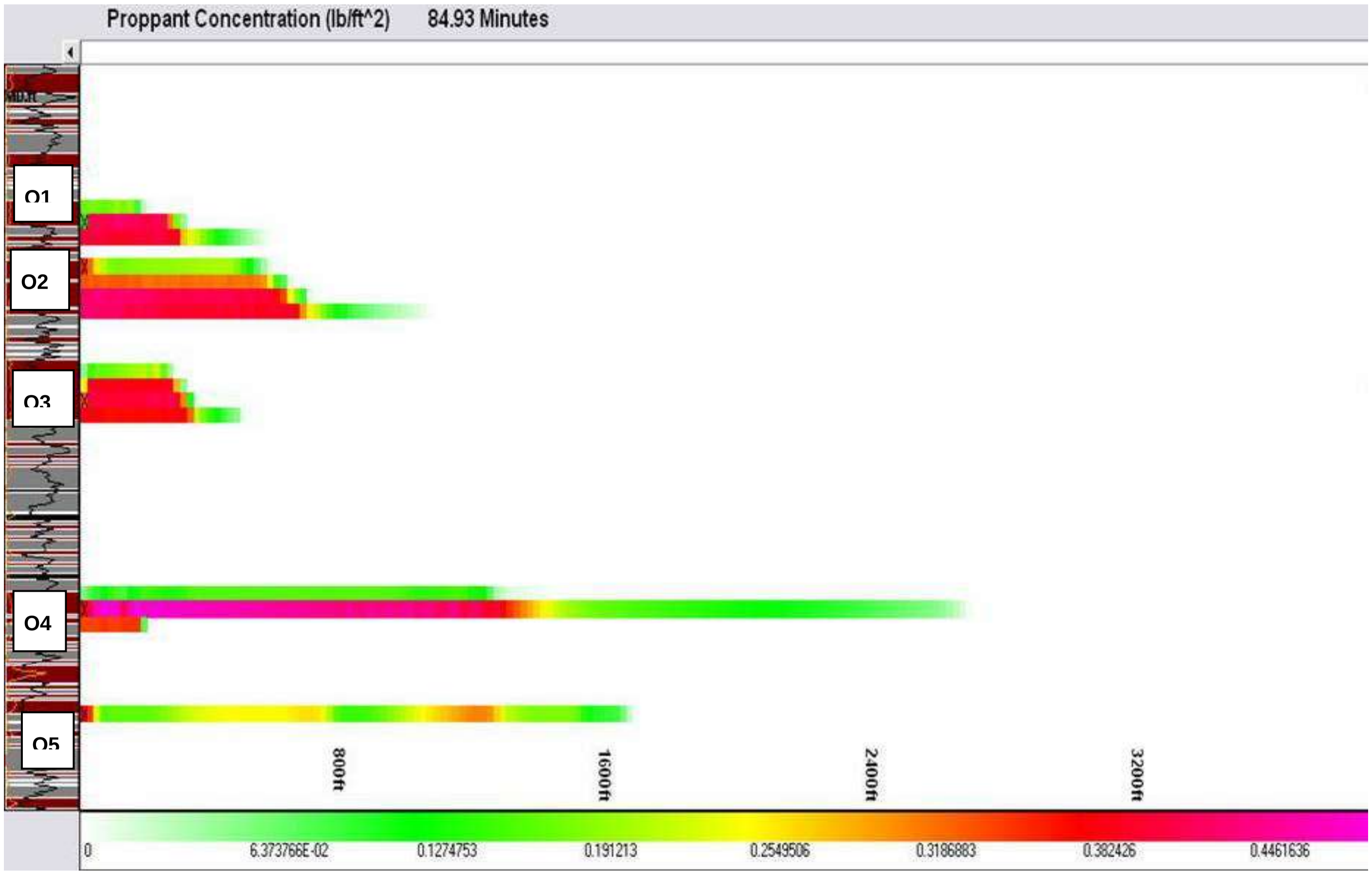

Figure 4-47: No Advanced Parameters. Case 6 output for Interval O showing the proppant concentration grid with the perforated zones highlighted.

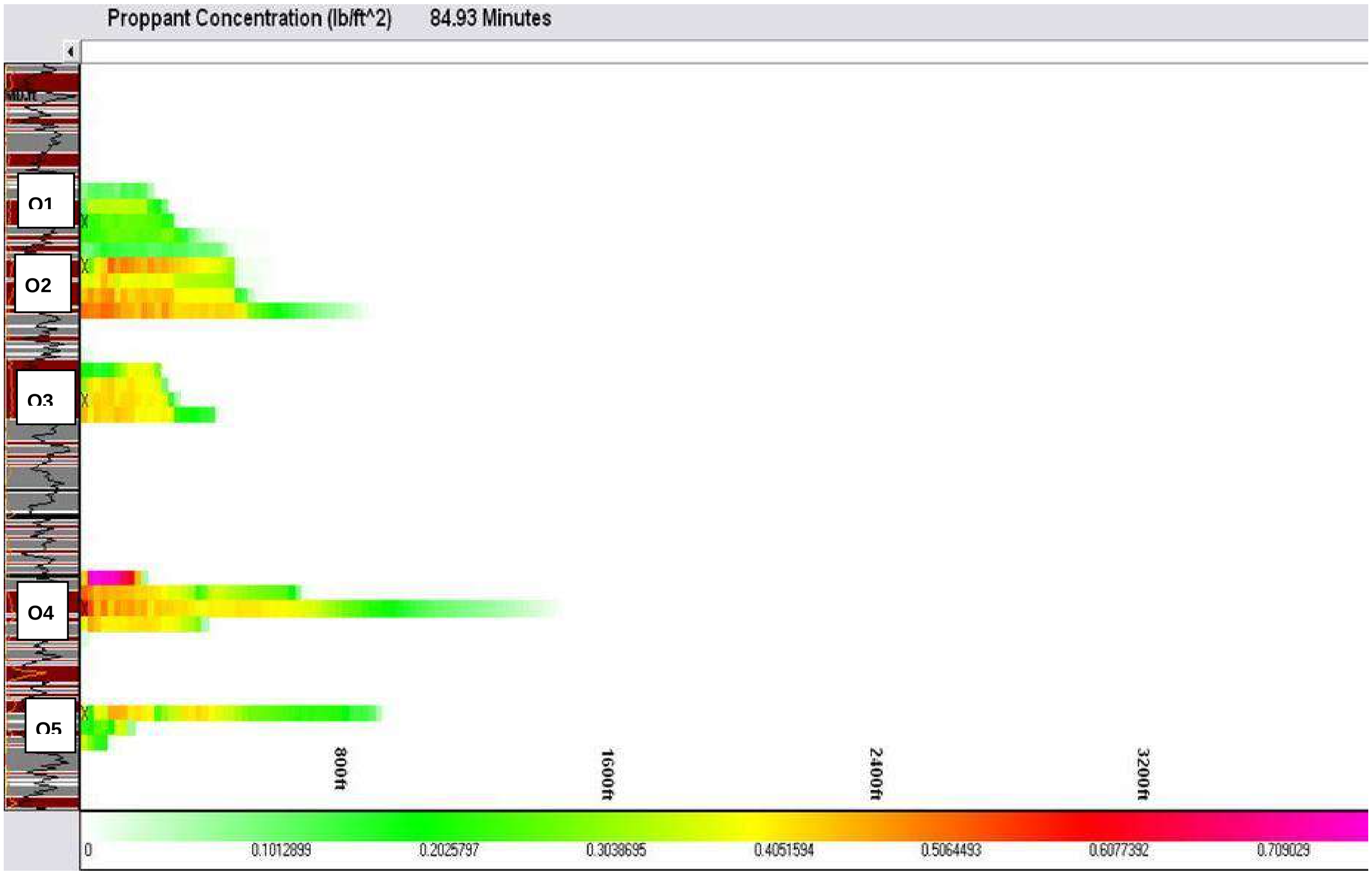

Figure 4-48: BIOTS (α_v=1). Case 7 output data for Interval O showing the proppant concentration grid with the perforated zones highlighted.

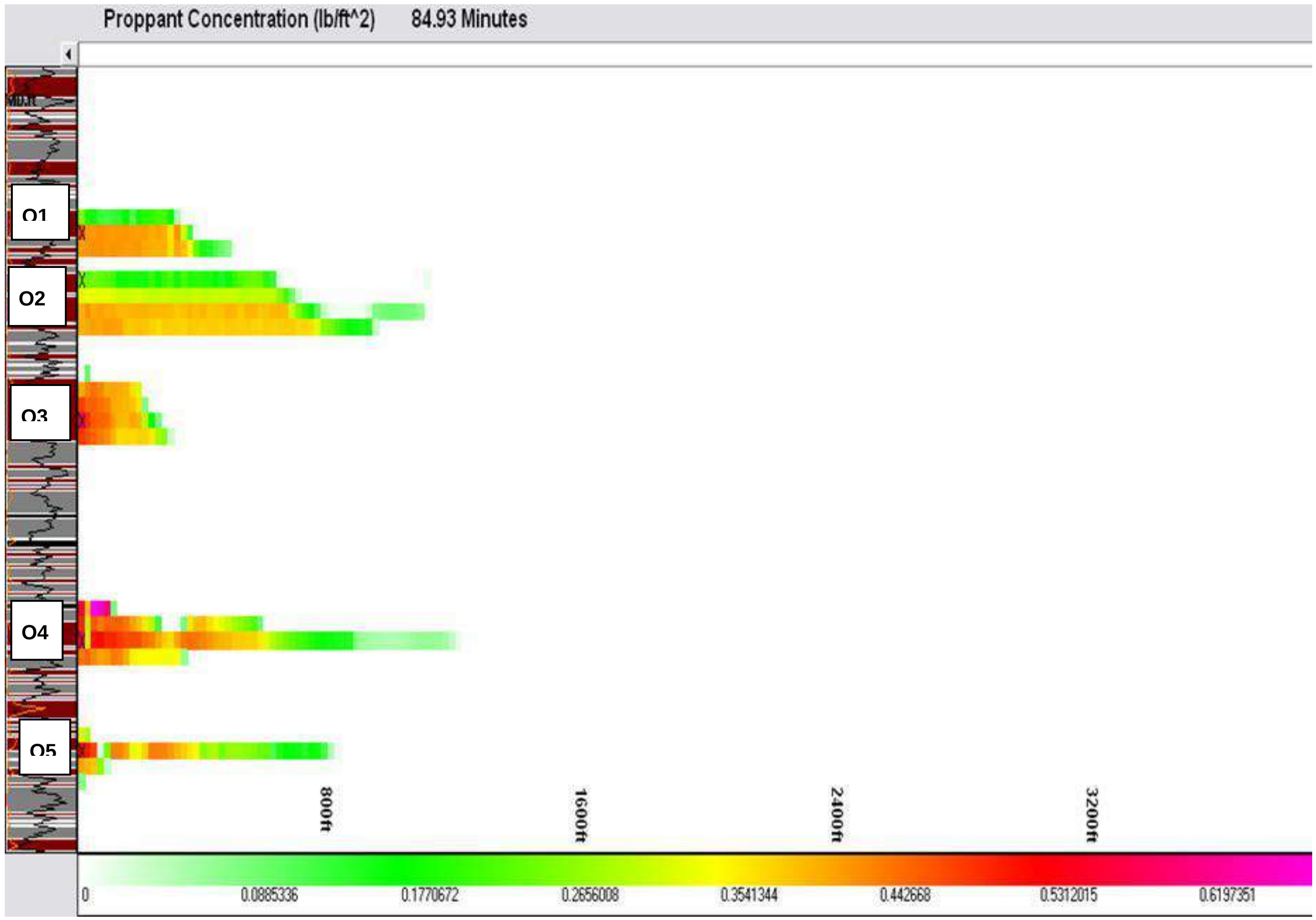

Figure 4-49: Default permeability correlation. Case 8 output for Interval O showing the proppant concentration grid with the perforated zones highlighted.

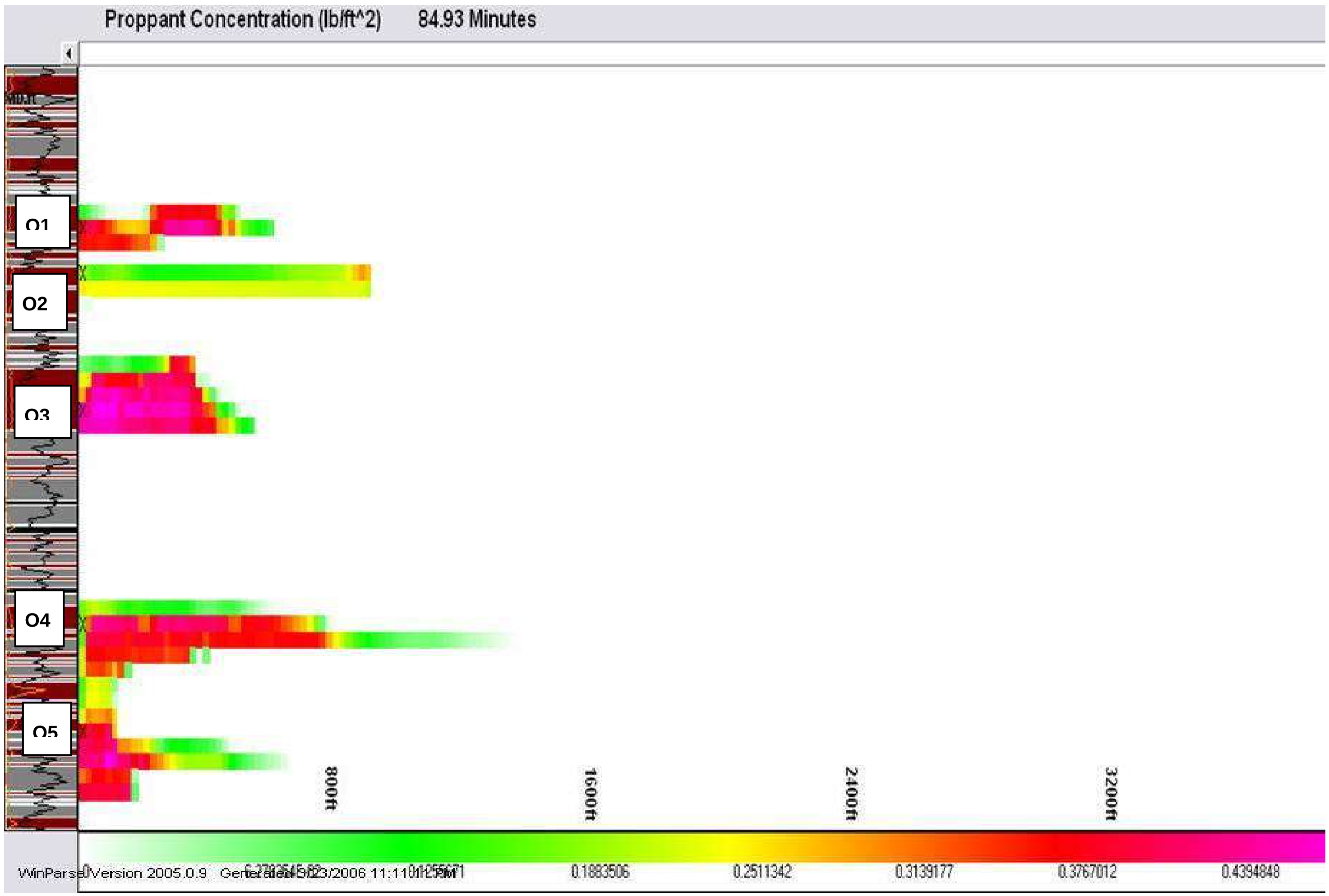

Figure 4-50: Default parameters. Case 9 output for Interval O showing the proppant concentration grid with the perforated zones highlighted.

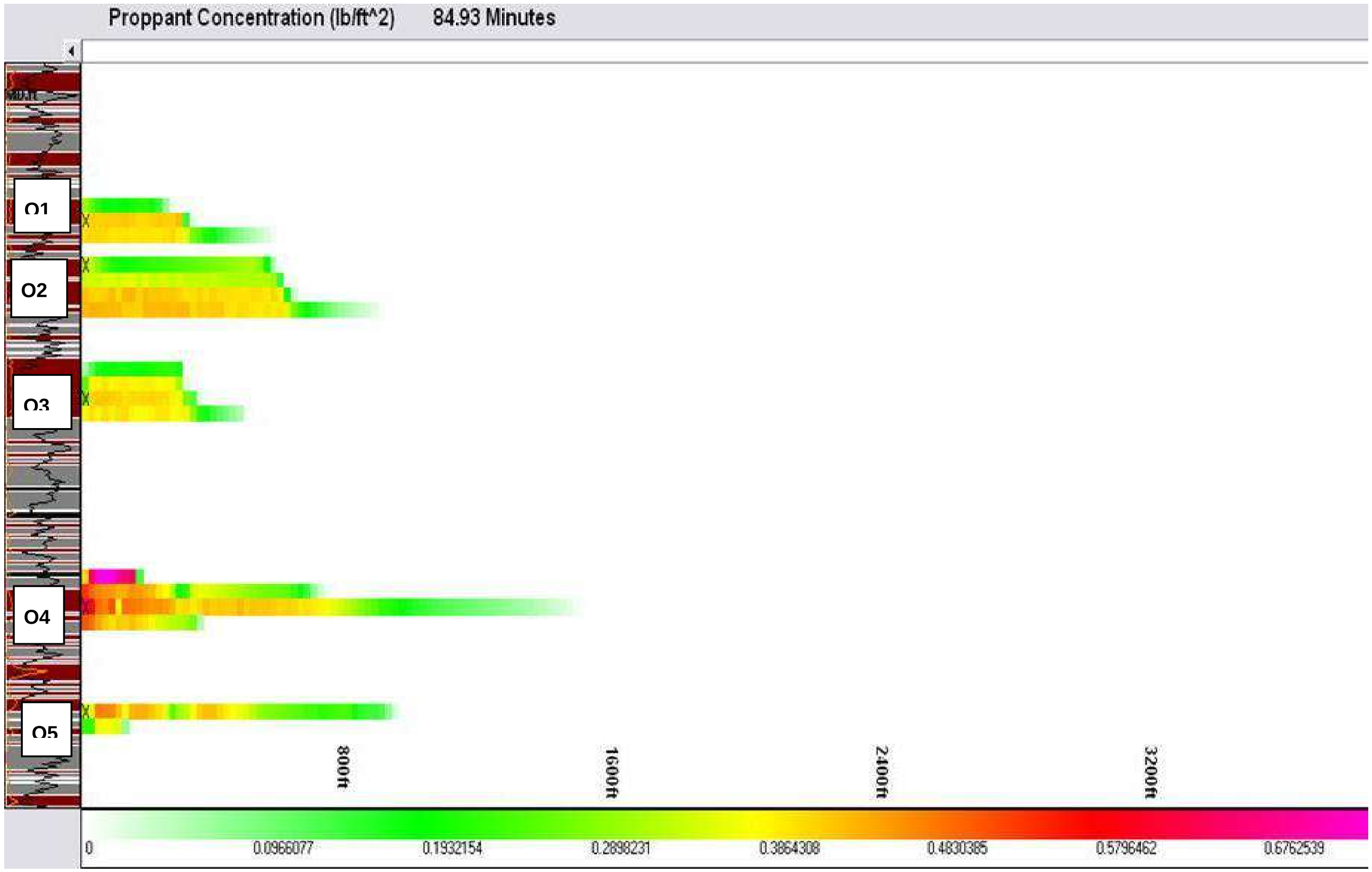

Figure 4-51: Total Stress minus 10%. Case 10 output for Interval O showing the proppant concentration grid with the perforated zones highlighted.

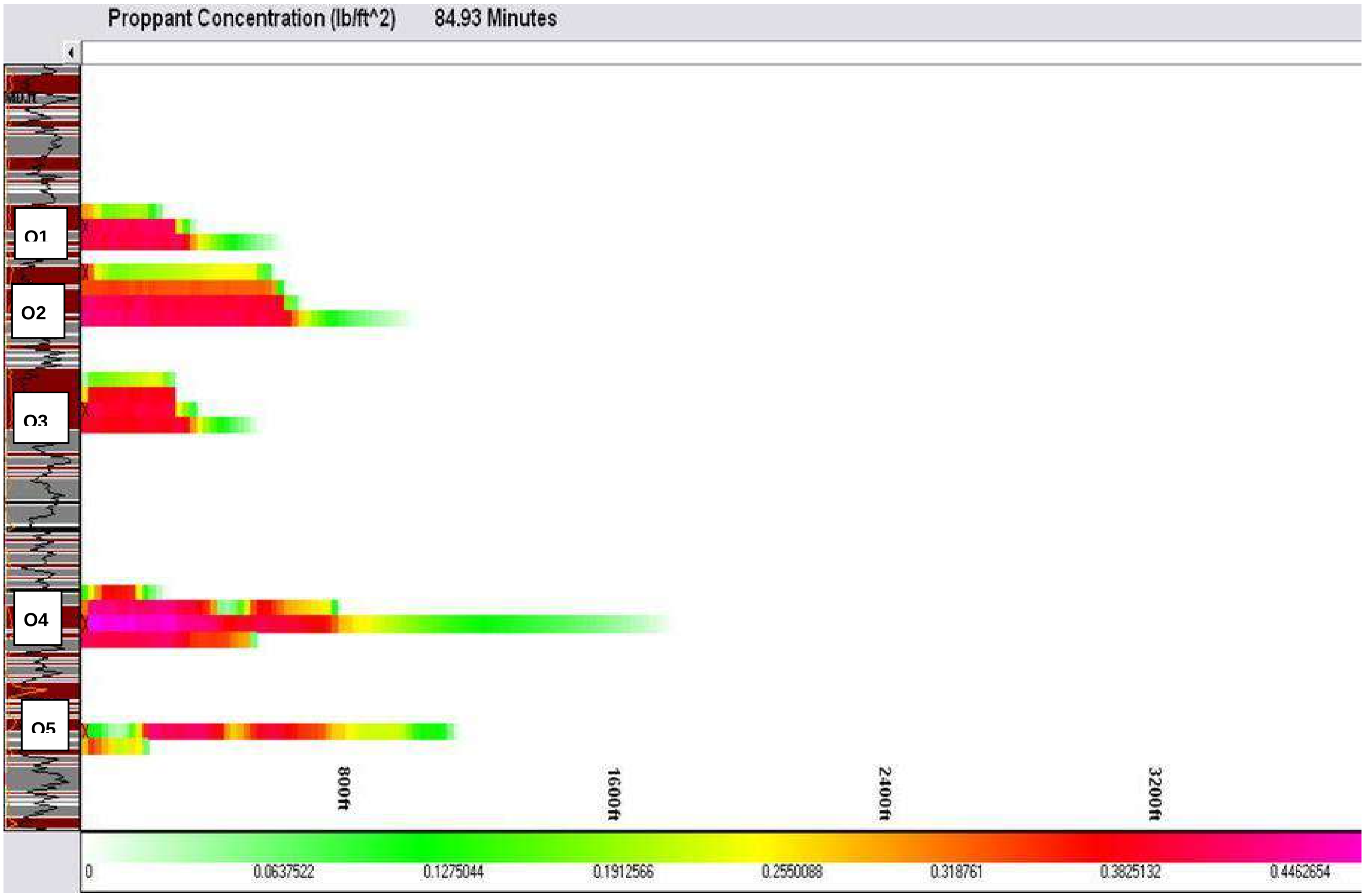

Figure 4-52: Total Stress minus 20%. Case 11 output for Interval O showing the proppant concentration grid with the perforated zones highlighted.

Results of Cases 3 & 4 – Poisson's ratio

The net pressure shows a wide variation with minimum values in Zone O5, but low values also occur in Zone O1. There is not much difference in the fracture distribution and widths between the matched model and Case 3, but Case 4 has increased fracture growth into Zone O2. Similarly, Case 3 shows little difference in proppant placement (see Figure 4-44) to the matched model, but Case 4 shows increased proppant placement into Zone O2 and decreased placement into Zone O1 (see Figure 4-45). The plots of net surface pressures for the matched model and Cases 3 and 4 have similar shapes, though there is a 200 psi pressure drop in Case 3 and a 400 psi pressure drop in Case 4.

Result of Cases 5 – Constant fluid gradient

The fluid gradient was set at the pressure of the largest interval sand from the final match. This was considered to be representative of a common case where only one zone is tested and the pore pressure used throughout the interval. With the constant fluid gradient, the net pressure output shows an uneven distribution throughout the interval, with a maximum in the lower Zones O4, O5 and also O2. Without significant stress differences, the fractures can grow upwards and fracture growth starts in the lower zones and moved upwards from each perforation. The largest differences are seen in the lower Zones O5 and O4, which have decreased fracture half-length growth, but increased height growth. Proppant concentrations are increased due to the increased fracture widths, and the proppant concentration is high and distributed evenly throughout all zones (see Figure 4-46). Within each zone, the widths and proppant concentrations are greatest at the bottom of each zone and decrease upwards. The net surface pressure graphs are approximately the same as the matched model plots.

Result of Cases 6- No advanced parameters

Without the use of advanced parameters there is little fluid leak-off or storage of liquid in the fractures as they grow, so more liquid is available for the treatment. Therefore, fractures grow longer and exhibit increased containment within each zone. The net pressure is greatest in the lower zones, O4 and O5, and the fracture width is also greatest at the tip of the fractures in these zones. However, proppant concentration is greatest in the upper three Zones O1, O2 and O3, with the greatest concentration at the bottom of the fractures (see Figure 4-47). The net surface pressure graphs are approximately the same as the matched model plots.

Result of Cases 7 – Vertical Biot's constant at 1

The net pressure distribution is approximately the same between Case 7 and the matched model. The upper zones, O1, O2 and O3, show increased upward growth of the fractures into the bounding shales. The proppant concentrations are similar in both the model and Case 7, with the only difference occurring where out-of-zone growth has placed additional proppant (see Figure 4-48). The net surface pressure graphs have similar shapes to the matched model plots, though the pressures are decreased by approximately 400 psi.

Result of Cases 8 – Permeability correlation

The net pressure distribution throughout the interval is similar to the matched model, apart from a minimum in the lower Zone T5. The lower zones have decreased fracture half-lengths, while the upper zones show increased containment and fracture half-lengths. The fracture widths and proppant concentration are both increased with the highest proppant concentration occurring in Zones O4 and O3 (see Figure 4-49). The matched model had the highest concentrations in Zones O2 and O4 (see Figure 4-41). The net surface pressure graphs are approximately the same for Case 8 and the matched model.

Result of Cases 9 – Default inputs used

The simulator's default inputs were used to provide an example of a model where: no well-specific data is available; all shot perforations are open to flow; the model default values are used for the advanced parameters; and, a constant pore pressure offset is applied for each zone. The proppant concentration output (see Figure 4-50) shows that the upper zones have increased containment while the lower zones grow out-of-zone. The net pressure is not evenly distributed, and a maximum occurs in the lower Zone O5. The fracture width is greatest in Zone O4 while proppant concentration is highest in Zone O3, with high concentrations occurring in Zones O4 and O5. There is significant out-of-zone placement of proppant in the lower Zones O4 and O5. The net surface pressure graphs are a similar shape to the matched model, though the values are approximately 1500 psi greater.

Results of Cases 10 & 11 – Stress – 10% and 20%

Decreasing the total stress of the interval generally leads to better containment of the fractures and an increased fracture half-length. Whereas the matched model had an even distribution of the net pressure throughout the interval, Cases 10 and 11 have minimums occurring in the lower zones, O4 and O5. The fracture widths are greatest in the two upper zones, O1 and O2, for both cases. Proppant concentration is higher in both cases with the highest proppant concentration is at the bottom of each zone (see Figures 4-51 and 4-52). The net surface pressure graphs are a similar shape to the matched data, though the pressure decreases about 500 psi in Case 10 and 1000 psi in Case 11.

CHAPTER 5
DISCUSSION

The ability to predict the results of hydraulic fracturing is perhaps one of the most complicated processes encountered in petroleum engineering. Rock properties are notoriously difficult to predict and measure in reservoirs with complicated geology. Unconventional tight gas reservoirs require changes in properties to occur on an inch scale, as opposed to the foot scale more usually applied in simulations. Another difficulty for the hydraulic fracture engineer is trying to model the various fluids and proppants and their behavior in the well during the hydraulic fracture treatment. Despite these problems, research in the field has been prolific since its inception, driven by the potential rewards for even partial success. Reservoirs that less than a decade ago were considered uneconomic, are now routinely completed using hydraulic fracturing to make them economic. However, some questions now being asked by operators are: is it possible to improve the hydraulic fracture process further and are there possible candidates for re-stimulation or re-completion? In order to further optimize the fracturing process, the most economical method is to model the process and identify the areas that need further investigation. Techniques can then be developed using suitable models and practical experience to investigate the problems associated with fracturing fluid design optimization i.e. the selection of fluids, additives, proppants, rates, etc.

For this study, the present best practice methodology for modeling tight gas reservoirs has been investigated. Chapters 3 and 4 describe the development of a very detailed simulator model by inputting information about the reservoir characteristics and the mechanical completion. Obviously, the more complete and consistent the input information, the more realistic the design will be. However, the problem of identifying critical information and ensuring that it is reliable is ongoing. The correct determination of reservoir parameters is necessary in order to determine the reservoir response to fracturing. Standard logging techniques readily provide information such as: static temperature and pressure, and reservoir thickness can be easily determined from logs. Similarly, reservoir fluid density, viscosity and compressibility are easy to obtain from reservoir fluid analysis. All of the data is reasonably accurate. The problems arise when trying to determine difficult to measure parameters such as rock mechanical properties and the in-situ stresses. This research investigated the current methods for determining these parameters and inputting them into a simulator and assessed the common errors that occur when incorrect data is used.

The effects of varying rock mechanical properties were investigated in Cases 1-4, shown in Tables 4-6 and 4-7. Previous research by hydraulic fracture modelers has suggested that rock mechanical properties are secondary factors in hydraulic fracture containment (Settari, 1988; Warpinski et al, 1998 c). From the sensitivity analysis in Chapter 4 it is clear that the rock mechanical properties do have significant effects on hydraulic fracture growth, and differences of between +50% to -14% were recorded for fracture dimensions. Rock mechanical properties are important for fracture model fracture propagation calculations. Cores are tested at reservoir conditions to derive the static values, but the parameters can also be estimated using log-derived data to define the rock elastic properties. For accurate values corrected logs correlated to mechanical measurements would normally be used, but these data were not available for this research. Log-derived values were checked against static data recorded in the area (Warpinski et al, 1998 c) and found to be reasonable. As described in Chapter 3, only the dynamic rock properties were determined from logs, and in-situ stresses were determined from mini-frac analyses of each sand zone within an interval. Overall, the differences were greater for Young’s modulus than Poisson’s ratio, but it should also be noted that Poisson’s ratio value are low (0.21) for both the sands and shales in the Mesaverde reservoir.

Cases 1 and 2 investigated Young's modulus, where changes will affect the stiffness of the rock. Decreasing Young's modulus causes an increase in the fracture half-length and width for both the 10% and 20% reduction case. The increase in fracture length and width causes a concurrent decrease in fracture height. Equations 5-1 and 5-2 (Gidley et al, 1989) are used to estimate width and net pressure for Geertsma-De Klerk models, with a height ratio of less than one. The results agree with the equations, as it can be seen that when the Young's modulus value is decreased, the net treating pressure will decrease but fracture width will increase. The variations in Young's modulus causes a 10% decrease in half-length but a 6% and 12% decrease in fracture height for Case 1 and Case 2 respectively. The average fracture width increase in both cases with a 22% increase in Case 1 which is more than doubled to 50% in Case 2.

$$w \approx \left(\frac{\mu i 4a^2}{E} \right)^{\frac{1}{4}} \tag{5-1}$$

and

$$P_n = P - \sigma_c \approx \frac{Ew}{2a} \tag{5-2}$$

where,	w	=	Width, ft
	P	=	Pressure in hydraulic fracture, psi
	P_n	=	Net fracturing pressure, psi
	a	=	Fracture half-height, ft
	E	=	Young's modulus, psi
	σ_c	=	Closure stress, psi
	i	=	Injection rate, bbl/min

Poisson's ratio has been found to vary little for hydrocarbon-bearing rocks and reasonable values can be easily determined using the rock type and an estimate of rock stiffness (Gidley et al, 1989). However, varying Poisson's ratio will cause changes to the value of the calculated total stress, as determined from

Equation 3-6, below. Therefore, Poisson's ratio has some importance for calculating the in-situ stress distribution in the model.

$$P_c(\sigma_{\min}) = \frac{\nu}{(1-\nu)}\left[D_{tv}\gamma_{ob} - \alpha_v\left(D_{tv}\gamma_p + P_{off}\right)\right] + \alpha_h\left(D_{tv}\gamma_p + P_{off}\right) + \varepsilon_x E + \sigma_t \quad (3\text{-}6)$$

where,	P_c	=	Closure pressure, psi
	ν	=	Poisson's ratio
	D_{tv}	=	True vertical depth, feet
	γ_{ob}	=	Overburden stress gradient, psi/ft
	γ_p	=	Pore fluid gradient, psi/ft
	α_v	=	Vertical Biot's poroelastic constant
	α_h	=	Horizontal Biot's poroelastic constant
	P_{off}	=	Pore pressure offset, psi
	ε_x	=	Regional horizontal strain, microstrains
	E	=	Young's Modulus, million psi
	σ_t	=	Regional horizontal tectonic stress

From this equation it can be seen that decreasing Poisson's ratio will decrease the Poisson's ratio factor ($^{\nu}/_{1-\nu}$) by 12% (Case 3) and 24% (Case 4). These effects can be seen in Cases 3 and 4 where the fracture width increases 9% and 12% respectively, while fracture half-length (14% and 6%) and height decrease (1% and 5%). This would be expected where the fracture is able to grow wider, due to a lowering of the stress in the fractured zone. Poisson's ratio is generally considered to be less important than Young's modulus and this was confirmed in the model. Nevertheless, Poisson's ratio is necessary for calculations of fracture width and the in-situ stress distribution.

Case 5 shows the effect of a constant pore pressure offset of 900 psi (a value determined for the virgin reservoir pressure using Figure 3-9). As would be expected, a constant offset pore pressure gradient was found to significantly affect the fracture distribution by altering the total stress calculated (see Equation 3-6). A number of intervals were modeled as depleted in the matched model in order to match the depletion indicated in the microseismic data. By using a constant pore pressure offset gradient, the stress contrasts between the fractured zones and the confining layers are decreased. Fracture growth follows the more theoretical fracture growth where the fracture starts in the lower zones first, and then moves up the zones in the interval. This lack of height containment type growth was also observed in the upper two intervals of the matched model, where there was no hydraulic fracture distribution constraint imposed by microseismic analysis. The fracture height and average width increased 29% and 18%, but the half-length and efficiency decreased 20% and 10% respectively.

Case 6 shows the effect of the advanced parameters, which are typically used at the end of matching process to finalize the fracture geometry to the field data. Without fluid leaking away and with no fluid stored in natural fractures, the fracture half-length (94%), width (75%) and treatment efficiency (72%) increase substantially, while height decreased 12%.

Case 7 shows the effect of varying the vertical Biot's constant. Biot's constant is another component used to determine the total stress (see Equation 3-6). When a uniform value is used the effects of pore pressure offset differences will become more pronounced. The created length decreased slightly (4%) but efficiency increased 20% and fracture width and height increased 15% and 10% respectively.

Case 8 investigated the effect of permeability. McGuire and Sikora (1960) have shown that well productivity results due to specific treatments depend directly on reservoir permeability. Their work showed that the stimulation ratio was inversely proportional to reservoir permeability. Therefore, the higher the permeability the lower the stimulation potential and this was shown in the results for Case 8. The default correlation for tight gas reservoirs was used ($K_1 = 50$, where K_1 is the constant in the equation to derive permeability $k = K_1\phi^{K_2}$). The derived value was slightly greater than double the value needed in the matched model (matched model - $K_1 = 17.5$). The resultant increase in permeability was found to significantly reduce fracture half length (15%) and efficiency (36%) in all zones, with a slight increase in fracture height (4%). As mentioned previously and shown in Figure 3-9, the permeability correlation needs further work to better represent the field measurements. The lack of a sufficiently accurate correlation might explain the high permeability readings and stringer growth in zones of several intervals. Normally, the growth in these zones is limited by reducing the permeability of these zones on an individual basis in the matching process.

Case 9 was a worst case scenario undertaken to assess differences that might occur if all the differences from the sensitivity analysis were incorporated into a single simulator run. Length and efficiency decreased 31% and 19% respectively, while height (34%) and width (18%) all increased. The height containment decreased as the stress contrasts were reduced and the fracture was able to grow upwards into the bounding shale layers

Cases 10 and 11 are perhaps the most important simulations, as they aimed to assess the effect of what hydraulic fracture modelers consider to be the primary factor controlling fracture growth, total stress variations. For this study the total minimum horizontal stress was determined from mini-fracture analysis. While the aim of the study was not to investigate the methods of determining closure pressures, during the quality control process it was necessary to critically assess the supplied data to ensure that closure pressures were properly determined. This work showed that no one single graphical method (G-function, square root-of-time, log-log plots etc.) could be used definitively to determine closure pressure. Therefore, it is probably quite conceivable that the determined closure stress data in the field is often at least 10% different to the correct value. There was found to be little difference between the 10% reduction (Case 10) and the matched model, with only the fracture width and efficiency increasing approximately 15%. However, in Case 11 there were significant differences to the fracture dimensions and distribution. Fracture half-length and width increased 25% and 30% respectively, which resulted in a 47% increase in efficiency.

The original matched hydraulic fracture simulator containment was found to be similar to the actual field data, without any changes being necessary to the stresses in bounding layers to give better containment. This would suggest that the log-derived stress differences between the reservoir sands and the bounding shale layers, seems to have been captured in the initial model using the determined pore pressure. The stress contrasts between sand and shale layers has previously been suggested as a controlling mechanism for fracture height containment in the Mesaverde reservoir (Miskimins, 2002; Warpinski et al, 1998 b and c). Research by Pantoja (1998) and Miskimins (2002) suggests that stress contrast is more important than the actual stress values themselves, for determining hydraulic fracture growth dimensions. In Case 10, the value for the stress was changed 10% and did not show a great difference when compared to the matched model fracture distribution. However, the net surface pressure was significantly reduced and the effect was even more pronounced when the stress was reduced 20%. In order to match the lower net surface pressures the pore pressure offsets would need to be increased in the simulator. Therefore, stress changes would significantly affect the identification of depleted zones that might exist as well as affect the fracture distribution throughout the interval. An important result of different cases of in-situ stress is that a hydraulic fracture does not seem to easily break out of a low stress sandstone, traverse higher stress confining rocks, and intersect other sandstones.

In this work one of the major problems was modeling the abnormally high net surface pressures recorded and in particular trying to match the high pressures at the end of the treatment. The high pressures at the end of treatments were modeled by shutting off perforations to force a tip screen-out behavior in the simulator, resulting in abnormally high net surface pressure. Barree (1998) has discussed how changing lateral rock properties 300 ft from the well can induce tip screen-out behavior and this could be one of a number of possible explanations for this behavior. Whilst this general high net surface pressure trend was noted in all intervals, there were also problems trying to match the pressure depletion observed in several intervals. In these intervals where the upper zones indicate significant fracturing the only way that they could be modeled was by making these sands severely depleted, done by significantly decreasing the pore pressure offset.

During this research there were found to be a number of interval specific changes for the various cases. However, as only one well was investigated, the general trends are discussed and a detailed analysis of interval specific differences was not undertaken due to the lack of comparison data. Future research would aim to investigate several wells and might be able to deduce the exact reasons for some of the variations.

Table 5-1 shows the sorted summary fracture dimension outputs data for all the sensitivity cases. Overall, considering all the simulated fracture dimensions (height, length and width) Case 8 (permeability) gives the greatest decrease, compared to the matched model dimensions. However, the greatest difference for every fracture output, apart from height, occurs for Case 6 (advanced parameters). This shows the importance of the advanced parameters in the final matching of real data, even after critical input data has been analyzed and validated. The second and third greatest differences are for Case 11 and Case 2, showing that the importance of stress and Young's modulus in determining hydraulic fracture dimensions. The importance of Young's modulus is also indicated by the subsequent 9% differences for Case 1. Of secondary importance for the simulator outcome seems to be indicated for the inputs in Case 9 (default parameters) and Case 7 (vertical Biot's) which showed a 7% difference; while Case 10 (10% stress) and Case 8 (Permeability) showed a 4% difference. Analysis of other fracture outputs shows some variation whereby Case 9 and Case 8 give the greatest decreases for half-length (31%) and width (1%) respectively. Case 6 still

Table 5-1: Summary Results for all Cases to Show the Maximum and Minimum Output Differences of the Sensitivity Cases Compared to the Matched Model

Case	Av. Fracture Dimensions	Case	Av. Half-Length	Case	Av. Width	Case	Av. Height
8	-4%	9	-31%	8	-1%	6	-12%
3	-2%	5	-20%	3	9%	2	-12%
4	0%	8	-15%	4	12%	1	-6%
10	4%	3	-14%	10	14%	4	-5%
7	7%	4	-6%	7	15%	10	-3%
9	7%	7	-4%	5	18%	3	-1%
1	9%	10	0%	9	18%	11	0%
5	9%	1	10%	1	22%	8	4%
2	16%	2	10%	11	30%	7	10%
11	18%	11	25%	2	50%	5	29%
6	52%	6	94%	6	75%	9	34%

has the greatest increase for height (94%) and width (75%), but this means that it also has the largest decrease in height (12%). The results from this research indicate the importance of several parameters, as shown in Table 5-1. The sensitivity analysis is similar to the results from previous research (Miskimins, 2002; Warpinski et al, 1998 b and c) whereby stress, or more precisely stress contrasts, and Young's modulus were shown to play a major role in determining hydraulic fracture dimensions.

Finally, one of the most important findings from the sensitivity analysis was that the often used process of 'net surface pressure matching' to derive a valid simulator model may lead to significant discrepancies, which could have as much as 94% error. This was as a result of noting the effect of the various inputs on the resulting net surface pressure plots, as can be seen in Figures 4-41 to 4-52. Several input changes resulted in net surface pressure graphs that are very similar to the real data, as well as the matched model.

CHAPTER 6
CONCLUSIONS AND RECOMMENDATIONS

The geological setting of the Mesaverde reservoir together with the unique data sets available for comparison and analysis, provided a unique opportunity to evaluate three-dimensional hydraulic fracture simulation and its application in highly laminated sand and shale reservoirs. The overall objective of the study is to investigate the 'best practice' methodology currently used to develop what practitioners consider to be accurate three-dimensional (3D) hydraulic fracture simulations of geologically complex reservoirs. This study aims to help identify the critical data inputs, i.e. the primary controlling factors, necessary for operators to develop relevant hydraulic fracture models. The use of log-derived rock mechanical properties and mini-fracture stress analysis has been analyzed. The effects of key simulator inputs have been assessed, and their effects on hydraulic fracture parameters quantified.

6.1 Conclusions

The conclusions from this study are:

- Log-derived properties have been found to give reasonable inputs for hydraulic fracture simulation.

  The in-situ stress and rock mechanical properties calculated from dynamic log measurements seem to accurately represent the composite layering effects of the reservoir, as well as defining reservoir geometry and layering. The results showed good containment within the fractured interval, which matches with microseismic data. The containment is likely due not only to alternating rock mechanical properties, but also shear slippage, as indicated by the presence of microseisms.

A correlation for deriving permeability from porosity has been described in this work. Clearly this correlation needs to be further investigated to better match the real data obtained from mini-fracture analyses. The inability to match the real data using a simple relationship is due to the heterogeneous nature of the reservoir and the existence of several flow units, which cannot be described by a single calculation.

- The uniaxial-strain model has been found to be valid for determining closure pressure in the studied well, using the measured pore pressure and log-derived Poisson's ratio.
- The importance of mini-fracture analysis for determining stress input parameters for the simulator has been shown. (The correct determination of closure pressure is critical for determining the total horizontal minimum stress values but is not always possible). Similarly, analysis of before- and after-closure data indicates that the technique provides relative pore pressure values, rather than absolute. Obviously, these conclusions could be based on errors in the input analysis or the model. Often the input data was hard to analyze due to multiple closures or non-closure. The mini-fracture data analysis also proved beneficial in deriving a model permeability correlation and providing pore pressure values, which are then modified to affect the created hydraulic fracture distribution to match real data.
- Simulators are commonly used to derive what are considered valid hydraulic fracture models by undertaking a history-matching process. For this methodology, the real net surface pressure data from the stimulation treatment is compared and matched to the simulator-predicted net surface pressure. From the sensitivity analysis results, it is clear that this process is

unable to differentiate between several solutions. Large discrepancies in the simulator outputs can result, which can differ from a constrained matched model (microseismic) by as much as 92%.

- The sensitivity analysis results show that the following are primary factors that govern the created hydraulic fracture dimensions: advanced parameters (MSF, PDL, TSC and permeability ratio) and total stress. All the other inputs analyzed (Young's modulus, Poisson's ratio, pore pressure offset, vertical Biot's constant and permeability) have been shown to be secondary factors, relatively easy to determine and with less effect on the simulator outcome.
- When undertaking hydraulic fracture modeling in geologically complex reservoirs, it has been shown that the model needs calibration in order to fully represent the real fracture geometry.
- The modeling process showed that there was an inability to capture dramatic variations in fracture growth that probably result from large-scale lateral reservoir heterogeneities (natural fractures, small faults, pinch-outs, etc). At the end of the treatments for instance, high net surface pressures were recorded, which were modeled by inducing a tip screen-out. This inability to match the real data may be more due to a lack of reservoir heterogeneity characterization than any shortcomings of the model or modeling software.

6.2 Hydraulic Fracture Model Field Input Recommendations

The aim of this study was to help operators identify what is the minimum analysis necessary to derive a valid model for field application. This work has shown that especially for infill drilling purposes in geologically complex reservoirs it is impossible to accurately predict reservoir depletion. The importance of mini-fracture analysis has been shown in this work where it proved to be an invaluable tool for accurate model input determination. It is recommended that in order to construct a suitable hydraulic fracture model, all the identified reservoir zones within an interval need to be analyzed. The full testing might not be possible due to economic constraints, or ever considered necessary in a new field. Therefore, the minimum amount of analyses that is recommended is that at least one reservoir zone from each interval should be tested with a mini-fracture test. For the mini-frac test the largest reservoir should be analyzed and the calculated pore pressure used to determine the pore pressure offset to be applied to the whole interval. However, it should be stressed that significant errors could still occur with the minimal testing method and the full analyses should be undertaken when possible.

6.3 Future Work

The overall aim of this work is to help develop an optimum methodology for application in geologically complex reservoirs. A unique data set was available for this study that allowed a through assessment of the standard techniques used to derive input data for what most practitioners consider to be an accurate hydraulic fracture model.

- One of the biggest problems of this research is that the study only fully investigates one well. Ideally, a number of wells from this and other similar fields would be analyzed and compared to verify and qualify some of the results. Also, the research undertaken was multi-disciplinary in nature and ideally should be undertaken by a multi-disciplinary research group or consortium, with experts in each field to validate the results and further develop these theories.
- The hydraulic fracture dimensions were compared to microseismic data assuming that only the microseisms indicated growth areas. This needs to be further analyzed and verified, and the data should be compared to

other dimension-measuring data to check hydraulic fracture dimensions, such as temperature logs or radioactive tracers.

- Log-derived data is important for the model set-up, and the data from this study should now be compared to a model using corrected logs. If containment differences were observed, this might provide some way of quantifying the composite layering effects of laminated reservoirs. Similarly the stress model is a critical input for the model, but knowledge of closure stress in the perforated interval is not always sufficient to accurately calculate the observed net surface pressure. Significant pressure drop or entry friction can occur near-wellbore, and other diagnostics, such as a step-down test, could be recommended to evaluate factors such as: tortuosity, perforation friction and the number of open perforations. Also, the use of full waveform sonic log data would be a useful comparison with the static and dynamic log-derived rock properties in deriving correlations for use in this and other similar reservoirs. Permeability has been shown to be an important input and the usual method for deriving a simple correlation to adequately describe the interval is detailed. However, this work has show the limitations of the correlation and future work should look at undertaking flow unit analysis and deriving correlations for use in individual flow units, which could then be incorporated into the simulator.

One of the reasons that this work has not been undertaken before is that the research is complex and a large number of accurate data inputs are required, there is a significant cost associated with such an undertaking. Nevertheless, this work has answered some of the present questions hydraulic fracturing practitioners have posed, and though this research answered a lot of questions on input sensitivity, the next step in the analysis of the hydraulic fracture simulation is to run the model in predictive mode.

- Research should investigate the fracture distribution of a matched model and compare it to well production, for instance production logs could be compared to proppant concentration, or the matched models well production could be matched to the actual production.
- An investigation into the effects of various fluids and proppant combinations, as well as the effect of different stages such as spacer stages, on the resultant fracture productivity would be one of the most beneficial projects to optimize hydraulic fracture treatment design.

NOMENCLATURE

A	=	Area
Advanced parameters	=	Pressure-dependent modulus stiffness factor (MSF), pressure-dependent leak-off coefficient (PDL), relative permeability ratio and transverse storage coefficient (TSC).
α_h	=	Horizontal Biot's poroelastic constant
α_h	=	Horizontal Biot's poroelastic constant
α_v	=	Vertical Biot's poroelastic constant
α_v	=	Vertical Biot's constant
α_z	=	Vertical Biot's poroelastic constant
d_1	=	Original diameter
D_{tv}	=	True vertical depth, feet
E	=	Young's modulus, million psi
ε_x	=	Regional horizontal strain, microstrains
ϕ_E	=	Shale-corrected effective porosity from the neutron density crossplot
F	=	Force acting on area, A
G	=	Shear modulus
γ_{ob}	=	Overburden stress gradient, psi/ft
γ_p	=	Pore fluid gradient, psi/ft
ISIP	=	Instantaneous shut-in pressure
k	=	Permeability, md
k_{air}	=	Core routine air permeability
k_g	=	Gas permeability
λ	=	Lamés coefficient
L_1	=	Original length
ν	=	Poisson's Ratio
P_c	=	Closure pressure, psi
P_{net}	=	Net pressure
P_{off}	=	Pore pressure offset, psi
P_{res} or P	=	Reservoir pressure
P_w	=	Pressure in the wellbore
PZS	=	Process zone stress
σ	=	Stress in directions x, y and z
σ_E	=	Any externally generated stress acting on the formation
σ_{ext}	=	Externally generated stress
σ_{min}	=	Total minimum horizontal stress $(\sim P_c)$

σ_t	=	Regional horizontal tectonic stress
σ_x	=	Total horizontal stress
σ_z	=	Total overburden stress
V_p	=	Compressional acoustic velocities from a sonic log
V_s	=	Shear acoustic velocities from a sonic log
Δd	=	Change in diameter
ΔL	=	Change in length (L_2-L_1)
ε	=	Strain
ε_{ax}	=	Strain in the axial direction
ε_{lat}	=	Strain in the lateral direction
ν	=	Poisson's ratio

REFERENCES

Addis, M.A. (1997): *"The Stress-Depletion Response of Reservoirs"*. Paper SPE 38720 presented at the 1997 SPE Annual Technical Conference and Exhibition, San Antonio, Oct. 5-8.

Ayoub, J.A., Brown, J.E., Barree, R.D. and Elphick, J.J. (1992): "*Diagnosis and Evaluation of Fracturing Treatments"*. Paper SPE 20581, Production Engineering, p. 39-46.

Barree, R.D. (1983): "*A Practical Numerical Simulator for Three-Dimensional Fracture Propagation in Heterogeneous Media*". Paper SPE 12273, Reservoir Simulation Symposium, San Francisco, California, p. 403-414.

Barree, R.D. (2000): "*Fracture Modeling with GOHFER Using Extensive Real-Data Input*". Presented at the Three Dimensional and Advanced Hydraulic Fracture Modeling Symposium, July 2000, Seattle, p 78-87.

Barree, R. D. and Mukherjee, H. (1996): *"Determination of Pressure Dependent Leakoff and Its Effect on Fracture Geometry"*. Paper SPE 36424, 71st Annual Technical Conference and Exhibition, Denver, Colorado, p. 85-94.

Barree, R. D. and Winterfield, P. H. (1998): *"Effects of Shear Planes and Interfacial Slippage on Fracture Growth and Treating Pressures"*. Paper SPE 48926, SPE Annual Technical Conference and Exhibition, New Orleans, Louisiana, p. 11-16.

Barree, R.D. (1998): *"Applications of Pre-Frac Injection/Falloff Tests in Fissured Reservoirs—Field Examples"*. Paper SPE 39932 presented at the 1998 SPE Rocky Mountain Regional/Low-Permeability Reservoirs Symposium, Denver, Apr. 5-8.

Bell, J.S. and Gough, D.T. (1982): *"The Use of Borehole Breakouts in the Study of Crystal Stress in Proc of Hydraulic Fracturing Stress Measurements"*. U.S. Geologic Survey Open File Report 82-1075, Denver, CO.

Cipolla, C.L. and Wright, C.A. (2000): *"State-of-the-Art in Hydraulic Fracture Diagnostics"*. Paper SPE 64434, SPE Asia Pacific Oil and Gas Conference and Exhibition, Brisbane, Australia, p. 1-15.

Clark, J. B. (1949): *"A Hydraulic Process for Increasing the Productivity of Wells"*. Petroleum Transactions, AIME, v. 186, p. 1-8.

Cleary, M.P. (1980): *"Comprehensive Design Formulae for Hydraulic Fracturing". Paper* SPE 9259 presented at the SPE Annual Technical Conference and Exhibition, Dallas, Sept 21-24.

Cleary, M.P. et al (1981): *"Theoretical and Laboratory Simulation of Underground Fracturing Operations"*. MIT-UFRAC First Annual Report (Aug, 1981).

Cluff, R.M and Graff, K. (2003): *Chapter 16 – "Production History Plots for Piceance Basin Oil and Gas Fields"*. 2003 Piceance Basin Guidebook, Rocky Mountain Association of Geologists, p 272-307.

Craig, D.P and Brown, T.D (1999): *"Estimating Pore Pressure and Permeability in Massively Stacked Lenticular Reservoirs Using Diagnostic Fracture-Injection Tests"*. Paper SPE 56600 presented at the SPE Annual Technical Conference and Exhibition Houston, Texas, 3–6 October, 1999.

Craig, D.P., Odegard, C.E, Pearson Jr., W.C. and Schroeder, J.E. (2000):*" Case History: Observations From Diagnostic Injection Tests in Multiple Pay Sands of the Mamm Creek Field, Piceance Basin, Colorado"*. Paper SPE 60321 presented at the 2000 SPE Rocky Mountain regional low permeability symposium Denver, Colorado, March 12-15, 2000.

Cumella, S.P. and Ostby, D.B (2003): *Chapter 10 – "Geology of the Basin-Centered Gas Accumulation, Piceance Basin"*. 2003 Piceance Basin Guidebook, Rocky Mountain Association of Geologists, p 171-193.

Daneshy, A.A. (1977): *"Hydraulic Fracture Propagation in Layered Formations"*. Paper SPE 6088, SPE-AIME 51st Annual Fall Technical Conference and Exhibition, New Orleans, Louisiana, p. 33-41.

Detournay, E. and Cheng, A.H-D. (1993): *"Fundamentals of Poroelasticity"*. Chapter 5 in Comprehensive Rock Engineering: Principles, Practice and Projects, Vol. II, Analysis and Design Method, ed. C. Fairhurst, Pergamon Press, p. 113-171, 1993.

DOE Report DOE/MC/30086 – 5077 (1994): *"Naturally Fractured Tight Gas Reservoir Detection Optimization - Annual Report"*. September 1993-September 1994, Advanced Resources International, p. 231.

Economides, M. J. and Nolte, K. G. (1981):*" Reservoir Stimulation"*. Schlumberger Educational Services, Houston, Texas, p. 2-1 to 2-21.

Ely, J. W., Brown T.D. and Reed S.D. (1994): *"Optimization of Hydraulic Fracture Treatments in the Williams Fork Formation of the Mesaverde Group"*. SPE Joint Rocky Mountain Regional Meeting/Low Permeability Reservoirs Symposium, Denver, CO, SPE-29551, proceedings, p. 97-105.

Gidley, J.L., Holditch, S.A., Nierode, D.E. and Veatch, R.W.J. (1989): *"Recent Advances in Hydraulic Fracturing"*. Henry L. Doherty SPE Monograph Series, v. 12, Richardson, Texas, SPE, p. 452.

GRI (1998): *"Guidelines & Procedures for Real-Data Fracture Pressure Analysis"*. GRI-98/0286 Technical Summary, p. 1-28.

Harts E&P (2005 - Supplement to Oil and Gas Investor): "*America's Independents: From Black Gold to Diamond Jubilee"*. Independent Petroleum Association of America (IPAA) 75th Anniversary Edition.

Hubbert, M.K. and Willis, D.G. (1957): *"Mechanics of Hydraulic Fracturing"*. Petroleum Transactions, AIME, v. 210, p. 153-163.

Jaeger, J.C. and Cook, N.G.W (1976): *"Fundamentals of Rock Mechanics"*. Halsted press, New York City.

Johnson, R.C., Flores, R.M. (2003): *Chapter 3 – "History of the Piceance Basin from Latest Cretaceous Through Early Eocene and the Characterization of Lower Tertiary Sandstone Reservoirs"*. 2003 Piceance Basin Guidebook, Rocky Mountain Association of Geologists.

Jones, F.O. and Owens, W.W. (1980): *"A Laboratory Study of Low-Permeability Gas Sands"*. Journal of Petroleum Technology (Sept. 1980), p. 1631-40.

Kunze, K.R. and Steiger, R.P. (1992): *"Accurate In-Situ Stress Measurements During Drilling Operations"*. Paper SPE 24593 presented at the 1992 SPE Annual Technical Conference, Washington D.C, Oct 3-6.

Kuuskraa, V.A., Decker, D., Squires, S., and Lynn, H.B. (1996): *"Naturally Fractured Tight Gas Reservoir Detection Optimization: Piceance Basin"*. The Leading Edge, Aug. 1996, p. 947-948.

Kuuskraa, V.A, Decker, D and Lynn, H. (1997): *"Optimizing Technologies for Detecting Natural Fractures in the Tight Sands of the Rulison Field, Piceance Basin"*. U.S. Department of Energy (DOE) 1997 Natural Gas Conference March 24-27 Houston, Texas, conference paper NG6-3.

Kuuskraa, V.A., and Campagna, D.J. (1999): *"Low Cost Methods for Finding Tight Gas, Gas Shales and Coalbed Methane"*. DOE Oil & Gas Conference June 28 - 30, Dallas, Texas, conference paper NG3a-1.

Lama, R.D. and Vutukuri, V.S. (1978): *"Handbook of Mechanical Properties of Rocks"*. Trans Tech Publications, Clausthal, Germany 1978, 2, 86-89, 145, p. 234.

Law, B.E. and Dickinson, W.W. (1985): *"Conceptual Model for Origin of Abnormally-Pressured Gas Accumulations in Low-Permeability Reservoirs"*. American Association of Petroleum Geologists Bulletin 69 (8), p. 1295-1304.

Lorenz, J.C. (1985): *"Predictions of Size and Orientation of Lenticular Reservoirs in the Mesaverde Group, Northwestern Colorado"*. Paper SPE/DOE 13851 in: Proceedings of the 1985 SPE/DOE Joint Symposium on Low Permeability Reservoirs, p. 23-28.

Lorenz, J.C. (1987): *"Reservoir Sedimentology of Mesaverde Rocks at the Multiwell Experiment Site and East-Central Piceance Creek Basin"*. Sandia National Laboratories report SAND87-0040, p. 40.

Lorenz, J.C. (2003): *"Chapter 5 - Fracture Systems in the Piceance Basin: Overview and Comparison with Fractures in the San Juan and Green River Basins"*. 2003 Piceance Basin Guidebook, Rocky Mountain Association of Geologists, p 75-95.

Lorenz, J.C. and Finley, S.J. (1991): *"Regional Fractures II: Fracturing or Mesaverde Reservoirs in the Piceance Basin, Colorado"*. AAPG Bulletin, v. 75, no. 11, p. 1738-57.

Lorenz, J.C. and Hill, R.E. (1991): *"Subsurface Fracture Spacing: Comparison of Interferences from Slant/Horizontal Core and Vertical Core in Mesaverde Reservoirs"*. Paper SPE 21877 Symposium on Low Permeability Reservoirs, Denver, Colorado, 1991, p 705-716.

Lorenz, J.C. and Teufel, L.W. and Warpinski, N.R. (1991): *"Regional Fractures I: A Mechanism for the Formation of Regional Fractures at Depth in Flat-Lying Reservoirs"*. AAPG Bulletins, v.75. no.11, p 1714-1737.

Lorenz, J.C., Billingsley, R.L and Evans, L.W. (1998): *"Permeability Reduction by Pyrobitumen, Mineralization and Stress along Large Natural Fractures in Sandstones at 18,300-ft depth: Destruction of a Reservoir"*. SPE Reservoir Evaluation and Engineering, v. 1, p. 52-56.

Lorenz, J.C., N.R. Warpinski, L.W. Teufel, P.T. Branagan, A.R. Sattler, and D.A. Northrop (1988): *"Results of the Multiwell Experiment; In-situ Stresses, Natural Fractures, and other Geological Controls on Reservoirs"*. EOS, Transactions, American Geophysical Union, v. 69, n. 35, p. 817, p. 825-826.

Mayerhofer, M., Ehlig-Economides, C.A. and Economides, M.J. (1995): *"Pressure-Transient Analysis of Fracture-Calibration Tests"*. Journal of Petroleum Technology, v. 47 (March 1995), 3, p. 229-234.

McGuire, W.J. and Sikora, V.J. (1960): *"The Effect of Vertical Fractures on Well Productivity"*. Trans., AIME, 219, p. 401-01.

Mercer, J.C. and Frohne, K.H. (1986): *"Production Characterization of Tight Lenticular Gas Sands in the Rulison Area or Western Colorado"*. SPE Unconventional Gas Technology Symposium Proceedings, paper SPE 15248, p. 1-6.

Miskimins, J.L. (2002): *"The Effect of Thin-Bedded Sands and Shales on Hydraulic Fracture Growth Through the use of Electrofacies and Hydraulic Fracture Modeling"*. PhD Dissertation - Petroleum Engineering, Colorado School of Mines, Golden, Colorado, p. 258.

Mukherjee, H., Poe B., Heidt H., Watson T. and Barree R.D. (1995): *"Effect of Pressure Depletion on Fracture Geometry Evolution and Production Performance"*. Paper SPE 30481 presented at the 1995 SPE Annual Technical Conference and Exhibition, Dallas, Oct.22-25.

Nolte K.G. (1986): *"A General Analysis of Fracturing Pressure Decline with Application to Three Models"*. SPEFE (Dec. 1986) 571-83, Trans AIME, p. 281.

Nolte, K.G. (1988): *"Principles for Fracture Design Based on Pressure Analysis"*. SPE Production Engineering 3. p. 31-42.

Nolte, K.G. (1997): *"Background for After-Closure Analysis of Fracture Calibration Tests"*. Paper SPE 39407, unsolicited companion to paper SPE 38676 presented at the 1997 SPE Annual Technical Conference and Exhibition, San Antonio, Texas 5-8 Oct.

Nolte, K.G., Maniere, J.L., and Owens, K.A (1997): *"After-Closure Analysis of Fracture Calibration Tests"*. Paper SPE 38676 presented at the 1997 SPE Annual Technical Conference and Exhibition, San Antonio, Oct. 5-8.

Northrop, D.A. and Frohne, K-H (1990): *"The MuItiwell Experiment—A Field Laboratory in Tight Gas Sandstone Reservoirs"*. Paper SPE 18286, Journal of Petroleum Technology (June 1990).

Pantoja, D. (1998): *"Petrophysical Analysis of Vuggy Carbonates and Thin-Bedded Sands and Shales for Improved Reservoir Management"*. MS Thesis - Petroleum Engineering, Colorado School of Mines, Golden, Colorado, p. 226.

Perkins, T.K. and Kearn, L.R. (1961): *"Widths of Hydraulic Fractures"*. Journal of Petroleum Technology (Sept 1961), 937-49; Trans., AIME, p. 222.

PTTC Basin-Centered Gas Symposium (2000), Rocky Mountain Region, The Rocky Mountain Association of Geologists and the Gas Technology Institute, October 6th 2000, Denver, Colorado.

Ren, N.K. and Hudson, P.J. (1985): *"Predicting In-situ Stress State Using Differential Wave Velocity Analysis"*. Proc 26th Symp. on Rock Mechanics, Rapid City, SD, p. 1235-46.

Ren, N.K. and Roegiers, J.C. (1983): *"Differential Strain Curve Analysis – A New Method for Determining the Pre-existing In-situ Stress State from Rock Core Measurements"*. Proc ISRM Congress, Melbourne, p. F117-27.

Rice, J. and Cleary, M. (1976): *"Some Basic Stress Diffusion Solutions for Fluid-Saturated Elastic Porous Media with Compressible Constituents"*. Rev. Geophys. And Space Phys., 14, p. 227-241.

Schroeder, J.E. (1997): *"MWX Final report: Hydraulic Fracture Model and Diagnostics Verification at GRI/DOE Multi-site Projects and Tight Gas Sand Program Support"*. July 28, 1993 – February 28, 1997, DOE Contract # DE-FC21-93MC30070.

Schubarth, S.K., Mullen M.J. and Seal, C.A. (1998): *"Reservoir Description Techniques Improves Completion Economics in Piceance Basin Mesaverde Project"*. Paper SPE 39918, presented at the 1996 Low Permeability Symposium, 5-8 April , p 57-61.

Settari, A. and Cleary, M.P. (1986): "*Development and Testing of a Psuedo-Three-Dimensional Model of Hydraulic Fracture Geometry"*. SPE Production Engineering, paper SPE 10505, p. 449-466.

Sikora, V.J. (1960): *"The Effect of Vertical Fractures on Well Productivity*". Trans., AIME (1960) 219, p. 401-03

Smith, M.B., Rosenberg, R.J. and Bowen, J.F. (1982): *"Fracture Width- Design versus Measurement"*. Paper SPE 10965 presented at the 1982 SPE Annual Technical Conference and Exhibition, New Orleans, Sept 26-29.

Shanley, K.W., Cluff, R.W. and Robinson J.W. (2004): *"Factors Controlling Prolific Gas Production from Low Permeability Sandstone Reservoirs: Implications for Resource Assessment, Prospect Development and Risk Analysis"*. AAPG Bulletin, Vol. 88, No. 8, 2004, p. 1089-1121.

Teufel, L. (1996): *"Influence of Pore Pressure and Production-induced Changes in Pore Pressure on In-situ Stress"*. SANDIA report SAND96-0534 UC-132, Feb 1996, p. 54.

Teufel, L.W. and Clark, J.A. (1984): *"Hydraulic Fracture Propagation in Layered Rock: Experimental Studies of Fracture Containment"*. SPE Journal, v. 24, 2, p. 19-32.

Tiab, D. and Donaldson, E.C. (1999): *"Petrophysics: Theory and Practice of Measuring Reservoir Rock and Fluid Transport Properties"*. Gulf Publishing Company, Houston, Texas, p. 706.

Tyler, R., and McMurry, R.G (1995): *"Genetic Stratigraphy, Coal Occurrence and Regional Cross Section of the Williams Fork Formation, Mesaverde Group, Piceance Basin, Northwestern Colorado"*. Colorado Geological Survey Open-File Report No 95-2: 42, 1 sheet.

Ward, J.S. and Morrow, N.R. (1987): *"Capillary Pressures and Gas Relative Permeabilities of Low-Permeability Sandstone"*. SPE Formation Evaluation (Sept. 1987), p. 345-56.

Warpinski, N.R., Moschovidis, Z.A., Parker, C.D. and Abou-Sayed, I.S. (1993): "*Comparison Study of Hydraulic Fracturing Models: Test Case--GRI-Staged Field Experiment No. 3"*. Paper SPE 25890, SPE Rocky Mountain Regional/Low Permeability Reservoirs Symposium, Denver, Colorado, p. 469-478.

Warpinksi, N.R, Branagan, P.T. and Wilmer R. (1985): *"In-Situ Stress Measurements at DOE's Multi-Well Experiment Site, Mesaverde Group, Colorado"*. J. Petro. Tech., 37, p. 527-36.

Warpinski, N.R. (1996): *"Hydraulic Fracture Diagnostics"*. Journal of Petroleum Technology, paper SPE 36361, p. 907-910.

Warpinski, N.R. and Smith, M.B. (2001): *SPE Monograph Volume 12 - "Recent Advances in Hydraulic Fracturing, Chapter 3: Rock Mechanics and Fracture Geometry"*. p.57-80.

Warpinski, N.R. and Teufel, L.W. (1987): *"Influence of Geologic Discontinuities on Hydraulic Fracture Propagation"*. Paper SPE 13224, Society of Petroleum Engineers Journal, v. 27, 2, p. 209-220.

Warpinski, N.R. and Teufel, L.W.(1989): *"In-situ Stress Measurements in Low Permeability, Non-Marine Rocks"*. J. Petro Tech., 41., p. 405-414.

Warpinski, N.R. and Teufel, L.W.(1992): *"Determination of the Effective Stress Law for Permeability and Deformation in Low-Permeability Rocks"*. SPE Formation Evaluation (June 1992), p. 123-31.

Warpinski, N.R. and Wright, T.B. (1996): *"Fracture Diagnostics Research at the GRI/DOE Multi-Site Project – Overview of the Concepts and Results"*. Paper SPE 36449, presented at the 1996 SPE Conference Denver, Colorado. 5-9th October.

Warpinski, N.R. et al.(1996): *"Microseismic Monitoring of the B Sand Hydraulic Fracture Experiment at the DOE/GRI Multi-Site Project"*. Paper SPE 36450 presented at the 1996 SPE Annual Technical Conference and Exhibition, Denver, Oct. 6-9.

Warpinski, N.R. (1989): *"Elastic and Viscoelastic Calculations of Stresses in Sedimentary Basins"*. SPE Formation Evaluation, 3, p. 522-530.

Warpinski, N.R., Branagan, P.T., Peterson, R.E., Wolhart, S.L. and Uhl, J.E. (1998 a): *"Mapping Hydraulic Fracture Growth and Geometry Using Microseismic Events Detected by a Wireline Retrievable Accelerometer Array"*. Paper SPE 40014, SPE Gas Technology Symposium, Calgary, Alberta, Canada, p. 335-346.

Warpinski, N.R., Branagan, P.T., Peterson, R.E. and Wolhart, S.L.. (1998 b): *"An Interpretation of M-Site Hydraulic Fracture Diagnostic Results"*. Paper SPE 39950 presented at the 1998 SPE Rocky Mountain Regional/Low-Permeability Reservoirs Symposium and Exhibition, Denver, CO, 5-8 April.

Warpinski, N.R., Peterson, R.E., Branagan, P.T., Engler, B.P. and Wolhart, S.L. (1998 c): *"In-Situ Stress and Moduli: Comparison of Values Derived from Multiple Techniques".* Paper SPE 49190, SPE Annual Technical Conference and Exhibition, New Orleans, Louisiana, 27-30 September, p. 569-583.

APPENDIX A

MODEL INPUTS

Summary of Data

The following section describes in more detail the G-function analysis mentioned in Chapter 2, Section 2.6 and the rock property correlations used in this study. The graphs used by LOCALC to calculate the rock properties (see Figures A-1 and A-2) used in the simulator set-up and the rock property data (see Table A-1 and A-2) from the MWX site are shown, as is the permeability from porosity correlation used by Ward and Morrow (1987) for tight gas sands (see Figure A-3).

Attached on the accompanying CD-ROM are the following that relate to this input section: the mini-frac analyses reports for both the comparison well (Reports A-1 to A23) and the study well (Reports A-24 to A-56).

A-1 G-Function Analysis

Nolte (1986) originally developed type-curves for pressure decline analysis and later (Gidley et al, 1989) derived the G-function for use in analyzing data. The following section describes Nolte's porous-balloon analogy which was used to describe the relationships of width, fluid efficiency, penetration and fluid-loss coefficients to both pressure decline and closure time after injection. The following is taken extensively from Nolte (Gidley et al, 1989).

After injection of a fluid into a formation, the fluid loss rate after shut-in is given by:

$$q_l(t) = \frac{2Cf_pA_f}{\sqrt{t_i}} f(t_d) \tag{A-1}$$

and,

$$t_D = \frac{(t - t_i)}{t_i} = \frac{t}{t_i} - 1 \tag{A-2}$$

where:	q_l	=	fluid loss rate
	C	=	fluid loss coefficient
	f_p	=	ratio of permeable to fracture areas
	A_f	=	fracture area
	$f(t_D)$	=	dimensionless fluid loss rate
	t_i	=	injection time
	t_D	=	dimensionless time ($^t/_{ti}$-1)
	t	=	time since the start of injection

Integrating Equation 3.1 gives the volume of fluid lost for the period of time after shut-in:

$$V_{ls} = 2Cf_p A_f \sqrt{t_i}\left[g(t_D) - g(0)\ \right] \tag{A-3}$$

where:	V_{ls}	=	volume loss after shut-in
	$g(t_D)$	=	dimensionless loss-volume function
	$g(0)$	=	$g(t_D = 0)$

The volume of fluid lost during pumping was shown to give the upper limit, g(0) = 4/3 where the dimensionless loss-volume fraction, $g(t_D)$ was defined as:

$$g(t_D) = \int f(t_D)dt_d = \frac{4}{3}\left[\ (1+t_D)^{\frac{3}{2}} - t_D^{\frac{3}{2}}\ \right] \tag{A-4}$$

Nolte (Gidley et al, 1989) then derived the pressure difference in terms of dimensionless time:

$$\Delta p_n(t_D{}^*, t_D) = \frac{2Cf_p\sqrt{t_i}}{c_f}\left[\ g(t_D) - g(t_D{}^*)\ \right] \tag{A-5}$$

Nolte (Gidley et al, 1989) then went on to define a dimensionless difference function $G(t_D,t_D{}^*)$ and a match pressure decline, p* where:

$$G(t_D, t_D*) = \frac{4}{\pi}[\ g(t_D) - g(t_D*)\ ] \tag{A-6}$$

and,

$$p* = \Delta p_n(t_D*, t_D) \text{ when } G(t_D, t_D*) = 1 \tag{A-7}$$

where:	$G(t_D,t_D*)$	=	dimensionless difference function
	$t*_D$	=	reference value of t_D at shut-in
	$p*$	=	match decline pressure
	Δp_n	=	difference in net pressure i.e. wellbore pressure (p_w) – closure pressure (p_c)

Fluid efficiency (η) is the volume stored in the fracture at the end of pumping (V_f) divided by the total volume injected (V_l). Where negligible fluid loss can be assumed the fracture growth can be calculated bounded by an upper limit (η = 1) similarly significant losses will be bounded by a lower limit (η = 0). In the Mesaverde the low permeability and minimal fluid loss mean that an upper limit boundary effect can be used for analysis and this was applied for the analysis. Substituting Equation A-6 in Equation A-5 gives:

$$\Delta p_n(t_D*, t_D) = \frac{2Cf_p\sqrt{t_i}}{c_f} G(t_D, t_D^*) \tag{A-8}$$

Therefore, Nolte showed that a linear plot of pressure versus G-Function, $G(t_D)$, should provide an estimate of p* and closure pressure (P_c), if P_c remains constant. For this to apply he assumed that the following remained constant throughout the procedure: fluid density, fracture area, dimensionless fluid distribution in the fracture, fracture compliance and fluid loss area and coefficient.

The major improvement in the sensitivity of the technique came about because of work by Ayoub et al (1992) who applied a pressure derivative (*dP/dG*), similar to that applied in the pressure transient analysis of wells. The pressure derivative provided a more sensitive method of determining closure pressure. Barree and Mukherjee (1996) have shown how the G-function analyses can be used to determine and quantify the type of leakoff mechanism occurring during the mini-fracture test. They used a G-function method that not only required plotting the bottomhole pressure, the derivative of pressure but also a "superposition" derivative (*GdP/dG*) against the G-function, to minimize diagnostic ambiguities. Leakoff mechanisms were identified by the characteristic shapes of the derivative curves and fracture closure identified when the data deviated from the extrapolated straight line. Barree (1998) later published work showing field examples where four main types of leakoff mechanism were identified: normal leakoff (where the superposition derivative follows a straight line extrapolated from the origin), pressure dependent leakoff from fissure opening, fracture tip extension after shut-in and changing compliance during shut-in.

A-2 Rock Properties

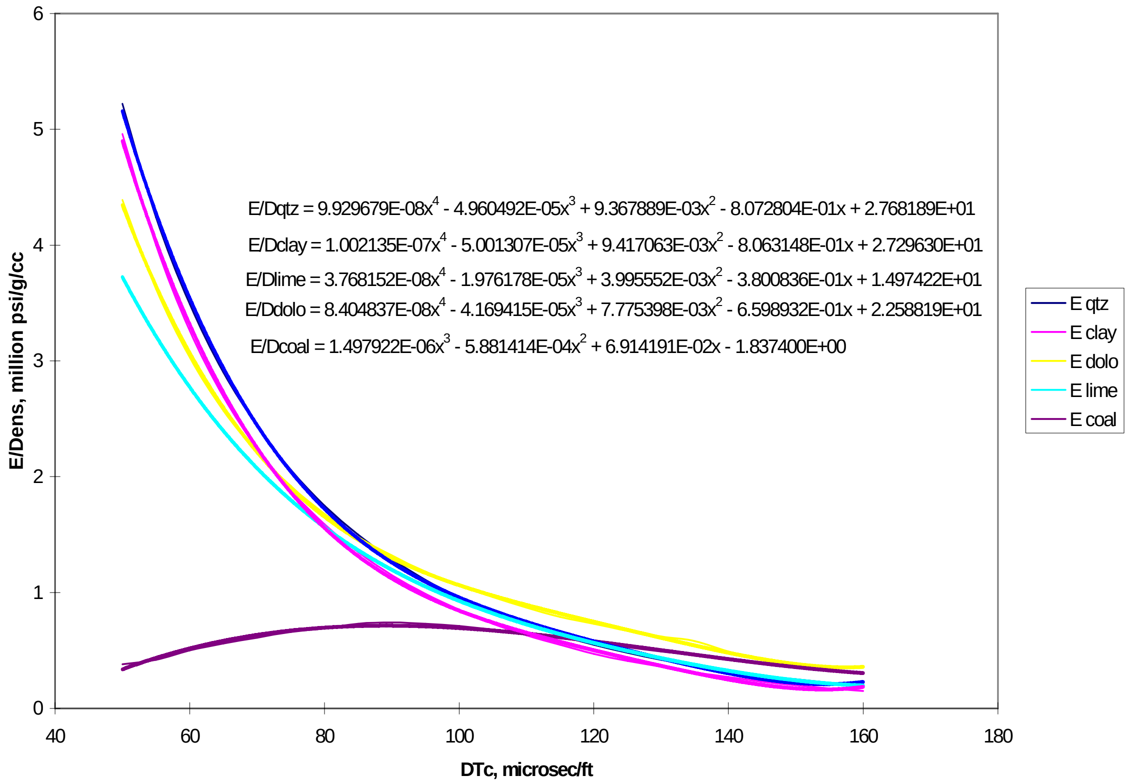

Figure A-1: Young's Modulus/Density ratio curves used to estimate lithology and compressional wave times in LOGCALC (courtesy of Barree and Associates).

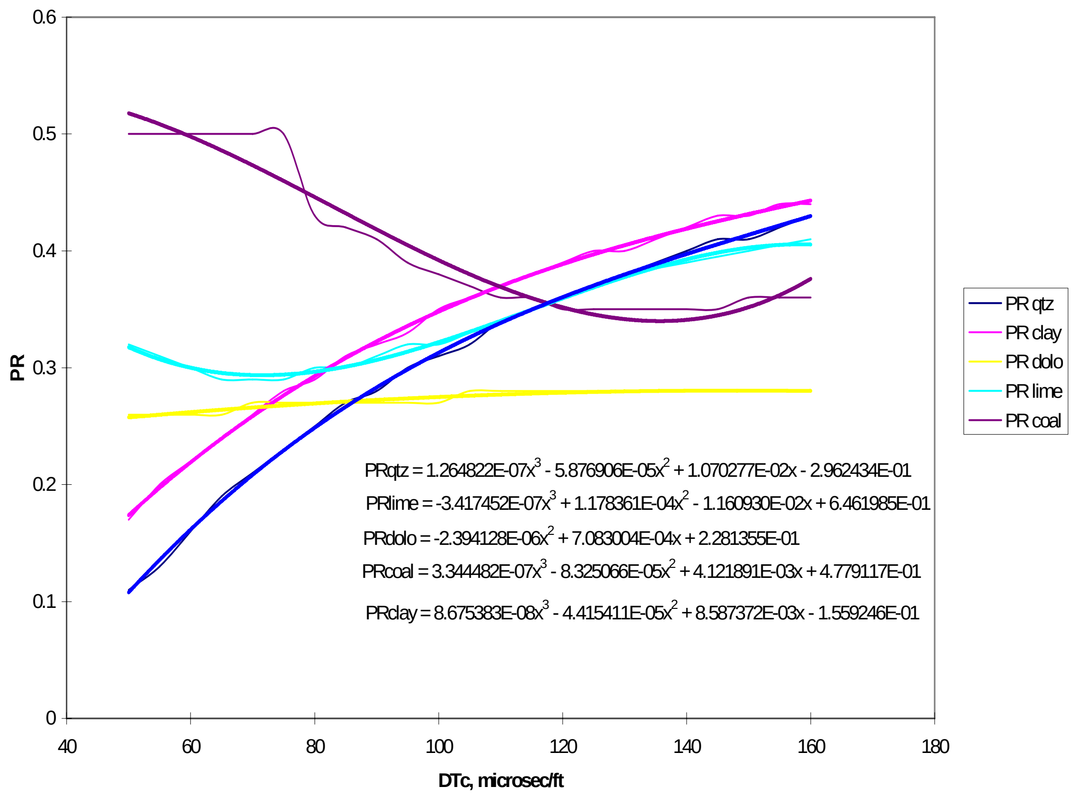

Figure A-2: Poisson's Ratio curves using estimated lithology and compressional wave times in LOGCALC (courtesy of Barree and Associates).

Table A-1: Rock Properties Measured at the MWX-1 Site

Lithology	Depth (ft)	Confining Stress (PSI)	Young's Modulus (PSI)	Poisson's Ratio	Tensile Strength (PSI)	Compressive Strength (PSI)	Fracture Toughness PSI sq(in)
MWX-1							
Sandstone	4300.3-4300.7	0	4,031,000	0.19	2183.7	16,951	1282.83
(C sand)	4301.7-4302.6	1450	4,814,000	0.18		31,030	
	4321.6-4322.8	2900	5,350,500	0.16		37,918	
		4350	5,582,500	0.2		44,153	
		7250	6,496,000	0.36		51,098	
Very fine sandstone with carbonaceous stringers	4492.7-4493.7	0				1628.56	
		1450	7,105,000	0.16		45,095	
		4350	7,511,000	0.17		49,561	
Mudstone	4498.4-4498.9	1450	2,102,500	0.13		11,716	
Sandstone	4550.6-4551.1	0			1223.8		
(B sand)		1203.5	4,089,000	0.19		28,333	
		4350	5,060,500	0.2		42,978	
Carbonaceous Mudstone	4612.6-4613.6	0			536.5		
Mudstone	4713.3-4714.4	0			1247		
		1450	2,421,500	0.13		14,152	
Siltstone	4893.5-4894.0	1450	5,394,000	0.17		33,060	
		2900	5,524,500	0.17		39,092	
		4350	6,191,500	0.17		36,845	
Silty Mudstone	4922.6-4923.2	1450	3,422,000	0.13		18,357	
		2900	3,567,000	0.13		23,331	
Sandstone	4946.0-4946.7	0	2,015,500	0.17	807.65	13,485	755.14
(A sand)	4947.2-4948.6	1450	3,277,000	0.17		20,576	
		2900	3,755,500	0.2		26,042	
		4350	3,871,500	0.17		30,044	
		7250	4,785,000	0.31		43,950	

Table A-2: Rock Properties Measured at the MWX-2. MWX-3 and Monitor Well Sites

Lithology	Depth (ft)	Confining Stress (PSI)	Young's Modulus (PSI)	Poisson's Ratio	Tensile Strength (PSI)	Compressive Strength (PSI)	Fracture Toughness PSI sq(in)
MWX-2							
Muddy Siltstone	4871.5-4872.9	0			1126.65	1473.89	
		1450	4,089,000	0.24		19,648	
		2900	4,364,500	0.2		25,172	
		4350	4,031,000	0.22		25,390	
Muddy Siltstone	4894.5-4895.6	0	3,233,500	0.24	1339.8	5,829	
		1450	3,378,500	0.21		18,169	
		2900	3,393,000	0.27		18,328	
Sandstone	4913.0-4913.8	0	3,335,000	0.19	1241.2	17,545	
(A sand)		1450	4,495,000	0.21		26,231	
		2900	4,857,500	0.2		32,625	
		4350	4,959,000	0.18		38,701	
Sandstone	4932.7-4933.7	0	3,219,000	0.18	1457.25	18,604	1000.79
(A sand)	4933.7-4934.7	1450	4,335,500	0.17		27,217	
		2900	4,712,500	0.17		31,494	
		4350	4,886,500	0.18		35,293	
MWX-3							
Sandstone	4913.9-4914.9	0			1522.5	1119.07	
(A sand)		1450	3,465,500	0.28		20,692	
		2900	4,089,000	0.22		26,187	
Monitor Well							
Sandstone	4316-4321	0				22,000	
(C sand)		500	5,400,000			28,500	
		480	5,400,000	0.22		29,600	
		1000	4,700,000	0.28		30,900	
		2000	5,100,000	0.23		36,300	
		4000	5,900,000	0.22		49,700	
		10000	6,400,000	0.16		74,800	

A-3 Permeability Correlation

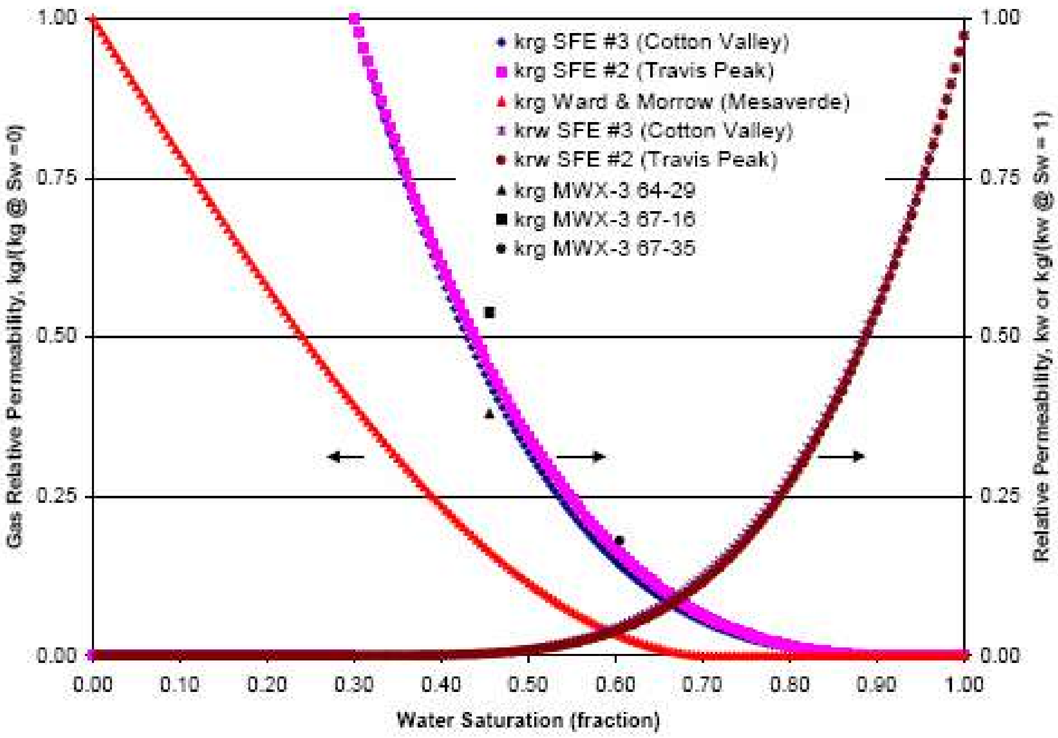

Figure A-3: A graph of the Ward and Morrow tight sandstone correlation, from Craig (1992).

APPENDIX B

SIMULATOR OUTPUTS: CASES 1 TO 11

Summary of Data

The attached CD-ROM contains the files for the matched model as well as the eleven sensitivity modeling cases, developed in Chapter 3 and discussed in Chapter 4, in the folder labeled "Appendix B." The eleven cases are in the respective folders and Each file contains the following simulator outputs: net surface pressure (psi) plots, net pressure (psi) output grid, fracture width (in) grid, proppant concentration (lb/ft^2) and conductivity grid (md-ft). Each file in the folders is labeled as follows:

B1 – Match
B2 - Case 1
B3 - Case 2
B4 – Case 3
B5 – Case 4
B6 – Case 5
B7 – Case 6
B8 – Case 7
B9 – Case 8
B10 – Case 9
B11 – Case 10
B12 – Case 11.